University Of Zagreb
Faculty Of Mechanical Engineering
and Naval Architecture

Université Paris-Saclay
École Normale Supérieure Paris-Saclay

Andrija Zaplatić

Characterization of thin structures under in-plane biaxial loading regimes using non-destructive testing methods

INTERNATIONAL DUAL DOCTORAL THESIS

Zagreb, 2025

University Of Zagreb
Faculty Of Mechanical Engineering
and Naval Architecture

Université Paris-Saclay
École Normale Supérieure Paris-Saclay

Andrija Zaplatić

Characterization of thin structures under in-plane biaxial loading regimes using non-destructive testing methods

INTERNATIONAL DUAL DOCTORAL THESIS

SUPERVISORS: Associate professor Zvonimir Tomičević, PhD
Research professor François Hild, PhD, hab.

Zagreb, 2025

Université de Zagreb
Faculté de Génie Mécanique et d'Architecture Navale

Université Paris-Saclay
École Normale Supérieure Paris-Saclay

Andrija Zaplatić

Caractérisation des structures minces sous régimes de chargement biaxial dans le plan à l'aide de méthodes d'essais non destructifs

THÈSE DOCTORALE INTERNATIONALE EN COTUTELLE

DIRECTEURS DE THÈSE: Zvonimir Tomičević, PhD, Professeur associé
François Hild, Directeur de recherche CNRS, PhD, habil.

Zagreb, 2025

Sveučilište u Zagrebu
Fakultet strojarstva i brodogradnje

Université Paris-Saclay
École Normale Supérieure Paris-Saclay

Andrija Zaplatić

Karakterizacija tankostijenih konstrukcija pri ravninskom dvoosnom opterećenju primjenom metoda nerazornih ispitivanja

MEĐUNARODNI DVOJNI DOKTORSKI RAD

MENTORI: Izv. Prof. dr. sc. Zvonimir Tomičević
Prof. dr. sc. François Hild

Zagreb, 2025

Bibliography data

Keywords:	Modified Arcan Fixture; Digital Image Correlation; Digital Volume Correlation; Infrared Thermography; Hybrid Multiview Correlation; Multi-modal Correlation; Inverse identification; Thin sheets; Composite; Dirichlet Boundary Conditions;
Scientific area:	Technical Sciences
Scientific field:	Mechanical Engineering
Institutions:	Faculty of Mechanical Engineering and Naval Architecture
	École Normale Supérieure Paris-Saclay
Thesis supervisors:	Dr. Zvonimir Tomičević, Associate Professor
	Dr. hab. François Hild, Research Professor
Number of pages:	352
Number of figures:	17
Number of tables:	7
Number of references:	131
Date of public defence:	September 5th, 2025.

Thesis committee:

Dr. Darko Ivančević, Associate professor, Chairman of the Defence Committee

Dr. Lovre Krstulović-Opara, Professor, member

Dr. Daniel Kytýř, Associate professor, reporter

Dr. Jan Neggers, Maître de conférences, member

Dr. Christophe Bouvet, Professor, member

Dr. Fabien Amiot, Directeur de recherche, reporter

Archive:	Faculty of Mechanical Engineering and Naval Architecture http://www.theses.fr/

Contents

List of figures

List of tables

List of abbreviations

Label	Full meaning
1D	One Dimensional
2D	Two Dimensional
3D	Three Dimensional
4D	Four Dimensional
AM	Arcan modifié
B	Brightness
BC(s)	Boundary Condition(s)
BCC	Brightness and Contrast Corrections
C	Contrast
CAD	Computer-Aided Design
CEGM	Constitutive Equilibrium Gap Method
CT	Computed Tomography
DIC	Digital Image Correlation
DOF(s)	Degree(s) Of Freedom
DVC	Digital Volume Correlation
EGM	Equilibrium Gap Method
FE	Finite Element
FEMU	Finite Element Model Updating
FRP	Fibre Reinforced Polymer
UNIZGFSB	University of Zagreb, Faculty of Mechanical Engineering and Naval Architecture
HMC	Hybrid Multiview Correlation

IR	InfraRed
IRT	Infrared Thermography
LEM	Laboratory of Experimental Mechanics
LMPS	Laboratoire de Mécanique Paris-Saclay
MAF	Modified Arcan Fixture
MMC	Multi Modal Correlation
NDT	Non-Destructive Testing
PDVC	Projection based Digital Volume Correlation
PMMA	Poly Methyl Methacrylate
PnP	Point-*n*-Perspective
RBM(s)	Rigid Body Motion(s)
ROI	Region Of Interest
SC	Stereocorrelation
SDIC	Stereo Digital Image Correlation
VFM	Virtual Fields Method
XCT	X-ray Computed Tomography

Abstract

The aim of this dissertation is to develop a robust experimental protocol for characterising thin metallic and composite structures under multiaxial loadings. Mechanical testing is crucial for predicting the material behaviour under complex loading conditions. Thin structures often experience buckling in compressed zones during shear, compromising their integrity and reducing service life. To address this issue, stabilisation adapters were designed and validated for the Modified Arcan Fixture (MAF) to suppress shear buckling and enable for accurate material characterisation. Their effectiveness was further validated using Finite Element (FE)-based stereocorrelation (SC). Finite Element Model Updating (FEMU) was employed to calibrate the friction coefficient between the adapters and the sample surface. The measured displacements were applied as Dirichlet boundary conditions in the numerical model, and their influence on the stress triaxiality fields was evaluated, demonstrating their critical role in the numerical model accuracy. Limited sample buckling could be simulated accurately. Furthermore, trustworthy material parameters were calibrated by including the stabilisation adapters in the numerical model. Moreover, FEMU was employed to evaluate two sample geometries and revealed that the sample geometry played a key role in activating specific material parameters.

The upgraded MAF setup was then applied to Fibre Reinforced Polymers (FRPs), which are widely used in demanding applications due to their high strength-to-weight ratio and customizable mechanical properties. To characterise FRPs, an FE-based hybrid multiview correlation method was used, integrating infrared and visible light imaging to quantify strain localisation and temperature variations in samples subjected to three different loading regimes, namely, tension, simple shear, and their combination at a 45° angle. Multiaxial mechanical testing revealed variations in strain and temperature distributions for different loading regimes. Additionally, a multi-modal correlation method was developed, incorporating visible light, infrared, and X-ray imaging within a unified FE framework. This approach enabled for detailed surface strain and temperature field measurements correlated with 3D bulk strain fields measured via Digital Volume Correlation (DVC), allowing for the identification of multiple damage mechanisms based on surface and bulk kinematics as well as correlation residuals.

Résumé

L'objectif de cette thèse est de développer un protocole expérimental robuste pour la caractérisation de structures minces métalliques et composites soumises à des chargements multiaxiaux. Les essais mécaniques sont essentiels pour prédire le comportement des matériaux sous des conditions de chargement complexes. Les structures minces subissent souvent du flambement dans les zones comprimées lors de chargements en cisaillement, ce qui compromet leur intégrité et réduit leur durée de vie. Pour remédier à ce problème, des adaptateurs de stabilisation ont été conçus et validés pour le dispositif Arcan modifié (AM), afin de supprimer le flambement en cisaillement et de permettre une caractérisation précise du matériau. Leur efficacité a été validée par stéréocorrélation d'images globale. La mise à jour de modèles éléments finis (FEMU) a été utilisée pour identifier le coefficient de frottement entre les adaptateurs et la surface de l'échantillon. Les déplacements mesurés ont été appliqués comme conditions aux limites de Dirichlet dans le modèle numérique, et leur influence sur les champs de triaxialité des contraintes a été évaluée, démontrant leur rôle essentiel dans la précision du modèle. Un flambement limité de l'échantillon a pu être simulé avec précision. De plus, des paramètres fiables ont été obtenus en incluant les adaptateurs de stabilisation dans le modèle numérique. Par ailleurs, la méthode FEMU a été utilisée pour évaluer deux géométries d'échantillons et a révélé que la géométrie jouait un rôle clé dans l'activation de certains paramètres matériels.

Le dispositif AM a ensuite été appliqué aux polymères renforcés de fibres (FRP), largement utilisés dans les applications fortement sollicitantes en raison de leur rapport résistance / masse élevé et de leurs propriétés mécaniques modulables. Pour caractériser ces FRP, une méthode de corrélation hybride basée sur les éléments finis a été utilisée, intégrant des images infrarouges et en lumière visible afin de quantifier la localisation des déformations et les variations de température dans des échantillons soumis à trois régimes de chargement différents : traction, cisaillement simple, et leur combinaison à un angle de 45°. Les essais mécaniques multiaxiaux ont mis en évidence des distributions différentes de déformation et de température selon le régime de chargement. De plus, une méthode de corrélation multi-modale a été développée, intégrant des images en lumière visible, infrarouge et par rayons X dans un cadre unique. Cette approche a permis des mesures détaillées des champs de déformation et de température en surface, corrélées

aux champs de déformation volumiques 3D mesurés par corrélation d'images volumiques (DVC), permettant l'identification de multiples mécanismes d'endommagement à partir des cinématiques de surface et de volume ainsi que les résidus de corrélation.

Sažetak

Cilj ove disertacije je razvoj robusnog eksperimentalnog protokola za karakterizaciju tankostijenih metalnih i kompozitnih konstrukcija izloženih višeosnim opterećenjima. Mehanička ispitivanja ključna su za predviđanje ponašanja materijala pod složenim režimima opterećenja. Tankostijene konstrukcije često doživljavaju izvijanje u tlačnim zonama tijekom smicanja, što narušava njihov mehanički integritet i skraćuje vijek trajanja. Kako bi se riješio ovaj problem, konstruirani su i validirani stabilizacijski adapteri za modificirani Arcan prihvat (eng. *Modified Arcan Fixture* - MAF), s ciljem sprječavanja izvijanja i omogućavanja potpune karakterizacije materijala uslijed smicanja. Njihova učinkovitost dodatno je potvrđena primjenom stereo korelacije (SC), temeljene na Metodi Konačnih Elemenata (MKE). Metoda ažuriranja modela konačnih elemenata (eng. *Finite Element Model Updating* – FEMU) korištena je za kalibraciju koeficijenta trenja između adaptera i površine ispitnog uzorka. Izmjereni pomaci primijenjeni su u numeričkom modelu kao Dirichletovi rubni uvjeti pomaka, a njihov je utjecaj na polja triaksijalnosti detaljno analiziran. Ustanovljeno je da imaju ključnu ulogu u osiguravanju točnosti numeričkog modela. Ograničeno izvijanje ispitnog uzorka bilo je moguće numerički simulirati. Uključivanjem stabilizacijskih adaptera u numerički model omogućena je kalibracija pouzdanih parametara materijala. Štoviše, FEMU metoda korištena je za evaluaciju dviju geometrija ispitnih uzoraka, pri čemu je pokazano da geometrija uzorka ima ključnu ulogu u aktivaciji osjetljivosti kalibracije određenih materijalnih parametara.

Unaprijeđeni MAF eksperimentalni postav zatim je primijenjen na polimerima ojačanim vlaknima (eng. *Fibre Reinforced Polymer* – FRP), koji se zbog visokog omjera čvrstoće i mase te prilagodljivih mehaničkih svojstava često koriste u konstrukcijama izloženima zahtjevnim opterećenjima. Za karakterizaciju FRP kompozita korišten je hibridni korelacijski algoritam temeljen na MKE metodi, koji integrira snimanje kamerama u vidljivom i infracrvenom spektru svjetlosti radi kvantificiranja lokalizacije deformacija i temperaturnih promjena na uzorcima podvrgnutima trima različitim režimima opterećenja: vlačnom, jednostavnom smiku te njihovoj kombinaciji pod kutom od 45°. Višeosna mehanička ispitivanja ukazala su na značajne odstupanja u raspodjeli deformacija i temperature, ovisno o vrsti primijenjenog opterećenja. Dodatno, razvijena je više-modalna korelacijska metoda koja integrira snimanje vidljivim svjetlom,

infracrvenim zračenjem i rendgenskim zrakama unutar jedinstvenog MKE okruženja. Ovaj pristup omogućio je detaljan uvid u polja deformacija i temperature povezane s trodimenzionalnim poljima deformacija unutar materijala, dobivena metodom Korelacije Digitalnih Volumena. Time je omogućena identifikacija različitih mehanizama oštećenja temeljenih na površinskoj i volumenskoj kinematici, kao i korelacijskim rezidualima.

Résumé Étendu

La caractérisation fiable des matériaux avancés soumis à des régimes de chargement complexes est essentielle pour prédire avec précision la durée de vie des composants mécaniques soumis aux charges en service prévues. L'intégration des simulations numériques dans le processus de conception a permis des avancées significatives dans la prédiction de la durée de vie des composants d'ingénierie [1]. Toutefois, la précision des calculs numériques dépend fortement des paramètres mécaniques du matériau étudié. Les industries mondiales telles que l'aéronautique et l'automobile utilisent des matériaux légers afin de réduire la masse des composants tout en conservant leur résistance. Les composites à matrice polymère renforcée de fibres (FRP) jouent un rôle clé dans ces secteurs, car leur architecture peut être adaptée à des régimes de chargement spécifiques. Cependant, pour caractériser avec précision les FRP, des investigations expérimentales approfondies à l'aide de méthodes avancées de caractérisation des matériaux doivent être réalisées. Il est donc important de mener des essais multiaxiaux afin de développer des prédictions plus fiables du comportement mécanique et des mécanismes d'endommagement des matériaux étudiés. Toutefois, les machines d'essai multiaxiales sont coûteuses et souvent indisponibles. Ainsi, des montages appropriés permettant d'appliquer des régimes de chargement biaxiaux sur des machines d'essai uniaxiales sont souvent utilisés comme alternative.

Le dispositif Arcan modifié (MAF) [2] se distingue comme le montage le plus polyvalent pour les machines d'essai uniaxiales en termes de chemins de chargement. Le concept du dispositif Arcan a été proposé afin de permettre l'application de trois modes de chargement en plan, à savoir (1) traction en plan, (2) cisaillement et (3) combinaisons biaxiales des deux. L'éprouvette correspondante (géométrie dite « papillon ») présente deux encoches en V symétriques [3]. Cette géométrie a été conçue pour induire des états de cisaillement quasi uniformes dans la zone de mesure située entre les encoches en V. Le dispositif Arcan proposé visait principalement à étudier le comportement des composites à matrice polymère renforcée de fibres (FRP) [4]. La caractérisation d'éprouvettes minces (épaisseur ≤ 3 mm) constituées de matériaux conventionnels soumis à des chargements complexes représente un défi. Des instabilités (c'est-à-dire du flambage) apparaissent lors des essais de cisaillement simple avec le MAF en raison du rapport important entre la largeur de la zone de mesure et l'épaisseur de l'éprouvette. De plus, des recherches antérieures [5] ont conclu que des perturbations de contraintes supplémentaires causées par le

serrage des éprouvettes dans les mors de la machine d'essai favorisent une initiation précoce du flambage et compromettent la fiabilité de la caractérisation des matériaux.

La méthode courante pour étudier le comportement des matériaux repose sur l'utilisation d'équipements de mesure classiques (par exemple, jauges de déformation, extensomètres mécaniques) permettant de déterminer l'historique des déformations. Cette approche ne fournit cependant la réponse du matériau qu'en un ou quelques points de la zone étudiée. Ainsi, la caractérisation de phénomènes localisés (par exemple, bandes de Lüders, bandes de cisaillement) n'est pas accessible. Pour capturer la réponse du matériau sur l'ensemble de la Région d'Intérêt (ROI), il est essentiel d'utiliser des méthodes de contrôle non destructif (CND) à champ complet. Grâce aux techniques optiques de CND à champ complet, les phénomènes de localisation tels que l'accumulation de déformations, l'initiation et l'évolution des dommages en surface deviennent observables. Parmi les différentes méthodes de mesure à champ complet, la Corrélation d'Images Numériques (CIN) [6] s'impose comme la plus largement utilisée en raison de son adaptabilité de l'échelle microscopique à l'échelle macroscopique. La CIN est un outil efficace pour capturer l'initiation et la propagation des dommages (par exemple, fissures) à partir des résidus de corrélation, c'est-à-dire la différence de niveaux de gris entre les images déformées corrigées et la configuration de référence au niveau des pixels [7]. Lors d'essais multiaxiaux, la CIN peut produire des mesures biaisées en raison de mouvements hors plan. Cet effet indésirable peut être évité en utilisant la stéréocorrélation pour mesurer les déplacements de surface en 3D [8]. Dans sa forme initiale, la CIN discrétise la ROI observée en un nombre fini de sous-ensembles (facettes) et mesure les déplacements au centre de chaque facette indépendamment de ses voisines. Cette approche est appelée CIN locale [9]. Cependant, les cinématiques mesurées indépendamment entraînent des discontinuités, ce qui nécessite une interpolation ultérieure entre les centres des facettes. À l'inverse, la CIN globale [10] repose sur une discrétisation par éléments finis (EF) et utilise un maillage EF correspondant à la géométrie de la ROI observée. La CIN basée sur les EF suppose la continuité du champ de déplacement (c'est-à-dire que toute la ROI maillée est utilisée pour minimiser les différences quadratiques entre les images de référence et déformées). Comparée à la CIN globale, l'approche locale est moins coûteuse en calcul. Toutefois, l'incertitude de mesure obtenue avec la CIN locale est plus élevée que celle de la méthode globale. De plus, puisque les résultats de la CIN globale sont des déplacements nodaux, elle constitue un choix approprié pour coupler les données mesurées expérimentalement avec les simulations numériques (EF) [11].

La méthode FEMU est la méthode de calibration des paramètres matériaux la plus largement utilisée, fondée sur la minimisation des moindres carrés des différences entre les données mesurées expérimentalement et les données numériques. Lecompte et al. [12] ont couplé des mesures locales de CIN et des simulations numériques dans une méthode inverse itérative de mise à jour de modèle par éléments finis (FEMU) [13] pour calibrer quatre paramètres élastiques et orthotropes indépendants de stratifiés en époxy renforcés par fibres de verre à partir d'essais biaxiaux. La méthode FEMU peut également être utilisée pour calibrer des paramètres élastoplastiques et de dommage [14]. En outre, Tomičević et al. [15] ont employé la méthode FEMU pour calibrer les paramètres des lois élastoplastiques et de dommage de la fonte à graphite sphéroïdal. Gras et al. [16] ont utilisé un environnement numérique unique pour calibrer les paramètres matériaux d'un spécimen en composite tissé 3D composé de quatre régions orthotropes locales différentes. Les champs de déplacement mesurés ont été obtenus par CIN globale, et le même maillage EF a été utilisé dans les simulations numériques. Une étude comparative menée par Roux et Hild [17], dans laquelle différentes méthodes d'identification inverse ont été analysées, a montré que la méthode FEMU pondérée présente la plus faible sensibilité à la présence de bruit dans les données.

Bien que la corrélation d'images numériques (CIN) puisse quantifier efficacement les zones d'accumulation de déformation, qui correspondent aux emplacements où des dommages macroscopiques ou mésoscopiques apparaîtront dans le cas des matériaux composites à matrice polymère (FRP), elle ne fournit pas d'information directe sur les mécanismes de dommage à l'intérieur du matériau. Par conséquent, plusieurs techniques de contrôle non destructif (CND) sont souvent utilisées pour la caractérisation des dommages [18]. La thermographie infrarouge (IRT) se distingue comme un outil fiable et indispensable pour l'observation CND des FRP, en raison de sa rapidité d'inspection, sa résolution élevée, sa sensibilité et sa capacité à détecter les défauts internes par la conduction thermique. Farmaki et al. [19] ont utilisé l'IRT pour évaluer les dommages dans les régions sous-jacentes d'une plaque composite. Wang et al. [20] ont utilisé l'IRT pour surveiller le flux thermique dans un acier austénitique en raison de dommages dus à la fatigue. Des méthodes couplant IRT et stéréocorrélation [21] ont été employées pour mesurer simultanément les distributions spatiales et temporelles des champs de température et de déplacement [22]. Wang et al. [23] ont amélioré la corrélation hybride en utilisant une caméra IR et deux caméras en lumière visible [24]. En outre, Charbal et al. [25] ont conçu une stratégie de régularisation spatio-temporelle pour les mesures hybrides, qui prend en compte les champs de

déplacement et de température en surmontant les grandes variations de niveaux de gris causées par les changements de température. Toutefois, l'IRT ne permet pas de caractériser l'interaction entre les déformations localisées et les dommages microstructuraux. Il est donc souhaitable, en complément de la corrélation hybride, d'employer également la tomographie par rayons X (XCT) couplée à la corrélation volumique numérique (DVC) [26]. Cela permet d'obtenir des informations sur l'architecture interne du composite [27]. Avec le protocole expérimental unique proposé, les trois méthodes de mesure indépendantes peuvent être intégrées dans une méthode de corrélation multimodale complète. Grâce à cette méthode d'inspection hybride, les champs de déplacement, de déformation et de température peuvent être déterminés à la surface de l'objet observé, tandis qu'avec la DVC, les champs de déplacement et de déformation peuvent être évalués à l'intérieur du volume de l'objet.

I. Objectif et hypothèses de recherche

L'objectif de cette recherche est le développement d'un protocole expérimental robuste pour la caractérisation complète des structures minces métalliques et composites soumises à des régimes de chargement multiaxiaux.

Hypothèses de recherche :

1. L'amélioration du montage Arcan avec des adaptateurs de stabilisation conçus pour les échantillons minces permettra d'effectuer des essais de cisaillement sans flambage des échantillons.

2. Le couplage de la Corrélation d'Images Numériques (DIC) et de la Thermographie Infrarouge (IRT) dans une méthode d'inspection hybride, combiné à l'utilisation de la tomographie par rayons X, offrira une compréhension complète du comportement des Polymères Renforcés de Fibres (PRF) soumis à des régimes de chargement multiaxiaux à l'aide du montage Arcan.

3. Les corrections de luminosité et de contraste des images numériques pendant les essais mécaniques amélioreront les champs de déplacement et de déformation obtenus par les caméras en lumière visible ainsi que les variations des champs de température mesurées par la caméra infrarouge.

II. Méthodes de recherche

Des conditions d'exploitation exigeantes nécessitent l'amélioration des propriétés mécaniques des matériaux d'ingénierie. Il est donc nécessaire de réaliser des essais mécaniques afin de prédire de manière fiable le comportement des matériaux utilisés lors de leur mise en service. Tout au long de leur durée de vie, les composants mécaniques sont soumis à des régimes de chargement complexes. Lorsque des structures minces sont soumises à un cisaillement, un flambage peut être initié dans les zones comprimées du matériau. L'apparition du flambage dégrade l'intégrité de la structure et réduit considérablement sa durée de vie. Il est donc crucial de déterminer les limites de chargement menant au flambage afin d'éviter ce phénomène indésirable. Il est nécessaire de réaliser des essais mécaniques sur des éprouvettes minces soumises au cisaillement. De plus, le flambage peut fausser la caractérisation du comportement du matériau lorsqu'on utilise des méthodes de mesure optiques. Dans le cadre de cette thèse, une solution de conception a été proposée pour éliminer le flambage des structures minces. Cette solution a été validée expérimentalement à l'aide du montage Arcan modifié, qui permet d'appliquer un cisaillement aux échantillons testés. Le dispositif expérimental amélioré a ensuite été utilisé pour caractériser les composites à matrice polymère renforcés de fibres (FRP), qui remplacent de plus en plus les matériaux d'ingénierie conventionnels dans les structures fortement sollicitées. Cela est dû à leur plus grande flexibilité d'adaptation des propriétés mécaniques aux charges prescrites, ainsi qu'à leur excellent rapport résistance/poids.

Le dispositif Arcan modifié (MAF) a été amélioré par l'ajout d'un adaptateur de stabilisation de l'éprouvette afin d'éviter le flambage de l'échantillon mince lors des essais en cisaillement simple. De plus, une contrainte supplémentaire de conception a été imposée à l'adaptateur de stabilisation : il devait être transparent pour permettre l'utilisation de la corrélation d'images numériques (DIC). Étant donné que des déplacements hors du plan étaient attendus, il a été nécessaire d'utiliser la stéréocorrélation. Comme la géométrie de l'échantillon était connue a priori, un algorithme global de stéréocorrélation par éléments finis (FE) a été utilisé, ce qui a permis à la fois la calibration du système de stéréovision et la mesure des déplacements.

Les essais de cisaillement simple, dans lesquels les adaptateurs de stabilisation de l'échantillon ont été utilisés, ont été analysés plus en détail. Étant donné que l'algorithme global

de stéréocorrélation est basé sur la méthode des éléments finis (EF), il est adapté pour être directement couplé aux simulations numériques grâce à la disponibilité du maillage EF. Ainsi, la méthode FEMU (mise à jour de modèle par éléments finis) a été utilisée pour déterminer les propriétés du matériau de la tôle mince soumise à un chargement en cisaillement simple. De plus, un modèle EF avancé, incluant les adaptateurs de stabilisation, a été défini, intégrant également le frottement entre l'échantillon et les adaptateurs. Le coefficient de frottement a ainsi pu être pris en compte dans la procédure d'identification. En outre, différentes combinaisons de conditions aux limites de type Dirichlet ont été prescrites au modèle EF de l'échantillon mince afin d'évaluer l'impact de ces conditions sur les champs de triaxialité des contraintes et les paramètres matériaux calibrés. La validation de la méthode FEMU a également été effectuée sur deux géométries d'échantillons distinctes en acier à haute résistance HARDOX 450 soumis à une traction uniaxiale.

En utilisant le MAF amélioré, des essais mécaniques multiaxiaux impliquant des échantillons en fibres de verre tissées de type "papillon" ont été réalisés. Les échantillons comportaient deux notches supplémentaires découpées dans les racines des notches en V afin de localiser davantage les déformations. Les échantillons ont été soumis à des chargements cycliques en traction, en cisaillement simple et à une combinaison de ces derniers à un angle de 45°. De plus, un système optique multimodal a été proposé, comprenant des caméras à lumière visible, une caméra infrarouge et un scanner CT (tomodensitométrie) à rayons X. Pendant les essais mécaniques, les échantillons ont été surveillés par les caméras hybrides à lumière visible/infrarouge, et entre les cycles de chargement prédéfinis, une tomodensitométrie a été réalisée. Les trois modalités ont été unifiées sur la même base EF pour obtenir les champs de déformation et de température de surface/volume pour la même discrétisation.

III. Résultats et conclusions

Dans cette thèse, des méthodes de mesure avancées ont été utilisées pour caractériser des matériaux en tôle mince soumis à des régimes de chargement complexes. La thèse est rédigée selon le modèle de thèse par articles multiples, qui se compose de sept articles scientifiques thématiquement reliés.

La procédure d'identification impliquant le FEMU a été définie dans **l'Article scientifique 1**, où elle a été appliquée à deux échantillons de géométries distinctes fabriqués à partir du même

matériau HARDOX 450. Le premier échantillon avait deux lignes parallèles dans la zone de mesure (DIN), tandis que le second était aminci avec des rayons au centre (forme de chien de chasse). Il a été conclu que la géométrie de l'échantillon influençait le protocole d'identification et donnait des paramètres matériels différents pour le même modèle. De plus, une analyse de sensibilité des paramètres matériels a été réalisée, où l'échantillon de type chien de chasse a montré une plus grande sensibilité aux paramètres élastiques. Une sensibilité similaire du stress de fluage a été observée pour les deux échantillons. En ce qui concerne les paramètres de durcissement, l'échantillon DIN était plus sensible, tandis que pour l'exposant de durcissement, l'échantillon de type chien de chasse a montré une plus grande sensibilité.

Dans **l'Article scientifique 2** et **l'Article scientifique 3**, l'analyse d'une expérience de cisaillement simple où le flambage a été supprimé a été rapportée. Tout d'abord, les adaptateurs de stabilisation ont été définis. Étant donnés qu'ils étaient fabriqués à partir de matériau transparent (polyméthacrylate de méthyle), l'utilisation de caméras optiques a été rendue possible. La stéréocorrélation a été utilisée pour mesurer la cinématique de la surface. Quatre expériences ont été réalisées avec différentes configurations expérimentales concernant l'épaisseur des adaptateurs de stabilisation, la rigidité de la connexion entre le MAF et la machine d'essai. Dans le cas où des adaptateurs de 10 mm d'épaisseur étaient utilisés et que la connexion n'était pas rigide, le flambage a été supprimé. Un test cyclique supplémentaire a été effectué pour valider le test monotone de cisaillement simple mentionné précédemment. De plus, en utilisant FEMU, le coefficient de friction entre les adaptateurs de stabilisation et l'échantillon a été évalué à $\nu = 0{,}33$, ce qui correspond aux valeurs rapportées dans la littérature. Cinq cas numériques ont été définis avec différentes définitions des conditions aux limites de Dirichlet mesurées. Les deux premiers cas ont été définis avec les adaptateurs de stabilisation, mais avec différents coefficients de friction. Le troisième cas ne considérait que les déplacements dans le plan, ce qui correspondait à un cas idéalisé. Le quatrième incluait des déplacements hors du plan sur les bords sollicités du modèle numérique. Le dernier cas testait les déplacements hors du plan prescrits à l'ensemble de la surface de mesure. En utilisant FEMU, l'influence des conditions aux limites sur les champs de triaxialité de contrainte a été évaluée. L'effet des conditions aux limites mesurées prescrites sur les paramètres matériels calibrés a également été évalué. Les cinq cas étudiés ont conduit à différents paramètres matériels, mais une influence négligeable sur les champs de triaxialité a été rapportée. Il a été conclu que, pour une calibration précise des paramètres matériels, le premier cas de test

était optimal car il incluait à la fois la friction et les adaptateurs de stabilisation. Le cinquième cas de test pouvait simuler un flambage limité, tandis que les deuxième, troisième et quatrième cas ne pouvaient pas. Ce cas a fourni une forme déformée précise d'une manière moins exigeante en termes de calculs que le premier cas de test.

Une méthode de corrélation semi-hybride a été proposée dans **l'Article scientifique 4**, où un essai de traction réalisé avec le MAF sur un échantillon de composite en fibres de verre tissées a été analysé. Dans cette procédure, les images de la caméra infrarouge ne sont pas directement impliquées dans le processus de corrélation. Cependant, les champs de température lagrangiens de la Région d'Intérêt pouvaient toujours être obtenus. En les comparant avec les champs de déformation obtenus par stéréocorrélation basée sur les éléments finis, les sources de chaleur correspondaient aux zones de dommage sur la surface de l'échantillon, et les régions de déformation par cisaillement étaient capturées à partir des entailles, bien que l'échantillon ait été soumis à une traction. Dans **l'Article scientifique 5** et **l'Article scientifique 6**, des expériences multiaxiales (traction, cisaillement simple et une combinaison de ces deux à un angle de 45°) réalisées via le MAF sur les échantillons de composite en fibres de verre tissées sont présentées. Pour **l'Article scientifique 5**, seule la méthode de stéréocorrélation en lumière visible a été utilisée, tandis que pour l'Article scientifique 6, la formulation hybride a été mise en œuvre. Dans la méthode de corrélation hybride, les images de la caméra infrarouge sont directement intégrées dans la procédure de corrélation. De plus, des corrections obligatoires de la luminosité et du contraste pour les images infrarouges sont introduites. Entre les expériences, l'essai de traction a montré les niveaux de contrainte les plus élevés, tandis que la charge combinée a entraîné les niveaux de déformation les plus élevés. Différentes distributions de déformation ont été observées entre les expériences. Dans l'essai de traction, deux bandes de déformation partant des racines des entailles ont été capturées. Pour le cisaillement simple et la charge combinée, une seule bande de déformation a été localisée entre les entailles V dans la région de jauge. Pour ce dernier, en raison de la traction, la bande de déformation était orientée sous un certain angle. De plus, plusieurs mécanismes de dommage ont pu être identifiés en utilisant uniquement les coupes de surface CT. Pour le cisaillement simple et la charge combinée, le décollement intra-fil a été capturé partant des entailles vers le centre de l'échantillon. Pour l'essai de traction, la rupture du fil, le décollement intra-fil et la fissuration de la matrice en surface ont été observés. Étant donné que la stéréocorrélation hybride a été utilisée, les champs de température lagrangiens ont également été

obtenus. Dans l'expérience de traction, les variations de température étaient principalement localisées autour des pointes des entailles, tandis que pour le cisaillement simple et la charge combinée, une seule bande de température a pu être identifiée entre les entailles.

Dans **l'Article scientifique 7**, la modalité des rayons X a été incluse dans la procédure de corrélation qui prenait en compte les images en lumière visible et infrarouge. Les trois modalités ont été combinées au sein d'un cadre FE unique dans une méthode de corrélation multimodale. Pour obtenir les données nécessaires à la procédure susmentionnée, une configuration optique hybride a été requise pendant la mise en charge de l'échantillon. De plus, un scanner de tomographie par rayons X a également été utilisé pour effectuer des scans ex-situ. Cette procédure a permis une caractérisation complète des échantillons de composite en fibres de verre tissées soumis à une traction avec le MAF. En utilisant la modalité en lumière visible, les champs de déplacement et de déformation ont été mesurés. Les images infrarouges ont été incluses dans la méthode de corrélation multivues et ont donné des champs de température lagrangiens définis sur le maillage FE. Le maillage FE de la stéréocorrélation hybride a également été utilisé pour la Corrélation Numérique de Volume (DVC) appliquée pour mesurer les champs de déplacement et de déformation dans le volume pour les scans CT. L'intégration de la tomographie par rayons X avec le cadre hybride multivue et une discrétisation FE unique a permis de révéler de multiples mécanismes de dommage tant en surface qu'à l'intérieur du matériau.

IV. Les contributions scientifiques

Les contributions scientifiques de la recherche présentée sont les suivantes :

1. Une configuration expérimentale robuste et modulaire pour les essais multiaxiaux de structures métalliques et composites minces utilisant le dispositif Arcan modifié, amélioré avec un adaptateur de stabilisation pour prévenir le flambage en cisaillement.

2. Un algorithme de corrélation multivue hybride, qui utilise des caméras visibles et infrarouges pour la mesure simultanée des champs de déplacement et de température, avec des corrections de luminosité et de contraste.

3. Un protocole expérimental multimodal, composé de trois modalités différentes (c'est-à-dire lumière visible, infrarouge et rayons X) pour une caractérisation complète des polymères renforcés de fibres.

Mots-clés : Dispositif d'Arcan modifié ; Structures minces ; Chargement multiaxial ; Essais non destructifs ; Matériaux composites ; Corrélation multimodale ; Identification inverse

Proširenisažetak

Pouzdano predviđanje odziva naprednih materijala podvrgnutih složenim (tj. višeosnim) opterećenjima je neophodno kako bi se pouzdano procijenio radni vijek inženjerskih komponenti izloženih očekivanim eksploatacijskim uvjetima. Implementacija numeričkih analiza u proces konstruiranja rezultirala je značajnim napretkom u predviđanju životnog vijeka inženjerskih konstrukcija [1]. Međutim, točnost numeričkih analiza znatno ovisi o definiranim mehaničkim svojstvima odabranih materijala. Globalne industrije poput zrakoplovne i automobilske koriste lagane materijale kako bi smanjile masu inženjerskih komponenti, istovremeno zadržavajući njihovu čvrstoću. Polimeri ojačani vlaknima (eng. *Fibre Reinforced Polymers* - FRP) imaju ključnu ulogu u tim industrijama jer se njihova arhitektura može prilagoditi specifičnim režimima opterećenja. Međutim, za pouzdanu opisivanje ponašanja FRP materijala potrebno je provoditi opsežna eksperimentalna ispitivanja primjenom naprednih metoda za karakterizaciju materijala. Stoga je nužno provoditi višeosna mehanička ispitivanja kako bi se poboljšalo razumijevanje ponašanja materijala te pouzdanije opisali mehanizmi loma. Međutim, zbog visoke cijene višeosnih ispitnih uređaja, često se koriste mehanički prihvati koji omogućuju provedbu višeosnih ispitivanja na jednoosnim ispitnim uređajima.

Modificirani Arcan prihvat (eng. *Modified Arcan Fixture* - MAF) [2] ističe se kao najkompletniji prihvat za jednoosne ispitne uređaje zbog mogućnosti prenošenja jednoosnih i dvoosnih ravninskih opterećenja. Konstrukcija Arcan prihvata omogućuje primjenu tri različita ravninska opterećenja: (1) vlak, (2) smik te (3) njihovu kombinaciju. Odgovarajući ispitni uzorak leptiraste geometrije sadrži dva simetrična V zareza [3] s ciljem omogućavanja kvazi-homogenog smičnog stanja naprezanja u mjernom području između vrhova V zareza. Predloženi prihvat je prvotno bio namijenjen za ispitivanje polimera ojačanih vlaknima [4]. Nadalje, karakterizacija tankih uzoraka (tj. debljina $\leq$ 3 mm) izrađenih iz konvencionalnih materijala pri složenim opterećenjima je iznimno zahtjevna. Tijekom ispitivanja uzoraka na jednostavni smik pomoću MAF prihvata dolazi do iniciranja nestabilnosti (tj. izvijanje) uslijed velikog omjera širine i debljine mjernog područja. Nadalje, istraživanja su pokazala kako pretjerano stezanje ispitnih uzoraka u čeljusti ispitnog uređaja uvodi dodatne perturbacije naprezanja što utječe na ranu pojavu izvijanja [5] i onemogućuje potpunu karakterizaciju materijala.

Određivanje ponašanja materijala uobičajeno se provodi određivanjem deformacija tijekom ispitivanja primjenom klasičnih mjernih uređaja (npr. mjerne trake, mehanički ekstenzometri). Međutim, konvencionalnim metodama moguće je odrediti odziv materijala samo u jednoj ili nekoliko odabranih točaka mjernog područje. Također, na ovaj način nije moguće zabilježiti pojavu lokalizacijskih fenomena poput Lüdersovih linija ili smičnih traka. Kako bi se ponašanje materijala promatralo na cijelom promatranom području interesa (eng. *Region Of Interest* - ROI), nužno je primijeniti nerazorne metode ispitivanja (eng. *Non-Destructive Testing* - NDT) . Primjenom optičkih NDT metoda moguće je zabilježiti te pratiti razvoj lokalizacijskih fenomena poput koncentracije deformacija, inicijacije i propagacije oštećenja na površini. Metoda korelacije digitalne slike (eng. *Digital Image Correlation* - DIC) [6] je najčešće korištena metoda mjerenja cijelog polja pomaka zbog mogućnosti primjene na različitim razinama (tj. od makro do mikro razine). DIC je također pouzdan alat za praćenje inicijacije i propagacije oštećenja (tj. pukotina) proučavajući korelacijske reziduale, tj. razlike nijansi sive boje između zabilježenih slika u referentnoj i korigiranoj deformiranoj konfiguraciji na razini piksela [7]. U slučaju višeosnih ispitivanja, mjerenja 2D DIC algoritmom postaju neadekvatna budući da se mogu javiti značajni izvanravninski pomaci koji dovode do skaliranja vrijednosti izmjerenih polje pomaka. Ovaj neželjeni efekt se može izbjeći primjenom stereo korelacijske (eng. *Stereocorrelation* - SC) metode za mjerenje 3D površinskih pomaka [8]. U svom izvornom obliku, DIC metoda razlaže promatrani ROI na niz manjih podskupova piksela (tj. faseta) te mjeri pomake u središtu svake fasete neovisno o susjednim fasetama. Navedeni protokol mjerenja pomaka naziva se lokalni DIC pristup [9]. Međutim, posljedica neovisno mjerenih pomaka su diskontinuiteti u polju pomaka. Stoga je nužna dodatna interpolacija između centara faseta. S druge strane, globalni DIC [10] pristup temelji se na Metodi Konačnih Elemenata (MKE) te koristi MKE mrežu koja odgovara geometriji promatranog objekta. Također, globalni DIC pretpostavlja kontinuiranost polja pomaka (tj. MKE mreža se koristi za minimiziranje razlika između referentne slike i slika u deformiranoj konfiguraciji) u cijeloj zoni interesa. U odnosu na globalni DIC, lokalni pristup nije toliko računalno zahtijevan. Međutim, mjerna nesigurnost lokalnog DIC algoritma je značajnije veća nego kod globalnog pristupa. Budući da su izlazni podaci globalne DIC metode čvorni pomaci, ovaj pristup omogućuje da se eksperimentalno izmjereni podaci povežu se numeričkim simulacijama temeljenim na MKE metodi [11].

Metoda ažuriranja modela konačnih elemenata (eng. *Finite Element Model Updating* - FEMU) je najčešće korištena metoda kalibracije materijalnih parametara temeljena na minimizaciji razlika između eksperimentalno izmjerenih i numerički izračunatih podataka metodom najmanjih kvadrata. Lecompte et al. [12] su povezali podatke izmjerene lokalnim DIC pristupom sa numeričkim proračunima u inverzno iterativnu FEMU metodu [13]. Na temelju dvoosnih eksperimenata, identificirana su četiri nezavisna elastična i ortotropna parametara kompozita ojačanog staklenim vlaknima. Nadalje, FEMU metoda je također korištena za kalibraciju elastoplastičnih parametara materijala i parametara oštećenja [14]. Tomičević et al. [15] koristili su FEMU metodu za određivanje elastoplastičnih materijalnih parametara nodularnoga lijeva kod različitih režima ravninskog dvoosnog opterećenja. Gras et al. [16] su koristili jedinstveno numeričko sučelje za kalibraciju parametara materijala 3D pletenog kompozitnog ispitnog uzorka sa četiri različite lokalne ortotropne zone. U ovom slučaju, globalna DIC metoda je korištena za mjerenje polja pomaka, a ista MKE mreža korištena je za identifikaciju materijalnih parametara. Roux i Hild [17] su usporedili različite inverzne identifikacijske metode te pokazali kako FEMU posjeduje najmanju osjetljivost na prisutnost šuma na slikama.

Iako je DIC metoda moćan alat za određivanje zona koncentracije deformacija na površini, koje odgovaraju mjestima nastanka makro- ili mezoskopskog oštećenja u vlaknima ojačanom kompozitu, DIC ne pruža izravan uvid u mehanizme oštećenja unutar materijala. Iz tog razloga se često primjenjuje više NDT metoda za karakterizaciju oštećenja [18]. Infracrvena termografija (eng. *Infrared Thermography* - IRT) se ističe kao pouzdan i neizostavan alat za nerazorna ispitivanja kompozita zbog veće inspekcijske brzine i rezolucije, osjetljivosti i mogućnosti detektiranja unutarnjih nesavršenosti uslijed prijenosa topline kondukcijom. Farmaki et al. [19] koristili su IRT radi procjene oštećenja ispod površine kompozitne ploče. Wang et al. [20] koristili su IRT radi praćenja promjene i protoka topline u austenitnom čeliku uslijed zamornom oštećenja. Nadalje, spreg IRT i stereo korelacijskih metoda u hibridnu inspekcijsku metodu [21] je korištena za istovremeno mjerenje prostorne i vremenske distribucije temperature i polja pomaka [22]. Wang et al. [23] unaprijedili su metodu hibridne korelacije koristeći jednu infracrvenu kameru te dvije vizijske kamere [24]. Nadalje, Charbal et al. [25] su predložili prostorno-vremensku regularizaciju za savladavanje velikih promjena sive skale boja koje su posljedica temperaturnih promjena kod hibridnih mjerenja. No međutim, IRT metoda ne pruža uvid u interakciju lokalizacije deformacija i oštećenja s mikrostrukturom kompozita. Stoga, uz hibridnu inspekcijsku metodu poželjno bi bilo

primijeniti i računalnu tomografiju rendgenskih zraka (eng. *X-ray Computed Tomography* – XCT) u spregu s korelacijom digitalnih volumena (eng. *Digital Volume Correlation* – DVC) [26]. Na taj način moguće je dobiti i uvid u unutrašnju arhitekturu kompozita [27]. Ovakvim jedinstvenim eksperimentalnim protokolom sve tri nezavisne mjerne metode mogu se sjediniti u sveobuhvatnu više-modalnu korelacijsku metodu. Hibridnom inspekcijskom metodom, mogu se odrediti polja pomaka, deformacija i temperaturna polja na površini promatranog objekta, a pomoću DVC mjerne metode izmjeriti polja pomaka i deformacija unutar promatranog objekta.

I. Cilj i hipoteze istraživanja

Cilj istraživanja je razvoj robusnog eksperimentalnog protokola za sveobuhvatnu karakterizaciju tankostijenih metalnih i kompozitnih konstrukcija pri višeosnim režimima opterećenja.

Hipoteze istraživanja:

1. Nadogradnja modificiranog Arcan prihvata pomoću adaptera za stabilizaciju tankih ispitnih uzoraka omogućit će provedbu mehaničkih ispitivanja na smik bez pojave izvijanja.

2. Spreg korelacije digitalne slike i infracrvene termografije u hibridnu inspekcijsku metodu te primjena računalne tomografije rendgenskih zraka pružit će sveobuhvatan uvid u odziv vlaknima ojačanih kompozita uslijed višeosnih opterećenja pomoću Arcan prihvata.

3. Korekcija promjena u svjetlini i kontrastu digitalnih slika tijekom mehaničkog ispitivanja pružit će točnija polja pomaka i deformacija za svjetlosne kamere i promjene temperaturnih polja za infracrvenu kameru.

II. Metode istraživanja

Zahtjevni eksploatacijski uvjeti potiču kontinuirano unaprjeđenje mehaničkih svojstava inženjerskih materijala. Stoga je nužno provoditi mehanička ispitivanja kako bi se ponašanje materijala pod opterećenjem moglo pouzdano predvidjeti. Tijekom radnog vijeka, inženjerske komponente izložene su složenim režimima opterećenja. Ako su tankostijene konstrukcije podvrgnute smičnom opterećenju, u zonama s prisutnim tlačnim naprezanjem može doći do pojave izvijanja. Ovaj fenomen narušava strukturni integritet i značajno skraćuje životni vijek

konstrukcije. Stoga je, u svrhu izbjegavanja nepoželjnog efekta izvijanja, nužno odrediti granična opterećenja pri kojima do njega dolazi. Iz tog razloga je potrebno provoditi mehanička ispitivanja tankostijenih konstrukcija na smik. Osim toga, pojava izvijanja onemogućuje potpunu karakterizaciju ponašanja materijala primjenom optičkih mjernih metoda. U ovom je radu stoga predloženo konstrukcijsko rješenje kojim se sprječava izvijanje tankostijenih konstrukcija. Nadalje, predloženo rješenje eksperimentalno je validirano pomoću modificiranog Arcan prihvata, koji omogućuje primjenu jednostavnog smika na tanke ispitne uzorke. Unaprijeđeni eksperimentalni postav potom je primijenjen za karakterizaciju FRP kompozita, koji sve češće zamjenjuju konvencionalne inženjerske materijale u konstrukcijama izloženima ekstremnim mehaničkim opterećenjima. Njihova prednost leži u velikoj fleksibilnosti pri prilagodbi mehaničkih svojstava specifičnim zahtjevima opterećenja te u visokom omjeru čvrstoće i mase.

MAF je unaprijeđen primjenom stabilizacijskih adaptera tijekom mehaničkih ispitivanja na jednostavni smik, s ciljem sprječavanja izvijanja tankih ispitnih uzoraka. Dodatno, adapteri su morali biti transparentni kako bi omogućili primjenu metode digitalne korelacije slike (DIC). Budući da su se očekivali izvanravninski pomaci, korištena je stereo korelacija. Zahvaljujući poznatoj geometriji ispitnih uzoraka, primijenjen je globalni MKE pristup stereo korelaciji, koji je omogućio kalibraciju stereo vizijskog sustava te trodimenzionalno mjerenje pomaka na površini promatranog uzorka.

Eksperimenti na jednostavni smik, pri kojima su korišteni stabilizacijski adapteri, dodatno su analizirani. Budući da je primijenjena stereo korelacijska metoda temeljena na metodi konačnih elemenata, omogućena je izravna povezanost s numeričkim simulacijama zahvaljujući dostupnosti MKE mreže. Stoga je FEMU metoda korištena za identifikaciju parametara materijala tankostijenog ispitnog uzorka izloženog jednostavnom smičnom opterećenju. Nadalje, definiran je napredni FE model koji uključuje stabilizacijske adaptere, pri čemu je u identifikacijsku proceduru bilo uključeno i trenje. Osim toga, različite kombinacije Dirichletovih rubnih uvjeta primijenjene su na FE model tankostijenog uzorka, kako bi se procijenio njihov utjecaj na polja triaksijalnosti i kalibrirane materijalne parametre. Validacija FEMU metode dodatno je provedena na dvjema različitim geometrijama uzoraka izrađenih od čelika visoke čvrstoće HARDOX 450, koji su bili podvrgnuti jednoosnom vlačnom ispitivanju.

Korištenjem unaprijeđenog MAF postava provedena su višeosna ispitivanja leptirastih ispitnih uzoraka izrađenih od polimernog kompozita ojačanog pletenim staklenim vlaknima. U vrhove V-zareza dodatno su urezana po dva zareza radi intenzivnije lokalizacije deformacija. Uzorci su bili podvrgnuti cikličkom vlačnom i smičnom opterećenju, kao i njihovoj kombinaciji pod kutom od 45°. Nadalje, predložen je više-modalni optički sustav koji uključuje svjetlosne kamere, infracrvenu kameru i XCT skener. Tijekom mehaničkih ispitivanja, uzorci su bili promatrani hibridnim sustavom kamera u vidljivom i infracrvenom spektru, dok se između unaprijed definiranih ciklusa opterećivanja provodilo CT skeniranje. Sva tri modaliteta objedinjena su unutar jedinstvenog MKE okruženja, čime je omogućeno istovremeno dobivanje površinskih i volumenskih deformacija te temperaturnih polja na jedinstvenoj MKE mreži.

III. Rezultati i zaključci

U ovoj disertaciji korištene su napredne mjerne metode za karakterizaciju tankostijenih materijala podvrgnutih složenim režimima opterećenja. Ovaj rad je napisan prema *multi-paper* modelu pisanja doktorske disertacije koji se sastoji od 7 tematski povezanih znanstvenih članaka.

FEMU identifikacijska procedura definirana je u **Znanstvenom članku 1**, gdje je primijenjena na dva jednoosna ispitna uzorka različitih geometrija, izrađena od HARDOX 450 čelika. Prvi ispitni uzorak imao je dva paralelna ruba u mjernom području (*DIN*), dok je drugi uzorak imao stanjeno područje s radijusom (*dogbone*). Zaključeno je da geometrija ispitnog uzorka značajno utječe na identifikacijski protokol, što je rezultiralo različitim parametrima materijala za isti materijalni model. Analiza osjetljivosti identifikacije parametara materijala pokazala je da je *dogbone* uzorak osjetljiviji na elastične parametre. Slična osjetljivost na granicu tečenja zabilježena je za oba uzorka. Međutim, za parametar očvršćenja, *DIN* uzorak je pokazao veću osjetljivost, dok je *dogbone* uzorak bio osjetljiviji na eksponent očvršćenja.

U **Znanstvenim člancima 2** i **3** provedena je analiza mehaničkog ispitivanja na jednostavni smik, pri čemu je uspješno spriječeno izvijanje ispitnog uzorka. U tu svrhu najprije su konstruirani i definirani stabilizacijski adapteri. Budući da su adapteri bili transparentni, omogućena je primjena optičkih kamera za snimanje deformacija tijekom ispitivanja. Za provedbu mjerenja površinskih pomaka primijenjen je MKE stereokorelacijski algoritam. Ukupno su provedena četiri mehanička ispitivanja s različitim eksperimentalnim konfiguracijama, pri čemu su varirane debljine

stabilizacijskih adaptera te krutost veze između MAF sustava i ispitnog uređaja. Izvijanje ispitnog uzorka uspješno je spriječeno u slučaju kada su korišteni stabilizacijski adapteri debljine 10 mm te kada veza između MAF sustava i ispitnog uređaja nije bila kruta. U svrhu validacije rezultata prethodno provedenog monotonog ispitivanja na jednostavni smik, provedeno je dodatno ciklično ispitivanje. Nadalje, FEMU metoda korištena je za kalibraciju koeficijenta trenja između stabilizacijskih adaptera i ispitnog uzorka, pri čemu je utvrđena vrijednost $\nu = 0{,}33$, što je u skladu s vrijednostima iz literature. Definirano je pet numeričkih slučajeva s različitim kombinacijama Dirichletovih rubnih uvjeta pomaka. U prva dva slučaja uključeni su stabilizacijski adapteri, ali uz različite vrijednosti koeficijenta trenja. U trećem slučaju numeričkom modelu ispitnog uzorka propisani su isključivo ravninski pomaci, što odgovara idealiziranom eksperimentalnom scenariju. U četvrtom slučaju uvedeni su izvanravninski pomaci na opterećene rubove modela, dok su u petom slučaju izvanravninski pomaci propisani cijeloj površini numeričkog modela. Korištenjem FEMU metode procijenjen je utjecaj propisanih rubnih uvjeta pomaka na polja triaksijalnosti te na kalibrirane materijalne parametre. Za svih pet numeričkih slučajeva dobiveni su različiti materijalni parametri, dok je utjecaj na polja triaksijalnosti bio zanemariv. Zaključeno je da je prvi numerički slučaj najpovoljniji za vjerodostojnu identifikaciju materijalnih parametara jer uključuje stabilizacijske adaptere i prethodno identificiran koeficijent trenja. U petom slučaju omogućena je simulacija ograničenog izvijanja, što nije bilo moguće postići u drugom, trećem i četvrtom slučaju. Osim toga, peti slučaj osigurao je vjerodostojan deformacijski oblik ispitnog uzorka, pri čemu je zahtijevao manje računalnih resursa u usporedbi s prvim slučajem.

U **Znanstvenom članku 4** predložena je semi-hibridna korelacijska metoda gdje je provedena analiza polimernog kompozita ojačanog pletenim staklenim vlaknima podvrgnutog vlačnom ispitivanju pomoću MAF prihvata. U semi-hibridnoj metodi, IR kamera nije direktno korištena u korelacijskoj proceduri. Međutim, bilo je moguće dobiti temperaturna polja ROI-a u Lagrangeovoj konfiguraciji. Uspoređujući ih sa poljima deformacija dobivenih pomoću MKE stereokorelacijskog algoritma, izvori topline su se poklapali sa zonama gdje je nastalo oštećenje. Također, zabilježene su zone posmičnih deformacija koje su proizašle kod vrhova zareza, iako je uzorak bio opterećen na vlak. **Znanstvenim člancima 5** i **6** predstavljena su višeosna ispitivanja (vlačno, jednostavni smik te njihova kombinacija pod kutom od 45°) provedena na polimernim kompozitima ojačanim pletenim staklenim vlaknima korištenjem unaprijeđenog MAF sustava. U **Znanstvenom članku 5** analiza je temeljena isključivo na slikama dobivenima svjetlosnim

kamerama, dok je u **Znanstvenom članku 6** primijenjena hibridna formulacija stereokorelacije. U hibridnoj formulaciji, IR slike su izravno uključene u korelacijsku proceduru. Nadalje, obavezne korekcije svjetline i kontrast su predstavljene. Od tri provedena ispitivanja, najveće vrijednosti naprezanja postignute su tijekom vlačnog testa, dok su najveće vrijednosti deformacija zabilježene kod kombiniranog opterećenja. Analizom rezultata uočene su različite raspodjele deformacija ovisno o režimu opterećenja. Kod vlačnog ispitivanja formirale su se dvije deformacijske trake koje su se širile iz vrhova zareza. Nasuprot tome, kod smičnog i kombiniranog opterećenja opažena je jedna dominantna deformacijska traka, smještena u središnjem mjernom području između vrhova V zareza. Međutim, kod kombiniranog opterećenja deformacijska traka bila je nagnuta, što je posljedica prisutnosti vlačne komponente opterećenja. Nadalje, analizom površinskih snimki dobivenih CT skeniranjem identificirano je više mehanizama oštećenja. Kod smičnog i kombiniranog ispitivanja opaženo je uzdužno pucanje pređe, koje se širilo od vrhova zareza prema središtu uzorka. Za vlačno ispitivanje, zabilježeno je poprečno i uzdužno pucanje pređe te pucanje površinske matrice. Primjenom hibridnog stereokorelacijskog algoritma omogućena je detekcija temperaturnih polja u Lagrangeovoj konfiguraciji. Za vlačno opterećenje, temperaturne promjene bile su dominantno lokalizirane oko vrhova zareza, dok je kod smičnog i kombiniranog opterećenja opažena kontinuirana temperaturna traka između zareza.

U **Znanstvenom članku 7** uveden je spektar rendgenskih zraka u korelacijsku proceduru, koja je uključivala slike snimljene u svjetlosnom i infracrvenom spektru. Sva tri spektra objedinjena su unutar jedinstvenog MKE okruženja, čime je omogućena primjena više-modalne korelacijske metode. Za prikupljanje potrebnih podataka za ovu proceduru bio je potreban hibridni optički postav tijekom opterećivanja ispitnih uzoraka. Osim toga, korišten je skener računalne tomografije rendgenskih zraka za provedbu *ex-situ* mjerenja. Ovakvom procedurom omogućena je sveobuhvatna karakterizacija polimernog kompozita ojačanog pletenim staklenim vlaknima, opterećenog na vlak pomoću MAF sustava. Korištenjem spektra vidljive svjetlosti izmjerena su polja pomaka, a na temelju njih izračunata polja deformacija. Infracrvene slike također su uključene u korelacijsku metodu, što je omogućilo dobivanje temperaturnih polja u Lagrangeovoj konfiguraciji. MKE mreža korištena u hibridnoj korelaciji primijenjena je u DVC algoritmu za mjerenje pomaka i izračunavanje deformacija unutar materijala. Kombinacijom tomografije rendgenskih zraka i hibridne korelacije s jedinstvenom diskretizacijom mreže konačnih elemenata, identificirani su različiti mehanizmi oštećenja na površini i unutar materijala.

IV. Očekivani znanstveni doprinos

Očekivani znanstveni doprinosi su:

1. Robustan i modularan eksperimentalni postav za višeosna ispitivanja tankostijenih metalnih i kompozitnih materijala pomoću modificiranog Arcan prihvata bez pojave fenomena izvijanja uz uporabu adaptera za stabilizaciju ispitnog uzorka.

2. Hibridni stereokorelacijski algoritam koji koristi vizijske i infracrvenu kameru za istovremeno mjerenje cijelog polja pomaka i temperaturnih polja uz primjenu korekcija svjetline i kontrasta.

3. Više-modalni eksperimentalni protokol koji se sastoji od tri različita modaliteta (tj. svjetlosni spektar, infracrveni spektar i rendgensko zračenje) za sveobuhvatnu karakterizaciju kompozita ojačanih pletenim staklenim vlaknima.

Ključne riječi: Modificirani Arcan Prihvat; Tankostijene konstrukcije; Višeosno opterećenje; Nerazorna ispitivanja; Kompozitni materijal; Više-modalna korelacija; Inverzna identifikacija

1. Introduction

The ever-growing industrial requirements for light-weight engineering components of high quality requires equally fast and adaptive production processes to meet the demand-supply equilibrium. As a result, at the end of the 20-th century, the implementation of numerical simulations and modelling of sheet metal forming processes gained traction. The role of numerical simulations was to predict material flow, analyse stress-strain relationships, and improve the quality of manufactured components [28]. By integrating Finite Element (FE) simulations into production workflows, the industries could reduce material waste, minimise defects, and accelerate the development of advanced forming techniques tailored to modern engineering needs [29]. Expensive and time-consuming trial and error methods for analysing production processes should be minimised. Industries such as automotive [30] and aerospace engineering [31] depend on light-weight materials to reduce the mass of their products and therefore lower fuel costs. Fibre Reinforced Polymers (FRP) composites are increasingly sought after [32] due to their ability to customise the architecture and geometry best suited for specific working conditions. Compared to traditional engineering materials like steel, FRP composites offer a superior strength-to-weight ratio. This advantage allows for a reduction in mass of engineering components while still meeting the necessary strength requirements, making them highly efficient for various applications. Moreover, this advantage is crucial in manufacturing, as it reduces material usage while still ensuring the necessary strength of the components, leading to greater efficiency and cost-effectiveness. Despite the numerous advantages of FRPs, their heterogeneous and intricate architecture, compared to homogeneous materials, makes it more challenging to predict their response under complex loading conditions. FRPs are susceptible to various damage mechanisms that affect the material behaviour during loading [6, 33, 34]. The damage mechanisms include fibre breakage [35], matrix microcracking [36], fibre pull-out [37], fibre/matrix debonding [38] and delamination of individual layers [39]. During manufacturing and real-world applications, both FRPs and conventional thin-sheet materials experience complex stress states. Therefore, extensive experimental investigations are required to replicate these conditions accurately. These studies help determine the material behaviour under both simple and complex loading regimes, providing valuable insights into their mechanical response.

1.1. State of the art

Throughout their service life, materials undergo complex loading regimes, including multi-axial loading histories. To accurately assess their performance, mechanical testing is essential to simulate realistic working conditions. Mechanical testing is most commonly performed using uniaxial tension due to its simplicity and accessibility. While tensile tests provide essential material properties, they are insufficient for fully characterising the material behaviour under complex loading conditions. To address this limitation in FRPs, one approach is to cut samples from composite plates at different angles, allowing for a more comprehensive assessment of their mechanical response [6]. For homogeneous sheet materials, samples are cut at various angles relative to the rolling direction to analyse anisotropic mechanical properties [40]. This approach is widely used; however, it does not subject the sample to multiaxial loading. An alternative method is to utilise biaxial or multiaxial testing machines, which allow for a more accurate representation of real-world loading conditions [15]. However, the limited availability and high cost of testing machines capable of applying complex loading regimes present significant constraints. A third approach involves using a specially designed testing apparatus that replicates intricate loading histories more efficiently. The most prominent of such devices are the Iosipescu [41] and Arcan [42] fixtures. The Iosipescu fixture is designed to apply only simple shear loading on flat specimens, whereas the Arcan rig offers greater versatility by accommodating a wide range of in-plane loading conditions.

Simple shear tests provide a comprehensive characterisation of flat samples at large strain levels [43, 44, 45]. Given the critical role of sample geometry in understanding the material response under simple shear loading, various researchers have proposed different designs. Moreover, the sample geometry directly influences the characterisation of material properties, such as elastoplasticity [44] and shear fracture [46, 47]. The sample design should aim to ensure a homogeneous shear stress distribution within the gauge area. Iosipescu [48] proposed a flat sample geometry with two symmetric V notches (*i.e.* butterfly specimen) in the gauge region to induce quasi uniform shear states between the V notches. Mohr and Henn [49] investigated the influence of the geometry of modified butterfly samples with thickness reduction in the gauge area on the stress triaxialities in the gauge region. This study enabled for the improvement of the existing biaxial testing machine [50], which was based on the Arcan fixture [42]. It allowed the authors to

investigate the material behaviour with butterfly samples under combined tensile and shear loadings [51]. Further improvements to the butterfly sample geometry [52] were proposed for investigating fracture under combined normal and shear stresses. Analysis [53, 54] between two sample geometries for shear testing [52, 46] on the fracture behaviour of thin sheets revealed that the butterfly samples achieved lower fracture strains than the Peirs' mini-shear sample [46]. However, it was deemed useful for quasi-static fracture characterisation in shear and plain strain stress states.

Butterfly specimens used with the Arcan fixture are typically designed with large gauge areas, unlike the previously discussed samples. However, this design presents a drawback—the high gauge width-to-thickness ratio—which increases the risk of sample buckling [5, 2, 55] under simple shear loading. Sample buckling restricts reliable material characterisation and the use of optical measurement methods, as it often leads to large out-of-plane displacements. However, buckling can be prevented by using stabilisation adapters for the samples [56, 5, 2]. Material characterisation during mechanical tests where complex loading regimes are employed call for advanced measurement methods. Therefore, classical contact measurement equipment (*e.g.* extensometers, strain gauges) are unreliable for such complex sample geometries.

The development of digital imaging enabled for the emergence of full-field measurement methods. The most versatile and widely used method is Digital Image Correlation (DIC) [57, 58, 59], which offers a wide range of applications and is not dependent on the material. 2D DIC is the most often employed measurement method due to its simplicity and availability. In general, two DIC approaches are employed, namely, local or global analyses. The local DIC approach [60, 61] discretises the observed image into local pixel subsets (*i.e.* facets) and searches for the displacement of the latter between the reference (undeformed) and deformed images. Such approach assesses displacements of each subset, independent of the neighbouring subsets. The drawback of such approaches is the independently measured kinematics (*i.e.* displacement of the centre of each subset), which results in discontinuities, thus requiring additional post-processing interpolation/smoothing. Conversely, global DIC [62, 63] employs Finite Element discretisation, *i.e.* the FE mesh defines the Region of interest (ROI). Such FE approach ensures the continuity of the displacement fields with no additional interpolation. Additionally, the FE mesh itself provides a further advantage, as it can be directly utilised in numerical simulations. As the name suggests,

2D DIC can only be used when only in-plane displacements are expected [64]. In cases when the observed object is non-planar or out-of-plane displacements are expected, Stereo DIC (SDIC) [65] is to be considered.

In stereocorrelation, image pairs are considered for shape measurements [66], calibration [67] and displacement measurements [68]. For stereocorrelation, image pairs are required, where each image captured the observed object from a different angle [69]. Therefore, an optical setup utilising sets of mirrors can be employed [70, 71] or multiple cameras are used [60], which is the most often practice. Similarly to its 2D counterpart, two approaches for stereocorrelation are employed, namely, local and global approaches. In global SDIC, an FE mesh is selected and the displacement measurement is carried out similarly to 2D DIC. However, before stereocorrelation can be carried out, a calibration of the optical system needs to be performed. The calibration procedure in global SDIC can be carried out in two ways, by using a calibration object or the known geometry of the observed object. The pre-defined CAD model [72] or FE mesh [73, 74] of the object are exploited. Although FE-based SDIC is a powerful measurement technique, it is restricted to surface kinematics, meaning only surface-level damage can be detected. To analyse the internal kinematics, an alternative measurement method is necessary.

X-ray Computed Tomography (XCT) is an imaging method that employs the X-ray spectrum of light (wavelength ranging from 10 nanometres to 10 picometres) to gain insight into the inner material structure. XCT scanning is used on a wide range of materials comprising cast iron [75] and composite materials [76]. XCT scanning provides 3D images based on the X-ray attenuation, which may, for instance, reveal fibre orientations and internal defects in composite materials [77]. Furthermore, additional quantitative measurements are obtained, such as porosity and fibre volume fraction in composite materials [26]. Using Digital Volume Correlation (DVC) on 3D images, 3D displacement fields are measured and the corresponding strain fields are computed. Similarly to 2D DIC and SDIC, global DVC employs FE discretisations of 3D volumes [78]. Furthermore, mechanical regularisation [79] can be implemented within 2D DIC/DVC algorithms [80], which introduces additional constraints to measured displacement fields. In general, two types of experiments involving XCT scanning are carried out, namely, *ex-situ* [58, 69] and *in-situ* [10, 81]. The main difference is the location of the testing machine. In the former approach, the sample is tested outside the CT scanner and later placed inside for imaging purposes. In the latter, the testing

machine is integrated within the CT scanner, allowing for real-time scanning during the experiment. Projections may be captured even during the loading steps. This method is commonly referred to as projection-based DVC (or P-DVC [82]). Such *in-situ* setup is unavailable without special loading devices [83]. With the *in-situ* experimental procedures, 4D experimental data (3D in space + time) can be acquired, which is especially important for composite materials [84, 85]. Even though *ex-situ* experimental protocols are powerful, the main drawback when testing composite materials is relaxation and crack closure when the samples are removed from the testing machine.

The resulting output of the presented measurement methods (FE-based 2D DIC, SDIC and DVC) are nodal displacements. Such advanced FE-based methods enable for straightforward coupling of measured quantities with numerical simulations in an inverse parameter identification framework [86, 87, 88]. The most widely used identification method is Finite Element Model Updating (FEMU). Using FEMU, the differences between the measured quantities (*e.g.* displacement fields and applied load) and the numerically calculated data (*e.g.* displacement fields and resultant forces) are iteratively minimised [89, 90]. The measured displacement fields are prescribed as Dirichlet boundary conditions to the FE model. Hence, experimentally driven numerical analyses can be carried out. FEMU is one of the most versatile identification methods. It was used to calibrate the material parameters of cast iron subjected to uniaxial [14] and biaxial [15] tension. Moreover, it is not limited to macroscopic constitutive laws. For instance, it was used to calibrate crystal plasticity parameters of stainless steel [91]. Compared to its inverse identification counterparts, Equilibrium Gap Method (EGM) [92], Constitutive Gap Method (CGM) [93] and Virtual Fields Method (VFM) [94], FEMU yields the most accurate material parameters using data corrupted with acquisition noise [90, 17].

FEMU is a sensitivity-based identification method [95, 96, 97]. In other words, FEMU utilises sensitivity matrices to represent the impact of material parameter changes on the calculated quantities. Consequently, FEMU can be applied to optimise test and sample geometries, ensuring the activation of specific material parameters [98]. The geometry of the specimen is crucial, as it directly influences the numerical model. Therefore, for thin samples where a plane stress state is expected, 2D DIC measurements may be sufficient. However, this approach becomes limited when 3D effects cannot be ignored, such as in the analysis of stress triaxiality fields [99]. Very few

studies combined DIC measurements and numerical simulations to analyse stress triaxiality fields [100, 101].

To enhance experimental investigations, additional cameras operating at different scales can be integrated. In recent decades, infrared (IR) thermography, with wavelengths ranging from 1 millimetre to 780 nanometres, has emerged as an efficient and widely used measurement technique. For composite materials, IR thermography has proven valuable in detecting and assessing damage [102]. Furthermore, it serves as a powerful tool for measuring temperature fields and analysing heat-related phenomena in composites [103, 104]. IR thermography is used across industry to monitor and assess structural integrity and to identify various defects [105, 106], especially in aerospace [19] and automotive [107] engineering. Additionally, IR thermography is utilised in mechanical testing to monitor materials under mechanical loading in real time [108]. IR thermography becomes even more powerful when combined with DIC in a hybrid correlation setting thus maximising the potential of both modalities [21, 109, 110, 69]. In this hybrid framework, displacement, strain, and temperature fields are simultaneously measured within a unified (Lagrangian) reference frame. The hybrid approach was employed to analyse thermomechanical fatigue tests [20], which revealed crucial insights into material damage under cyclic loading. The integration of IR and visible-light modalities comes with unique challenges, particularly fluctuations in digital levels caused by thermomechanical interactions [25] or damage-related effects in composites [102]. These fluctuations may lead to various biases. To overcome this issue, IR images undergo brightness and contrast corrections [111, 112], ensuring that temperature variations are properly accounted for. The corrected temperature variations are analysed along with the strain fields, allowing for the assessment of localised thermal changes within the same Lagrangian frame. The hybrid correlation registers both the surface (DIC) and subsurface (IR) phenomena thereby offering a more comprehensive analysis of dissipation effects and temperature variations in relation to strain fields [113]. Linking these datasets enables researchers to analyse how materials degrade, how damage spreads, and how structures perform under stress. This method significantly advances the understanding of the thermomechanical behaviour of composites and serves as a powerful tool for assessing their integrity in complex loading scenarios.

Both XCT and IR thermography provide complementary information for SDIC, which then contributes to a more comprehensive analysis of the material behaviour. All three methods offer distinct capabilities and complement each other. SDIC provides only surface kinematics, IR enables sub-surface phenomena to be detected, and DVC yields full 3D kinematic fields of the tested material. By integrating three modalities (*i.e.*, visible light, infrared, and X-rays) into a unified multimodal correlation (MMC) framework, a robust method for comprehensive material characterisation under loading can be developed. Moreover, combining FE-SDIC, IR thermography and X-ray imaging in the same Lagrangian setting enables for a comprehensive analysis by establishing the relationship between heat release (both on the surface and within the bulk) and material damage. Furthermore, analysing the 3D kinematics within the material bulk enhances the depth of mechanical characterisation.

1.2. Objectives and hypotheses of the research

The goal of this research is the development of a robust experimental protocol for comprehensive characterisation of thin metallic and composite structures under multiaxial loading regimes. A comprehensive measurement method for characterising Fibre Reinforced Polymers will be established by combining stereocorrelation, infrared thermography and computed tomography into a multimodal correlation procedure.

Hypotheses of research:

1. Improvement of an Arcan fixture with stabilisation adapters designed for thin samples will enable shear tests to be conducted with no (or limited) buckling.

2. Coupling Digital Image Correlation and Infrared Thermography into a hybrid inspection method with the application of X-ray tomography will provide comprehensive insights into the behaviour of Fibre Reinforced Polymers subjected to multiaxial loading regimes.

3. Brightness and contrast corrections of digital images acquired during mechanical tests will provide improved displacement and strain fields for visible light cameras and changes in temperature fields for the infrared camera.

1.3. Scientific contributions of the research

The scientific contribution of the proposed research includes:

1. A robust and modular experimental setup for multiaxial testing of thin metallic and composite structures using a Modified Arcan Fixture upgraded with sample stabilisation adapters to prevent shear buckling.

2. Hybrid multiview correlation algorithm, which utilises visible light and infrared cameras for simultaneous measurements of displacement and temperature fields with brightness and contrast corrections.

3. A multimodal experimental protocol, which consists of three different modalities (*i.e.*, visible light, infrared and X-ray spectra) for a comprehensive characterisation of Fibre Reinforced Polymers.

1.4. Dissertation structure overview

This doctoral dissertation is structured according to the *multi-paper* (*i.e. collection-of-scientific-papers*) PhD model.

Building on the previously presented literature review, this dissertation primarily aims to develop a robust experimental methodology for testing thin sheet samples. Additionally, it presents numerical analyses driven by experimentally measured data. Accurately defining boundary conditions in numerical simulations is often challenging. The approach proposed herein allows real measured data to be directly applied to numerical models. The impact of prescribed Dirichlet boundary conditions on stress triaxiality fields is thoroughly examined. Furthermore, the experimental framework is enhanced by integrating additional modalities to visible light, namely, infrared and X-ray imaging. These advanced techniques enable for a more comprehensive characterisation of thin sheet samples under complex loading conditions.

Chapter 2 presents a detailed discussion of the applied methods and obtained results. The first subchapter introduces the core measurement method used in this dissertation, covering three FE-based techniques, namely, 2D DIC, StereoDIC, and DVC. Each method is explained in detail. The

subsequent subchapter focuses on advanced techniques employed in both experimental and numerical investigations.

Chapter 3 presents the unified conclusions of the dissertation. Additionally, potential future research directions based on the findings presented herein are outlined.

According to the *multi-paper* PhD model, the relevant published scientific publications are attached at the end and serve as an obligatory appendix that provides the core substance and basis of this dissertation.

2. Discussion on methods and results

This chapter comprises the topics directly related to the published scientific papers attached at the end of this dissertation. The main topics of the scientific papers are as follows:

- The influence of two sample geometries subjected to uniaxial tensile loading on parameter identification via Finite Element Model Updating (FEMU), Scientific paper 1.
- Enhancing the stability of thin sheet samples subjected to simple shear with the Modified Arcan fixture using stability adapters (Scientific paper 2),
- Comparison of different experimentally measured Dirichlet boundary conditions prescribed on the numerical model of a simple shear experiment (Scientific paper 3).
- Enhancing stereocorrelation measurements by including the infrared modality (Scientific paper 4, Scientific paper 5, Scientific paper 6, Scientific paper 7).
- Enriching hybrid correlation measurements by considering three different modalities, namely visible light, infrared and X-rays in a unique framework (Scientific paper 6 and Scientific paper 7).

Supplementary material with regards to the conducted research and some findings omitted in published papers due to their length are also provided.

2.1. FE-based measurement methods

This subchapter introduces the three primary measurement methods employed in this dissertation, namely, DIC, StereoDIC, and DVC. All three techniques utilise an FE mesh to measure displacement fields within the ROI and rely on the conservation of grey levels between images or scans. The subchapter is structured into three sections. First, 2D DIC is introduced, followed by StereoDIC, and finally, DVC is presented.

2.1.1. Digital Image Correlation

Digital Image Correlation is one of the most widely used full field measurement methods. It is based on registering the image grey levels of the observed object. DIC is based on the conservation of the brightness between the reference image $f(\mathbf{x})$, captured in the reference (usually) unloaded state, and series of images acquired in the deformed state $g(\mathbf{x})$

$$f(\mathbf{x}) = g(\mathbf{x} + \mathbf{u}(\mathbf{x})), \tag{2.1}$$

where $\mathbf{x}$ is the location of any pixel in the ROI and $\mathbf{u}(\mathbf{x})$ the sought displacement field $\mathbf{u}(\mathbf{x})$. DIC is an optimisation problem, and the algorithm consists in minimising the sum of squared differences ϕ^2 over the ROI

$$\phi^2 = \sum_{ROI} \left\| f(\mathbf{x}) - g(\mathbf{x} + \mathbf{u}(\mathbf{x})) \right\|^2. \tag{2.2}$$

Global FE-DIC [62] assumes the continuity of the displacement field over the whole ROI. However, the problem is inherently nonlinear and ill-posed. To address this, the displacement field is written as the function of the FE mesh shape functions

$$\mathbf{u}(\mathbf{x}) = \sum_{i=1}^{DOF} u_i \boldsymbol{\psi}_i(\mathbf{x}), \tag{2.3}$$

where u_i are the nodal displacement amplitudes associated with the selected shape functions $\boldsymbol{\psi}_i(\mathbf{x})$. By introducing small displacement increments $\delta\mathbf{u}(\mathbf{x})$, a Taylor expansion is applied to the deformed image

$$g(\mathbf{x} + \mathbf{u}(\mathbf{x}) + \delta\mathbf{u}(\mathbf{x})) \approx g(\mathbf{x} + \mathbf{u}(\mathbf{x}) + \delta\mathbf{u}(\mathbf{x})) \cdot \nabla f(\mathbf{x}), \tag{2.4}$$

where $\nabla f(\mathbf{x})$ is the gradient of the reference image. Finally, a Gauss-Newton iterative algorithm is applied to solve linear systems

$$\{\delta\mathbf{u}\} = [\mathbf{M}]^{-1} \{\mathbf{b}\}, \tag{2.5}$$

where $[\mathbf{M}]$ is the Hessian (or DIC) matrix

$$M_{\mathrm{ij}} = \sum_{ROI} \left(\nabla f\left(\mathbf{x}\right) \cdot \boldsymbol{\psi}_{\mathrm{i}}\left(\mathbf{x}\right) \right) \left(\nabla f\left(\mathbf{x}\right) \cdot \boldsymbol{\psi}_{\mathrm{j}}\left(\mathbf{x}\right) \right) \tag{2.6}$$

and $\{\mathbf{b}\}$ the second member

$$b_i = \sum_{ROI} \left(\nabla f\left(\mathbf{x}\right) \cdot \boldsymbol{\psi}_{\mathrm{i}}\left(\mathbf{x}\right) \right) \left(f\left(\mathbf{x}\right) - \tilde{g}\left(\mathbf{x}\right) \right), \tag{2.7}$$

where $\tilde{g}\left(\mathbf{x}\right)$ is the corrected deformed image with the current displacement field. It is computed iteratively and equals to $g\left(\mathbf{x} + \mathbf{u}^{\mathrm{it}}\left(\mathbf{x}\right)\right)$ where *it* denotes the iteration number. Usually, the DIC matrix $[\mathbf{M}]$ is calculated only once, and the second member $\{\mathbf{b}\}$ needs to be computed for each iteration.

2.1.2. Stereocorrelation

Compared to 2D DIC, for stereocorrelation two or more image series are needed while observing the same object surface. A stereocorrelation algorithm usually consists of two steps, namely, the optical system calibration and correlations for kinematic measurements. The stereocorrelation algorithm presented in this dissertation is based on the pinhole camera model, which enables the projection of 3D FE meshes onto 2D image planes of each camera

$$s^{\mathrm{c}} \cdot \begin{Bmatrix} x^{\mathrm{c}} \\ y^{\mathrm{c}} \\ 1 \end{Bmatrix} = \left[\mathbf{\Pi}^{\mathrm{c}}\right] \begin{Bmatrix} X \\ Y \\ Z \\ 1 \end{Bmatrix}, \tag{2.8}$$

where $\left[\mathbf{\Pi}^{\mathrm{c}}\right]$(3×4) is the camera projection matrix, s^{c} the scale factor, x^{c} and y^{c} the 2D projections of the 3D nodal coordinates *X*, *Y* and *Z*. The projection matrix $\left[\mathbf{\Pi}^{\mathrm{c}}\right]$ is calculated by multiplying the camera intrinsic $\left[\mathbf{K}^{\mathrm{c}}\right]$(3×3) and extrinsic $\left[\mathbf{T}^{\mathrm{c}}\right]$(3×4) matrices

$$\left[\mathbf{\Pi}^{\mathrm{c}}\right] = \left[\mathbf{K}^{\mathrm{c}}\right]\left[\mathbf{T}^{\mathrm{c}}\right] = \begin{bmatrix} f_x & \xi & c_x \\ 0 & f_y & c_y \\ 0 & 0 & 1 \end{bmatrix} \begin{bmatrix} r_{11} & r_{12} & r_{13} & t_x \\ r_{21} & r_{22} & r_{23} & t_y \\ r_{31} & r_{32} & r_{33} & t_z \end{bmatrix}. \tag{2.9}$$

where f_{x} and f_{y} are the horizontal and vertical scale factors expressed in pixels, c_{x} and c_{y} the positions of the optical centre, and ξ the skew angle, which is often disregarded since the horizontal

and vertical scale factors are identical. The extrinsic matrix $\left[\mathbf{T}^{c}\right]$ consists of the rotation matrix $\left[\mathbf{R}^{c}\right]$ and the translation vector $\left\{\mathbf{t}^{c}\right\}$

$$\left[\mathbf{T}^{c}\right]=\left[\left[\mathbf{R}^{c}\right]\left\{\mathbf{t}^{c}\right\}\right]. \tag{2.10}$$

The parameters r_{ij} in the extrinsic matrix $\left[\mathbf{T}^{c}\right]$ refer to three Euler angles ψ, φ and θ and their combinations

$$\left[\mathbf{R}^{c}\right]=\begin{bmatrix}\cos\psi & -\sin\psi & 0\\ -\sin\psi & \cos\psi & 0\\ 0 & 0 & 1\end{bmatrix}\begin{bmatrix}\cos\varphi & 0 & -\sin\varphi\\ 0 & 1 & 0\\ -\sin\varphi & 0 & \cos\varphi\end{bmatrix}\begin{bmatrix}1 & 0 & 0\\ 0 & \cos\vartheta & -\sin\vartheta\\ 0 & -\sin\vartheta & \cos\vartheta\end{bmatrix} \tag{2.11}$$

The last three parameters of the extrinsic matrix $\left[\mathbf{T}^{c}\right]$ are the translations t_x, t_y and t_z in the x-, y- and z-directions, respectively. During the calibration procedure, the extrinsic and intrinsic parameters are determined for each camera to construct the projection matrices $\left[\mathbf{\Pi}^{c}\right]$.

The calibration procedure is a critical step. A robust initial estimate of the projection matrices is mandatory. This estimate can be obtained by resorting to a Point-n-Perspective (PnP) [114] solution in which specific nodes of the FE mesh are selected together with the corresponding pixels in each camera image. With the known 2D and 3D coordinates, the projection matrices $\left[\mathbf{\Pi}^{c}\right]$ are extracted via Direct Linear Transform [115]. Concerning PnP, utilising a calibration object with an a priori known geometry for which the FE mesh was designed is desirable. However, the calibration procedure is identical if all camera parameters are calibrated or just intrinsic or extrinsic ones. Therefore, from now on, only the extrinsic parameters $\left\{\mathbf{p}^{c}\right\}$ are considered

$$\left\{\mathbf{p}^{c}\right\}=\left\{\psi,\varphi,\vartheta,t_x,t_y,t_z\right\}. \tag{2.12}$$

In cases when cameras with different grey level renderings are used (*i.e.*, 8-bit, 16-bit) or when an IR camera is employed, it is necessary to perform an image (*i.e.* histogram) normalisation. With such normalisation, all grey level intensities are reduced to a similar order of magnitude. The normalisation procedure is performed in two steps, namely, (i) centering the grey level distribution about zero, (ii) scaling the new image histogram with the image (or the ROI) standard deviation

$$\tilde{f}^c = \frac{f^c - \mu\left(f^c\right)}{\mathrm{std}\left(f^c\right)}. \tag{2.13}$$

The intrinsic texture of the speckle pattern $\hat{f}(\mathbf{X})$ visible on the sample surface can be reconstructed as the average of the grey levels at the projected physical points $\mathbf{x}^c$ for all cameras [72, 68, 112]

$$\hat{f}(\mathbf{X}) = \frac{1}{Nc}\sum_{c=1}^{Nc}\left(\tilde{f}^c\left(\mathbf{x}^c\right)\right) \tag{2.14}$$

where $\mathbf{x}^c$ represents the projected physical points, which are dependent on the 3D positions of the FE mesh $\mathbf{X}$ and the corresponding projection matrices $\left[\mathbf{\Pi}^c\right]$

$$\mathbf{x}^c = \mathbf{x}^c\left(\mathbf{X}, \left[\mathbf{\Pi}^c\right]\right). \tag{2.15}$$

The calibration procedure is then reduced to calibrating all cameras over a single unique reference image $\hat{f}(\mathbf{X})$. Hence, the calibration cost function is written as a least squares minimisation problem

$$\rho^2\left(\left\{\mathbf{p}^c\right\}\right) = \sum_{c=1}^{Nc}\sum_{ROI}\left\|\tilde{f}^c\left(\mathbf{x}^c\right) - \hat{f}(\mathbf{X})\right\|^2 \tag{2.16}$$

where the sought intrinsic and/or extrinsic parameters are gathered in $\left\{\mathbf{p}^c\right\}$, and hence the projection matrices $\left[\mathbf{\Pi}^c\right]$ are iteratively updated. It should be noted that the initial intrinsic texture $\hat{f}(\mathbf{X})$ is constructed using the initial PnP projection matrices. Therefore, $\hat{f}(\mathbf{X})$ should also be iteratively updated. When only two cameras are employed, the cost function can also be written as a least square minimisation problem where differences between the two cameras are minimised over the chosen ROI

$$\rho^2\left(\left\{\mathbf{p}^c\right\}\right) = \left\|\tilde{f}_1\left(\mathbf{x}_1\right) - \tilde{f}_2\left(\mathbf{x}_2\right)\right\|^2. \tag{2.17}$$

In the following discussion, only the former approach will be considered.

The calibration cost function can be Taylor expanded over each sought parameter and minimised using a Gauss-Newton scheme [8]. Similarly to established material parameter optimisation methods [11], the sensitivity fields need to be computed. By introducing a small variation to the parameters, a pseudo displacement field is computed in each 2D camera plane for each projected physical point $\mathbf{x}^{\mathrm{c}}$ to $\mathbf{x}^{\mathrm{c}}+\partial\mathbf{x}^{\mathrm{c}}$. Hence, the displacement sensitivity fields read

$$\left\{\mathbf{S}_{p^{\mathrm{c}}}\left(\mathbf{x}^{\mathrm{c}}\right)\right\}=\frac{\partial\mathbf{x}^{\mathrm{c}}}{\partial p^{\mathrm{c}}}\left(\mathbf{x}^{\mathrm{c}}\right) \tag{2.18}$$

for each considered camera parameter p^{c}. The computed sensitivities are 2D vector fields defined at each physical point $\mathbf{x}^{\mathrm{c}}$. With the known sensitivities, the camera-wise Hessian matrices are constructed

$$H_{\mathrm{kl}}^{\mathrm{c}}=\sum_{ROI}\left(\nabla\tilde{f}^{\mathrm{c}}\left(\mathbf{x}^{\mathrm{c}}\right)\cdot\left\{\mathbf{S}_{p_{\mathrm{k}}^{\mathrm{c}}}\left(\mathbf{x}^{\mathrm{c}}\right)\right\}\right)\left(\nabla\tilde{f}^{\mathrm{c}}\left(\mathbf{x}^{\mathrm{c}}\right)\cdot\left\{\mathbf{S}_{p_{\mathrm{l}}^{\mathrm{c}}}\left(\mathbf{x}^{\mathrm{c}}\right)\right\}\right) \tag{2.19}$$

where $\nabla\tilde{f}^{\mathrm{c}}\left(\mathbf{x}^{\mathrm{c}}\right)$ is the respective camera image gradient. Similarly, the second member reads

$$B_{\mathrm{k}}^{\mathrm{c}}=\sum_{ROI}\left(\nabla\tilde{f}^{\mathrm{c}}\left(\mathbf{x}^{\mathrm{c}}\right)\cdot\left\{\mathbf{S}_{p_{\mathrm{k}}^{\mathrm{c}}}\left(\mathbf{x}^{\mathrm{c}}\right)\right\}\right)\left(\tilde{f}^{\mathrm{c}}\left(\mathbf{x}^{\mathrm{c}}\right)-\hat{f}\left(\mathbf{X}\right)\right). \tag{2.20}$$

With the known Hessian matrices and the second member, the camera parameter corrections are calculated at each iteration step

$$\left\{\delta\mathbf{p}^{\mathrm{c}}\right\}=\left[\mathbf{H}^{\mathrm{c}}\right]^{-1}\left\{\mathbf{B}^{\mathrm{c}}\right\}. \tag{2.21}$$

The iterations are repeated until the convergence criterion is reached for parameter stationarity

$$\left\{\delta\mathbf{p}^{\mathrm{c}}\right\}\varnothing\left\{\mathbf{p}^{\mathrm{c}}\right\}\leq 10^{-3}. \tag{2.22}$$

When lighting and perspective differences for each camera are negligible or non-existent, the grey level conservation between each reference image $\tilde{f}^{\mathrm{c}}\left(\mathbf{x}^{\mathrm{c}}\right)$ and the intrinsic texture $\hat{f}\left(\mathbf{X}\right)$ is satisfied [112]. Otherwise, such conditions may impact the stability of multiview correlation algorithms since the grey level conservation between cameras is no longer satisfied, especially when an IR camera is included. Using brightness and contrast corrections (BCCs) for each camera *c*, the corrected reference image $\hat{f}^{\mathrm{c}}\left(\mathbf{x}^{\mathrm{c}}\right)$ is built

$$\hat{f}^{\mathrm{c}}\left(\mathbf{x}^{\mathrm{c}}\right)=\left(1+c^{\mathrm{c}}\left(\mathbf{x}^{\mathrm{c}}\right)\right)\tilde{f}^{\mathrm{c}}\left(\mathbf{x}^{\mathrm{c}}\right)+b^{\mathrm{c}}\left(\mathbf{x}^{\mathrm{c}}\right) \tag{2.23}$$

where $b^{\mathrm{c}}\left(\mathbf{x}^{\mathrm{c}}\right)$ and $c^{\mathrm{c}}\left(\mathbf{x}^{\mathrm{c}}\right)$ represent the brightness and contrast correction fields for each camera. Equation (2.23) corresponds to an affine correction, where b^{c} is the brightness field, and c^{c} the contrast field. The corresponding cost function becomes

$$\xi^2\left(b,c\right)=\sum_{c=1}^{Nc}\sum_{ROI}\left\|\left(1+c^{\mathrm{c}}\left(\mathbf{x}^{\mathrm{c}}\right)\right)\tilde{f}^{\mathrm{c}}\left(\mathbf{x}^{\mathrm{c}}\right)+b^{c}\left(\mathbf{x}^{\mathrm{c}}\right)-\hat{f}\left(\mathbf{X}\right)\right\|^2. \tag{2.24}$$

Both $b^{\mathrm{c}}\left(\mathbf{x}^{\mathrm{c}}\right)$ and $c^{\mathrm{c}}\left(\mathbf{x}^{\mathrm{c}}\right)$ fields are defined over the 2D image plane. However, they can be rewritten in the 3D space of the sample surface $b^{c}\left(\mathbf{X}\right)$ and $c^{\mathrm{c}}\left(\mathbf{X}\right)$ to be consistent for all cameras. The BC fields are decomposed over an FE mesh using a set of spatial shape functions ψ_i

$$\left\{b^{\mathrm{c}}\left(\mathbf{X}\right)\right\}=\sum_{i=1}^{DOF}b_{\mathrm{i}}^{\mathrm{c}}\psi_{\mathrm{i}}\left(\mathbf{X}\right), \tag{2.25}$$

and

$$\left\{c^{\mathrm{c}}\left(\mathbf{X}\right)\right\}=\sum_{i=1}^{DOF}c_{\mathrm{i}}^{\mathrm{c}}\psi_{\mathrm{i}}\left(\mathbf{X}\right), \tag{2.26}$$

where $\left\{b^{\mathrm{c}}\left(\mathbf{X}\right)\right\}$ and $\left\{c^{\mathrm{c}}\left(\mathbf{X}\right)\right\}$ gather all nodal brightness and contrast corrections for each camera c, and DOF denotes the number of degrees of freedom. Employing the same FE formulation as previously, brightness and contrast sensitivities read as

$$S_{\mathrm{b}}^{\mathrm{c}}\left(\mathbf{X}\right)=1, S_{\mathrm{c}}^{\mathrm{c}}\left(\mathbf{X}\right)=\tilde{f}^{\mathrm{c}}\left(\mathbf{X}\right). \tag{2.27}$$

The BCC Hessian matrices consist of four sub-Hessian matrices related to brightness and contrast corrections

$$\left[\mathbf{H}_{\mathrm{BCC}}^{\mathrm{c}}\right]=\begin{bmatrix}\mathbf{h}_{\mathrm{BB}}^{\mathrm{c}} & \mathbf{h}_{\mathrm{BC}}^{\mathrm{c}}\\ \mathbf{h}_{\mathrm{CB}}^{\mathrm{c}} & \mathbf{h}_{\mathrm{CC}}^{\mathrm{c}}\end{bmatrix}, \tag{2.28}$$

where the individual sub-Hessians are expressed as

$$\left(h_{\mathrm{kl}}^{\mathrm{c}}\right)_{\mathrm{ij}}=\sum_{ROI}S_{\mathrm{k}}^{\mathrm{c}}\left(\mathbf{X}\right)\psi_{\mathrm{i}}\left(\mathbf{X}\right)S_{\mathrm{l}}^{\mathrm{c}}\left(\mathbf{X}\right)\psi_{\mathrm{j}}\left(\mathbf{X}\right) \tag{2.29}$$

where k and l represent B and C for each camera c. The second member is written as a column vector concatenating individual second members for brightness and contrast corrections

$$\left(B_k^c\right)_i = \sum_{ROI} S_{\mathrm{k}}^{\mathrm{c}}\left(\mathbf{X}\right)\psi_{\mathrm{i}}\left(\mathbf{X}\right)\left(\left(1+c^{\mathrm{c}}\left(\mathbf{x}^{\mathrm{c}}\right)\right)\tilde{f}^{\mathrm{c}}\left(\mathbf{x}^{\mathrm{c}}\right)+b^c\left(\mathbf{x}^{\mathrm{c}}\right)-\hat{f}\left(\mathbf{X}\right)\right). \tag{2.30}$$

The nodal BCCs are computed in a single step by solving the following linear system

$$\left\{\mathbf{p}_{\mathrm{BCC}}^{\mathrm{c}}\right\} = \left[\mathbf{H}_{\mathrm{BCC}}^{\mathrm{c}}\right]^{-1}\left\{\mathbf{B}_{\mathrm{BCC}}^{\mathrm{c}}\right\} \tag{2.31}$$

where $\left\{\mathbf{p}_{\mathrm{BCC}}^{\mathrm{c}}\right\}$ gathers all nodal unknowns $b_{\mathrm{i}}^{\mathrm{c}}$ and $c_{\mathrm{i}}^{\mathrm{c}}$. The full calibration procedure can be implemented in a staggered way. In such a procedure, the calibration is performed until the parameters converge. Upon reaching a pre-converged solution, BCCs are performed. The next step is to perform the parameter identification with updated BCCs again. Table 1 presents the complete step-by-step calibration algorithm.

Table 1. Stereocorrelation calibration algorithm

Initialise the extrinsic and intrinsic parameters $\{\mathbf{p}^c\}$ from pre-calibration	
Image normalisation and gradient computation	►Eq. (2.13)
Construct the intrinsic texture $\hat{f}(\mathbf{X})$	►Eq. (2.14)
while pre-convergence of parameters $\{\mathbf{p}^c\}$ not reached **do**	►Eq. (2.22)
Calculate camera-wise sensitivity fields	►Eq. (2.18)
Compute the camera-wise Hessian matrix $[\mathbf{H}^c]$	►Eq. (2.19)
Compute the camera-wise second member $\{\mathbf{B}^c\}$	►Eq. (2.20)
Calculate the parameter increment $\{\delta\mathbf{p}^c\}$ and update $[\mathbf{\Pi}^c]$	►Eq. (2.21)
Update the interpolated image and the intrinsic texture $\hat{f}(\mathbf{X})$	►Eq. (2.14)
If pre-convergence reached, **then**	
Compute BCC Hessian matrix $[\mathbf{H}^c_{\mathrm{BCC}}]$	►Eq. (2.28)
Compute BCC second member $\{\mathbf{B}^c_{\mathrm{BCC}}\}$	►Eq. (2.30)
Compute nodal brightness and contrast fields $\{\mathbf{p}^c_{\mathrm{BCC}}\}$	►Eq. (2.31)
Update reference images with BCCs	►Eq. (2.23)
end if	
end while	

After convergence of the calibration algorithm, the next step is to measure displacement fields $\mathbf{U}(\mathbf{X},t)$ at each time *t*. Stereocorrelation consists in minimising the sum of squared differences in which the normalised reference images $\tilde{f}^{\mathrm{c}}(\mathbf{x}^{\mathrm{c}})$ and the normalised corrected deformed images $\tilde{g}_{\mathrm{U}}^{\mathrm{c}}(\tilde{\mathbf{x}}^{\mathrm{c}},t)$ are considered

$$\mathbf{U}(\mathbf{X},t)=\arg\min\sum_{c=1}^{Nc}\sum_{ROI}\left(\tilde{g}_{\mathrm{U}}^{\mathrm{c}}(\tilde{\mathbf{x}}^{\mathrm{c}},t)-\tilde{f}^{\mathrm{c}}(\mathbf{x}^{\mathrm{c}})\right)^{2} \tag{2.32}$$

where $\mathbf{U}(\mathbf{X},t)$ is the measured instantaneous nodal displacement field, and the normalised corrected deformed images are computed as

$$\tilde{g}_{\mathrm{U}}^{\mathrm{c}}(\tilde{\mathbf{x}}^{\mathrm{c}},t)=\tilde{g}^{\mathrm{c}}(\mathbf{x}^{\mathrm{c}}(\mathbf{X}+\mathbf{U}(\mathbf{X},t)),t). \tag{2.33}$$

The continuity of the displacement field $\mathbf{U}(\mathbf{X},t)$ is ensured by using a set of spatial shape functions $\psi_{\mathrm{i}}(\mathbf{X})$

$$\mathbf{U}(\mathbf{X},t)=\sum_{i=1}^{DOF}u_{\mathrm{i}}(t)\psi_{\mathrm{i}}(\mathbf{X}) \tag{2.34}$$

where $u_i(t)$ are nodal displacements of the T3 FE mesh made of 3 noded triangles gathered in $\{\mathbf{u}(t)\}$. The nodal displacements are determined via a Gauss-Newton algorithm. Similarly to the calibration step, first, the Hessian matrix $[\mathbf{H}^{\mathrm{U}}]$

$$H_{\mathrm{ij}}^{\mathrm{U}}=\sum_{c=1}^{Nc}\sum_{ROI}\left(\nabla\tilde{f}^{\mathrm{c}}(\mathbf{x}^{\mathrm{c}})\cdot\frac{\partial\mathbf{x}^{\mathrm{c}}}{\partial\mathbf{X}}\cdot\psi_{\mathrm{i}}(\mathbf{X})\right)\left(\nabla\tilde{f}^{\mathrm{c}}(\mathbf{x}^{\mathrm{c}})\cdot\frac{\partial\mathbf{x}^{\mathrm{c}}}{\partial\mathbf{X}}\cdot\psi_{\mathrm{j}}(\mathbf{X})\right) \tag{2.35}$$

and the second member $\{\mathbf{B}^{\mathrm{U}}\}$

$$B_{\mathrm{i}}^{\mathrm{U}}=\sum_{c=1}^{Nc}\sum_{ROI}\left(\nabla\tilde{f}^{\mathrm{c}}(\mathbf{x}^{\mathrm{c}})\cdot\frac{\partial\mathbf{x}^{\mathrm{c}}}{\partial\mathbf{X}}\cdot\psi_{\mathrm{i}}(\mathbf{X})\right)\left(\tilde{f}^{\mathrm{c}}(\tilde{\mathbf{x}}^{\mathrm{c}})-\tilde{g}_{\mathrm{U}}^{\mathrm{c}}(\tilde{\mathbf{x}}^{\mathrm{c}},t)\right) \tag{2.36}$$

are computed, where $\frac{\partial\mathbf{x}^{\mathrm{c}}}{\partial\mathbf{X}}$ are the displacement sensitivities. The corrections to the nodal displacements read

$$\{\delta\mathbf{u}\} = \left[\mathbf{H}^{\mathrm{U}}\right]^{-1}\left\{\mathbf{B}^{\mathrm{U}}\right\} \tag{2.37}$$

and the nodal displacement vector is updated

$$\left\{\mathbf{u}(t)\right\} = \left\{\mathbf{u}(t)\right\} + \{\delta\mathbf{u}\}. \tag{2.38}$$

At each iteration step, the instantaneous grey level residuals are evaluated as a root mean square of individual normalised camera residuals

$$\rho_{\text{instant}} = \sqrt{\frac{1}{Nc}\sum_{c=1}^{Nc}\left(\frac{\tilde{g}_{\mathrm{U}}^{\mathrm{c}}\left(\tilde{\mathbf{x}}^{\mathrm{c}},t\right)-\tilde{f}^{\mathrm{c}}\left(\tilde{\mathbf{x}}^{\mathrm{c}}\right)}{\max\left(\tilde{f}^{\mathrm{c}}\left(\tilde{\mathbf{x}}^{\mathrm{c}}\right)\right)-\min\left(\tilde{f}^{\mathrm{c}}\left(\tilde{\mathbf{x}}^{\mathrm{c}}\right)\right)}\right)^2}. \tag{2.39}$$

The Gauss-Newton scheme is repeated until the stationarity of the instantaneous residuals is reached for that iteration at time *t*

$$\{\delta\rho_{\text{instant}}\} \oslash \{\rho_{\text{instant}}\} \leq 10^{-5}. \tag{2.40}$$

For Hybrid Multiview Correlation (HMC), *i.e.* when the IR modality is included in the correlation scheme, brightness and contrast corrections are mandatory for kinematic measurements and the computation of the apparent temperature. The grey level conservation between the intrinsic texture and the corrected deformed image becomes

$$\tilde{g}_{\mathrm{U}}^{\mathrm{c}}\left(\tilde{\mathbf{x}}^{\mathrm{c}},t\right) = \left(1+c\left(\mathbf{x}^{\mathrm{c}},t\right)\tilde{f}^{\mathrm{c}}\left(\tilde{\mathbf{x}}^{\mathrm{c}}\right)+b\left(\mathbf{x}^{\mathrm{c}},t\right)\right) \tag{2.41}$$

where $b\left(\mathbf{x}^{\mathrm{c}},t\right)$ and $c\left(\mathbf{x}^{\mathrm{c}},t\right)$ characterise the local brightness and contrast variations. For IR images, the temperature fields $\tilde{g}_{\mathrm{T}}^{\mathrm{c}}\left(\tilde{\mathbf{x}}^{\mathrm{c}},t\right)$ are obtained using the previous equation (2.41), which gives access to local temperature variations during the experiment in the reference (*i.e.* Lagrangian) frame.

By using the HMC algorithm, kinematic and temperature fields are measured [21], and the new cost function reads

$$\eta^2 = \sum_{c=1}^{Nc}\sum_{ROI}\left(1+c\left(\mathbf{x}^{\mathrm{c}},t\right)\tilde{f}^{\mathrm{c}}\left(\tilde{\mathbf{x}}^{\mathrm{c}}\right)+b\left(\mathbf{x}^{\mathrm{c}},t\right)-\tilde{g}_{\mathrm{U}}^{\mathrm{c}}\left(\tilde{\mathbf{x}}^{\mathrm{c}},t\right)\right)^2. \tag{2.42}$$

Brightness and contrast fields are determined camera-wise at each time step. The corrected deformed images are updated with the respective brightness $b\left(\mathbf{x}^{\mathrm{c}},t\right)$ and contrast $c\left(\mathbf{x}^{\mathrm{c}},t\right)$ can be written as

$$\tilde{g}^{\mathrm{c}}_{\mathrm{U,BCC}}\left(\tilde{\mathbf{x}}^{\mathrm{c}},t\right)=\frac{\tilde{g}^{\mathrm{c}}_{\mathrm{U}}\left(\tilde{\mathbf{x}}^{\mathrm{c}},t\right)-b\left(\mathbf{x}^{\mathrm{c}},t\right)}{1+c\left(\mathbf{x}^{\mathrm{c}},t\right)}. \tag{2.43}$$

A staggered scheme (U-BCC-U) was implemented, and the registration is performed in three consecutive steps for each image set. First, kinematic pre-convergence is sought with the first U step, followed by a BCC step. In the last step, the kinematic field is recomputed with an initial guess corresponding to the pre-converged estimate and corrected with the determined B and C fields. The complete U-BCC-U staggered approach is presented in Table 2.

Table 2. Stereocorrelation correlation algorithm (U-BCC-U procedure)

Image normalisation and gradient computation	►Eq. (2.13)
Compute the instantaneous Hessian matrix for displacement $\left[\mathbf{H}^{\mathrm{U}}\right]$	►Eq. (2.35)
Compute the instantaneous Hessian matrix for BCC $\left[\mathbf{H}^{\mathrm{c}}_{\mathrm{BCC}}\right]$	►Eq. (2.28)
while convergence of ρ_{instant} is not reached for image at time *t* **do**	►Eq. (2.40)
Update instantaneous second member $\left\{\mathbf{B}^{\mathrm{U}}\right\}$	►Eq. (2.36)
Compute incremental displacement correction $\left\{\delta\mathbf{u}\right\}$	►Eq. (2.37)
Update instantaneous displacement field $\left\{\mathbf{u}\left(t\right)\right\}$	►Eq. (2.38)
if pre-convergence is reached of ρ_{instant} **then**	
Compute BCCs second member $\left\{\mathbf{B}^{\mathrm{c}}_{\mathrm{BCC}}\right\}$	►Eq. (2.29)
Compute $\mathbf{U}\left(\mathbf{X},t\right)$ and BC fields $b^{c}\left(\mathbf{X},t\right)$, $c^{c}\left(\mathbf{X},t\right)$	
Update $\tilde{g}^{\mathrm{c}}_{\mathrm{U}}\left(\tilde{\mathbf{x}}^{\mathrm{c}},t\right)$ with $b^{c}\left(\mathbf{X},t\right)$, $c^{c}\left(\mathbf{X},t\right)$	►Eq. (2.41)
end if	
Update the global residuals ρ_{instant}	►Eq. (2.39)
Re-initialise the stereocorrelation using BC corrections and $\mathbf{U}\left(\mathbf{X},t\right)$	
end while	

2.1.3. Digital Volume Correlation

Digital Volume Correlation is the 3D extension of 2D DIC. Instead of using 2D images, DVC utilises 3D reconstructed CT volumes where each voxel contains a grey level information determined by the absorption coefficient to X-rays. The grey level conservation is assumed between the reference volume F and the deformed volume G

$$F(\mathbf{x}) = G(\mathbf{x} + \mathbf{u}(\mathbf{x})), \tag{2.44}$$

where **x** is the voxel position, and **u**(**x**) the 3D displacement field. As in 2D and stereo DIC, the unknown displacement field is determined by minimising the sum of squared differences

$$\zeta^2 = \sum_{ROI} \left(F(\mathbf{x}) - G(\mathbf{x} + \mathbf{u}(\mathbf{x})) \right)^2, \tag{2.45}$$

where the grey level residuals are minimised over the ROI. Furthermore, as in the aforementioned DIC methods, the displacement field is parametrised using FE shape functions

$$\mathbf{u}(\mathbf{x}) = \sum_{i=1}^{DOF} u_i \boldsymbol{\psi}_i(\mathbf{x}), \tag{2.46}$$

where $\boldsymbol{\psi}_i(\mathbf{x})$ are the shape functions, and u_i the nodal displacement amplitudes. The cost function is linearised using a Taylor expansion, and ζ^2 is iteratively minimised with a Gauss-Newton scheme [116]. However, such framework is ill-posed. It becomes well-posed by introducing mechanical regularisation [80, 79], which is based on the equilibrium gap in linear elasticity. Within this framework, the L2-norm of the unbalanced bulk nodal forces and traction-free surfaces is considered. The equilibrium gap cost function is defined as

$$\Xi_b^2(\{\mathbf{u}\}) = \{\mathbf{u}\}^T [\mathbf{K}_b]^T [\mathbf{K}_b] \{\mathbf{u}\}, \tag{2.47}$$

where $[\mathbf{K}_b]$ is the partial stiffness matrix for the bulk and traction free nodes. The nodal degrees of freedom on the loaded surfaces (*i.e.* Dirichlet boundaries) are not included in the aforementioned. An additional penalisation is required since the external forces are unknown [80]. Another cost function is introduced

$$\Xi_{\mathrm{s}}^{2}\left(\{\mathbf{u}\}\right)=\{\mathbf{u}\}^{\mathrm{T}}\left[\mathbf{K}_{\mathrm{s}}\right]^{\mathrm{T}}\left[\mathbf{L}\right]\left[\mathbf{K}_{\mathrm{s}}\right]\{\mathbf{u}\}, \tag{2.48}$$

where $\left[\mathbf{L}\right]$ is the Laplace-Beltrami operator, and $\left[\mathbf{K}_{\mathrm{s}}\right]$ the partial stiffness matrix for the boundary nodes. By combining the three cost functions (2.45), (2.47) and (2.48) into a single cost function Ξ_{tot} with proper weighting

$$\Xi_{\mathrm{tot}}=\tilde{\zeta}^{2}\left(\{\mathbf{u}\}\right)+\alpha_{\mathrm{b}}\tilde{\Xi}_{\mathrm{b}}^{2}\left(\{\mathbf{u}\}\right)+\alpha_{\mathrm{s}}\tilde{\Xi}_{\mathrm{s}}^{2}\left(\{\mathbf{u}\}\right), \tag{2.49}$$

with

$$\tilde{\zeta}^{2}\left(\{\mathbf{u}\}\right)=\frac{\zeta^{2}\left(\{\mathbf{u}\}\right)}{\{\mathbf{v}\}^{\mathrm{T}}\left[\mathbf{M}\right]\{\mathbf{v}\}}, \tag{2.50}$$

$$\tilde{\Xi}_{\mathrm{b}}^{2}\left(\{\mathbf{u}\}\right)=\frac{\Xi_{\mathrm{b}}^{2}\left(\{\mathbf{u}\}\right)}{\Xi_{\mathrm{b}}^{2}\left(\{\mathbf{v}\}\right)}, \tag{2.51}$$

$$\tilde{\Xi}_{\mathrm{s}}^{2}\left(\{\mathbf{u}\}\right)=\frac{\Xi_{\mathrm{s}}^{2}\left(\{\mathbf{u}\}\right)}{\Xi_{\mathrm{s}}^{2}\left(\{\mathbf{v}\}\right)} \tag{2.52}$$

where $\{\mathbf{v}\}$ gathers the nodal displacements associated with a trial displacement field defined for a shear wave of wavevector **k**, and the weighted penalties are defined for the chosen regularisation lengths λ

$$\alpha_{\mathrm{b}}=\left(\lambda_{\mathrm{b}}\left|\mathbf{k}\right|\right)^{4}, \tag{2.53}$$

$$\alpha_{\mathrm{s}}=\left(\lambda_{\mathrm{s}}\left|\mathbf{k}\right|\right)^{4}. \tag{2.54}$$

Mechanical regularisation can be considered as a low-pass filter, which imposes smoothness of the measured displacement fields through the regularisation lengths λ. It should be noted that mechanical regularisation is active only for lengths larger than the element size.

2.2. Material parameter identification

Finite Element Model Updating (FEMU) [117] is an inverse identification method that minimises the differences between measured and numerically obtained quantities. In present case, displacement fields measured with global T3 DIC approach, and measured load applied on the samples were considered. The advantage of using global DIC is that the same FE mesh used for displacement measurement can be employed in the FEMU algorithm. Moreover, the same FE mesh can be modified if the T3 elements are not suitable for numerical analyses. The measured displacements are prescribed to the FE mesh nodes on the loaded edges as Dirichlet boundary conditions (BCs). The corresponding nodal reaction forces are extracted and summed, which are then compared to the measured forces.

In the minimisation procedure, the cost function considering the displacements is formulated as the weighted squared differences between measured $\{\mathbf{u_m}\}$ and calculated $\{\mathbf{u_c}\}$ nodal displacements

$$\chi_{\mathrm{u}}^2\{\mathbf{p}\} = \frac{1}{\gamma_u{}^2 N_{\mathrm{u}}}\left\|\{\mathbf{u_m}\}-\{\mathbf{u_c}\}\right\|^2, \tag{2.55}$$

where γ_{u} is the standard displacement uncertainty. In the present case, the minimisation is performed by resorting to the χ squared estimate

$$\chi_{\mathrm{u}}^2\{\mathbf{p}\} = \frac{1}{N_{\mathrm{u}}}\left(\{\mathbf{u_m}\}-\{\mathbf{u_c}\}\right)^t\left[\mathbf{C_u}\right]^{-1}\left(\{\mathbf{u_m}\}-\{\mathbf{u_c}\}\right), \tag{2.56}$$

where $\{\mathbf{p}\}$ is the column vector containing all the sought material parameters, $[\mathbf{C_u}]$ the covariance matrix equal to $2\gamma_f{}^2[\mathbf{M}]^{-1}$ with [**M**] being the DIC Hessian matrix [9], $2\gamma_f{}^2$ the variance of the Gaussian white noise associated with image acquisition, and N_{u} the number of kinematic degrees of freedom [118].

The cost function that considers the measured $\{\mathbf{F_m}\}$ and calculated $\{\mathbf{F_c}\}$ forces extracted from the Dirichlet edges of the FE mesh is expressed as

$$\chi_{\mathrm{F}}^2\left\{\mathbf{p}\right\}=\frac{1}{\gamma_{\mathrm{F}}^2\cdot N_{\mathrm{F}}}\left\|\left\{\mathbf{F_m}\right\}-\left\{\mathbf{F_c}\right\}\right\|^2, \tag{2.57}$$

where γ_{F} is the standard uncertainty of the load cell, and N_{F} the number of load data. To combine the previous two cost functions, a weight ω is introduced

$$\chi_{\mathrm{tot}}^2\left\{\mathbf{p}\right\}=(1-\omega)\chi_{\mathrm{u}}^2+\omega\chi_{\mathrm{F}}^2. \tag{2.58}$$

By setting the weight ω to 0.5, equal weight is given to the kinematic and static data.

The minimisation of the kinematic cost function is carried out by evaluating the kinematic sensitivity fields. A Taylor expansion is applied to the computed displacement vector, at any iteration *i*

$$\mathbf{u_c}\left(\mathbf{x},t,\left\{\mathbf{p}^{(i)}\right\}\right)=\mathbf{u_c}\left(\mathbf{x},t,\left\{\mathbf{p}^{(i-1)}\right\}\right)+\frac{\partial\mathbf{u_c}}{\partial\left\{\mathbf{p}\right\}}\left(\mathbf{x},t,\left\{\mathbf{p}^{(i-1)}\right\}\right)\left\{\partial\mathbf{p}\right\}, \tag{2.59}$$

where $\left\{\partial\mathbf{p}\right\}$ is the increment of the sought material parameters. From equation (2.59), the sensitivity matrix reads

$$\left[\mathbf{S_u}\right]=\frac{\partial\mathbf{u_c}}{\partial\left\{\mathbf{p}\right\}}. \tag{2.60}$$

The sensitivity matrix is updated at each iteration *i* and it accounts for the changes in the displacement fields for a small change in the sought parameters. The linearised system is written as

$$\left\{\partial\mathbf{p_u}\right\}=\left[\mathbf{H_u}^{(i-1)}\right]^{-1}\left\{\mathbf{b_u}^{(i-1)}\right\}, \tag{2.61}$$

where $\left[\mathbf{H_u}^{(i-1)}\right]$ is the Hessian matrix expressed as a function of the sensitivity matrix

$$\left[\mathbf{H_u}^{(\mathrm{i}-1)}\right]=\left[\mathbf{S_u}^{(\mathrm{i}-1)}\right]^t\left[\mathbf{M}\right]\left[\mathbf{S_u}^{(\mathrm{i}-1)}\right], \tag{2.62}$$

and $\left\{\mathbf{b_u}^{(i-1)}\right\}$ is the second member, which is a function of the sensitivity fields and the difference between the measured and calculated displacement fields and can be expressed as

$$\left\{\mathbf{b}_{\mathbf{u}}{}^{(i-1)}\right\}=\left[\mathbf{S}_{\mathbf{u}}{}^{(i-1)}\right]^{t}\left[\mathbf{M}\right]\left(\left\{\mathbf{u}_{\mathbf{m}}\right\}-\left\{\mathbf{u}_{\mathbf{c}}{}^{(i-1)}\right\}\right). \tag{2.63}$$

An identical procedure is applied to the force cost function, where the force sensitivity matrix is expressed as

$$\left[\mathbf{S}_{\mathbf{F}}\right]=\frac{\partial\mathbf{F}_{\mathbf{c}}}{\partial\left\{\mathbf{p}\right\}}. \tag{2.64}$$

The change in the parameters is then calculated as

$$\left\{\partial\mathbf{p}_{\mathbf{F}}\right\}=\left[\mathbf{H}_{\mathrm{F}}{}^{(i-1)}\right]^{-1}\left\{\mathbf{b}_{\mathbf{F}}{}^{(i-1)}\right\}. \tag{2.65}$$

where $\left[\mathbf{H}_{\mathrm{F}}{}^{(i-1)}\right]$ is the Hessian matrix written as a function of the force sensitivity matrix

$$\left[\mathbf{H}_{\mathbf{F}}{}^{(i-1)}\right]=\frac{1}{\gamma_{\mathrm{F}}^{2}}\left[\mathbf{S}_{\mathbf{F}}\right]^{t}\left[\mathbf{S}_{\mathbf{F}}\right], \tag{2.66}$$

and the second member $\left\{\mathbf{b}_{\mathbf{F}}{}^{(i-1)}\right\}$ depends on the force sensitivity matrix and the force residuals

$$\left\{\mathbf{b}_{\mathbf{F}}{}^{(i-1)}\right\}=\frac{1}{\gamma_{\mathrm{F}}^{2}}\left[\mathbf{S}_{\mathbf{F}}\right]^{(i-1)}\left\{\mathbf{F}_{\mathbf{m}}-\mathbf{F}_{\mathbf{c}}{}^{(i-1)}\right\}. \tag{2.67}$$

Both Hessian matrices $\left[\mathbf{H}_{\mathbf{U}}\right]$ and $\left[\mathbf{H}_{\mathbf{F}}\right]$ are combined in a global Hessian matrix $\left[\mathbf{H}_{\mathbf{UF}}\right]$ by applying the weight factor ω

$$\left[\mathbf{H}_{\mathbf{UF}}\right]=\left(1-\omega\right)\left[\mathbf{H}_{\mathbf{U}}\right]+\omega\left[\mathbf{H}_{\mathbf{F}}\right]. \tag{2.68}$$

The same mathematical operation is performed to obtain the global second member $\left\{\mathbf{b}_{\mathbf{UF}}\right\}$

$$\left\{\mathbf{b}_{\mathbf{UF}}\right\}=\left(1-\omega\right)\left\{\mathbf{b}_{\mathbf{u}}\right\}+\omega\left\{\mathbf{b}_{\mathbf{F}}\right\}. \tag{2.69}$$

The global change in material parameters using kinematic and static data becomes

$$\left\{\partial\mathbf{p}\right\}=\left[\mathbf{H}_{\mathbf{UF}}\right]^{-1}\left\{\mathbf{b}_{\mathbf{UF}}\right\}. \tag{2.70}$$

FEMU was applied to two uniaxial tensile experiments where the samples, made of HARDOX 450 steel, had two distinct shapes. First, the sample (*DIN*) displayed in Figure 1(a) was designed with two parallel edges located in the entire gauge region. Near the ends, the section was widened to ensure larger gripping surfaces and to disable any sample slip. The design induced two regions with increased strain concentrations. The second (*dogbone*) sample (Figure 1(b)) was thinned in the centre of the gauge area with a radius of 75 mm, thus ensuring a unique region where strain localisation may occur.

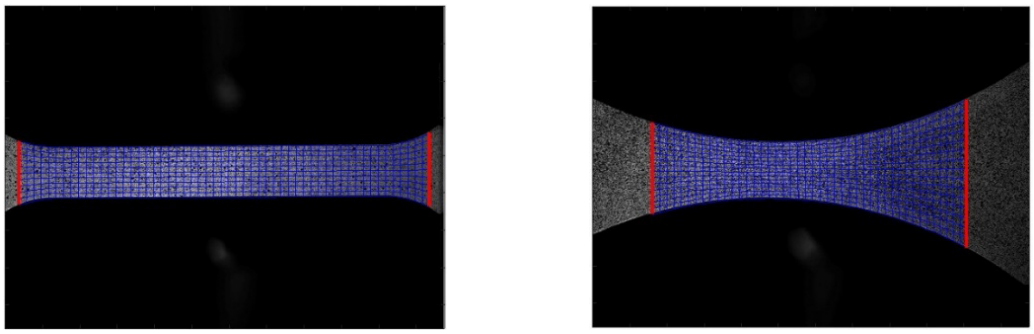

(a) (b)

Figure 1. Finite element meshes used in the identification procedure for the *DIN* (a) and *dogbone* (b) samples. The red lines depict areas where measured nodal displacements were prescribed as Dirichlet boundary conditions

For the FE simulations, the T3 FE mesh was extruded and converted into an 8-noded C3D8R mesh with reduced integration. Moreover, alongside elastic material properties, plasticity was described with Ludwik's isotropic hardening law

$$\sigma_{\mathrm{eq}} = \sigma_{\mathrm{y}} + K\varepsilon_{\mathrm{pl}}{}^{-n}, \tag{2.71}$$

where σ_{eq} corresponds to Von Mises' equivalent stress, and $\varepsilon_{\mathrm{pl}}$ the cumulated plastic strain. The sought parameters were the Young's modulus E, yield stress σ_{y}, hardening modulus K and hardening exponent n. The Poisson's ratio was not calibrated and was kept constant and equal to 0.3 since it was difficult to calibrate [14]. For both samples, the initial parameters were identical. Following the FEMU-UF procedure, it was observed that the sample geometry led to significant differences in calibrated parameters (Table 3). For both samples, the Young's modulus increased; for the *dogbone* geometry the value increased more. Moreover, for the latter, the calibrated values of the yield stress σ_{y} and hardening exponent n were higher than for the *DIN* sample. For both

samples, the hardening modulus K increased; for the *DIN* sample it increased more. Lower identification residuals were achieved for the *dogbone* sample.

Table 3. Calibrated material parameters for two sample geometries

	E, GPa	σ_Y, MPa	K, MPa	n, -	χ_{total}
Initial	210	1200	700	0.2	-
DIN	211	1060	980	0.18	41
Dogbone	219	1150	920	0.19	33

For both samples, a sensitivity analysis was conducted, where the influence of the sample geometry was evaluated. The *dogbone* sample displayed higher sensitivity for the elastic parameters (*i.e.*, Young's modulus E and Poisson's ratio v). Similar sensitivity for the yield stress σ_Y was reported for both samples. For the hardening modulus K, the *DIN* sample displayed higher sensitivity, whereas for the hardening exponent n, the *dogbone* sample exhibited higher sensitivity [11].

2.3. Improvement of the Modified Arcan Fixture experimental setup

The Modified Arcan Fixture (MAF) is a versatile loading apparatus mounted on a uniaxial testing machine. By rotating the MAF, it is possible to apply different loading types, namely, tension, simple shear and combinations thereof with step-angles of 15°, as displayed in Figure 2. The MAF was used to test samples with a thickness ranging from 1 to 5 mm.

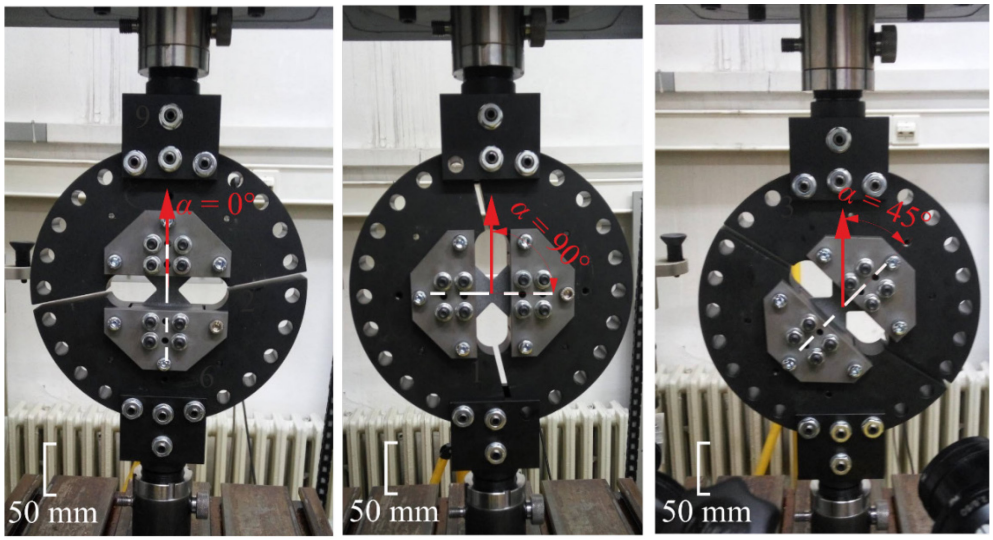

Figure 2. The Modified Arcan Fixture loading configurations

A specially designed butterfly geometry with V-notches in the gauge area was developed to ensure strain localisation around the notches. The samples are mounted within the MAF using clamps and two sets of four screws. Once the sample is fixed inside the MAF, only a 30 × 48 mm region remains visible (Figure 3).

Although the MAF offers significant advantages, testing thin sheets (*i.e.*, thickness ≤ 2 mm) under simple shear loading presents challenges. Such samples have a large gauge width to thickness ratio, which induces folding or wrinkling of the sample. In simple shear loading, two distinct stressed zones - compressive and tensile - develop on opposite ends of the visible area near the clamped regions (Figure 3(a)). Consequently, buckling initiates in the compressed zones and propagates throughout the Region Of Interest (ROI) [5, 119, 44] (Figure 3(b)). Due to the resulting large out-of-plane displacements, conventional 2D DIC is unsuitable. Therefore, stereocorrelation

is required to capture the displacement fields accurately. If the out-of-plane displacements become excessively large, even stereocorrelation may fail to provide reliable measurements.

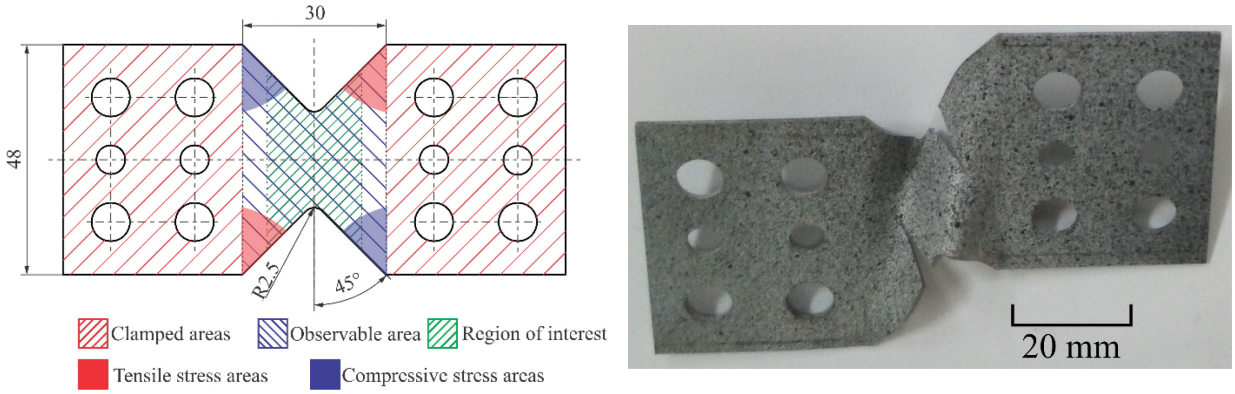

(a) (b)

Figure 3. (a) Butterfly specimen geometry with various stressed areas during simple shear loading, (b) buckled sample

The unwanted buckling mechanism, which initiates in the compression zones, can be prevented by using additional stabilisation adapters placed on the observable ROI [5], or by changing the sample gauge width [44]. The latter would require changing the MAF geometry. hence it was ruled out. Therefore, anti-buckling stabilisation adapters were designed to prevent sample buckling. The adapters in the form of two transparent plates made of *Poly Methyl Methacrylate* (PMMA) were selected (Figure 4(a)). The adapters had a transparency requirement since stereocorrelation was used to quantify out-of-plane displacements. Such configuration was already used to successfully prevent sample wrinkling in 1D and 2D tests on sub-millimetre sheets [120, 56].

For this study, 1-mm thick butterfly samples, made of C60 high carbon steel, were tested. Four configurations were defined, varying the thickness of the PMMA stabilisation adapter and the stiffness of the connection between the MAF and the testing machine. The connection stiffness needed to be evaluated since previous research [5] indicated that clamping of the fixture induces stress perturbations in the sample, thereby leading to buckling initiation. The first configuration (E1) was characterised by a loosened connection between the MAF and the testing machine. Furthermore, no additional support was applied. However, even with the allowed self-alignment of the MAF, buckling of the sample occurred. In the second configuration (E2), an additional support with 5-mm thick PMMA plates was employed. Higher stiffness of the MAF was achieved and the measured preload was higher compared to other configurations. Although the PMMA support was applied, buckling of the sample was observed, which fractured the plates. For that

reason, the third configuration (E3) employed 10-mm thick plates, and a loosened connection between the MAF and the testing machine. This configuration suppressed buckling initiation. An additional cyclic loading test (E4) was then performed with the third configuration for further validation purposes. The measured applied force on the samples for the first and the third configurations are shown in Figure 4(b) (E1 – red, E3 – blue). From these results, it is observed that the agreement between the curves is satisfactory until plasticity occurred (*i.e.*, after the yield stress was reached). When the curves diverge, the case where buckling was prevented reached the maximum load, whereas for the first case, the load decreased when the sample experienced buckling.

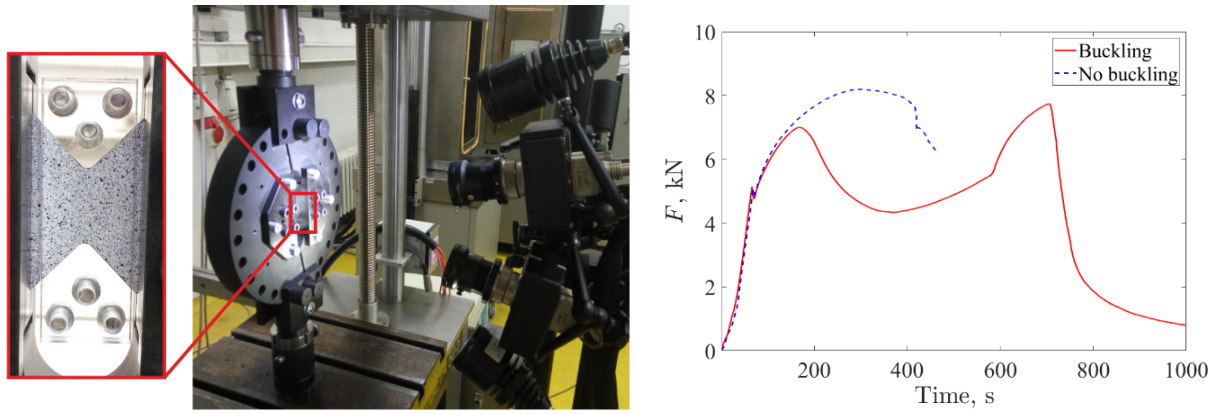

(a) (b)

Figure 4. (a) Optical stereovision setup with the extracted detail of the anti-buckling stabilisation adapter. (b) Measured force comparison between a buckled and an unbuckled sample

Table 4. gathers characteristic values for each experiment. Similar yield stresses were observed regardless of the employed configuration. It is concluded that instability initiated in the plastic regime. Furthermore, the highest ultimate load was achieved in tests E3 and E4 for a corresponding shear strain of 48%, and an ultimate shear strength of 417 MPa. A good reproducibility between the reported quantities for tests E3 and E4 is noted, which fully validated the third configuration. With the application of the PMMA plates onto sample E2, buckling was delayed, thereby leading to a 43 MPa higher ultimate shear strength compared to test E1. With thicker stabilisation adapters and loosened connection, the ultimate strength further increased by 25 MPa compared to test E2. The resulting shear strains at the ultimate load are 10-30% higher for tests E3 and E4 compared to tests E2 and E1, respectively.

Table 4. Characteristic values for the four simple shear tests on the Modified Arcan Fixture

Test	Yield stress	Ultimate shear strength	Ultimate load	Shear strain at ultimate load
E1	259 MPa	349 MPa	7.3 kN	17.5 %
E2	243 MPa	392 MPa	8.2 kN	35.6 %
E3	258 MPa	417 MPa	8.71 kN	48.7 %
E4	261 MPa	417 MPa	8.66 kN	47.4 %

2.4. Experimentally driven numerical analyses using measured Dirichlet boundary conditions

Following the previous subchapter, in this subchapter the focus is on the numerical analysis of shear experiments. The effect of friction between the PMMA plates and the sample is studied. The influence of the Dirichlet boundary conditions on the stress triaxiality fields is also explored.

First, an FE numerical model had to be developed on which the Dirichlet boundary conditions were prescribed. Two analyses were carried out on the monotonic experiment where buckling was suppressed. In the first one (T1), only the sample with the measured boundary conditions was used (Figure 5(a)), and in the second, the PMMA plates were added to the existing FE model (T2) (Figure 5(b)).

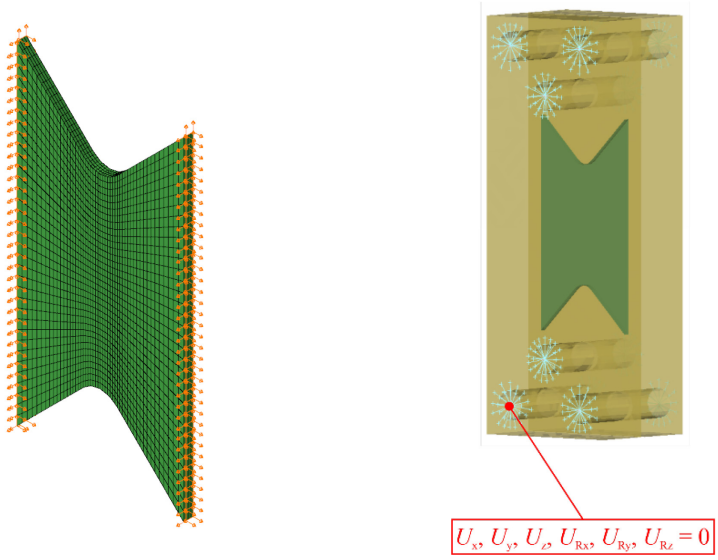

(a) (b)

Figure 5. FE model of the experiment where buckling was suppressed. (a) FE model with measured displacements prescribed as Dirichlet boundary conditions. (b) Assembly of the sample model with identical boundary conditions and the PMMA plates

In the stereocorrelation analysis, a T3 FE mesh was used to measure the displacement fields. For the FE analysis, the T3 mesh was extruded and converted into a C3D8R mesh with reduced integration. The PMMA plates were discretised with C4D4 tetrahedra elements. The measured displacements were prescribed along the loaded edges of the mesh as Dirichlet boundary conditions. The elastic parameters (*i.e.* Young's elasticity modulus E and Poisson's ratio ν) were kept constant and the plasticity parameters of the Armstrong-Frederick's model [121] were calibrated. Thus, the sought parameters were the yield stress σ_y, hardening modulus C and nonlinear coefficient c. The identification results of the model with no PMMA support are listed in Table 5. Since damage initiation and growth was out of scope for this work, the simulations were carried out for the un-damaged sample history (*i.e.* until the shear strength level).

Table 5. FEMU-UF identification results for the non-buckled sample model without PMMA support (T1)

	σ_y, MPa	C, GPa	c, -	χ_U	χ_F
Initial	250	6000	15	35	116
Calibrated	365	4635	13	23	11

Once calibrated, the parameters yielded significant decreases in both displacement and force residuals. For the T2 analysis, the rigid body motions were removed from the prescribed displacements. Between the sample and PMMA surfaces, general contact was defined by a Coulomb friction law [122]. In the available literature, the reported values of friction coefficient between PMMA and steel vary [123, 124, 125, 126], but the estimated levels generally range from 0.3 to 0.4. First, FEMU-UF was run to calibrate the plastic parameters for a very low friction coefficient (*i.e.*, $\mu = 0.01$). The calibrated parameters are reported in Table 6. The calibrated parameters were similar to those obtained previously even though the FE model was without PMMA supports. The calibrated material parameters were then used to initialise the second FEMU-UF analysis where, additionally, the friction coefficient was sought. The initial value was set to $\mu = 0.3$, which corresponds to the lower bound found in the surveyed literature. The parameters calibrated along with μ all decreased (the hardening modulus C experienced the largest relative reduction). The global residual only slightly decreased. The final calibrated friction coefficient was $\mu = 0.33$ which is consistent with the literature data.

Table 6. FEMU-UF identification results for the non-buckled sample model with PMMA support (T2)

	σ_y, MPa	C, GPa	c, -	χ_{tot}
$\mu = 0.01$	365	4616	13.1	43
$\mu = 0.3$	357	3860	11.8	42.6

For the stress triaxiality field analysis, five different numerical cases were proposed as depicted in Figure 6 and Table 7. The test cases were evaluated on the stress triaxiality fields and sample buckling modelling. For each studied case, the FE model of the sample was discretised with C3D8R elements. The first two test cases E1 and E2 were identical, except for the friction coefficient between the PMMA plates and the sample. In the third test case (E3), only planar (*i.e.* 2D) displacements were prescribed on the stressed surfaces (Figure 6(b) - R). However, this was deemed an idealised configuration as buckling could not be simulated due to a lack of any imperfection. Case E4 was identical to test cases E1 and E2 where out-of-plane U_z displacements were prescribed on the edges of the stressed surfaces (Figure 6(b) - Y). In the last test case, the entire surface (Figure 6(b) - B) was constrained with the measured out-of-plane displacements to probe the simulation validity regarding buckling.

Table 7. Test cases with their boundary conditions

Case	Description
E1	Measured U_x and U_y displacements on stressed surfaces and U_z displacements on the stressed edges of Surface 1 + PMMA plates ($\mu = 0.33$) (Figure 6(a,b) - R and Y)
E2	Measured U_x and U_y displacements on stressed surfaces and U_z displacements on the stressed edges of Surface 1 + PMMA plates ($\mu = 0.01$)
E3	Measured U_x and U_y displacements on stressed surfaces
E4	E3 and U_z displacements on stressed edges (Figure 6(b) - R and Y)
E5	E3 and U_z displacements on Surface 1 (Figure 6(b) – R, Y and B)

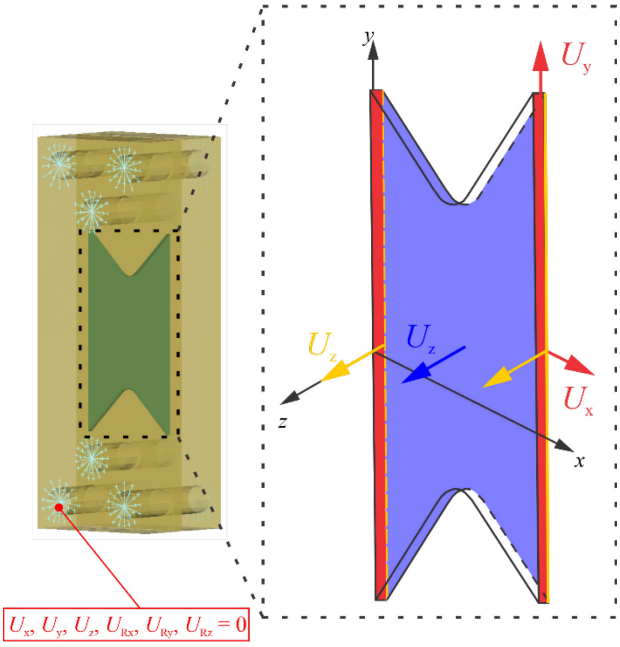

(a) (b)

Figure 6. (a) FE model with the PMMA supports. Different sets of boundary conditions. Red (R) - in-plane displacements (U_x, U_y) on entire surfaces, Yellow (Y) - out-of-plane displacements U_z on the edges, and blue (B) - out-of-plane displacements U_z on the entire surface

In Figure 7, the stress triaxiality fields are displayed for each test case and extracted from the back surface (Figure 6(b) - B). The triaxiality fields for test cases E1 and E2 (Figure 7(a, b)) are almost identical, which indicates a negligible influence of friction on the triaxiality fields. For case E3 (Figure 7(c)), by prescribing only in-plane displacements measured on the stressed surfaces of the FE model, limited wrinkling was not accounted for. Interestingly, the stress triaxiality fields are close to the previous estimates and constituted a first estimate if wrinkling had been fully prevented. By considering the out-of-plane displacements on the stressed edges of the sample for case E4 (Figure 7(d)), buckling was observed in the simulations. The resulting deformed shape is not consistent with the measured one. Different stress triaxiality fields are observed, and it was concluded that they were not physical. Last, prescribing all out-of-plane displacements as BCs on the sample surface in case E5 (Figure 7(e)), limited buckling was accurately simulated. The drawback is the inclusion of additional measurement uncertainties through such BCs. As a result, the stress triaxiality fields are more fluctuating, yet close to the levels observed when modelling the anti-buckling fixture. This case provided, by construction, accurate deformed shapes in a less computationally demanding manner than the first one.

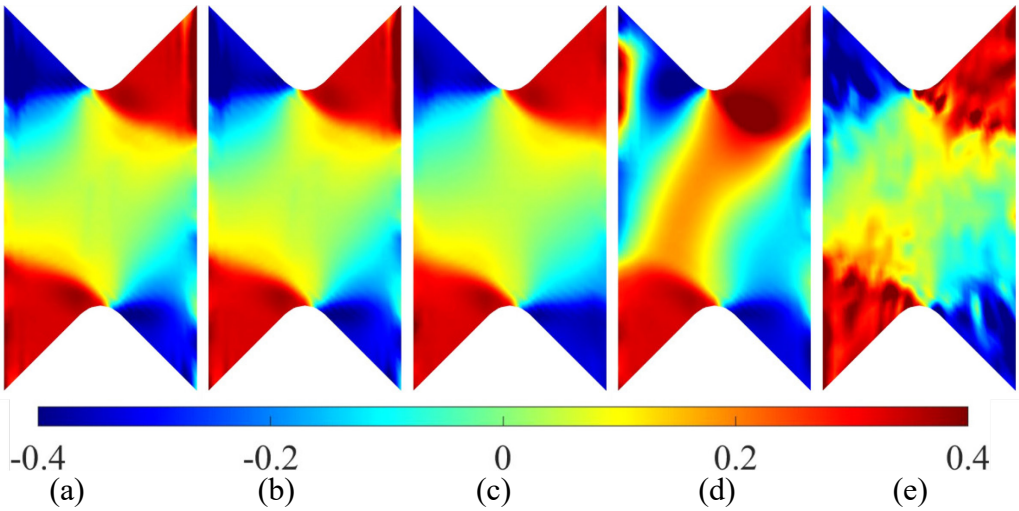

Figure 7. Stress triaxiality fields extracted from the back surface for cases (a) E1, (b) E2, (c) E3, (d) E4 and (e) E5

2.5. Semi-hybrid infrared and visible light correlation applied to a woven fibre composite Arcan sample

The previous subchapters focused on the enhancement of the MAF using stereocorrelation and numerical analyses. This part introduces the IR modality to the optical setup employed for multiaxial experiments on woven composite butterfly specimens. The semi-hybrid stereocorrelation method is introduced, where the term hybrid implies the inclusion of the IR camera. Generally, with hybrid optical setups, displacements and temperatures on the surface of the specimen are measured simultaneously using hybrid multiview correlation algorithms [72, 21, 23]. In other words, the IR images are employed directly in the correlation algorithms. However, since the IR images were not used directly in the HMC algorithm in this case, it become a semi-hybrid procedure. Furthermore, brightness and contrast corrections were not used.

The employed 3-mm thick butterfly specimen was made of woven glass fibres infused with a vinylester resin. The yarns were oriented at 0°/90° along the uniaxial tensile loading direction of the MAF (Figure 8(a)). Two notches were cut with a band saw in the central gauge area of the sample. The depth of the notches was approximately 2 mm, and the width 1 mm. The sample was loaded with a 0.24 mm/min rate in a displacement control mode.

The speckle pattern on the sample was created by spraying a thin layer of white paint on the surface, and then fine black speckles were applied using a airbrush. However, the speckle pattern was not visible in the IR spectrum (Figure 8 (b)), hence uniform emissivity ($\varepsilon = 0.96$ [127]) was assumed over the observed ROI. Since the speckle pattern was indistinguishable in the IR spectrum, IR images could not therefore be used in the stereocorrelation algorithm for the present case. Hence, only the images from the two visible light cameras observing the sample surface could be used to measure the displacement fields. Since the IR image could not be used in the calibration or the stereocorrelation algorithm, the projection matrix $\left[\mathbf{\Pi}_{\mathrm{IR}}\right]$ was obtained only via the PnP solution (Figure 8(b)).

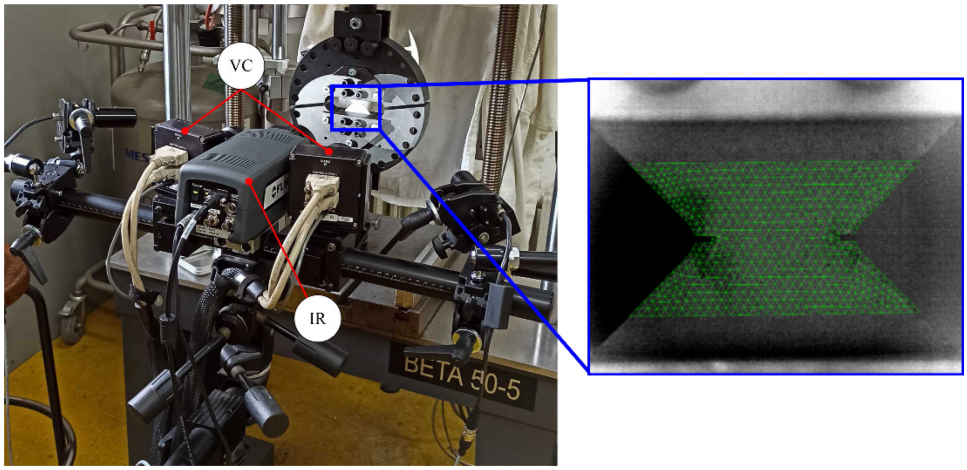

(a) (b)

Figure 8. (a) MAF experimental and optical setup. (b) Projected 3D FE mesh over the IR image

The displacement and strain fields were determined using the visible light camera images. To obtain the Lagrangian temperature fields of the ROI, the measured displacements $\mathbf{U}(\mathbf{X},t)$ needed to be transformed from the FE mesh perspective to the IR camera plane. Therefore, the nodal displacements in the IR camera plane $\mathbf{u}^{\mathrm{IR}}$ are defined as

$$\left[\mathbf{u}^{\mathrm{IR}}\right]=\left[\mathbf{x}_f^{\mathrm{IR}}\right]-\left[\mathbf{x}_g^{\mathrm{IR}}\left(t\right)\right], \tag{2.72}$$

where $\mathbf{x}_f^{\mathrm{IR}}$ is the position of any projected FE mesh node on the IR image in the reference configuration and $\mathbf{x}_g^{\mathrm{IR}}\left(t\right)$ that in the deformed configuration. The next step was to determine the projector matrix $\left[\mathbf{p}\right]$ which is used to interpolate nodal values to pixel positions. By using the

known nodal displacements, computation of the displacement fields for any pixel position can be computed

$$\begin{aligned}\left\{\mathbf{u}_x^{\mathrm{px}}(t)\right\} &= \left[\mathbf{p}\right]\cdot\left\{\mathbf{u}_x^{\mathrm{IR}}(t)\right\},\\ \left\{\mathbf{u}_y^{\mathrm{px}}(t)\right\} &= \left[\mathbf{p}\right]\cdot\left\{\mathbf{u}_y^{\mathrm{IR}}(t)\right\},\end{aligned} \tag{2.73}$$

where $\left[\mathbf{u}^{\mathrm{px}}\right]$ are the pixel-wise displacement fields of the ROI. Finally, the IR images could then be corrected using the pixel-wise displacements

$$T(\mathbf{x},t) = g^{\mathrm{IR}}\left(\mathbf{x}+\left[\mathbf{u}^{\mathrm{px}}(\mathbf{x},t)\right],t\right), \tag{2.74}$$

where $T(\mathbf{x},t)$ is the pixel-wise Lagrangian temperature fields of the ROI.

The woven composite Arcan sample was subjected to uniaxial cyclic tension using the MAF. The results presented herein are displayed for the maximum tensile strength stage (*i.e.*, approximately 289 MPa). The reported IR results were corrected by subtracting the current temperature field *T* with the first image of the corresponding loading cycle. This operation is possible thanks to the fact that Lagrangian fields were obtained.

In Figure 9 the strain in the loading direction ε_y (Figure 9(a)) and shear strains ε_{xy} (Figure 9(b)) are reported. Furthermore, Lagrangian temperature field is also displayed (Figure 9 (c)). Two strain band emanating from the tips of the notches can be observed in for the ε_y and ε_{xy} strain fields. The highest strain levels were reached above the left notch where also a faint variation in temperature can be observed indicating that the strain levels were reached earlier, leading to lower temperature and more diffuse signature. Above the right notch, increased strain levels are also present. This is also observable in the IR image (Figure 9(c)) where increased changes in temperature are present due to energy dissipation during damage initiation.

Figure 9 Measured strain and temperature fields for the ultimate tensile strength stage (289 MPa). (a) $\mathcal{E}_y$, (b) $\mathcal{E}_{xy}$ and (c) $\Delta T = T - T_0$ (in °C)

Although unidirectional tensile load was applied on the sample, shear strain bands emanated from the two notches because of the sample geometry and the underlying woven architecture. Damage initiated and developed asymmetrically around both notches, which indicates a significant influence of the woven fabric.

2.6. Multi-modal correlation method

In this subchapter, the Multi Modal Correlation (MMC) method is introduced. Compared to the previous subchapter where the IR modality was introduced separately from the stereocorrelation, herein, the conventional hybrid correlation was used. An additional modality is introduced in terms of X-ray Computed Tomography. Therefore, the MMC method incorporates *three* modalities, namely, visible light, IR and X-ray imaging within the same FE framework applied to woven composite Arcan specimens subjected to multiaxial loadings. First, a comparison of multiaxial experiment results is reported. Second, the MMC results are presented for the tensile experiment.

In Figure 10(a) the hybrid optical setup is shown. Three experiments were carried out with different imposed loading type, namely, tensile WF00 (Figure 10(b)), simple shear WF90 (Figure 10(c)) and a combined loading at a 45° angle WF45 (Figure 10(d)). The butterfly specimens were made of woven glass fibres infused with vinylester resin. The yarns were oriented at 0°/90° with respect to each other. Two notches were cut in the roots of both V sections. The notches were 2 mm long and 0.5 mm wide, reducing the net section area to approximately 48 mm^2. The samples were loaded with a 0.24 mm/min velocity in a displacement control mode. The entire experimental and optical setups were covered in black fabric (Figure 10(e)) to prevent any outside lighting

perturbations that would impact the brightness and contrast conditions of the visible light camera images during the experiments. The hybrid multiview optical setup consisted of two visible light and one infrared cameras. All three cameras observed the same ROI from different angles. Since the black and white speckles had similar emissivity as the composite sample, they were invisible in the IR spectrum. Therefore, coarse graphite speckles were also deposited onto the sample surface, which were visible to all three cameras.

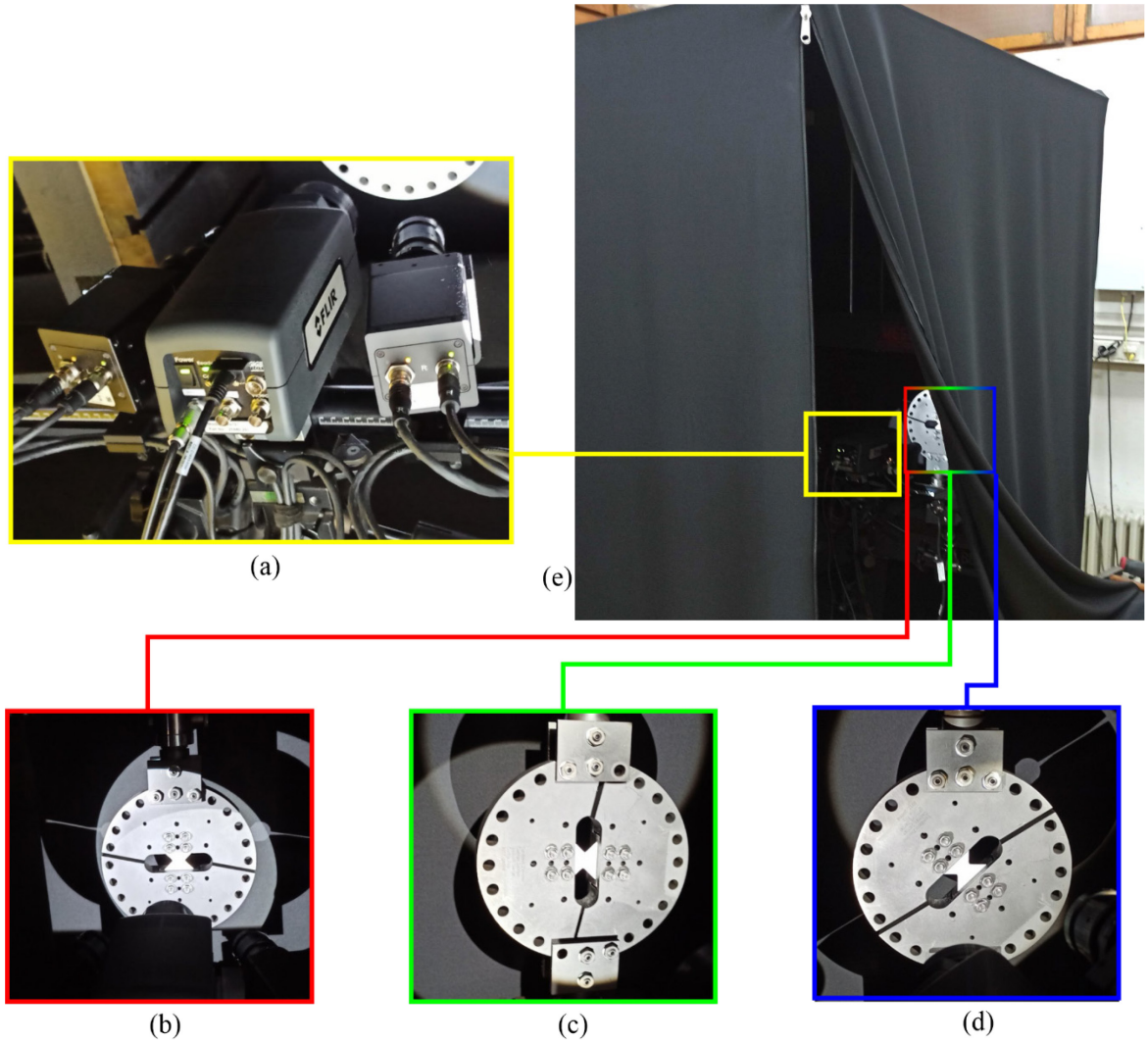

Figure 10. (a) Multimodal optical setup. (b) Tensile, (c) simple shear, (c) combined loading (at 45° angle) configurations and e) experimental and optical setup covered by black fabric

The experimental protocol for all three experiments was identical. The experiments consisted of nine loading/unloading cycles (Figure 11). The prescribed loading regime was interrupted to acquire *ex-situ* CT scans of the unloaded states. Before starting the experiment, three scans were acquired, namely Scan 0, Scan 0-bis, and Scan 0-rbm. Scan 0-bis was acquired immediately after

Scan 0. These two scans were used to evaluate the displacement and strain resolutions. The third, Scan 0-rbm, was performed to evaluate the influence of rigid body motions (RBMs) on the DVC uncertainties since the sample was periodically mounted and unmounted from the CT scanner.

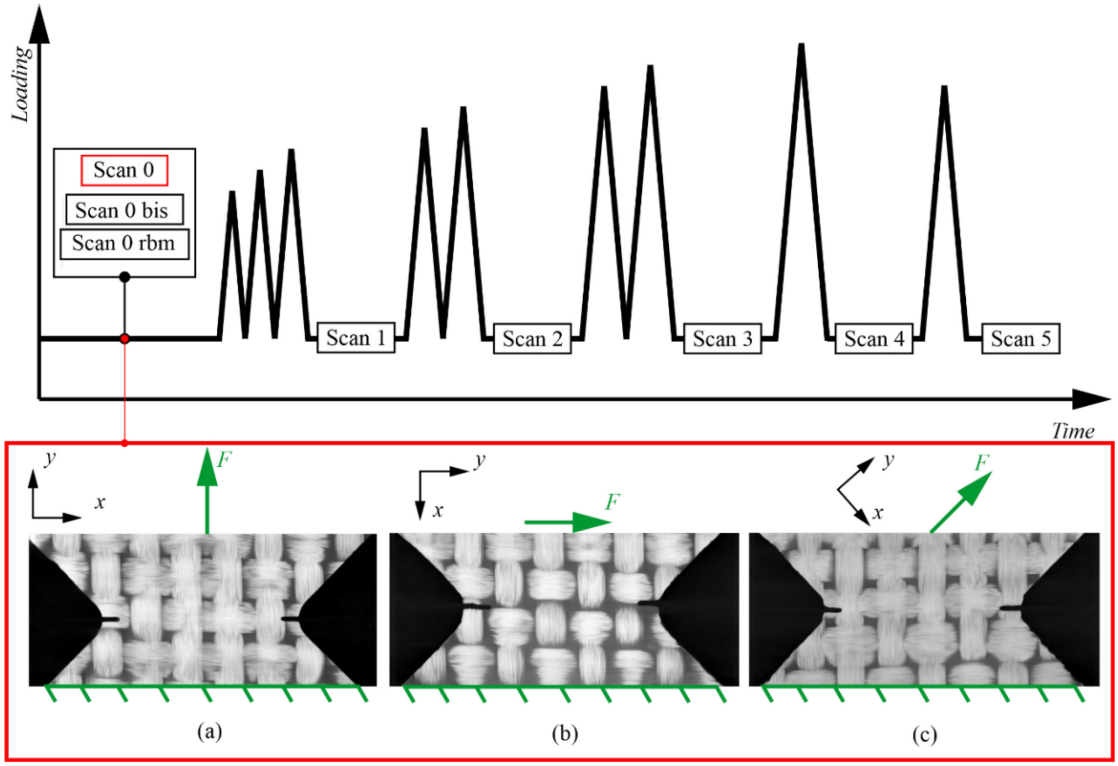

Figure 11. *Ex-situ* scanning protocol with regards to the loading history with extracted Scan 0 sections for (a) WF00, (b) WF90 and (c) WF45 tests. Additional depictions are added to display the loading directions

In Figure 12, the strain history of each experiment is displayed. The strain history was calculated by averaging the nodal strains located inside the virtual gauge defined over the FE mesh (Figure 12). The mean strains $\varepsilon_x, \varepsilon_y, \varepsilon_{xy}$ and ε_1 are compared. For the tensile experiment WF00, the strains in the loading direction *y* (Figure 11(a)) are the highest aside from the major eigenstrains ε_1. Moreover, it is observed that both transverse ε_x and shear strains ε_{xy} contribute to the major eigenstrains. For the simple shear experiment WF90 (Figure 12(b)), the shear strains are the highest. For the combined loading WF45 (Figure 12(c)), the shear strain ε_{xy} was the most prominent for the first seven cycles even though the sample was subjected to multiaxial loading. After the eighth cycle, the strain in the longitudinal direction *y* (Figure 11(c)) became dominant with respect to the shear strain. Moreover, the ε_x strain levels were comparable to those of ε_y in the WF00 test.

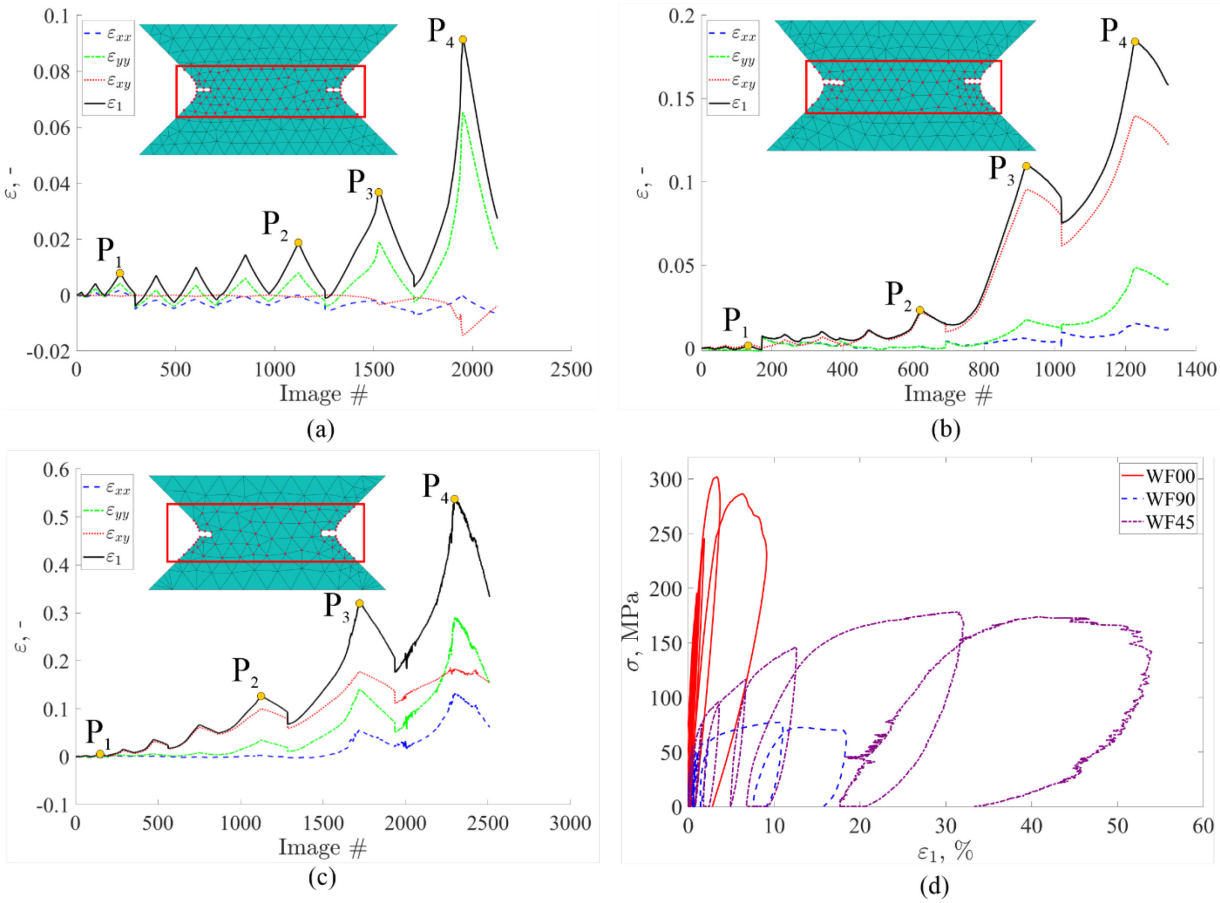

Figure 12. Strain histories with denoted virtual gauges (red boxes) for tests (a) WF00, (b) WF90, (c) WF45. (d) Comparison of the net section stress vs. major eigenstrains for all three experiments

In Figure 13, the hybrid multiview correlation results are displayed for the three experiments. The major eigenstrain and correlation residual fields are reported for the peak of the last cycle, *i.e.* point P4 in Figure 12. For the WF00 experiment (Figure 13(a)), two strain bands are observed, which originated from the roots of the notches. Four strained bands occurred in the peripheral areas. In the correlation residuals, the highest levels were detected around the root of the left notch. Two vertical residual bands are observed in the same locations as in the strain fields, and indicate damage to the speckle pattern. Several horizontal cracks are also observed, which indicate surface matrix cracking. On the peripheral areas, four cracks are visible as in the strain fields. These cracks initiated due to the differences in rigidity of the material caused by the sample geometry.

For the simple shear experiment WF90, a single strained band is observed between the roots of the V notches (Figure 13(b)). The strain band expanded outward and was not entirely located in the middle of the gauge region. In the correlation residual field, a crack is observed, which emanated from the left notch toward the centre of the sample. When compared to the surface slice

of the CT scan (Figure 11(b)), it is concluded that intra-yarn debonding occurred near the edge of the middle yarn. Furthermore, increased residuals are also visible in the entire middle part of the sample, and are attributed to damage of the speckle pattern due to the wrinkling of the material in that area.

For the combined loading experiment WF45 (Figure 13(c)), a strained band is seen, and it spans across the entire ROI at an angle. The strain levels are the highest out of all three experiments. The strain distribution aligns with the loading direction. In the correlation residuals, several crack are detected. The damage occurring at the roots of the notches is once again attributed to intra-yarn debonding since the notches were cut directly in the middle yarn (Figure 11(c)).

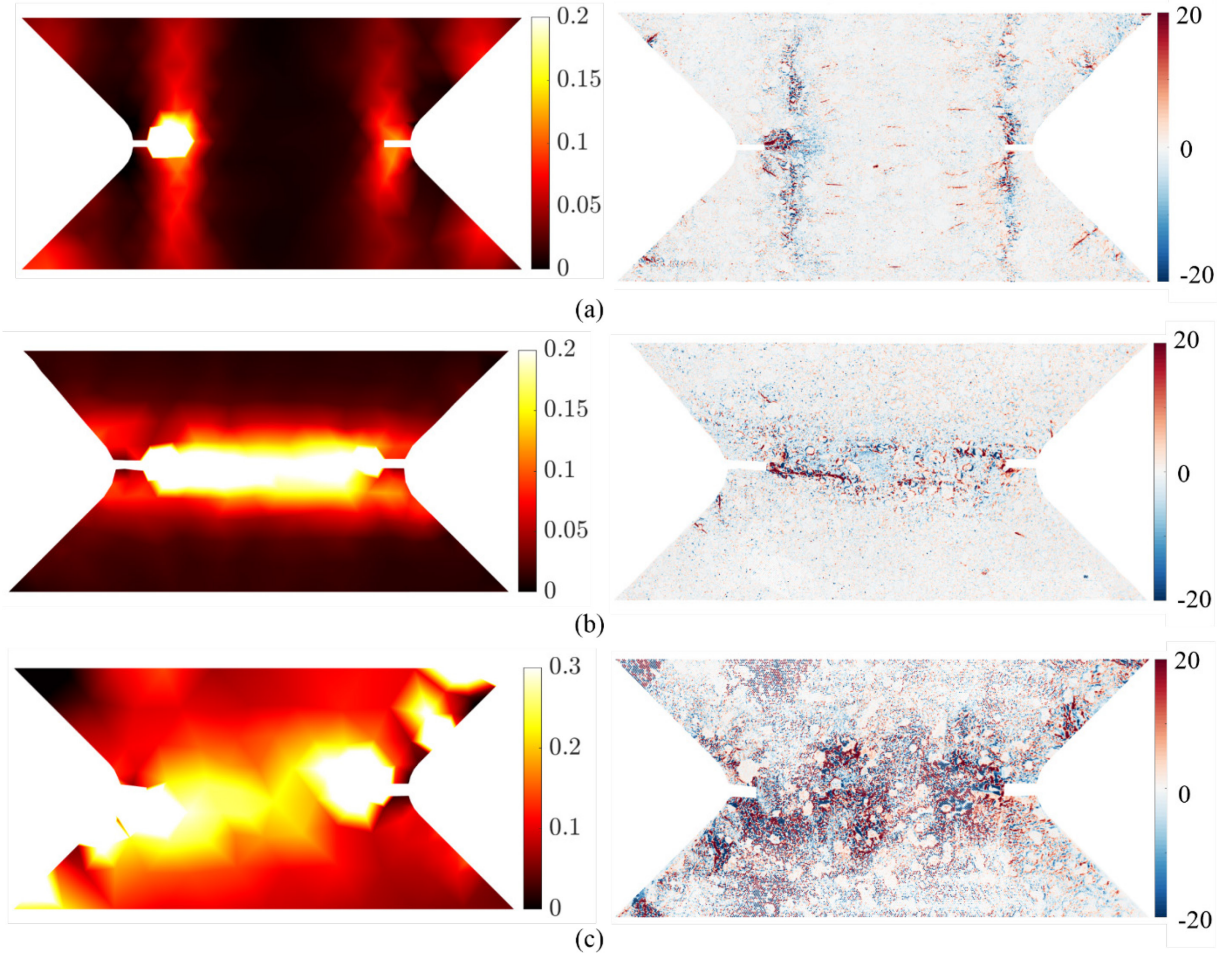

Figure 13. Major eigenstrain fields (left) and correlation residuals fields for one visible light camera (right) for the peak of the last loading cycle P4 for tests (a) WF00, (b) WF90 and (c) WF45

In Figure 14, the radiometric temperature fields are reported for the three experiments for the peak of the last cycle. For the WF00 experiment (Figure 14(a)), changes in the temperature fields

were captured. They correspond to the damage initiation and propagation around the root of the left notch. Moreover, a weaker signal was also captured around the root of the right notch. For test WF90, a single thermal band corresponding to the observed strained band is seen. This thermal band was present throughout the experiment and is attributed to inner friction between the yarns and their interplay with the matrix inside the material [128] and plastic deformation [129]. For test WF45, the temperature distribution is similar to that of test WF90. The temperature band did not lie between the notches, it was slightly tilted at an angle due to the nature of the mechanical loading.

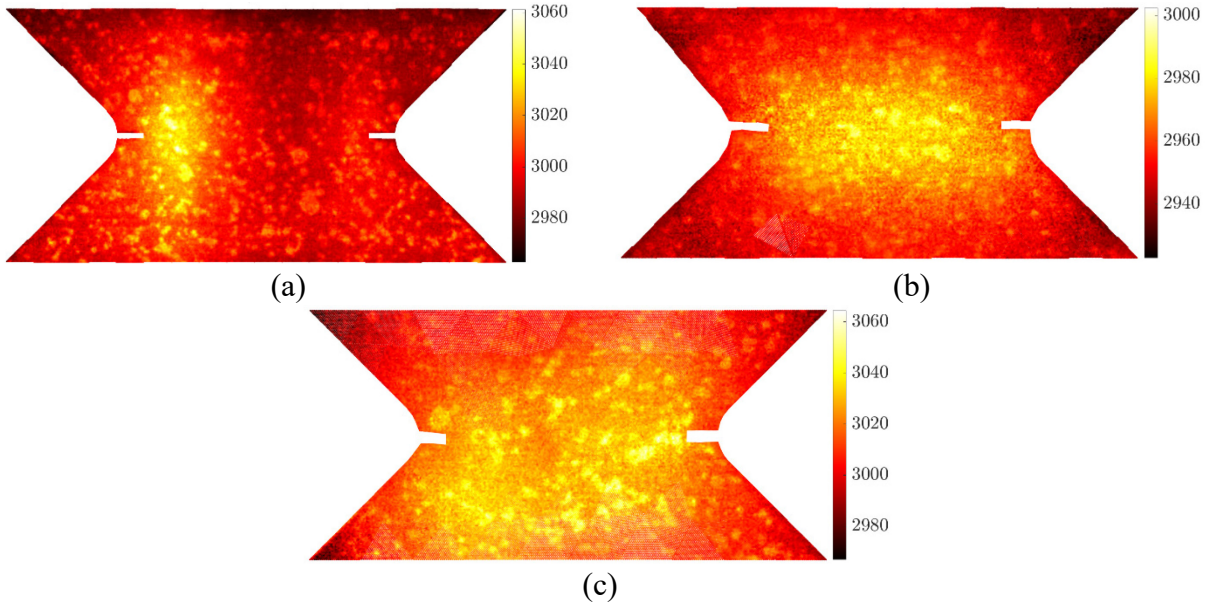

Figure 14. Radiometric temperature fields (expressed in digital levels) for test (a) WF00, (b) WF90 and (c) WF45

In the following figures, the MMC results for the tensile test WF00 are displayed for the final loading cycle (Figure 11). The analysis of the major eigenstrain and shear strain fields (Figure 15(a, b)) revealed numerous strained bands near both notches. Very high gradients are observed in the longitudinal displacement field next to the left notch (Figure 15(c)) as well as for the lower peripheral areas. The highest change in the temperature field (Figure 15(d)) was located next to the left notch. The examination of the correlation residuals (Figure 15(e, f)) confirms the development of surface damage. Notably, vertical residual stripes, indicative of shear bands, were more pronounced when emanating from the notches. Additionally, four new cracks developed around the V notches peripheral areas due to the sample geometry since these areas were less rigid than the middle one. In the correlation residuals of the IR images (Figure 15(g)), the cracks are not

visible due to the camera resolution. However, slightly increased residuals were detected around the left notch. Last, the histogram of digital level residuals for the IR camera (Figure 15(h)) was centred after BCCs were performed which further confirmed the robustness of the algorithm even in events with significant dissipation due to damage.

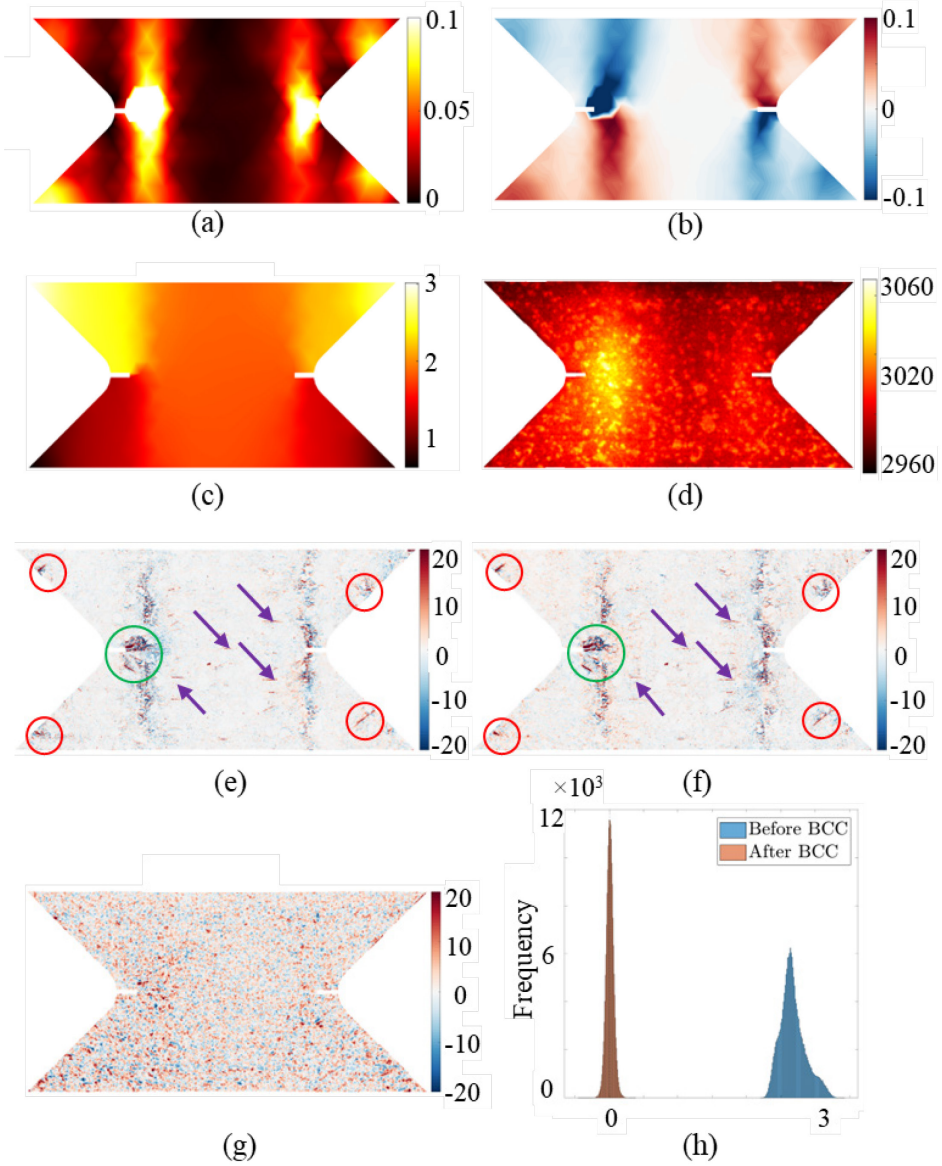

Figure 15. Hybrid multiview correlation results for test WF00.
(a) Major eigenstrain field, (b) ε_{xy} field, (c) displacement in loading direction expressed in mm, (d) temperature field expressed in digital levels. Correlation residuals of (e) the first visible light camera, (f) second visible light camera, and (g) IR camera. (f) Histogram of IR residuals before and after BCCs. The green circles denote damage development in the gauge region, whereas the red circles highlight damage on the peripheral areas. Purple arrows highlight the horizontal cracks

In the shear strain field of the last scan (Figure 16(a)), the strain distribution is similar as for the HMC observations (Figure 15(b)). The middle region exhibited lower strain levels due to the increased rigidity compared to the weakened notched areas. Higher strain levels were obtained via HMC in the peripheral regions. The reason is twofold. First, a larger ROI could be used, and second, no regularisation was used in HMC analyses. An area of increased residuals around the right notch is visible in the DVC residuals (Figure 16(b)), which was not observed in HMC (Figure 15(e, f)). This result indicates that, around the right notch, damage developed within the composite sample. A low heat signature is also visible in the IR image (Figure 15(d)), indicating growing damage within the bulk.

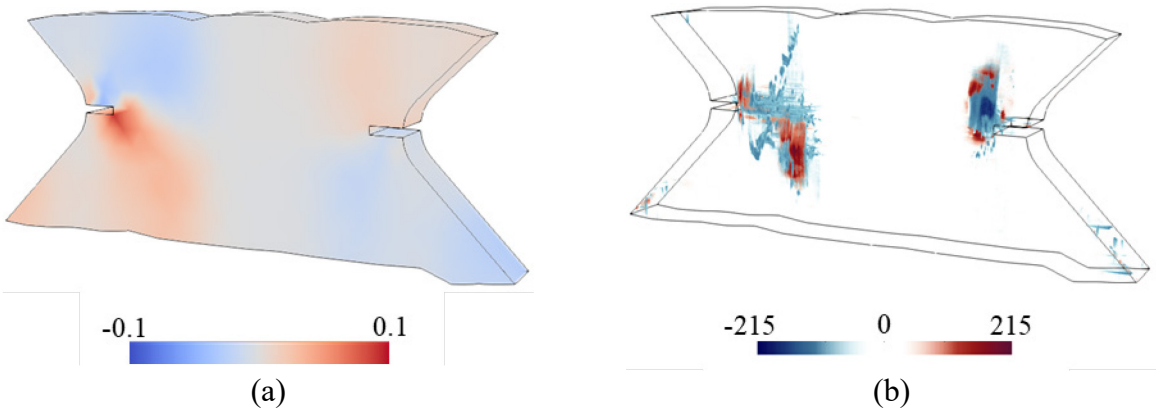

(a) (b)

Figure 16. DVC results for the final Scan 5 for test WF00. (a) ε_{xy} and (b) correlation residual fields

Figure 17 displays the corrected CT volume for the final scan, where most damage has propagated. This volume was corrected with the measured DVC displacement field (Equation (2.45)) to show it in the reference (Lagrangian) configuration. The grey level difference between the reference and the corrected deformed volumes results in the correlation residuals, highlighting areas where brightness conservation was not satisfied due to accumulated damage. Figure 17(a) highlights damage on the corrected volume. The red circles depict cracks developing on the peripheral areas of the sample, which were also observed in the HMC residuals laid over the corrected volume (Figure 17(c)). The main crack that developed in the matrix (blue square) is visible in the DVC and HMC results. A significant difference is observed in the DVC and HMC residuals (Figure 17(b, c)). The vertical bands observable in the HMC results are not visible in the DVC residuals. Additionally, the residual bands laid over the corrected volume correspond to yarn edges. It is concluded that shear did occur. However, there was no significant damage within the bulk of the sample, mainly on the speckle pattern. The cracking of the speckle pattern thus

explained the absence of vertical residual bands in DVC analyses. Several damage mechanisms were determined from the present results. The green regions depict major damage observed with all three modalities, which corresponds to yarn breakage. The red circles denote intra-yarn debonding, which was only revealed by having access to the bulk architecture of the material. The blue square highlights matrix cracking. Using the latter, horizontal surface matrix cracks across the ROI were detected but not distinguished using DVC. This finding highlights the drawback of the *ex-situ* CT protocol since the surface cracks closed while unloaded.

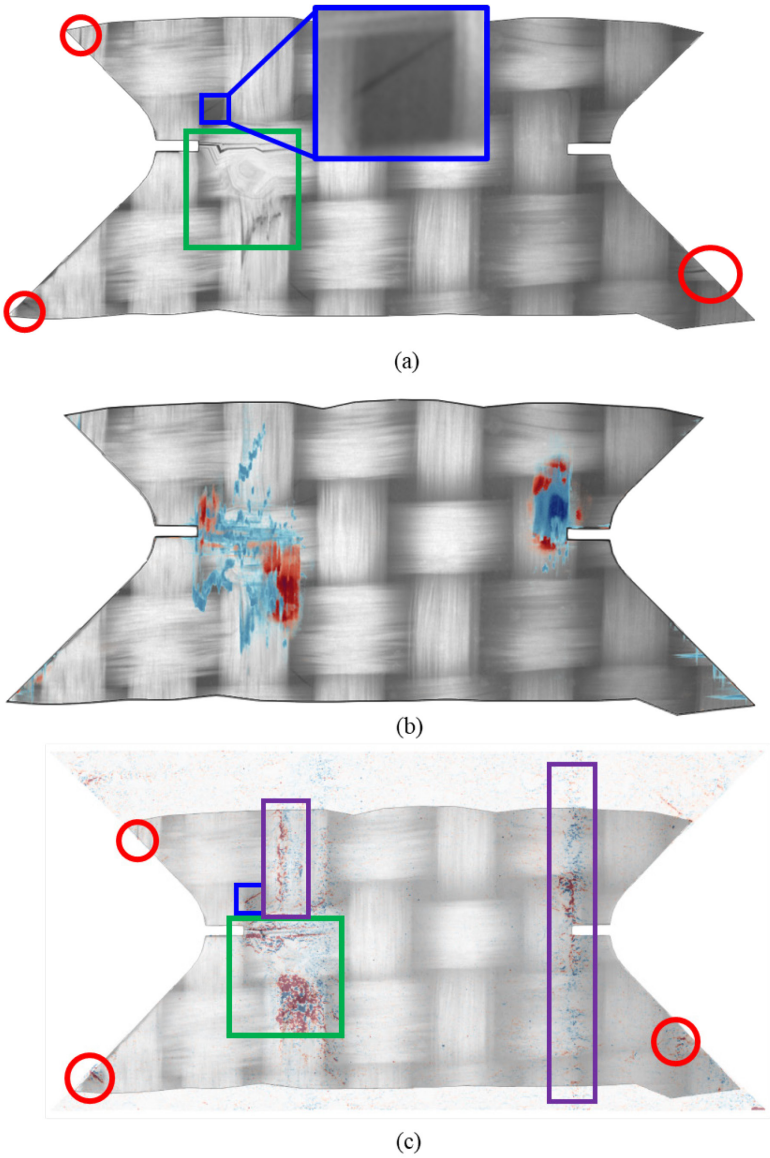

Figure 17. Corrected deformed Scan 5 for test WF00 (surface view). (a) Depicted damaged zones, (b) laid over the corresponding DVC residual map, and (c) laid over HMC residuals of the first visible light camera at the same loading stage. The green and blue squares denote major damage in the gauge region, whereas the red circles highlight damage in the peripheral areas. The purple rectangles highlight the vertical residual HMC correlation bands

3. Conclusions and future work

3.1. Conclusions

In this dissertation, advanced measurement methods were used to characterise thin sheet materials subjected to complex loading regimes. These methods included material parameter calibration via Finite Element Model Updating, 2D Digital Image Correlation, Stereocorrelation, Digital Volume Correlation, and advanced Multimodal correlation.

The first aim of the dissertation was to improve the Modified Arcan fixture for conducting multiaxial experiments on thin sheet materials. By subjecting thin specimens to simple shear or loading where shear is dominant, sample buckling may occur due to the large sample width to thickness ratio. Sheets with a thickness less than 2 mm are especially affected. As a result of sample buckling, it was not possible to obtain reliable material responses even with advanced measurement methods such as stereocorrelation during the prescribed loading regime.

Improvements to the Modified Arcan Fixture were introduced in the form of transparent stabilisation adapters made of PMMA. By employing the adapters, buckling was successfully mitigated, and reliable mechanical responses of 1 mm thick C60 steel samples were obtained. The same experiment was repeated for cyclic simple shear loading, which confirmed its repeatability. Furthermore, the friction coefficient between the PMMA plates and the sample was evaluated numerically using FEMU. The influence of the PMMA plates and the friction between them and the sample was evaluated on the stress triaxiality fields. It was concluded that friction had a minimal influence on the triaxiality fields. However, the Dirichlet boundary conditions displayed a major influence on the triaxiality fields, and the calibrated material parameters. It was concluded that the PMMA plates had to be included in the identification procedure to obtain reliable material parameters. Prescribing all measured out-of-plane displacements provided reliable stress triaxiality fields and limited buckling could be simulated accurately.

The second aim of the dissertation was the development of a hybrid stereocorrelation algorithm that used visible light and infrared cameras. Brightness and contrast corrections were mandatory since the digital levels on the infrared images change due to thermomechanical couplings. Such

hybrid framework was especially useful for the characterisation of composite materials since breakage of individual fibres and yarns could be captured.

Two stereocorrelation algorithms were developed, which employed both visible light and infrared camera images. The first algorithm was semi-hybrid since the infrared images were not directly involved in the correlation analysis. Yet, Lagrangian temperature fields could be extracted from the infrared images. For this algorithm, brightness and contrast corrections were not necessary. Conversely, in the second algorithm, the infrared images were directly incorporated and used alongside the visible light camera images in the correlation analysis. Brightness and contrast corrections were required to obtain Lagrangian temperature fields over the region of interest defined by the finite element mesh. Corrected temperature fields, expressed in digital levels, could be calculated and compared to the measured displacement and strain fields. Three experiments with different loading regimes were carried out. The highest stress levels were observed for the tensile test, whereas the highest strain levels were achieved with the combined loading experiment. For the tensile test, two strained bands emanated from the notches parallel to the loading direction. For the simple shear and combined loading, a single strained band was captured. For the latter, the strained band was slightly inclined at an angle due to the influence of tension. Damage mechanisms could be identified using only Computed Tomography slices. For the simple shear and combined loadings, intra-yarn debonding emanated from the notches towards the sample centre. For the tensile test, yarn breakage, intra-yarn debonding and surface matrix cracking were observed. In the temperature fields of the tensile test, temperature changes were mostly localised around the notches, whereas for the other two experiments, there was a single temperature band between the notches due to yarn inner friction.

The final aim of the dissertation was to develop a multimodal experimental protocol and correlation procedure. Such procedure incorporated three spectra, namely, visible light, infrared, and X-ray radiations within the same finite element framework. Such multimodal correlation method is ideal for a comprehensive characterisation of fibre reinforced polymer composites. From the first two spectra, which were used in the hybrid stereocorrelation algorithm, surface-wise displacement, strain and temperature fields were measured. From the X-ray spectrum, using Computed Tomography and Digital Volume Correlation, 3D displacement and strain fields in the bulk of the tested material were obtained. Consistent results were reported between the hybrid

correlation and Digital Volume Correlation data. Furthermore, using the infrared data, damage within the bulk of the material was observed. This observed was also confirmed by the Digital Volume Correlation residuals. The same damage was not seen using the visible light cameras. The multimodal correlation procedure represents the most comprehensive characterisation method used on the fibre reinforced polymer composites. No such method, which incorporates all three modalities within the same framework, was found in the literature.

3.2. Future work

Within this dissertation, several numerical and experimental methods were presented, which open many possibilities for further improvement and implementation to real engineering purposes. Several questions remain open for future research.

First, additional mechanical experiments may be conducted using the Modified Arcan fixture across a wide range of loading angles. Such an experimental campaign would allow for the analysis of the influence of tensile versus shear loading in combined conditions (at varying angles). Investigating the damage mechanisms that occur under different loading regimes in fibre-reinforced polymer composites would provide valuable insights into their mechanical behaviour.

Next, more advanced numerical analyses could be performed for the analyses of stress triaxiality fields. In these simulations, out-of-plane displacements could be incorporated into the numerical model using numerical springs with varying stiffness, allowing for a relaxation of Dirichlet boundary constraints on the surface. This approach would help minimise the influence of measurement uncertainties, leading to more accurate stress triaxiality field predictions.

Regarding the multimodal correlation procedure and experimental setup, the *ex-situ* approach was not ideal. Removing the sample from the Modified Arcan Fixture introduced significant rigid body motions. Although stereocorrelation tracks these motions, temperature variations may occur between unmounting and remounting the sample. In contrast, *in-situ* experiments would provide a more stable environment for both the sample and the optical system. However, the primary challenge lies in the constraints of the CT scanner. Traditional enclosed CT scanners are unsuitable for this setup, necessitating the use of open scanners that offer sufficient space to accommodate the optical system.

Last, material parameter identification procedures, such as FEMU, could be applied to various multiaxial loading experiments. Utilising multimodal correlation data, two distinct analyses could be performed, namely, one based on stereocorrelation data and another one using DVC measurements, where CT scanning was performed either *ex-situ* or *in-situ*.

Literature

[1] M. Zistl, M. Brünig and S. Gerke, "Analysis of damage and fracture behavior in ductile metal sheets undergoing compression and shear preloading," *International Journal of Material Forming,* vol. 15, no. 4, doi: 10.1007/s12289-022-01705-4

[2] A. Zaplatić, Z. Tomičević, D. Čakmak and F. Hild, "Improvement of the Arcan Setup for the Investigation of Thin Sheet Behavior Under Shear Loading," *Experimental Mechanics,* vol. 62, no. 2, pp. 313-332, doi: 10.1007/s11340-021-00762-1

[3] P. Hao, I. U. Din and S. Panier, "Development of Modified Arcan Fixture for biaxial loading response of fiber-reinforced composites," *Polymer Testing,* vol. 80, doi: 10.1016/j.polymertesting.2019.106148

[4] W. Li, Y. Qiao, J. Fenner, K. Warren, M. Salviato, Z. P. Bažant and G. Cusatis, "Elastic and fracture behavior of three-dimensional ply-to-ply angle interlock woven composites: Through-thickness, size effect, and multiaxial tests," *Composites Part C: Open Access,* vol. 4, doi: 10.1016/j.jcomc.2020.100098

[5] C. H. Pham, F. Adzima, J. Coër and P. Y. Manach, "Anti-Buckling Device for Ultra-Thin Metallic Sheets Under Large and Reversed Shear Strain Paths," *Experimental Mechanics,* vol. 57, no. 4, pp. 593-602, doi: 10.1007/s11340-017-0256-4

[6] A. Vrgoč, Z. Tomičević, B. Smaniotto and F. Hild, "Application of different imaging techniques for the characterization of damage in fiber reinforced polymer," *Composites Part A: Applied Science and Manufacturing,* vol. 150, doi: 10.1016/j.compositesa.2021.106576

[7] R. Vargas, A. Tsitova, F. Bernachy-Barbe, B. Bary, R. B. Canto and F. Hild, "On the identification of cohesive zone model for curved crack in mortar," *Strain,* vol. 56, no. 6, p. e12364, doi: 10.1111/str.12364

[8] M. Berny, T. Archer, P. Beauchêne, A. Mavel and F. Hild, "Displacement Uncertainty Quantifications in T3-Stereocorrelation," *Experimental Mechanics,* vol. 61, no. 5, pp. 771-790, doi: 10.1007/s11340-021-00690-0

[9] F. Hild and S. Roux, "Comparison of Local and Global Approaches to Digital Image Correlation," *Experimental Mechanics,* vol. 52, no. 9, pp. 1503-1519, doi: 10.1007/s11340-012-9603-7

[10] A. Vrgoč, Z. Tomičević, B. Smaniotto and F. Hild, "Characterization of glass fiber reinforced polymer via digital volume correlation: Quantification of strain activity and damage growth," *Composites Science and Technology,* vol. 234, no. March, p. 109932, doi: 10.1016/j.compscitech.2023.109932

[11] A. Zaplatić, Z. Tomičević, D. Čakmak and F. Hild, "Identifiability of Ludwik's law parameters depending on the sample geometry via inverse identification procedure," *Coupled Systems Mechanics,* vol. 11, no. 2, pp. 133-149, doi: 10.12989/csm.2022.11.2.133

[12] D. Lecompte, A. Smits, H. Sol, J. Vantomme and D. V. Hemelrijck, "Mixed numerical-experimental technique for orthotropic parameter identification using biaxial tensile tests on cruciform specimens," *International Journal of Solids and Structures,* vol. 44, no. 5, pp. 1643-1656, doi: 10.1016/j.ijsolstr.2006.06.050

[13] A. Zaplatić, A. Vrgoč, Z. Tomičević and F. Hild, "Boundary condition effect on the evaluation of stress triaxiality fields," *International Journal of Mechanical Sciences,* vol. 246, doi: 10.1016/j.ijmecsci.2023.108127

[14] Z. Tomičević, J. Kodvanj and F. Hild, "Characterization of the nonlinear behavior of nodular graphite cast iron via inverse identification-Analysis of uniaxial tests," *European Journal of Mechanics, A/Solids,* vol. 59, pp. 140-154, doi: 10.1016/j.euromechsol.2016.02.010

[15] Z. Tomičević, J. Kodvanj and F. Hild, "Characterization of the nonlinear behavior of nodular graphite cast iron via inverse identification: Analysis of biaxial tests," *European Journal of Mechanics, A/Solids,* vol. 59, pp. 195-209, doi: 10.1016/j.euromechsol.2016.03.006

[16] R. Gras, H. Leclerc, F. Hild, S. Roux and J. Schneider, "Identification of a set of macroscopic elastic parameters in a 3D woven composite: Uncertainty analysis and regularization," *International Journal of Solids and Structures,* vol. 55, pp. 2-16, doi: 10.1016/j.ijsolstr.2013.12.023

[17] S. Roux and F. Hild, "Optimal procedure for the identification of constitutive parameters from experimentally measured displacement fields," *International Journal of Solids and Structures,* vol. 184, pp. 14-23, doi: 10.1016/j.ijsolstr.2018.11.008

[18] R. Yang, Y. He and H. Zhang, *Progress and trends in nondestructive testing and evaluation for wind turbine composite blade,* vol. 60, Elsevier Ltd, 2016, pp. 1225-1250.

[19] S. Farmaki, D. A. Exarchos, I. K. Tragazikis, T. E. Matikas and K. G. Dassios, "A novel infrared thermography sensing approach for rapid, quantitative assessment of damage in

aircraft composites," *Sensors (Switzerland),* vol. 20, no. 15, pp. 1-16, doi: 10.3390/s20154113

[20] Y. Wang, A. Charbal, F. Hild, S. Roux and L. Vincent, "Crack initiation and propagation under thermal fatigue of austenitic stainless steel," *International Journal of Fatigue,* vol. 124, pp. 149-166, doi: 10.1016/j.ijfatigue.2019.02.036

[21] A. Charbal, J. E. Dufour, F. Hild, M. Poncelet, L. Vincent and S. Roux, "Hybrid Stereocorrelation Using Infrared and Visible Light Cameras," *Experimental Mechanics,* vol. 56, no. 5, pp. 845-860, doi: 10.1007/s11340-016-0127-4

[22] A. Jung, K. A. Majthoub, C. Jochum, S. M. Kirsch, F. Welsch, S. Seelecke and S. Diebels, "Correlative digital image correlation and infrared thermography measurements for the investigation of the mesoscopic deformation behaviour of foams," *Journal of the Mechanics and Physics of Solids,* vol. 130, pp. 165-180, doi: 10.1016/j.jmps.2019.06.009

[23] Y. Wang, A. Charbal, J. E. Dufour, F. Hild, S. Roux and L. Vincent, "Hybrid Multiview Correlation for Measuring and Monitoring Thermomechanical Fatigue Test," *Experimental Mechanics,* vol. 60, p. 13–33, doi: 10.1007/s11340-019-00500-8

[24] A. Zaplatić, Z. Tomičević, X. Chang, I. Skozrit, S. Roux and F. Hild, "Hybrid infrared-visible multiview correlation to study damage in a woven composite complex-shaped specimen," *Coupled Systems Mechanics,* vol. 12, doi: doi.org/10.12989/csm.2023.12.5.000

[25] A. Charbal, S. Roux, F. Hild and L. Vincent, "Spatiotemporal regularization for digital image correlation: Application to infrared camera frames," *International Journal for Numerical Methods in Engineering,* vol. 114, no. 12, pp. 1331-1349, doi: 10.1002/nme.5788

[26] A. Vrgoč, Z. Tomičević, B. Smaniotto and F. Hild, "Characterization of glass fiber reinforced polymer via Digital Volume Correlation: Investigation of notch sensitivity," *Mechanics of Materials,* vol. 177, no. February, p. 104552, doi: 10.1016/j.mechmat.2022.104552

[27] A. Bartulović, Z. Tomičević, A. Bubalo and F. Hild, "Assessment of DVC measurement uncertainty on GFRPs with various fiber architectures," *Coupled Systems Mechanics,* vol. 11, no. 1, pp. 15-32, doi: 10.12989/csm.2022.11.1.015

[28] M. Tisza, "Numerical Modeling and Simulation in Sheet Metal Forming Academic and Industrial Perspectives," *Materials Science Forum,* Vols. 473-474, pp. 407-414, doi: 10.4028/www.scientific.net/msf.473-474.407

[29] A. E. Tekkaya, J. M. Allwood, P. F. Bariani, S. Bruschi, J. Cao, S. Gramlich, P. Groche, G. Hirt, T. Ishikawa, C. Lobbe, J. Lueg-Althoff, M. Merklein, W. Z. Misiolek, M. Pietrzyk, R. Shivpuri and J. Yanagimoto, "Metal forming beyond shaping: Predicting and setting product properties," *CIRP Ann. - Manuf. Technol.,* vol. 64, no. 2, pp. 629-653, doi: 10.1016/j.cirp.2015.05.001

[30] F. Khan, N. Hossain, J. J. Mim, S. M. Rahman, M. J. Iqbal, M. Billah and M. A. Chowdhury, "Advances of composite materials in automobile applications – A review," *Journal of Engineering Research,* doi: 10.1016/j.jer.2024.02.017

[31] M. E. Torbali, A. Zolotas and N. P. Avdelidis, "A State-of-the-Art Review of Non-Destructive Testing Image Fusion and Critical Insights on the Inspection of Aerospace Composites towards Sustainable Maintenance Repair Operations," *Applied Sciences,* vol. 13, no. 4, p. 2732, doi: 10.3390/app13042732

[32] R. Hsissou, R. Seghiri, Z. Benzekri, M. Hilali, M. Rafik and A. Elharfi, "Polymer composite materials: A comprehensive review," *Composite Structures,* vol. 262, p. 113640, doi: 10.1016/j.compstruct.2021.113640

[33] N. Li and Y. D. Zhou, "Failure mechanism analysis of fiber-reinforced polymer composites based on multi-scale fracture plane angles," *Thin-Walled Structures,* vol. 158, p. 107195, doi: https://doi.org/10.1016/j.tws.2020.107195

[34] J. Du, H. Wang, C. Chen, M. Ni, C. Guo, S. Zhang, H. Ding, H. Wang and Y. Bi, "Damage classification and evolution in composite under low-velocity impact using acoustic emission, machine learning and wavelet packet decomposition," *Engineering Fracture Mechanics,* vol. 306, p. 110238, doi: 10.1016/j.engfracmech.2024.110238

[35] Y. Ma, L. Wu, L. Yu, E. A. Elbadry, W. Yang, X. Huang, X. Yan and H. Cao, "Effect of fiber breakage position on the mechanical performance of unidirectional carbon fiber/epoxy composites," *REVIEWS ON ADVANCED MATERIALS SCIENCE,* vol. 60, no. 1, pp. 352-364, doi: 10.1515/rams-2021-0029

[36] M. Gu, C. Wu, X. Chen, Y. Wan, Y. Liu, S. Zhou, H. Cai, B. Jia, R. Wang and W. Li, "Stress-Induced Microcracking and Fracture Characterization for Ultra-High-Temperature Ceramic Matrix Composites at High Temperatures," *Materials,* vol. 15, no. 20, p. 7074, doi: 10.3390/ma15207074

[37] T. Kanakubo, S. Echizen, J. Wang and Y. Mu, "Pullout Behavior of Bundled Aramid Fiber in Fiber-Reinforced Cementitious Composite," *Materials,* vol. 13, no. 7, p. 1746, doi: 10.3390/ma13071746

[38] B. Sabuncuoglu and S. V. Lomov, "Micro-scale numerical study of fiber/matrix debonding in steel fiber composites," *Journal of Engineered Fibers and Fabrics,* vol. 15, p. 1558925020910726, doi: 10.1177/1558925020910726

[39] F. Paundra, D. Istanto, E. Pujiyulianto, M. Arif and S. Hastuti, "Effect of Layers on Delamination and Tensile Strength of Woven Fiber Composites with Polyester Matrix," *Journal Teknik Mesin,* vol. 21, no. 1, doi: 10.9744/jtm.21.1.11-20

[40] J. Neggers, F. Mathieu, F. Hild and S. Roux, "Simultaneous full-field multi-experiment identification," *Mechanics of Materials,* vol. 133, pp. 71-84, doi: 10.1016/j.mechmat.2019.03.001

[41] L. Zhang and N. Yang, "Evaluation of a modified Iosipescu shear test method for determining the shear properties of clear wood," *Wood Science and Technology,* vol. 51, no. 2, pp. 323-343, doi: 10.1007/s00226-016-0888-z

[42] M. Arcan, Z. Hashin and A. Voloshin, "A Method to Produce Uniform Plane-stress States with Applications to Fiber-reinforced Materials," *Experimental Mechanics,* vol. 18, no. 4, pp. 141-146, doi: 10.1007/BF02324146

[43] E. F. Rauch, *Plastic anisotropy of sheet metals determined by simple shear tests,* vol. 241, 1998, pp. 179-183.

[44] S. Bouvier, H. Haddadi, P. Levée and C. Teodosiu, "Simple shear tests: Experimental techniques and characterization of the plastic anisotropy of rolled sheets at large strains," *Journal of Materials Processing Technology,* vol. 172, no. 1, pp. 96-103, doi: 10.1016/j.jmatprotec.2005.09.003

[45] A. Abedini, J. Noder, C. P. Kohar and C. Butcher, "Accounting for Shear Anisotropy and Material Frame Rotation on the Constitutive Characterization of Automotive Alloys using Simple Shear Tests," *Mechanics of Materials,* vol. 148, p. 103419, doi: 10.1016/j.mechmat.2020.103419

[46] J. Peirs, P. Verleysen and J. Degrieck, "Novel Technique for Static and Dynamic Shear Testing of Ti6Al4V Sheet," *Experimental Mechanics,* vol. 52, no. 7, pp. 729-741, doi: 10.1007/s11340-011-9541-9

[47] C. C. Roth and D. Mohr, "Ductile fracture experiments with locally proportional loading histories," *International Journal of Plasticity,* vol. 79, pp. 328-354, doi: 10.1016/j.ijplas.2015.08.004

[48] N. Iosipescu, "New Accurate Procedure for Single Shear Testing of Metals," *Journal of Materials,* vol. 2, no. 3, pp. 537-566,

[49] D. Mohr and S. Henn, "Calibration of stress-triaxiality dependent crack formation criteria: A new hybrid experimental-numerical method," *Experimental Mechanics,* vol. 47, no. 6, pp. 805-820, doi: 10.1007/s11340-007-9039-7

[50] D. Mohr and M. Doyoyo, "A new method for the biaxial testing of cellular solids," *Experimental Mechanics,* vol. 43, no. 2, pp. 173-182, doi: 10.1007/BF02410498

[51] D. Mohr and M. Oswald, "A new experimental technique for the multi-axial testing of advanced high strength steel sheets," *Experimental Mechanics,* vol. 48, no. 1, pp. 65-77, doi: 10.1007/s11340-007-9053-9

[52] M. Dunand and D. Mohr, "Optimized butterfly specimen for the fracture testing of sheet materials under combined normal and shear loading," *Engineering Fracture Mechanics,* vol. 78, no. 17, pp. 2919-2934, doi: 10.1016/j.engfracmech.2011.08.008

[53] A. Abedini, C. Butcher, D. Anderson, M. Worswick and T. Skszek, "Fracture Characterization of Automotive Alloys in Shear Loading," *SAE International Journal of Materials and Manufacturing,* vol. 8, no. 3, pp. 774-782, doi: 10.4271/2015-01-0528

[54] A. Abedini, C. Butcher and M. J. Worswick, "Fracture Characterization of Rolled Sheet Alloys in Shear Loading: Studies of Specimen Geometry, Anisotropy, and Rate Sensitivity," *Experimental Mechanics,* vol. 57, no. 1, pp. 75-88, doi: 10.1007/s11340-016-0211-9

[55] S. Boni, C. G'Sell, E. Weynant and J. M. Haudin, "Microscopic in situ observation of the plastic deformation of polybutene-1 films under simple shear," *Polymer Testing,* vol. 3, no. 1, pp. 3-24, doi: 10.1016/0142-9418(82)90009-5

[56] M. Bertin, F. Hild and S. Roux, "On the identifiability of Hill-1948 plasticity model with a single biaxial test on very thin sheet," *Strain,* vol. 53, no. 5, doi: 10.1111/str.12233

[57] M. A. Sutton, "Computer vision-based, noncontacting deformation measurements in mechanics: A generational transformation," *Applied Mechanics Reviews,* vol. 65, no. 5, doi: 10.1115/1.4024984

[58] J. Holmes, S. Sommacal, R. Das, Z. Stachurski and P. Compston, "Digital image and volume correlation for deformation and damage characterisation of fibre-reinforced composites: A review," *Composite Structures,* vol. 315, p. 116994, doi: 10.1016/j.compstruct.2023.116994

[59] M. A. Sutton and F. Hild, "Recent Advances and Perspectives in Digital Image Correlation," *Experimental Mechanics,* vol. 55, no. 1, pp. 1-8, doi: 10.1007/s11340-015-9991-6

[60] M. A. Sutton, J. J. Orteu and H. Schreier, Image Correlation for Shape, Motion and Deformation Measurements: Basic Concepts,Theory and Applications, Springer US, 2009, pp. 1-321.

[61] T. C. Chu, W. F. Ranson and M. A. Sutton, "Applications of digital-image-correlation techniques to experimental mechanics," *Experimental Mechanics,* vol. 25, no. 3, pp. 232-244, doi: 10.1007/BF02325092

[62] G. Besnard, F. Hild and S. Roux, ""Finite-element" displacement fields analysis from digital images: Application to Portevin-Le Châtelier bands," *Experimental Mechanics,* vol. 46, no. 6, pp. 789-803, doi: 10.1007/s11340-006-9824-8

[63] Y. Sun, J. Pang, C. Wong and F. Su, "Finite-element formulation for a digital image correlation method," *Applied Optics,* vol. 44, pp. 7357-7363,

[64] M. Flores, D. Mollenhauer, V. Runatunga, T. Beberniss, D. Rapking and M. Pankow, "High-speed 3D digital image correlation of low-velocity impacts on composite plates," *Composites Part B: Engineering,* vol. 131, pp. 153-164, doi: https://doi.org/10.1016/j.compositesb.2017.07.078

[65] R. Fouque, R. Bouclier, J.-C. passieux and J.-N. ël Périé, "Stereo digital image correlation: formulations and perspectives," *Comptes Rendus. Mécanique,* vol. 349, no. 3, pp. 453-463, doi: https://doi.org/10.5802/crmeca.93

[66] X. Chang, C. L. Gourriéreca, L. Turpin, M. Berny, F. Hild and S. Roux, "Proper Generalized Decomposition stereocorrelation to measure kinematic fields for high speed impact on laminated glass," *Computer Methods in Applied Mechanics and Engineering,* vol. 415, p. 116217, doi: 10.1016/j.cma.2023.116217

[67] B. Beaubier, J.-E. Dufour, F. Hild, S. Roux, S. Lavernhe and K. L. Taillard, "CAD-Based Calibration and Shape Measurement with StereoDIC principle and Application on Test and Industrial Parts," *Experimental Mechanics,* vol. 54, no. 3, pp. 329-341, doi: ff10.1007/s11340-013-9794-6ff.ffhal-00974363

[68] J.-E. Dufour, B. Beaubier, F. Hild and S. Roux, "CAD-based displacement measurements with Stereo-DIC," *Experimental Mechanics,* vol. 55, p. 1657–1668, doi: https://doi.org/10.1007/s11340-015-0065-6

[69] A. Zaplatić, Z. Tomičević, X. Chang, P. Kosec, S. Roux and F. Hild, "Advanced FE-based multimodal correlation analyses for the characterization of woven composite," *Mechanical Systems and Signal Processing,* vol. 224, p. 112079, doi: 10.1016/j.ymssp.2024.112079

[70] G. Besnard, J.-M. Lagrange, F. Hild, S. Roux and C. Voltz, "Characterization of necking phenomena in high speed experiments by using a single camera," *EURASIP Journal on Image and Video Processing,* vol. 2010, p. 215956,

[71] L. Yu and B. Pan, "Single-camera stereo-digital image correlation with a four-mirror adapter: optimized design and validation," *Optics and Lasers in Engineering,* vol. 87, pp. 120-128, doi: 10.1016/j.optlaseng.2016.03.014

[72] J.-E. Dufour, F. Hild and S. Roux, "Shape, displacement and mechanical properties from isogeometric multiview stereocorrelation," *The Journal of Strain Analysis for Engineering Design,* vol. 50, no. 7, pp. 470-487, doi: 10.1177/0309324715592530ï

[73] L. Dubreuil, J.-E. Dufour, Y. Quinsat and F. Hild, "Mesh-Based Shape Measurements with Stereocorrelation Principle and First Results," *Experimental Mechanics,* vol. 56, pp. 1231-1242, doi: 10.1007/s11340-016-0158-

[74] J.-E. Pierré, J.-C. Passieux and J.-N. ël Périé, "Finite Element Stereo Digital Image Correlation: Framework and Mechanical Regularization," *Experimental mechanics,* vol. 57, p. pages443–456, doi: 10.1007/s11340-016-0246-y

[75] H. Liu and F. Hild, "Quantifying 3D crack propagation in nodular graphite cast iron using advanced digital volume correlation and X-ray computed tomography," *Engineering Fracture Mechanics,* vol. 296, p. 109824, doi: 10.1016/j.engfracmech.2023.109824

[76] E. Maire and P. J. Withers, *Quantitative X-ray tomography,* vol. 59, 2014, pp. 1-43.

[77] J. Holmes, S. Sommacal, R. Das, Z. Stachurski and P. Compston, "Characterisation of off-axis tensile behaviour and mesoscale deformation of woven carbon-fibre/PEEK using digital image correlation and X-ray computed tomography," *Composites Part B: Engineering,* vol. 229, p. 109448, doi: https://doi.org/10.1016/j.compositesb.2021.109448

[78] S. Yang, H. Liu, L. Mao, F. Li, B. Wei, Y. Ju and F. Hild, "Damage quantification in concrete under uniaxial compression using microcomputed tomography and digital volume correlation with consideration of heterogeneity," *Mechanics of Materials,* vol. 199, p. 105178, doi: 10.1016/j.mechmat.2024.105178

[79] Z. Tomičevć, F. Hild and S. Roux, "Mechanics-aided digital image correlation," *Journal of Strain Analysis for Engineering Design,* vol. 48, no. 5, pp. 330-343, doi: 10.1177/0309324713482457

[80] A. Mendoza, J. Neggers, F. Hild and S. Roux, "Complete mechanical regularization applied to digital image and volume correlation," *Computer Methods in Applied Mechanics and Engineering,* vol. 355, pp. 27-43, doi: 10.1016/j.cma.2019.06.005

[81] L. Mao, H. Liu, Y. Zhu, Z. Zhu, R. Gue and F. Chiang, "3D Strain Mapping of Opaque Materials Using an Improved Digital Volumetric Speckle Photography Technique with X-Ray Microtomography," *Applied Sciences,* vol. 9, no. 7, p. 1418, doi: doi.org/10.3390/app9071418

[82] V. Kosin, A. Fau, C. Jailin, B. Smaniotto, T. Wick and F. Hild, "A projection-based approach to extend digital volume correlation for {4D} spacetime measurements," *Comptes Rendus Mécanique,* vol. 351, pp. 265-280, doi: 10.5802/crmeca.192

[83] A. Buljac, C. Jailin, A. Mendoza, J. Neggers, T. Taillandier-Thomas, A. Bouterf, B. Smaniotto, F. Hild and S. Roux, "Digital Volume Correlation: Review of Progress and Challenges," *Experimental Mechanics,* vol. 58, no. 3, doi: 10.1007/s11340-018-0390-7

[84] R. F. Agyei, I. Hanhan and M. D. Sangid, "Detecting damage initiation in short fiber composites via in-situ X-ray tomography and digital volume correlation," *Composites Communications,* vol. 22, p. 100524, doi: doi.org/10.1016/j.coco.2020.100524

[85] M. Mehdikhani, C. Breite, Y. Swolfs, J. Soete, M. Wevers, S. V. Lomov and L. Mehdikhani, "Digital volume correlation for meso/micro in-situ damage analysis in carbon fiber reinforced composites," *Composites Science and Technology,* vol. 213, no. 8, p. 108944, doi: 10.1016/j.compscitech.2021.108944

[86] S. Avril, M. Bonnet, A. Bretelle, M. Gr\'ediac, F. Hild, P. Ienny, F. Latourte, D. Lemosse, S. Pagano, E. Pagnacco and F. Pierron, "Overview of identification methods of mechanical parameters based on full-field measurements," *Experimental Mechanics,* vol. 48, no. 4, pp. 381-402, doi: 10.1007/s11340-008-9148-y

[87] M. Grédiac and F. Hild, Full-Field Measurements and Identification in Solid Mechanics, London: Wiley, 2012.

[88] F. Pierron and M. Grédiac, "Towards Material Testing 2.0. A review of test design foridentification of constitutive parameters from full-field measurements," *Strain,* vol. 57, p. e12370, doi: 10.1111/str.12370

[89] P. Prates, A. Pereira, N. Sakharova, M. Oliveira and J. Fernandes, "Inverse Strategies for Identifying the Parameters of Constitutive Laws of Metal Sheets," *Advanced Material Science,* vol. 2016, no. 1, pp. 1-18, doi: 10.1155/2016/4152963

[90] J. M. P. Martins, A. Andrade-Campos and S. Thuillier, "Comparison of inverse identification strategies for constitutive mechanical models using full-field measurements," *International Journal of Mechanical Sciences,* vol. 145, pp. 330-345, doi: 10.1016/j.ijmecsci.2018.07.013

[91] A. Guery, F. Hild, F. Latourte and S. Roux, "Identification of crystal plasticity parameters using DIC measurements and weighted FEMU," *Mechanics of Materials,* vol. 100, pp. 55-71, doi: 10.1016/j.mechmat.2016.06.007

[92] D. Claire, F. Hild and S. Roux, "A finite element formulation to identify damage fields: The equilibrium gap method," *International Journal for Numerical Methods in Engineering,* vol. 61, no. 2, pp. 189-208, doi: 10.1002/nme.1057

[93] G. Geymonat, F. Hild and S. Pagano, "Identification of elastic parameters by displacement field measurement," *Comptes Rendus Mécanique,* vol. 330, pp. 403-408, doi: 10.1016/S1631-0721(02)01476-6

[94] M. Grédiac and F. Pierron, "Applying the Virtual Fields Method to the identification of elasto-plastic constitutive parameters," *International Journal of Plasticity,* vol. 22, no. 4, pp. 602-627, doi: 10.1016/j.ijplas.2005.04.007

[95] M. Bertin, F. Hild, S. Roux, F. Mathieu, H. Leclerc and P. Aimedieu, "Integrated Digital Image Correlation applied to elasto-plastic identification in a biaxial experiment," *Journal of Strain Analysis for Engineering Design,* vol. 51, no. 2, pp. 118-131, doi: 10.1177/0309324715614759

[96] P. A. Prates, A. F. G. Pereira, M. C. Oliveira and J. V. Fernandes, "Analytical sensitivity matrix for the inverse identification of hardening parameters of metal sheets," *European Journal of Mechanics, A/Solids,* vol. 75, pp. 205-215, doi: 10.1016/j.euromechsol.2019.01.010

[97] J. Neggers, F. Mathieu, F. Hild, S. Roux and N. Swiergiel, "Improving full-field identification using progressive model enrichments," *International Journal of Solids and Structures,* Vols. 118-119, pp. 213-223, doi: 10.1016/j.ijsolstr.2017.03.013

[98] M. Bertin, F. Hild and S. Roux, "Optimization of a Cruciform Specimen Geometry for the Identification of Constitutive Parameters Based Upon Full-Field Measurements," *Strain,* vol. 52, no. 4, pp. 307-323, doi: 10.1111/str.12178

[99] D. Lindner, F. Mathieu, F. Hild, O. Allix, C. H. Minh and O. Paulien-Camy, "On the evaluation of stress triaxiality fields in a notched titanium alloy sample via integrated digital image correlation," *Journal of Applied Mechanics, Transactions ASME,* vol. 82, no. 7, doi: 10.1115/1.4030457

[100] M. Brünig, M. zistl and S. Gerke, "Biaxial experiments on characterization of stress-state-dependent damage in ductile metals," *Production Engineering,* vol. 14, pp. 87-93, doi: 10.1007/s11740-019-00930-2

[101] H. Panwitt, H. Heyer and M. Sander, "Experimental and Numerical Investigation of the Fracture Behavior of Welded Aluminum Cross," *Materials,* vol. 13, no. 4310, pp. 1-23, doi: 10.3390/ma13194310

[102] M. Gao, Z. Zhou, K. Ding and X. Wang, "Detection of crack defects in carbon fiber composites using passive infrared thermography," *Ferroelectrics,* vol. 607, no. 1, pp. 154-172, doi: 10.1080/00150193.2023.2198383

[103] S. A. Keo., F. Brachelet, F. Breaban and D. Defer, "Defect detection in CFRP by infrared thermography with CO2 Laser excitation compared to conventional lock-in infrared thermography," *Composites Part B: Engineering,* vol. 69, pp. 1-5, doi: https://doi.org/10.1016/j.compositesb.2014.09.018

[104] F. Ciampa, P. Mahmoodi, F. Pinto and M. Meo, "Recent Advances in Active Infrared Thermography for Non-Destructive Testing of Aerospace Components," *Sensors,* vol. 18, doi: 10.3390/s18020609

[105] V. Munoz, B. Valès, M. Perrin, M. L. Pastor, H. Welemane, A. Cantarel and M. Karama, "Damage detection in CFRP by coupling acoustic emission and infrared thermography," *Composites Part B: Engineering,* vol. 85, pp. 68-75, doi: 10.1016/j.compositesb.2015.09.011

[106] C. Maierhofer, M. Röllig, M. Gower, M. Lodeiro, G. Baker, C. Monte, A. Adibekyan, B. Gutschwager, L. Knazowicka and A. Blahut, "Evaluation of Different Techniques of Active Thermography for Quantification of Artificial Defects in Fiber-Reinforced Composites Using Thermal and Phase Contrast Data Analysis," *International Journal of Thermophysics,* vol. 39, no. 61, doi: 10.1007/s10765-018-2378-z

[107] M. A. Farooq, W. Shariff, D. O'callaghan, A. Merla and P. Corcoran, "On the Role of Thermal Imaging in Automotive Applications: A Critical Review," *IEEE Access,* vol. 11, pp. 25152-25173, doi: 10.1109/ACCESS.2023.3255110

[108] J. Zalameda and W. Winfree, "Passive Thermography Measurement of Damage Depth During Composites Load Testing," *Frontiers in Mechanical Engineering,* vol. 7, p. 651149, doi: 10.3389/fmech.2021.651149

[109] N. Cholewa, P. Summers, S. Feih, A. Mouritz, B. Lattimer and S. Case, "A Technique for Coupled Thermomechanical Response Measurement Using Infrared Thermography and Digital Image Correlation (TDIC)," *Experimental Mechanics,* vol. 56, pp. 145-164, doi: 10.1007/S11340-015-0086-1

[110] Y. Wang, A. Charbal, J. E. Dufour, F. Hild, S. Roux and L. Vincent, "Hybrid Multiview Correlation for Measuring and Monitoring Thermomechanical Fatigue Test," *Experimental Mechanics,* vol. 60, no. 1, pp. 13-33, doi: 10.1007/s11340-019-00500-8

[111] A. Charbal, S. Roux, F. Hild and L. Vincent, "Regularised digital-level corrections for infrared image correlation," *Quantitative InfraRed Thermography Journal,* vol. 15, no. 2, pp. 172-193, doi: 10.1080/17686733.2018.1425955

[112] X. Chang, C. L. Gourriérec, F. Hild and S. Roux, "Brightness and contrast corrections for stereocorrelation Global and instantaneous formulation with spatial regularization," *Mechanical Systems and Signal Processing,* vol. 208, p. 111057, doi: doi.org/10.1016/j.ymssp.2023.111057

[113] M. Stamm, P. Krüger, H. Pfeiffer, B. Köhler, J. Reynaert and M. Wevers, "In-Plane Heatwave Thermography as Digital Inspection Technique for Fasteners in Aircraft Fuselage Panels," *Applied Sciences,* vol. 11, no. 1, p. 132, doi: 10.3390/app11010132

[114] V. Lepetit, F. Moreno-Noguer and P. Fua, "EPnP: An accurate O(n) solution to the PnP problem," *International Journal of Computer Vision,* vol. 81, no. 2, pp. 155-166, doi: 10.1007/s11263-008-0152-6

[115] F. Barone, M. Marrazzo and C. J. Oton, "Camera Calibration with Weighted Direct Linear Transformation and Anisotropic Uncertainties of Image Control Points," *Sensors,* vol. 20, no. 4, p. 1175, doi: 10.3390/s20041175

[116] S. Roux, F. Hild, P. Viot and D. Bernard, "Three-dimensional image correlation from X-ray computed tomography of solid foam," *Composites Part A: Applied Science and Manufacturing,* vol. 39, no. 8, pp. 1253-1265, doi: 10.1016/j.compositesa.2007.11.011

[117] K. T. Kavanagh and R. W. Clough, "Finite element applications in the characterization of elastic solids," vol. 7, no. 1, pp. 11-23, doi: 10.1016/0020-7683(71)90015-1

[118] F. Mathieu, H. Leclerc, F. Hild and S. Roux, "Estimation of Elastoplastic Parameters via Weighted FEMU and Integrated-DIC," *Experimental Mechanics,* vol. 55, no. 1, pp. 105-119, doi: 10.1007/s11340-014-9888-9

[119] S. Boni, C. G'Sell, E. Weynant and J. Haudin, "Microscopic in situ observation of the plastic deformation of polybutene-1 films under simple shear," *Polymer Testing,* vol. 3, no. 1, pp. 3-24, doi: 10.1016/0142-9418(82)90009-5

[120] M. Bertin, F. Hild and S. Roux, "On the identifiability of the Hill-1948 model with one uniaxial tensile test," *Comptes Rendus Mécanique,* vol. 345, no. 6, pp. 363-369, doi: 10.1016/j.crme.2017.04.001

[121] C. Frederic and P. Armstrong, "A Mathematical Representation of the Multiaxial Bauscinger Effect," *Materials at High Temperatures,* vol. 24, pp. 1-26, doi: 10.3184/096034007X207589

[122] C. C, Theorie des machines simples, Paris: Bachelier, 1821.

[123] A. Lim, S. Castagne and C. Wong, "Effect of Friction Coefficient on Finite Element Modeling of the Deep - Cold Rolling Process," *International Conference on Shot Peening,* pp. 376-380,

[124] N. Nuño, M. Amabili, R. Groppetti and A. Rossi, "Static coefficient of friction between Ti-6A1-4V and PMMA for cemented hip and knee implants," *Journal of Biomedical Materials Research,* vol. 59, no. 1, pp. 191-200, doi: 10.1002/jbm.1233

[125] N. Nuño, R. Groppetti and N. Senin, "Static coefficient of friction between stainless steel and PMMA used in cemented hip and knee implants," *Clinical Biomechanics,* vol. 21, no. 9, pp. 956-962, doi: 10.1016/j.clinbiomech.2006.05.008

[126] L. Rabbe, J. Rieu, A. Lopez and P. Combrade, "Fretting deterioration of orthopaedic implant materials: Search for solutions," *Clinical Materials,* vol. 15, pp. 221-226, doi: 10.1016/0267-6605(94)90049-3

[127] C. Leistner, M. Löffelholz and S. Hartmann, "Model validation of polymer curing processes using thermography," *Polymer Testing,* vol. 77, doi: 10.1016/j.polymertesting.2019.05.009

[128] Z. Pan, Z. Wu and J. Xiong, "Localized temperature rise as a novel indication in damage and failure behavior of biaxial non-crimp fabric reinforced polymer composite subjected to impulsive compression," *Aerospace Science and Technology,* vol. 103, p. 105885, doi: 10.1016/j.ast.2020.105885

[129] P. S. Singh, R. Narayan, I. Sen, D. Hofmann and U. Ramamurty, "Effect of strain rate and temperature on the plastic deformation behaviour of a bulk metallic glass composite," *Materials Science and Engineering A-structural Materials Properties Microstructure and Processing,* vol. 534, pp. 476-484, doi: 10.1016/J.MSEA.2011.11.096

[130] A. Benelli, R. Ciardiello, C. B. Niutta and L. Goglio, "Experimental and numerical characterization of adhesive joints with composite substrates by means of the Arcan test," *International Journal of Adhesion and Adhesives,* vol. 122, doi: 10.1016/j.ijadhadh.2022.103321

[131] R. Ciardiello, L. Greco, M. Miranda, F. D. Sciullo and L. Goglio, "Experimental investigation on adhesively bonded U-shaped metallic joints using the Arcan test," *Journal of Advanced Joining Processes,* vol. 1, doi: 10.1016/j.jajp.2020.100010

Curriculum vitae

Andrija Zaplatić was born on June 15, 1994, in Zagreb, Croatia. In 2013, he finished the Archbishop grammar school (Nadbiskupska klasična gimnazija) in Zagreb, and started his studies at the Faculty of Mechanical Engineering and Naval Architecture (FAMENA), University of Zagreb. He finished his studies at FAMENA in 2019 with *magna cum laude* honours. Since 2019, he has been employed by the Faculty of Mechanical Engineering and Naval Architecture, University of Zagreb, at the Department of Applied Mechanics, Chair of Experimental Mechanics as a teaching assistant and a PhD student under the supervision of Associate Professor Zvonimir Tomičević, PhD. He is involved in teaching the undergraduate and graduate courses Mechanics I (Cro. *Mehanika I*), Mechanics II (Cro. *Mehanika II*), Digital Image Correlation (Cro. *Korelacija digitalne slike*), Theory of Elasticity (Cro. *Teorija elastičnosti*), Experimental Mechanics (Cro. *Eksperimentalna mehanika*), Photogrammetry and Object Visualization (Cro. *Fotogrametrija i vizaluzacija objekata*). In 2021, he enrolled at Université Paris-Saclay under a joint PhD agreement between FAMENA and Université Paris-Saclay, under the joint supervision of both Associate Professor Zvonimir Tomičević, PhD and Research Professor François Hild, PhD, hab. During his PhD studies, he authored or co-authored 8 Current Contents (CC) published scientific research papers in renowned journals with international peer-review. He is a member of the Croatian Society of Mechanics.

List of publications

CRORIS: https://tinyurl.com/eyuw5tvh, **Google scholar**: https://tinyurl.com/2fm9pm7x

Declaration: Most of the work presented in this Dissertation has been published in some of the articles listed below.

List of CC Scientific Journal Papers:

- A. Vrgoč, Z. Tomičević, A. Zaplatić, F. Hild, "Damage analysis in glass fibre reinforced epoxy resin via Digital Image Correlation", FAMENA, vol. 45, no. 2, pp. 1-12, doi: 10.21278/TOF.452024020
- A. Zaplatić, Z. Tomičević, D. Čakmak, and F. Hild, "Improvement of the Arcan Setup for the Investigation of Thin Sheet Behavior Under Shear Loading," Exp Mech, vol. 62, no. 2, pp. 313–332, Feb. 2022, doi: 10.1007/s11340-021-00762-1.
- Zaplatić, Z. Tomičević, D. Čakmak, and F. Hild, "Identifiability of Ludwik's law parameters depending on the sample geometry via inverse identification procedure," Coupled Systems Mechanics, vol. 11, no. 2, pp. 133–149, 2022, doi: 10.12989/csm.2022.11.2.133.
- Zaplatić, A. Vrgoč, Z. Tomičević, and F. Hild, "Boundary condition effect on the evaluation of stress triaxiality fields," Int J Mech Sci, vol. 246, May 2023, doi: 10.1016/j.ijmecsci.2023.108127.
- A. Zaplatić, Z. Tomičević, X. Chang, I. Skozrit, S. Roux, and F. Hild, "Hybrid infrared-visible multiview correlation to study damage in a woven composite complex-shaped specimen," Coupled Systems Mechanics, vol. 12, no. 5, pp. 445–459, 2023, doi: 10.12989/csm.2023.12.5.445.
- A. Zaplatić, Z. Tomičević, F. Hild, "Characterization of woven composite material under multiaxial loading regimes using FE-based stereocorrelation", Acta Polytechnica CTU Proceedings, vol. 48, pp. 56-60., 2024, doi: 10.14311/APP.2024.48.0056
- A. Zaplatić, Z. Tomičević, X. Chang, P. Kosec, S. Roux, F. Hild, "Advanced FE-based multimodal correlation analyses for the characterization of woven composite", Mechanical systems and signal processing, vol. 224, no. 24, pp. 112079, 2025, doi: 10.1016/j.ymssp.2024.112079

Summary of publications

This chapter provides a summary of the published scientific papers that are related to the topic of the Dissertation. All the presented scientific papers are self-contained and tied through a common topic.

Scientific paper 1

A. Zaplatić, Z. Tomičević, D. Čakmak, and F. Hild, "Identifiability of Ludwik's law parameters depending on the sample geometry via inverse identification procedure," Coupled Systems Mechanics, vol. 11, no. 2, pp. 133–149, 2022, doi: 10.12989/csm.2022.11.2.133.

The accurate prediction of elastoplasticity under prescribed workloads is essential in the optimisation of engineering structures. Mechanical experiments are carried out with the goal of obtaining reliable sets of material parameters for a chosen constitutive law via inverse identification. In this work, two sample geometries made of high strength steel plates were evaluated to determine the optimal configuration for the identification of Ludwik's nonlinear isotropic hardening law. Finite element model updating (FEMU) was used to calibrate the material parameters. FEMU computed the parameter changes based on Hessian matrices, and the sensitivities that report changes of computed fields with respect to material parameter changes. A sensitivity analysis was performed to determine the influence of the sample geometry on parameter identifiability. It was concluded that the sample with thinned gauge region with a large curvature radius provided more reliable material parameters.

Author contributions

A. Zaplatić: *Conceptualisation, Methodology, Validation, Formal analysis, Investigation, Data curation, Writing – original draft*

Z. Tomičević: *Conceptualisation, Methodology, Validation, Data curation, Supervision, Project administration, Funding acquisition, Writing - Review & Editing*

D. Čakmak: *Conceptualisation, Methodology, Validation*

F. Hild: *Conceptualisation, Methodology, Validation, Data curation, Supervision, Writing - Review & Editing*

Scientific paper 2

A. Zaplatić, Z. Tomičević, D. Čakmak, and F. Hild, "Improvement of the Arcan Setup for the Investigation of Thin Sheet Behavior Under Shear Loading," Exp Mech, vol. 62, no. 2, pp. 313–332, Feb. 2022, doi: 10.1007/s11340-021-00762-1.

The accurate prediction of thin sheet material springback during forming processes is of great interest in industry. Thin sheets are susceptible to buckling under shear loading. The present research aimed at improving the so-called Arcan setup for testing thin (1-5 mm) sheet samples with large gauge areas (*i.e.* width about 21 mm) by introducing anti-buckling devices to mitigate sample buckling. Three monotonic and one cyclic simple shear mechanical tests were carried out on 1 mm thick C60 high carbon steel samples. The use of the proposed anti-buckling device resulted in the suppression of sample buckling. Numerical analyses of the experiment where buckling was eliminated revealed predominantly shear stress states in the gauge area (*i.e.* low stress triaxiality), which highlighted the minor influence of the anti-buckling device on the sample stress state. To suppress buckling, the use of anti-buckling devices was essential. Moreover, the friction coefficient between the sample and the proposed devices was calibrated (μ = 0.33) in addition to kinematic hardening parameters.

Author contributions

A. Zaplatić: *Conceptualisation, Methodology, Validation, Formal analysis, Investigation, Data curation, Writing – original draft*

Z. Tomičević: *Conceptualisation, Methodology, Validation, Data curation, Supervision, Project administration, Funding acquisition, Writing - Review & Editing*

D. Čakmak: *Conceptualisation, Methodology, Validation*

F. Hild: *Conceptualisation, Methodology, Validation, Data curation, Supervision, Writing - Review & Editing*

Scientific paper 3

A. Zaplatić, A. Vrgoč, Z. Tomičević, and F. Hild, "Boundary condition effect on the evaluation of stress triaxiality fields," Int J Mech Sci, vol. 246, May 2023, doi: 10.1016/j.ijmecsci.2023.108127.

A general framework was presented for evaluating stress triaxiality fields using five different configurations of Dirichlet boundary conditions. The latter ones were measured via stereocorrelation for a simple shear test on a thin sample where buckling was mitigated with an anti-buckling fixture. Friction and material parameters displayed negligible influence on the stress triaxiality fields. Accounting for the anti-buckling fixtures provided the most realistic stress triaxiality fields, but was computationally demanding. Prescribing all out-of-plane displacements, noisier but trustworthy stress triaxiality fields were also obtained by using much less computational resources.

Author contributions

A. Zaplatić: *Conceptualisation, Methodology, Validation, Formal analysis, Investigation, Data curation, Writing – original draft*

A. Vrgoč: *Conceptualisation, Methodology, Validation*

Z. Tomičević: *Conceptualisation, Methodology, Validation, Data curation, Supervision, Project administration, Funding acquisition, Writing - Review & Editing*

F. Hild: *Conceptualisation, Methodology, Validation, Data curation, Supervision, Writing - Review & Editing*

Scientific paper 4

A. Zaplatić, Z. Tomičević, X. Chang, I. Skozrit, S. Roux, and F. Hild, "Hybrid infrared-visible multiview correlation to study damage in a woven composite complex-shaped specimen," Coupled Systems Mechanics, vol. 12, no. 5, pp. 445–459, 2023, doi: 10.12989/csm.2023.12.5.445.

In this study, a cyclic tensile test on a notched butterfly specimen made of woven glass fibre composite was performed on a modified Arcan fixture. During the mechanical test, the sample was monitored with a hybrid stereovision system comprising two visible light cameras and one infrared camera. The visible light cameras were employed for kinematic measurements using a finite-element-based correlation technique. A semi-hybrid correlation approach was followed, providing Lagrangian temperature fields of the Region of Interest. Due to the complex composite architecture and specimen shape, localised shear was observed during tensile loading. Furthermore, asymmetrical damage developed around the notches as revealed by localised strains and thermal hot spots.

Author contributions

A. Zaplatić: *Conceptualisation, Methodology, Validation, Formal analysis, Investigation, Data curation, Writing – original draft*

Z. Tomičević: *Conceptualisation, Methodology, Validation, Data curation, Supervision, Project administration, Funding acquisition, Writing - Review & Editing*

X. Chang: *Conceptualisation, Methodology, Validation, Writing - Review & Editing*

I. Skozrit: *Funding acquisition*

S. Roux: *Conceptualisation, Methodology, Validation, Writing - Review & Editing*

F. Hild: *Conceptualisation, Methodology, Validation, Data curation, Supervision, Writing - Review & Editing*

Scientific paper 5

A. Zaplatić, Z. Tomičević, F. Hild, "Characterization of woven composite material under multiaxial loading regimes using FE-based stereocorrelation", Acta Polytechnica CTU Proceedings, vol. 48, pp. 56-60., 2024, doi: 10.14311/APP.2024.48.0056

In this paper, woven glass fibre composite samples were subjected to three different cyclic loading histories (i.e., tensile, shear and combined loading at 45°) with a Modified Arcan Fixture. During the experiments, the samples were monitored by a stereovision system. Finite Element based stereocorrelation was used to measure the displacement and strain fields. The analysis of the experiments revealed different damage mechanisms. Furthermore, for the 45° experiment, the highest strain levels were reached, whereas for the tensile test, the highest stress levels were achieved.

Author contributions

A. Zaplatić: *Conceptualisation, Methodology, Validation, Formal analysis, Investigation, Data curation, Writing – original draft*

Z. Tomičević: *Conceptualisation, Methodology, Validation, Data curation, Supervision, Project administration, Funding acquisition, Writing - Review & Editing*

F. Hild: *Conceptualisation, Methodology, Validation, Data curation, Supervision, Writing - Review & Editing*

Scientific paper 6

A. Zaplatić, X. Chang, Z. Tomičević, S. Roux, F. Hild, "Hybrid infrared and visible light correlation for woven composite samples subjected to three in-plane loadings", Submitted to……

This paper presents a detailed analysis of woven glass fibre composite samples subjected to complex in-plane loading regimes. Three Arcan samples, each with two notches in the gauge region, were tested under tensile, simple shear, and combined tensile/ shear loading at 45° angle with a Modified Arcan Fixture. An advanced optical setup, consisting of two visible-light cameras and one infrared camera, was utilised. Hybrid multiview correlation was employed to measure surface displacement, strain, and Lagrangian temperature fields. The highest stress levels were achieved for the tensile loading configuration. For the combined tensile/simple shear loading configuration, the highest strain levels were reached. The combined loading exhibited features of both tensile and simple shear loadings. Additionally, during combined loading, the shear strains were dominant until significant damage occurred, after which the strains in the loading direction took over. A linear relationship between temperature changes and shear strain was also observed in the simple shear experiment.

Author contributions

A. Zaplatić: *Conceptualisation, Methodology, Validation, Formal analysis, Investigation, Data curation, Writing – original draft*

X. Chang: *Conceptualisation, Methodology, Validation, Writing – original draft*

Z. Tomičević: *Conceptualisation, Methodology, Validation, Data curation, Supervision, Project administration, Funding acquisition, Writing - Review & Editing*

S. Roux: *Conceptualisation, Methodology, Validation, Writing - Review & Editing*

F. Hild: *Conceptualisation, Methodology, Validation, Data curation, Supervision, Writing - Review & Editing*

Scientific paper 7

A. Zaplatić, Z. Tomičević, X. Chang, P. Kosec, S. Roux, F. Hild, "Advanced FE-based multimodal correlation analyses for the characterization of woven composite", Mechanical systems and signal processing, vol. 224, no. 24, pp. 112079, 2025, doi: 10.1016/j.ymssp.2024.112079

This paper presents a comprehensive characterisation of a woven glass fibre composite sample with two notches in the gauge area subjected to cyclic tension using an Arcan fixture. An advanced optical setup was developed, comprising two visible light cameras and an infrared camera. Additionally, an X-ray scanner was employed to image *ex-situ* the bulk for monitoring microstructural changes during the experiment. A multimodal correlation method was introduced that combined hybrid (infrared-visible) multiview correlations and Digital Volume Correlation to measure displacement, strain, and temperature fields within the same Lagrangian framework. The strain fields obtained from both algorithms were consistent. The findings revealed the presence of asymmetric shear bands and damage originating from the notch roots due to the underlying woven architecture. Several damage mechanisms were identified from both frameworks.

Author contributions

A. Zaplatić: *Conceptualisation, Methodology, Validation, Formal analysis, Investigation, Data curation, Writing – original draft*

Z. Tomičević: *Conceptualisation, Methodology, Validation, Data curation, Supervision, Project administration, Funding acquisition, Writing - Review & Editing*

X. Chang: *Conceptualisation, Methodology, Validation, Writing - Review & Editing*

P. Kosec: *Funding acquisition*

S. Roux: *Conceptualisation, Methodology, Validation, Writing - Review & Editing*

F. Hild: *Conceptualisation, Methodology, Validation, Data curation, Supervision, Writing - Review & Editing*

Scientific paper 1

A. Zaplatić, Z. Tomičević, D. Čakmak, and F. Hild, “Identifiability of Ludwik’s law parameters depending on the sample geometry via inverse identification procedure,” Coupled Systems Mechanics, vol. 11, no. 2, pp. 133–149, 2022, doi: 10.12989/csm.2022.11.2.133.

Preprint of the published journal article.

Identifiability of Ludwik's law parameters depending on the sample geometry via inverse identification procedure

Andrija Zaplatić[1a], Zvonimir Tomičević[*1], Damjan Čakmak[1b] and François Hild[2c]

[1]*University of Zagreb, Faculty of mechanical engineering and naval architecture, Ivana Lučića 5, 10002 Zagreb, Croatia*
[2] *Université Paris-Saclay, ENS Paris-Saclay, CNRS, LMT – Laboratoire de mécanique et technologie, 91190 Gif-sur-Yvette, France*

(Received keep as blank , Revised keep as blank , Accepted keep as blank)

Abstract. The accurate prediction of elastoplasticity under prescribed workloads is essential in the optimization of engineering structures. Mechanical experiments are carried out with the goal of obtaining reliable sets of material parameters for a chosen constitutive law via inverse identification. In this work, two sample geometries made of high strength steel plates were evaluated to determine the optimal configuration for the identification of Ludwik's nonlinear isotropic hardening law. Finite element model updating (FEMU) was used to calibrate the material parameters. FEMU computes the parameter changes based on the Hessian matrix, and the sensitivity fields that report changes of computed fields with respect to material parameter changes. A sensitivity analysis was performed to determine the influence of the sample geometry on parameter identifiability. It was concluded that the sample with thinned gauge region with a large curvature radius provided more reliable material parameters.

Keywords: sensitivity analysis; inverse identification; full-field measurements; HARDOX 450; sample geometry

1. Introduction

The development of advanced high strength materials requires optimization procedures of engineering structures and components. The optimization is carried using numerical tools, *e.g.*, finite element (FE) simulations (Tisza, 2005). To run reliable numerical simulations, trustworthy material properties are needed. Therefore, mechanical tests are conducted to determine material parameters.

Classical measuring devices (*e.g.*, mechanical extensometer, load cells) provide only global data. The drawback of the latter ones is that local effects cannot be captured. The development of digital imaging and full-field measurement methods provide means to capture localized phenomena. Digital Image Correlation or DIC (Sutton *et al.*, 2009) stands out nowadays as the most versatile and most widely used measurement technique in experimental mechanics. The application of DIC is straightforward as digital images are used as the source of information, *i.e.*, capturing the motions

*Corresponding author, Assistant Professor, E-mail: zvonimir.tomicevic@fsb.hr
[a] Ph.D. Student, E-mail: andrija.zaplatic@fsb.hr
[b] Ph.D. E-mail: damjan.cakmak@fsb.hr
[c] Research Professor, E-mail: francois.hild@ens-paris-saclay.fr

of monitored surfaces. Besnard *et al.* (2006) developed FE-based DIC where FE meshes were utilized to discretize the observed region of interest, and the output were measured nodal displacements. Such approach is powerful since experimental data and numerical simulations can be directly coupled in inverse identification schemes (Lecompte *et al*., 2007, Cooreman *et al.*, 2008).

Finite Element Model Updating or FEMU (Kavanagh and Clough, 1971) is a well-known identification procedure, which was considered in the present work. FEMU is an iterative scheme that minimizes the differences between experimentally measured and numerically computed quantities (Prates *et al.*, 2016, Martins *et al.*, 2018), *e.g.* measured and calculated displacement fields and measured load and calculated global reaction forces on the FE model. FEMU is one of the most versatile identification procedures as it can be employed for, say, uniaxial (Tomičević *et al*., 2016a) and biaxial (Tomičević *et al*., 2016b) tests. Furthermore, FEMU is not limited to macroscopic laws. Guery *et al.* (2016) used the same framework to calibrate crystal plasticity parameters of AISI 316LN stainless steel. Compared to other inverse identification methods (*e.g.*, Virtual Fields Method (Grediac and Pierron, 2006), Constitutive Equation Gap Method (Geymonat *et al*., 2002) and the Equilibrium Gap Method (Claire *et al*., 2004), FEMU was proven to provide the most accurate results in the presence of data corrupted with acquisition noise (Martins *et al.*, 2018, Roux *et al*., 2020). FEMU is a sensitivity-based identification method (Tarantola 1987), *i.e.*, the influence of material parameter changes on observed quantities is evaluated. Therefore, FEMU was also used for sample optimization to tailor the geometry to activate specific material parameters. Bertin *et al.* (2016) used the aforementioned procedure to optimize the fillet radii of a cruciform specimen for biaxial testing. Furthermore, FEMU was then used to calibrate material parameters of the Hill-1948 plasticity model with a *single* biaxial test (Bertin *et al*., 2017).

The aim of this paper is to evaluate two distinct sample geometries used in tensile tests for parameter identification. The samples were made from high strength steel plates. The goal was to determine the best of the two geometries for calibrating Ludwik's nonlinear isotropic hardening law. FEMU was deemed a suitable choice for the sensitivity analysis. Using FEMU, sensitivity fields (Neggers *et al*., 2017, Ahmed *et al*., 2019, Prates *et al*., 2019) and the Hessian matrices (Bertin *et al*., 2016) were extracted to evaluate the parameter sensitivity with respect to the sample geometry.

2. Experimental investigation

Within this research, the experimental investigation was carried out on 2 mm thick samples made of HARDOX 450 steel. Two distinct sample geometries were considered for the mechanical tests. The *DIN* sample (Fig. 1(a)) was designed with two parallel edges located in the entire gauge region. Near the ends, the sample was widened to ensure larger gripping surfaces and to disable any sample slip. Furthermore, the design induced two regions with increased stress concentrations. The second *dogbone* sample (Fig. 1(b)) was thinned in the center of the gauge area with a radius of 75 mm, thus ensuring a unique region where strain localization may occur.

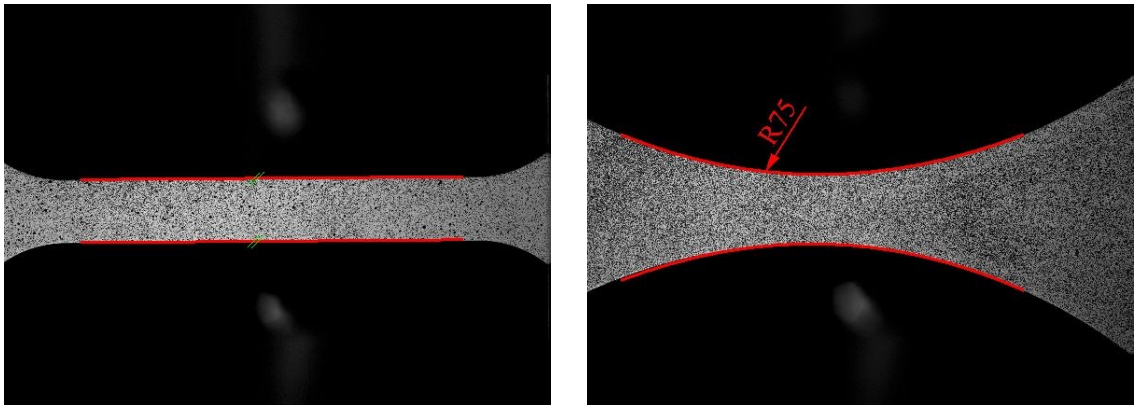

(a) (b)

Fig. 1 Considered geometries. (a) *DIN* and (b) *dogbone* samples with specific geometric characte ristics highlighted with red lines

Two mechanical tests were carried out on a uniaxial testing machine (*Messphysik Beta* 50-5, Fig. 2(T)). The samples were subjected to uniaxial and monotonic tensile loadings under displacement control with a prescribed rate of 1 mm / min.

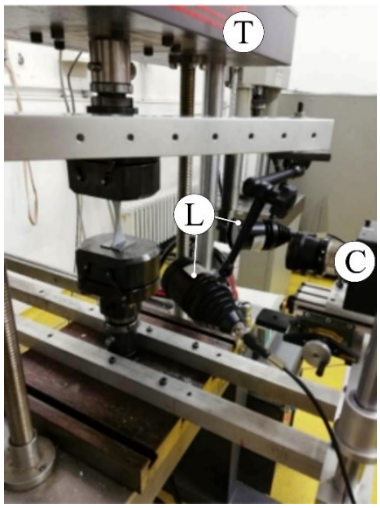

Fig. 2 Experimental setup consisting of two light sources and a single digital camera. See text for the description of the labels

The surfaces of the samples were monitored by a single CCD *Dalsa Falcon* camera (Fig. 2(C)) with a definition of 2358 × 1728 pixels and an image acquisition rate of 1 fps. Two light sources (Fig. 2(L)) were used to ensure uniform sample illumination. The hardware parameters of the optical setup are listed in Table 1.

Table 1. Hardware parameters of the optical setup

Camera	*Dalsa Falcon* 4M60
Definition	2358 × 1728 pixels (B/W images)
Color filter	None
Digitization	8 bits
Lens	Titanar 50 mm
Aperture	f/2.8
Field of view	44.4 cm^2
Stand-off distance	30 cm
Image acquisition rate	1 fps
Patterning technique	B/W paints
Pattern feature size	15 px

2.1 Full-field measurement results

For this study, Finite element (FE) based DIC was employed to measure displacement fields on the observed Region of Interest (ROI). The correlation framework *Correli 3.0.* (Leclerc *et al*., 2015) was used. The ROI was discretized with 3-noded triangular (T3) elements (Fig. 3). Furthermore, mechanical regularization (Tomičević *et al*., 2013) was implemented within the algorithm. The full analysis parameters are reported in Table 2.

Before each experiment, 10 images were acquired in the unloaded state to obtain the noise floor estimates by calculating the standard deviations of the nodal displacements and strains. For the *DIN* sample, the displacement noise floor was slightly lower than for the *dogbone* sample. On the other hand, the strain noise floor was lower for the *dogbone* sample. However, both displacement and strain noise floors were of the same order of magnitude.

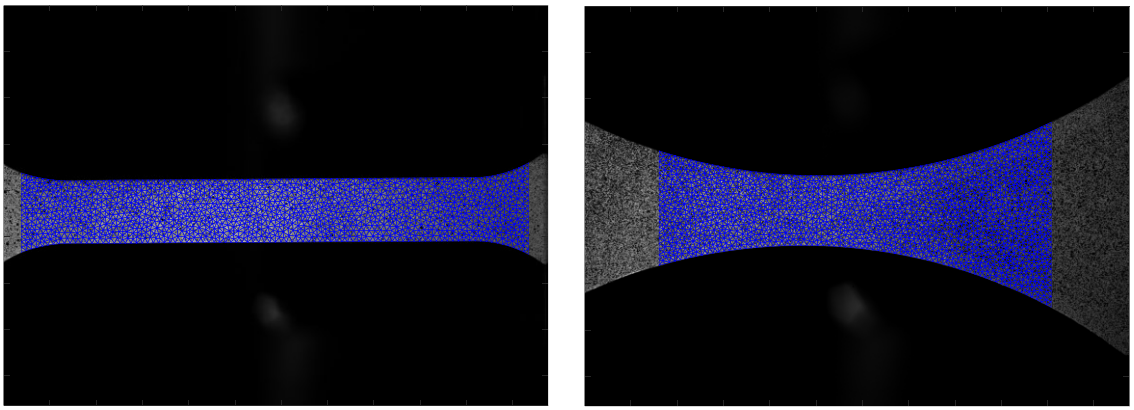

(a) (b)

Fig. 3 Three noded finite element meshes used in the DIC procedure for (a) *DIN* and (b) *dogbone* sample

Table 2. DIC analysis parameters

DIC software	Correli 3.0	
Image filtering	None	
Average element length	20 pixels	
Shape functions	Linear (T3 elements)	
Matching criterion	Penalized sum of squared differences	
Regularization length	Bulk	Edge
	100 pixels	200 pixels
Displacement noise floor	*DIN*	*Dogbone*
	0.6 µm	0.7 µm
Strain noise floor	2×10^{-4}	10^{-4}

The analysis of the calculated Green-Lagrange strain fields revealed two strained bands forming an X. A single dominant band developed fully until failure for both cases (Fig. 4). Strain localization occurred in different regions. For the *DIN* sample, the strains localized on the left side near the widening area close to the grips. For the *dogbone* sample, strain localization developed in the ligament, as expected from its geometry. A first advantage of *dogbone* samples is that they allow for a direct control of the location of the strained zone. With the *DIN* sample, localization may occur near each end of the sample. Therefore, to monitor both possible concentration zones, a larger ROI needs to be considered. Conversely, since for the *dogbone* sample the location is known in advance, the optical setup can be put closer to the sample to capture strain localization in greater details. Moreover, multi-scale DIC (Passieux *et al.*, 2015) can also be employed since the strained band location is known a priori.

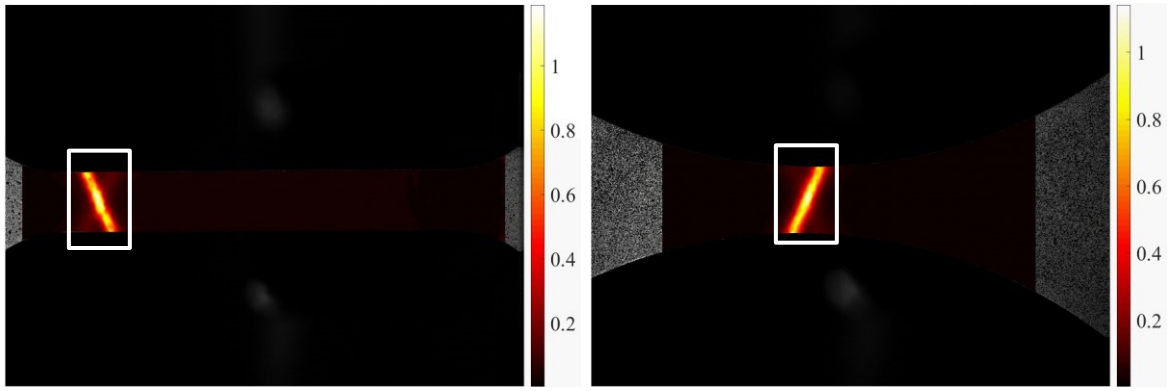

(a) (b)

Fig. 4 Major principal strain fields for the last image captured before fracture for the *DIN* (a) and *dogbone* (b) samples. The white boxes denote the virtual strain gauge used to calcula te average strain levels

The macroscopic stress-strain curves of both experiments are reported in Fig. 5. The engineering stress was calculated by dividing the measured force by the initial cross-sectional area. The Green-Lagrange strain levels were obtained by using virtual strain gauges (Fig. 4) positioned over the captured strain localization zones. In the virtual gauge, the nodal strains within the gauge were

averaged for each temporal registration.

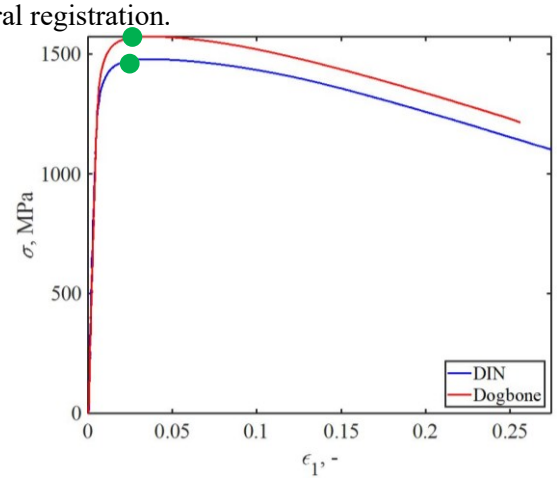

Fig. 5 Macroscopic engineering stress vs. Green Lagrange strain curves. The green circles denote the ultimate stresses where the numerical analyses were stopped

The *dogbone* sample displayed slightly prolonged elasticity (*i.e.*, higher yield stress) than the *DIN* sample. However, for the *DIN* sample, 2% larger strains at failure were achieved (the *dogbone* sample fractured earlier due to increased strains in the localization band (Nam Do *et al.*, 2015)). Moreover, a higher ultimate tensile strength was reached with the *dogbone* sample. Beyond the stress peak, material softening was very similar in both tests, which is confirmed by the strain field patterns shown in Fig. 4.

3. Finite element model updating

The goal of FEMU is to iteratively minimize differences between experimentally measured and numerically calculated quantities. The minimization framework iteratively updates the desired material parameters by calculating Hessian matrices that are based on sensitivity fields (Tarantola, 1987). In the present analyses, measured and calculated displacement fields were considered, as well as measured forces and global reaction forces extracted from the FE model. The employed FE meshes (Fig. 5) were prepared for the identification scheme by prescribing measured nodal displacements as Dirichlet boundary conditions on the stressed edges of the model (outlined by red lines in Fig. 6).

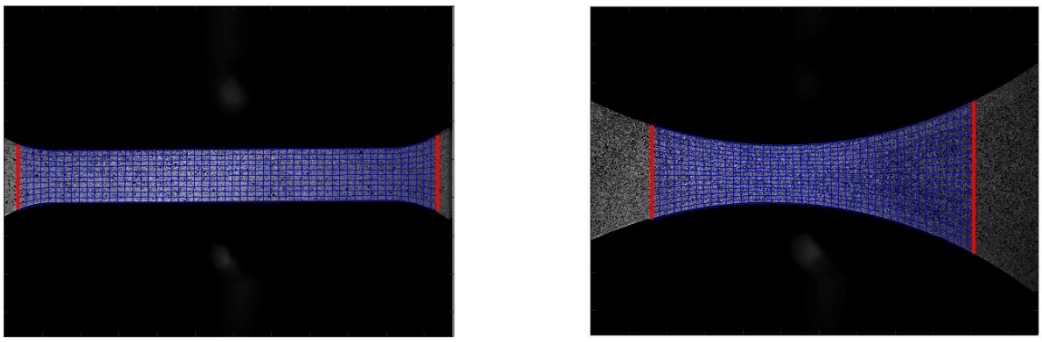

(a) (b)

Fig. 6 Finite element meshes used in the identification procedure for the *DIN* (a) and *dogbone* samples. The red lines depict areas where measured nodal displacements were defined as Dirichlet boundary conditions

The FEMU mesh was constructed from the DIC mesh. The T3 mesh was converted into four-noded quadrilateral elements (Q4). Lindner *et al*. (2015) reported that 3D meshes were necessary to accurately evaluate stress states in plasticity. Therefore, the Q4 mesh was extruded to obtain a 3D mesh made of C3D8R elements with reduced integration.

In the minimization procedure, the cost function considering measured displacements is formulated as the *weighted* squared difference between the measured $\mathbf{u_m}$ and calculated $\mathbf{u_c}$ nodal displacements

$$\chi_{\mathrm{u}}^2\left\{\mathbf{p}\right\} = \frac{1}{N_{\mathrm{u}}}\left(\left\{\mathbf{u_m}\right\}-\left\{\mathbf{u_c}\right\}\right)^t\left[\mathbf{C_u}\right]^{-1}\left(\left\{\mathbf{u_m}\right\}-\left\{\mathbf{u_c}\right\}\right), \tag{1}$$

where $\{\mathbf{p}\}$ is the vector column gathering all the sought material parameters, $[\mathbf{C}_{\mathrm{u}}]$ the covariance matrix equal to $2\gamma_f^2[\mathbf{M}]^{-1}$, $[\mathbf{M}]$ the global DIC matrix (Hild and Roux, 2012), γ_f^2 the variance of Gaussian white noise associated with image acquisition, and N_{u} the number of kinematic degrees of freedom (Mathieu *et al.,* 2015).

The cost function considering measured load and extracted reaction forces from the stressed edges of the FE mesh are expressed as

$$\chi_{\mathrm{F}}^2\left\{\mathbf{p}\right\} = \frac{1}{\gamma_{\mathrm{F}}^2\cdot N_{\mathrm{F}}}\left\|\left\{\mathbf{F_m}\right\}-\left\{\mathbf{F_c}\right\}\right\|^2, \tag{2}$$

where γ_{F} is the standard uncertainty of the load cell, and N_{F} the number of load data.

By introducing a weight ω, the two previous cost functions are combined as

$$\chi_{\mathrm{tot}}^2\left\{\mathbf{p}\right\} = (1-\omega)\chi_{\mathrm{u}}^2+\omega\chi_{\mathrm{F}}^2, \tag{3}$$

For the present study, ω was set to 0.5 to provide equal weight to kinematic and static data.

The minimization of the kinematic cost function was carried out thanks to the evaluation of kinematic sensitivity fields. The computed displacement vector, for any iteration i, is Taylor expanded as

$$\mathbf{u}_\mathbf{c}\left(\mathbf{x},t,\left\{\mathbf{p}^{(i)}\right\}\right)=\mathbf{u}_\mathbf{c}\left(\mathbf{x},t,\left\{\mathbf{p}^{(i-1)}\right\}\right)+\frac{\partial\mathbf{u}_\mathbf{c}}{\partial\{\mathbf{p}\}}\left(\mathbf{x},t,\left\{\mathbf{p}^{(i-1)}\right\}\right)\{\partial\mathbf{p}\},\tag{4}$$

where $\{\partial\mathbf{p}\}$ is the increment to the sought parameters, and from Eq. (4), the displacement sensitivity matrix becomes

$$\left[\mathbf{S}_\mathbf{u}\right]=\frac{\partial\mathbf{u}_\mathbf{c}}{\partial\{\mathbf{p}\}}.\tag{5}$$

The displacement sensitivity matrix accounts for changes in displacement fields due to a small variation of each sought material parameter, and is updated for each iteration. The parameter increment is then expressed as a function of the sensitivity matrix

$$\{\partial\mathbf{p}\}=\frac{1}{2\gamma_f^2}\left[\mathbf{H}_\mathbf{u}{}^{(i-1)}\right]^{-1}\left[\mathbf{S}_\mathbf{u}{}^{(i-1)}\right]^t\left[\mathbf{M}\right]\left(\{\mathbf{u}_\mathbf{m}\}-\left\{\mathbf{u}_\mathbf{c}{}^{(i-1)}\right\}\right),\tag{6}$$

where $[\mathbf{H}_\mathbf{u}{}^{(i-1)}]$ is the Hessian matrix expressed as a function of the sensitivity matrix

$$\left[\mathbf{H}_\mathbf{u}{}^{(\mathrm{i}-1)}\right]=\frac{1}{2\gamma_f^2}\left[\mathbf{S}_\mathbf{u}{}^{(\mathrm{i}-1)}\right]^t\left[\mathbf{M}\right]\left[\mathbf{S}_\mathbf{u}{}^{(\mathrm{i}-1)}\right].\tag{7}$$

The parameter increment considering only measured loads and computed global reaction forces reads

$$\{\partial\mathbf{p}\}=\left(\left(\left[\mathbf{S}_\mathbf{F}\right]^{(i-1)}\right)^t\left[\mathbf{S}_\mathbf{F}\right]^{(i-1)}\right)^{-1}\left[\mathbf{S}_\mathbf{F}\right]^{(i-1)}\left\{\mathbf{F}_\mathbf{m}-\mathbf{F}_\mathbf{c}{}^{(i-1)}\right\}.\tag{8}$$

where $[\mathbf{S}_\mathbf{F}]$ denotes the force sensitivity matrix. The Hessian matrix considering force data is expressed as

$$\left[\mathbf{H}_\mathrm{F}\right]=\frac{1}{\gamma_\mathrm{F}^2}\left[\mathbf{S}_\mathbf{F}\right]^t\left[\mathbf{S}_\mathbf{F}\right].\tag{9}$$

For the proposed FEMU-UF (Mathieu *et al*., 2015, Tomičević *et al*., 2016) approach, the global Hessian matrix $[\mathbf{H}_\mathbf{UF}]$ then becomes the sum of the kinematic and static Hessian matrices

$$\left[\mathbf{H}_\mathbf{UF}\right]=\left[\mathbf{H}_\mathbf{U}\right]+\left[\mathbf{H}_\mathbf{F}\right].\tag{10}$$

In the following, the total Hessian matrix $[\mathbf{H}_\mathbf{UF}]$, displacement and force sensitivity fields are evaluated and compared for both considered sample geometries.

3.1 Identification results

The identification procedure was carried out for both samples *independently*. The FE analyses were carried out until the ultimate strength was reached, *i.e.*, before strain softening. For the *DIN* sample, the analyses were performed until the strain levels reached 4% (*i.e.*, time step 435) and for the *dogbone* geometry up to 3.2% (*i.e.*, time step 220), see Fig. 5. In the FE simulations, plasticity

was described with Ludwik's isotropic hardening law (Ludwik, 1909)

$$\sigma_{eq} = \sigma_y + K\varepsilon_{pl}^{-n}, \tag{11}$$

where σ_{eq} corresponds to von Mises' equivalent stress, and ε_{pl} the cumulated plastic strain. The sought material parameters were the Young's modulus E, yield stress σ_y, hardening modulus K and hardening exponent n. The Poisson's ratio was not calibrated and was kept constant at 0.3 since it was difficult to calibrate (Tomičević *et al*., 2016a). However, the sensitivity of the latter to sample geometry was evaluated.

For both samples, the initial parameters were identical. After the FEMU-UF procedure was run, it was observed that the sample geometry led to significant differences in calibrated parameters (Table 3). For both samples, the Young's modulus increased; for the *dogbone* geometry the value increased more. Moreover, for the latter, the calibrated values of the yield stress σ_y and hardening exponent n were higher than for the *DIN* sample. For both samples, the hardening modulus K increased; for the *DIN* sample it increased more. Lower identification residuals were achieved for the *dogbone* sample.

Table 3 Calibrated material parameters for the studied geometries

	E, GPa	σ_Y, MPa	K, MPa	n, -	χ_{total}
Initial	210	1200	700	0.2	-
DIN	211	1060	980	0.18	41.3
Dogbone	219	1150	920	0.19	33.3

The identification procedure led to parameters that provided a good description of the nonlinear behavior for both samples. In Fig. 7, the global reaction forces are displayed for the initial and calibrated material parameters. For the *DIN* sample, the onset of plasticity was not described as accurately, which led to increased global FEMU-UF residuals (*i.e.*, χ_{total}). Conversely, for the *dogbone* geometry lower deviations from the *Reference* curve were observed for the reaction force with the calibrated parameters.

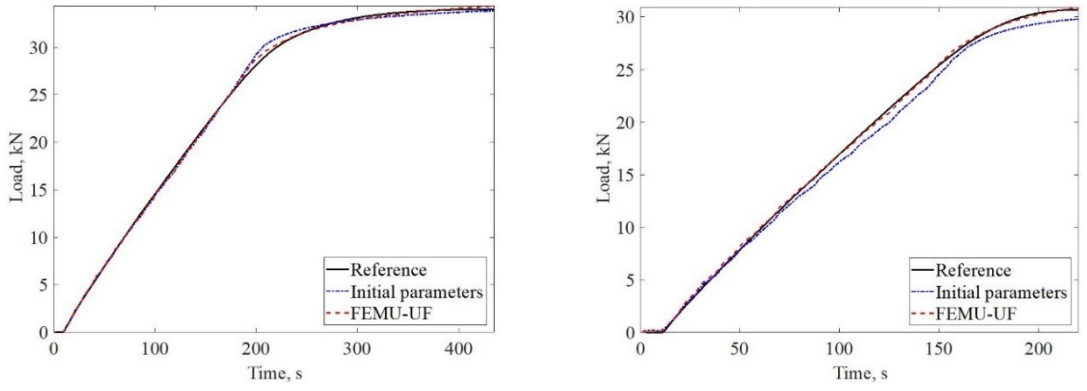

Fig. 7 Comparison of measured load (Reference) and reaction forces extracted from the FE model for the initial and calibrated elastoplastic parameters via FEMU-UF. (a) *DIN* and (b) *dogbone* samples

4. Sensitivity analysis

The parameter sensitivity for the two considered sample geometries (*i.e.*, *DIN* and *dogbone*) was evaluated with the Hessian matrices calculated within FEMU framework. The Hessian matrix is of size $n \times n$, where n corresponds to the number of sought parameters. Furthermore, the Hessian matrix gathers displacement *and* force sensitivities to parameter changes. The diagonal terms in the Hessian matrices describe the parameter sensitivities when considered independently, whereas the off-diagonal terms report on correlative influences of parameters. The evaluation of the Hessian matrix was performed prior to the identification procedure to determine the optimal strategy for material parameter calibration.

The Hessian matrices are shown in Fig. 8. For the *DIN* sample, twice as much images were captured and analyzed (*i.e.*, 435 images) compared to the *dogbone* sample (*i.e.*, 220 images). Therefore, a first order approximation was carried out on the *DIN* Hessian so it could be compared to the *dogbone* Hessian. First, all members of the *DIN* Hessian matrix were divided by the number of images (*i.e.*, 435) and then multiplied by the number of images captured for the *dogbone* sample.

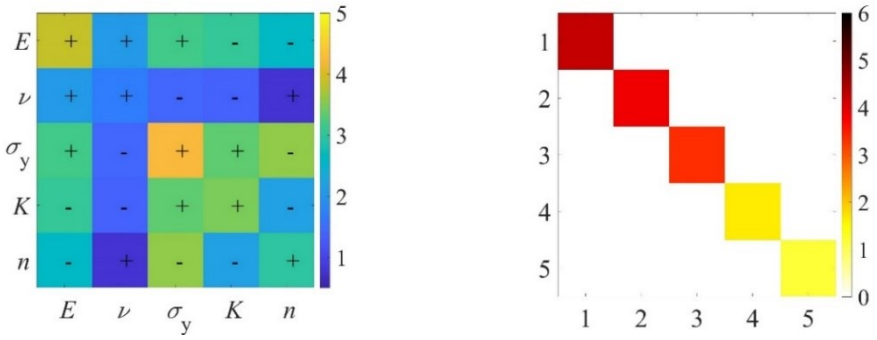

(a)

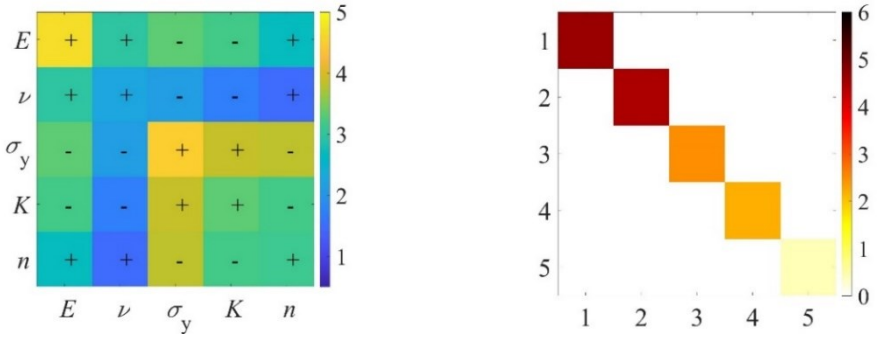

(b)

Fig. 8 Decimal logarithm of Hessian matrices [$\mathbf{H}_{UF}$] (first column) and corresponding diagonalized matrices (second column) for the *DIN* (a) and *dogbone* (b) geometries

It is observed that for the Young's E, the highest sensitivity is achieved by the *dogbone* geometry. This result also applies for the Poisson's ratio ν and hardening exponent n. The correlative influences between E and other parameters are slightly higher for the *DIN* sample. Furthermore, for the Poisson's ratio, the *dogbone* sample provided the highest sensitivity. This property can also be stated for the correlative influences, which are higher than for the *DIN* sample. The yield stress σ_y

sensitivity is similar for both geometries, although it is slightly higher for the *DIN* sample. Opposite trends are observed for the correlative influences between σ_y and E. For the *DIN* sample, they are correlated, whereas for the *dogbone* sample they are anti-correlated. The hardening parameter K exhibits greater sensitivity for the *DIN* sample than for its counterpart. However, the correlative influences of other parameters on K also need to be considered, which are on average higher for the *dogbone* sample. For the latter, the sensitivity of the hardening exponent n is seven times higher than for the *DIN* sample, thus rendering it easier to calibrate.

Last, the conditioning of the two matrices was estimated from the spectrum of eigen values (Fig. 8). For the *DIN* sample, the condition number was equal to 3, whereas for the *dogbone* it was 4. The condition number is preferred to be as small as possible thus indicating that the eigen values for all parameters are similar, and therefore easier to calibrate. In this case, the *DIN* sample provides the smallest condition number and all eigen values are greater than 1. On the other hand, for the *dogbone* sample, the lowest eigenvalue expressed in decimal logarithm is below 1. Furthermore, the largest eigenvalue was found for the *dogbone* sample. Moreover, the first two eigenvalues are much higher for the *dogbone* sample than for the *DIN* sample. From the presented data, it is observed that the *dogbone* sample provides the highest sensitivities (as observed from the Hessian and its eigen values). Yet, with the aforementioned sample, the lowest eigenvalue is also achieved, which is a drawback.

Figures 9-13 display the displacement sensitivity fields [$\mathbf{S_u}$] for each considered material parameter and for each sample geometry. A parameter offset $\varepsilon = 1\%$ was considered. Each figure is composed of two subfigures, which are divided into four sensitivity fields. Each figure is also divided into two rows, where the first one displays sensitivities with respect to the x-axis, and the second to the y-axis. On each sensitivity field, a vertical dashed line is depicted, which corresponds to the column of pixels used to create the sensitivity history with respect to analyzed images (*i.e.*, subfigures next to sensitivity fields). The positive x-axis is oriented to the right, whereas the positive y-axis is oriented toward the top of the page. For most parameters, the sensitivities in elasticity are small in comparison to plasticity. To calibrate the Young's modulus, elasticity is sufficient.

The Young's modulus sensitivity fields for both samples are different in terms of distribution (Fig. 9). For the *dogbone* sample, increased sensitivities occur around the strain localization zone (*i.e.*, in plasticity). For the *DIN* sample, increased sensitivities occur in the center of the specimen, away from the localization zones. In the x-direction, the *dogbone* geometry displays more heterogeneous sensitivities. For the y-direction, the *DIN* sample also displays heterogeneous distributions. Yet, it is more uniform through the loading history for the *dogbone* sample. The *dogbone* sensitivity fields are more pronounced than for the for *DIN* sample.

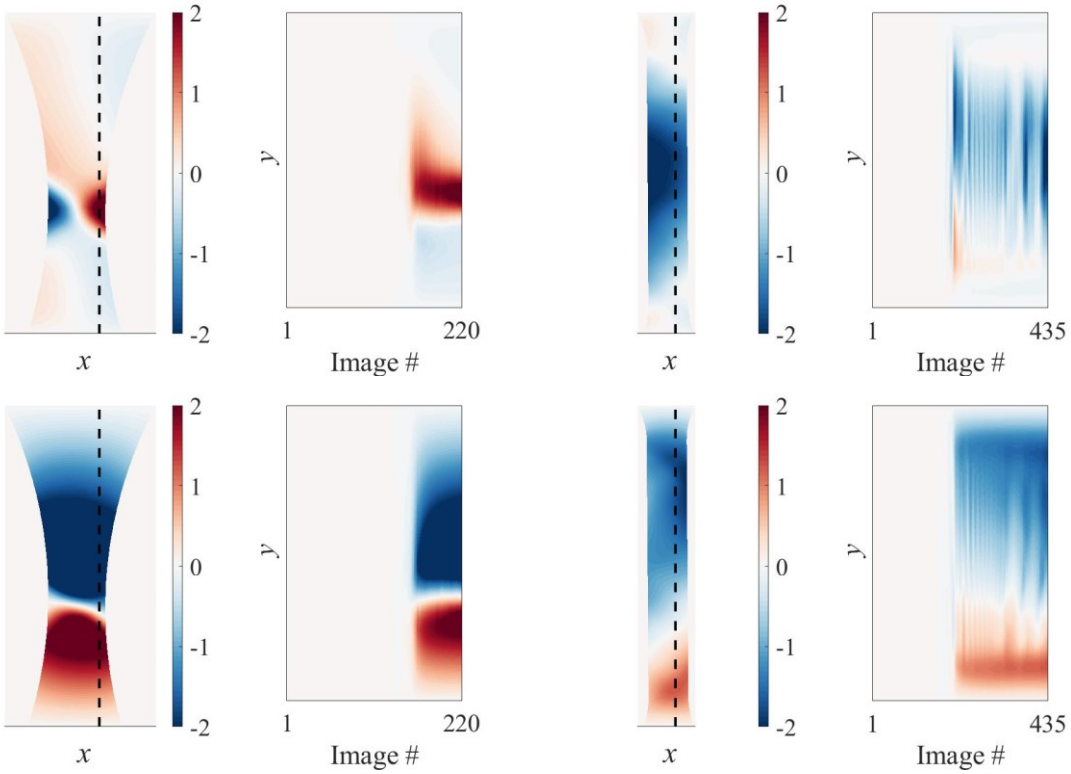

(a) (b)

Fig. 9 Displacement sensitivity fields for E in terms of x (first row) and y (second row) displacements expressed in pixel/ε. The sensitivity fields are displayed for the last analyzed image. A line of pixels is plotted for each analyzed image next to the sensitivity field

The Poisson's ratio displacement sensitivity fields [$\mathbf{S_u}$] in the x-direction are similar for both geometries (Fig. 10). From the sensitivity history plot, it is observed that for the *dogbone* sample the sensitivity levels are slightly higher. For the y-direction, the sensitivities are smaller, thereby indicating, as expected, lower sensitivities in the loading direction. The Poisson's ratio sensitivities are the lowest compared to the other parameters.

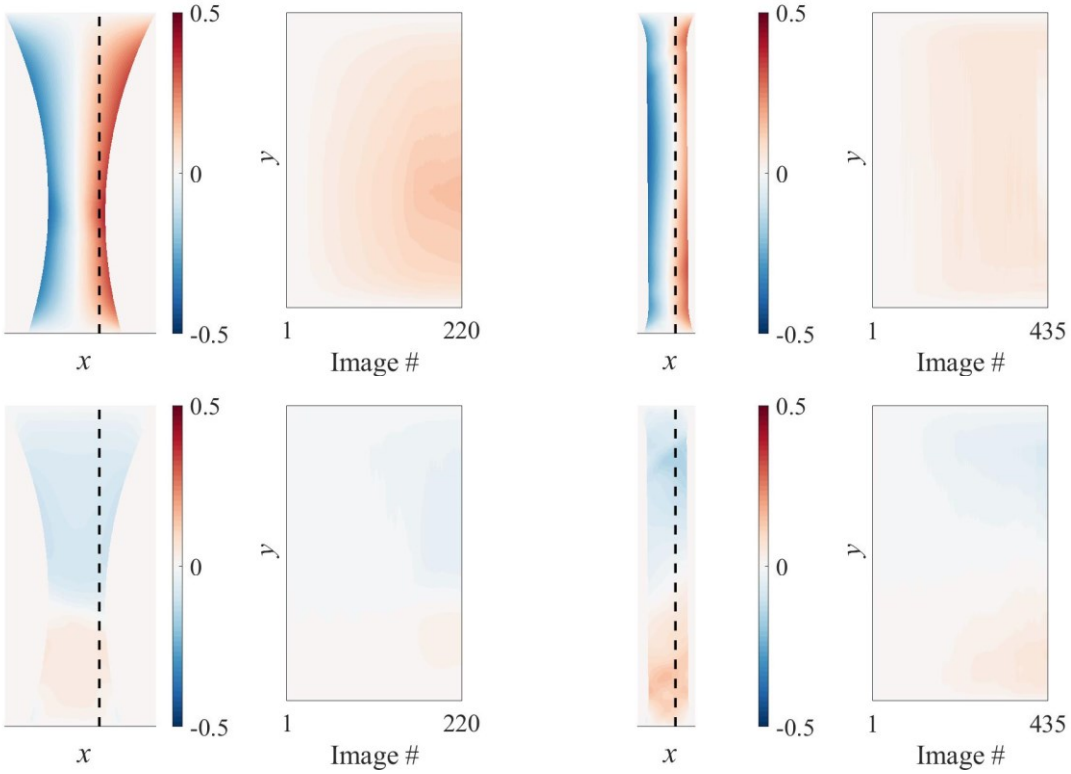

(a) (b)

Fig. 10 Displacement sensitivity fields for v in terms of x (first row) and y (second row) displacements expressed in pixel/ε. The sensitivity fields are displayed for the last analyzed image. A line of pixel values is plotted for each analyzed image next to the sensitivity field

The yield stress displacement sensitivity [$\mathbf{S_u}$] is more pronounced for the *DIN* sample in both directions, whereas for the *dogbone* sample the y-direction is more noticeable (Fig. 11). The latter exhibits more uniformly distributed and higher sensitivities in the history plot than its *DIN* counterpart. Increased sensitivities are present around the strain localization zone. For the *DIN* sample, throughout the sensitivity history, nonuniform distributions are observed. Moreover, a change in sensitivity values from negative to positive occurred at both ends (*i.e.*, areas of increased stress concentration) of the *DIN* sample in both directions.

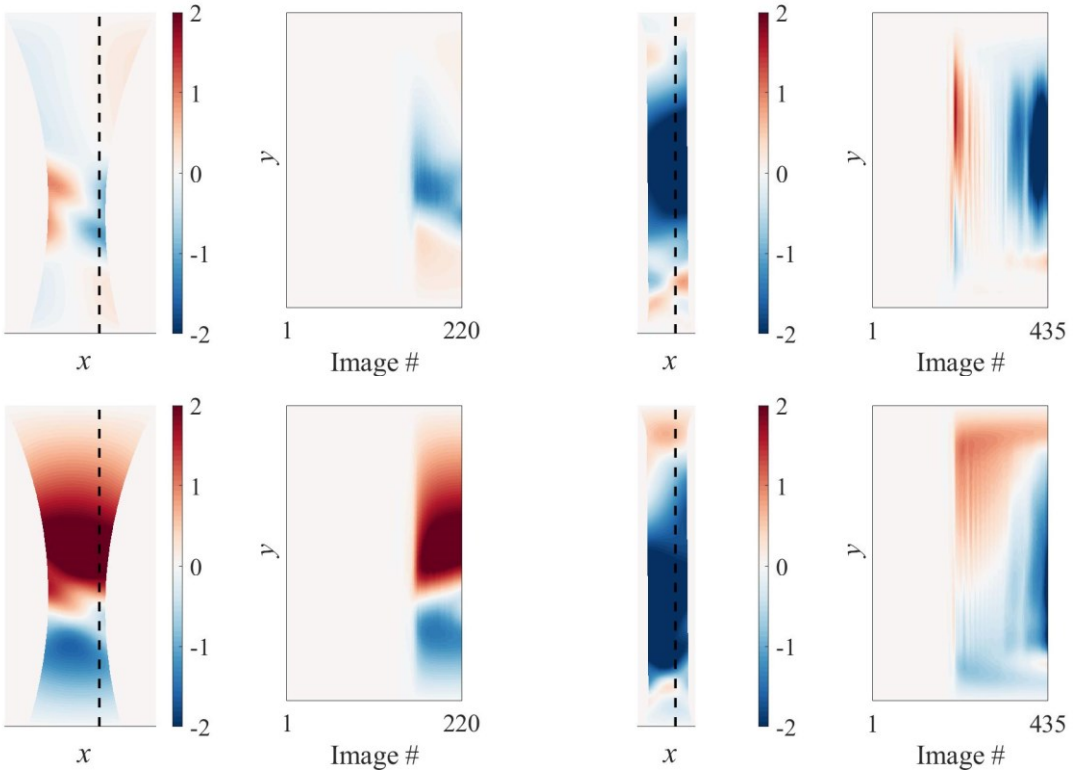

(a) (b)

Fig. 11 Displacement sensitivity fields for σ_Y in terms of the x (first row) and y (second row) displacements expressed in pixel/ε. The sensitivity fields are displayed for the last analyzed image respectively. A line of pixel values is plotted for each analyzed image next to the sensitivity field

For the hardening modulus K, the *dogbone* sample displays localized areas of increased positive sensitivities, whereas in the *DIN* sample they encompass almost the entire region of interest. However, around the reported strain band, the change from positive to negative sensitivities is observed in both x- and y-directions, as is the case for the *dogbone* sample. Moreover, for the *DIN* sample, the sensitivity fields are similar in both directions. The same observation applies for the *dogbone* sample. However, the sensitivities are more pronounced in the y-direction. As was the case in the Hessian matrix analysis, the *DIN* sample overall exhibits more pronounced sensitivities. However, it is numerically easier to describe the *dogbone* sample response as the strain localization zone is known *a priori*. Therefore, the FE algorithm can accurately predict where localization will occur. Without prescribed experimentally measured displacements, the FE algorithm may not predict the strain localization zone for the *DIN* sample.

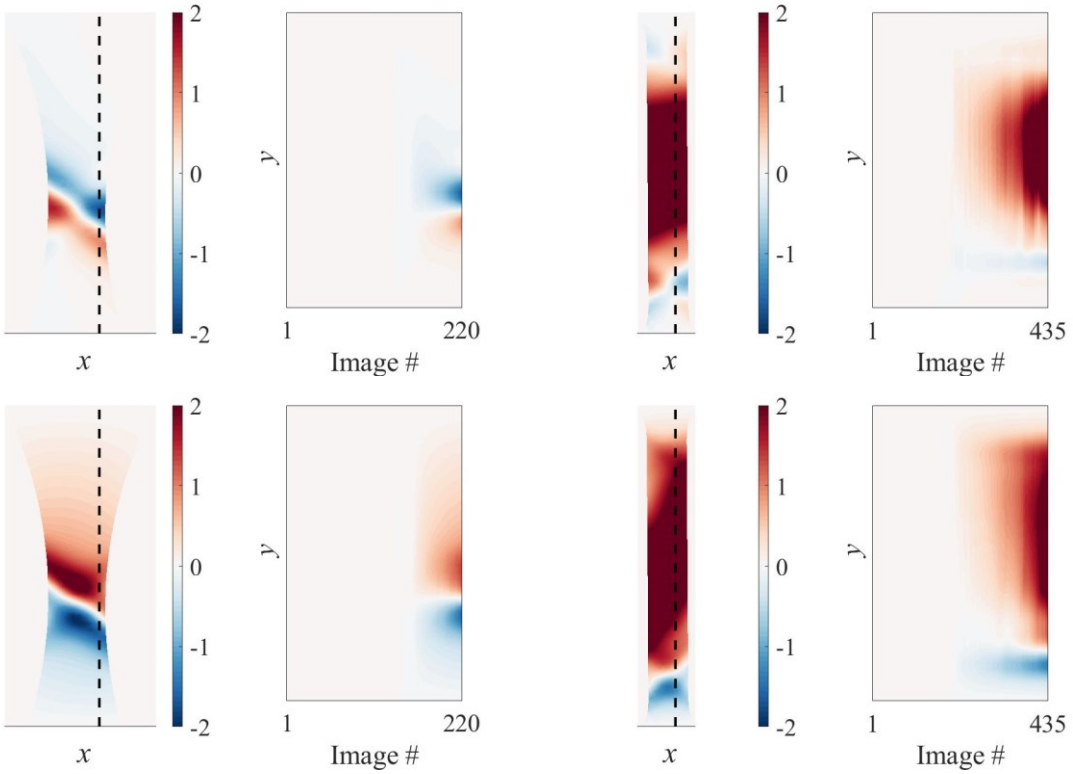

(a) (b)

Fig. 12 Displacement sensitivity fields for K in terms of x (first row) and y (second row) displacements expressed in pixel/ε. The sensitivity fields are displayed for the last analyzed image. A line of pixels is plotted for each analyzed image next to the sensitivity field

When comparing the sensitivities for the hardening exponent n (Fig. 13), the fields for the *DIN* sample display more pronounced sensitivities. However, as previously displayed for the *dogbone* sample, the sensitivities are localized around the strain band location, whereas for the *DIN* sample most of the region of interest contains positive sensitivities. From the *DIN* sensitivity field and history, it is observed that the sensitivities are also localized around the detected strain band, near the gripped part of the sample.

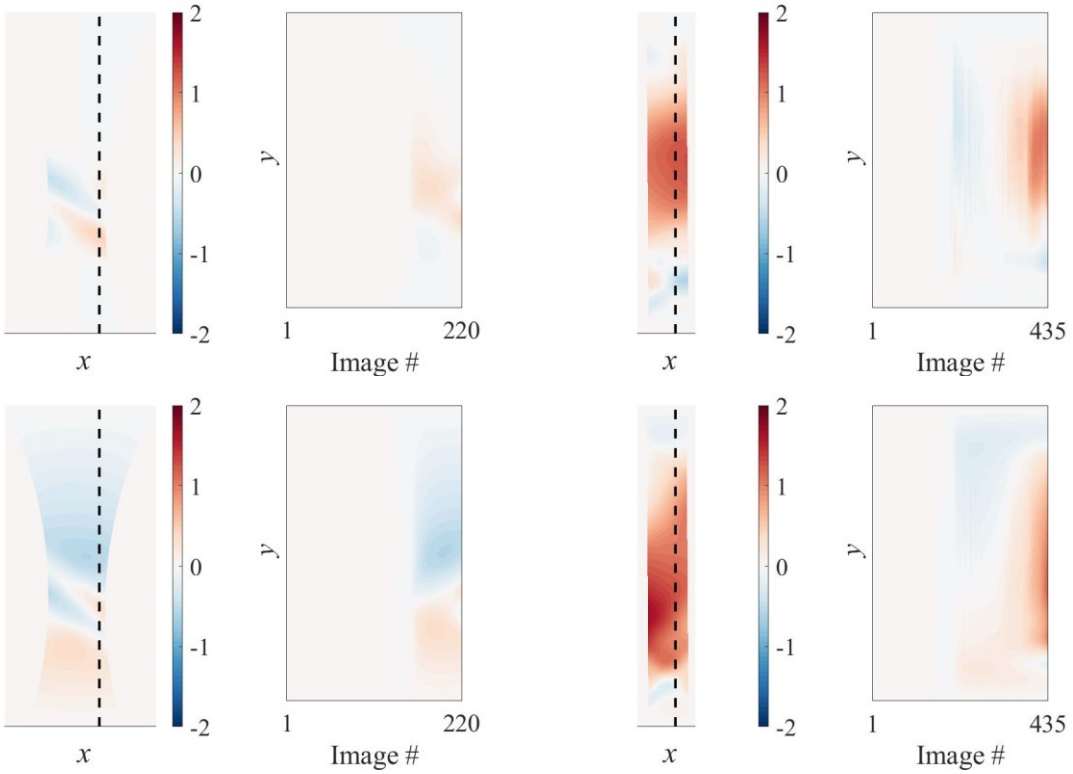

(a) (b)

Fig. 13 Displacement sensitivity fields for n in terms of x (first row) and y (second row) displacements expressed in pixel/ε. The sensitivity fields are displayed for the last analyzed image. A line of pixels is plotted for each analyzed image next to the sensitivity field

Figure14 displays the influence of individual parameter changes on the computed reaction forces. The force sensitivities are expressed as load [N] divided by parameter offset ε. Similar trends are observed for both samples. The sensitivity levels for the *dogbone* sample are slightly lower than for the *DIN* geometry. For both geometries, the Young's modulus E displays the highest sensitivity from all considered parameters; the highest levels are in elasticity. In plasticity, E displays reduced force sensitivities. As expected, the Poisson's ratio displays negligible influence on the force and displacement sensitivities. The yield stress leads to the second highest sensitivity. It is the only parameter that provides sensitivities of the same order of magnitude as E. Conversely, the hardening parameters display an order of magnitude lower sensitivities. When comparing E with the plastic parameters, it is observed that when E reaches the lowest sensitivity values the latter ones reach their maximum levels.

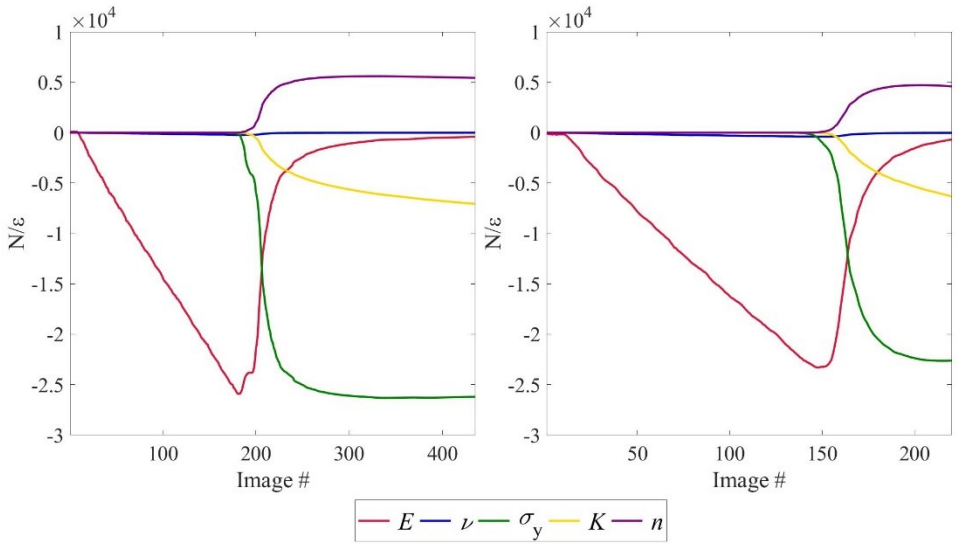

Fig. 14 Force sensitivities expressed in N/ε for the *DIN* (left) and *dogbone* (right) geometries

5. Conclusions

An experimental and numerical comparison of the two considered configurations (*i.e.*, *DIN* and *dogbone*) was performed to determine the sample geometry with highest parameter sensitivities in uniaxial tensile tests for the calibration of Ludwik's law parameters. The *DIN* sample contained two parallel edges in the gauge region, whereas the *dogbone* sample was thinned in the center with a radius of 75 mm. The main results of this work are:

- the *DIN* sample provided better condition number of the diagonalized Hessian matrix,
- the *dogbone* sample displayed higher sensitivity for the elastic parameters (*i.e.*, Young's modulus E and Poisson's ratio ν),
- similar sensitivities were reported for the yield stress σ_y,
- higher sensitivity for the hardening modulus K was observed for the *DIN* sample, whereas for the hardening exponent n, higher sensitivity was observed for its counterpart,
- the *Dogbone* sample exhibited increased sensitivity to parameter changes around the strain localization zone.

Both samples exhibited advantages and drawbacks with respect to each other, especially in the identifiability of material parameters. However, due to the *a priori* known strain localization area, the *dogbone* sample is a more suitable choice since a smaller region of the sample can be monitored in more detail.

Last, it is worth noting that the present framework, which was applied to Ludwik's law up to the ultimate load, can be used to analyze different constitutive postulates as well as different geometries. The framework is generic and versatile provided the numerical simulations are able to capture the main experimental features of the considered experiment.

Acknowledgments

This work was performed within the FULLINSPECT project supported by the Croatian Science

Foundation (UIP-2019-04-5460 Grant).

References

Ahmed, S.T., Aguib, S., Toufik, T., Noureddine, C. and Ahmed, C. (2019) “Effects of the geometrical parameters of the core on the mechanical behavior of sandwich honeycomb panel”, Coupled Systems Mechanics, **8**(6), 473-488, 10.12989/csm.2019.8.6.473

Bertin, M., Hild, F. and Roux, S. (2016) “Optimization of a Cruciform Specimen Geometry for the Identification of Constitutive Parameters Based Upon Full-Field Measurements”, *Strain*, **52**(4), 307-323. 10.1111/str.12178

Bertin, M., Hild, F. and Roux, S. (2017) “On the identifiability of Hill-1948 plasticity model with a single biaxial test on very thin sheet”, *Strain*, **53**(5), e12233, 10.1111/str.12233

Bertin, M., Hild, F., Roux, S., Mathieu, F., Leclerc, H. and Aimedieu, P. (2016), “Integrated digital image correlation applied to elastoplastic identification in a biaxial experiment”, *J. Strain Analysis Eng. Des*., **51**(2), 118-131. 10.1177/0309324715614759

Besnard, G., Hild, F. and Roux, S. (2006), “"Finite-element" displacement fields analysis from digital images: Application to Portevin-Le Châtelier bands”, Exp. Mech., **46**(6), 789-803. 10.1007/s11340-006-9824-8

Claire, D., Hild, F. and Roux, S. (2004) “A finite element formulation to identify damage fields: the equilibrium gap method”, *Int. J. Numer. Methods Eng.*, **61**(2), 189-208. 10.1002/nme.1057

Cooreman, S., Lecompte, D., Sol, H., Vantomme, J. and Debruyne, D. (2008) “Identification of mechanical material behavior through inverse modeling and DIC”, *Conf. Proc. Soc. Exp. Mech. Ser.*, **65**(4), 421-433. 10.1007/s11340-007-9094-0

Geymonat, G., Hild, F. and Pagano S. (2002) “Identification of elastic parameters by displacement field measurement”, *Comptes Rendus Mécanique*, **330**, 403-408. https://doi.org/10.1016/S1631-0721(02)01476-6

Grediac, M. and Pierron F. (2006) “Applying the Virtual Fields Method to the identification of elasto-plastic constitutive parameters”, *Int. J. Plast.*, **22**(4), 602-627. 10.1016/j.ijplas.2005.04.007

Guery, A., Hild, F., Latourte, F. and Roux, S. (2016), “Identification of crystal plasticity parameters using DIC measurements and weighted FEMU”, *Mech. Mater.*, **100**, 55-71. https://doi.org/10.1016/j.mechmat.2016.06.007

Hild, F. and Roux, S. (2012) “Comparison of local and global approaches to digital image correlation”, *Exp. Mech.*, **52**(9), 1503-1519. 10.1007/s11340-012-9603-7

Kavanagh, K.T. and Clough, R.W. (1971), “Finite element applications in the characterization of elastic solids”, *Int. J. Solids. Struct*., **7**(1), 11-23. 10.1016/0020-7683(71)90015-1

Leclerc H., Neggers J., Mathieu F.., Hild F., Roux S. (2015)., “Correli 3.0.”, Agence pour la Protection des Programmes, Paris (France), IDDN.FR.001.520008.000.S.P.2015.000.31500

Lecompte, D., Smits, A., Sol, H., Vantomme, J. and Van Hemelrijck, D. (2007) “Mixed numerical–experimental technique for orthotropic parameter identification using biaxial tensile tests on cruciform specimens”, *Int. J. Solids. Struct*., **44**(5), 1643-1656. 10.1016/j.ijsolstr.2006.06.050

Lindner, D., Mathieu, F., Hild F., Alix, O., Minh, C.H. and Paulien-Camy, O. (2015) “On the evaluation of stress triaxiality fields in a notched titanium alloy sample via integrated digital image correlation”, *J. Appl. Mech.-T. ASME*, **82**(7), 1-10, 10.1115/1.4030457

Ludwik, P. (1909) “Elemente der Technologischen Mechanik”, Verlag von Julius Springer, Berlin, Germany

Martins, J.M.P., Andrade-Campos, A. and Thuilier, S. (2018) “Comparison of inverse identification strategies for constitutive mechanical models using full-field measurements”, *Int. J. Mech. Sci.*, **145**, 330-345, 10.1016/j.ijmecsci.2018.07.013

Mathieu, F., Leclerc, H., Hild, F. and Roux, S. (2015) “Estimation of Elastoplastic Parameters via Weighted FEMU and Integrated-DIC”, *Exp. Mech.*, **55**, 105-1129. https://doi.org/10.1007/s11340-014-9888-9

Nam Do, X., Ibrahimbegović, A. and Brancherie, D. (2015) “Combined hardening and localized failure with

softening plasticity in dynamics", *Coupled Systems Mechanics*, **4**(2), 115-136, 10.12989/csm.2015.4.2.115
Neggers, J., Mathieu, F., Hild, F., Roux, S. and Swiergiel, N. (2017) "Improving full-field identification using progressive model enrichments", *Int. J. Solids. Struct*., **118**(7), 213-223. https://doi.org/10.1016/j.ijsolstr.2017.03.013
Passieux, J.C., Bugarin, F., David, C., Perie, J.N. and Robert, L. (2015) "Multiscale Displacement Field Measurement Using Digital Image Correlation: Application to the Identification of Elastic Properties", *Exp. Mech.*, **5**, 121-137. https://doi.org/10.1007/s11340-014-9872-4
Prates, P.A., Pereira, A.F.G., Oliveira, M.C. and Fernandes, J.V. (2019), "Analytical sensitivity matrix for the inverse identification of hardening parameters of metal sheets", *Eur. J. Mech. A Solids*., **75**, 205-215. 10.1016/j.euromechsol.2019.01.010
Prates, P.A., Pereira, A.F.G., Sakharova, N.A., Oliveira, M.C. and Fernandes, J.V. (2016) "Inverse Strategies for Identifying the Parameters of Constitutive Laws of Metal Sheets", *Adv. Mater. Sci. Eng.*, **2016**, 1-18. 10.1155/2016/4152963
Roux, S. and Hild, F. (2020) "Optimal procedure for the identification of constitutive parameters from experimentally measured displacement fields", *Int. J. Solids. Struct*., **184**(2), 14-23. https://doi.org/10.1016/j.ijsolstr.2018.11.008
Sutton, M.A., Orteu, J.J. and Schreier, H.W. (2009) "Image Correlation for Shape, Motion and Deformation Measurements", Springer, New York, United States of America
Tarantola, A. (1987) "Inverse Problems Theory. Methods for Data Fitting and Model Parameter Estimation", Elsevier Applied Science, Southampton, United Kingdom
Tisza, M. (2005) "Numerical modeling and simulation in sheet metal forming academic and industrial perspectives", *Mater. Sci. Forum*, **473-474**, 407-414. 10.4028/www.scientific.net/msf.473-474.407
Tomičević, Z., Hild, F. and Roux S. (2013), "Mechanics-aided digital image correlation", *J. Strain Analysis Eng. Des.*, **48**(5), 330-343. 10.1177/0309324713482457
Tomičević, Z., Kodvanj, J. and Hild, F. (2016a) "Characterization of the nonlinear behavior of nodular graphite cast iron via inverse identification: Analysis of uniaxial tests", *Eur. J. Mech. A Solids*., **59**, 140-154. https://doi.org/10.1016/j.euromechsol.2016.02.010
Tomičević, Z., Kodvanj, J. and Hild, F. (2016b) "Characterization of the nonlinear behavior of nodular graphite cast iron via inverse identification: Analysis of biaxial tests", *Eur. J. Mech. A Solids*., **59**, 195-209. https://doi.org/10.1016/j.euromechsol.2016.02.010

Scientific paper 2

A. Zaplatić, Z. Tomičević, D. Čakmak, and F. Hild, “Improvement of the Arcan Setup for the Investigation of Thin Sheet Behavior Under Shear Loading,” Exp Mech, vol. 62, no. 2, pp. 313–332, Feb. 2022, doi: 10.1007/s11340-021-00762-1.

Preprint of the published journal article.

Improvement of the Arcan setup for the investigation of thin sheet behavior under shear loading

A Zaplatić, Z Tomičević, D Čakmak, François Hild

Experimental Mechanics manuscript No.
(will be inserted by the editor)

Improvement of the Arcan setup for the investigation of thin sheet behavior under shear loading

A. Zaplatić · Z. Tomičević · D. Čakmak · F. Hild

Received: date / Accepted: date

Abstract Background: Accurate predictions of thin sheet material springback during forming processes are of great interest in the forming industry. However, thin sheets are susceptible to buckling under shear loading. Objective: The present research aims at improving the so-called Arcan setup for testing thin (1-5 mm) sheet samples with large gauge areas (*i.e.,* width about 21 mm) by introducing anti-buckling devices to mitigate sample buckling. Method: Three monotonic and one cyclic shear tests were carried out on 1 mm thick C60 high carbon steel. Results: The use of the proposed anti-buckling device resulted in the suppression of sample buckling. Numerical analyses of the experiment where buckling was eliminated revealed predominant shear stress states in the gauge area (*i.e.,* stress triaxiality =

A. Zaplatić, Z. Tomičević*, D. Čakmak

University of Zagreb, Faculty of Mechanical Engineering and Naval Architecture, Ivana Lučića 5, 10002 Zagreb, Croatia

*Corresponding author. Email: zvonimir.tomicevic@fsb.hr

F. Hild

Université Paris-Saclay, ENS Paris-Saclay, CNRS

LMT - Laboratoire de Mécanique et Technologie, 91190 Gif-sur-Yvette, France

0), which highlights minor influences of the anti-buckling device on the sample stress state. Conclusion: To suppress buckling, the use of anti-buckling devices was essential. Moreover, the friction coefficient between the sample and the proposed devices was calibrated ($\mu = 0.33$) in addition to kinematic hardening parameters.

Keywords Arcan fixture · Buckling · Simple shear · Stereocorrelation · Thin sheet

1 Introduction

The growing demand for light-weight engineering components of high quality requires equally fast and adaptive production processes in order to meet the demand-supply balance. As a result, at the end of the 20-th century, the implementation of numerical simulations and modeling of sheet metal forming processes gained traction. The role of numerical simulations was to predict material flow, to analyze stress-strain relationships, and to improve the quality of manufactured components [1]. Expensive and time consuming trial and error methods for analyzing production processes had to be minimized. For instance, industries involving metal forming relied on numerical simulations of manufacturing processes where shear is an important stress state [2]. Since pure shear cannot be obtained experimentally, mechanical tests involving simple shear are often carried out on thin sheets.

Simple shear tests provide a comprehensive characterization of the anisotropy of flat samples experiencing large strains [3, 4, 5]. Since the sample geometry is essential in understanding the material response due to simple shear, many authors have proposed different approaches to their design. Furthermore, the sample geometry directly determines which material property is sought (*e.g.,* elasto-plasticity [6, 4], shear fracture [7, 8]). The design of samples should possibly provide homogeneous shear stress states in the gauge area.

Miyauchi [6] proposed a complex geometry containing three clamped bars linked by the two sheared zones (*i.e.,* gauge areas). By pulling the central bar, shear stress states were induced in the gauge areas. The sample geometry according to ASTM B831 standard [9] contains two slant slits, thereby establishing a single shear zone in the middle of the sample. Merklein and Biasutti [10] modified the ASTM geometry to enable for compressive loadings. A comprehensive study carried out by Yin *et al.* [11], where the aforementioned geometries were compared, yielded good agreement for the shear stress vs. strain responses for each investigated test.

Peirs *et al.* [7] developed a flat shear sample, which was based upon the geometry proposed by Bao *et al.*[12], with asymmetric rounded off notches with eccentricity that promoted shear stress states in the gauge area (*i.e.,* stress triaxiality close to zero). Reyes *et al.* [13] optimized the geometry containing two slant slits with respect to stress homogeneity and triaxiality for static and dynamic shear experiments. The geometry of the slits was changed to a semi-circular shape with V notches to promote uniform strain distributions. Roth and Mohr [14] carried out a comprehensive study of Peirs' shear sample to obtain reliable shear strain measurements at fracture. As a result, three modified geometries were proposed for various levels of material ductility. Furthermore, Roth and Mohr [15, 8] optimized the so-called *smiley* geometry with two parallel gauge sections for in plane shear testing by modifying the notch geometry to avoid premature fracture initiation near the free gauge boundaries. To prevent buckling of the sample, the width and height of the gauge section were of the same order of magnitude as the thickness.

Iosipescu [16] proposed a flat sample geometry with two symmetric V notches (*i.e.,* butterfly sample) in the gauge region to induce quasi uniform shear states between V notches. Mohr and Henn [17] designed butterfly specimens with thickness reduction in the gauge area for investigating the fracture of metallic materials in a wide range of triaxialities. Moreover,

Mohr and Oswald [18] improved the biaxial testing machine developed by Mohr and Doyoyo [19], which was based on the Arcan fixture [20]. It enabled the authors to investigate the material behavior with the aforementioned butterfly sample under combined tensile and shear loadings. Further improvements to the sample geometry [21] were proposed for investigating fracture under combined normal and shear stresses. Abedini *et al.* [22, 23] analyzed the influence of two sample geometries (*i.e.,* Peirs' mini-shear sample [7] and the butterfly geometry [21]) on the fracture of thin sheets. The butterfly sample achieved lower fracture strains than its counterpart. However, it was deemed useful for quasi-static fracture characterization in shear and plane strain/stress states. Furthermore, Peshekhodov *et al.* [24] developed a butterfly sample for fracture characterization of advanced high strength steel sheets under shear, tensile and combined stress states.

The aim of this research is to discuss a modified Arcan setup to investigate the behavior of butterfly specimens made of 1 mm C60 high carbon steel. The thin sheet samples were designed with *large* gauge areas (*i.e.,* height equal to 21 mm), whereas the previously discussed shear geometries contained small gauge zones (*i.e.,* < 3 mm). The latter ones were designed to promote uniform shear stress states and to reduce buckling [25, 4, 26]. However, samples with large gauge areas are prone to buckling due to increased width to thickness ratios. Buckling restricts the use of standard optical measurement methods for determining the material response under simple shear loading. Therefore, to prevent buckling, transparent anti-buckling devices made of acrylic glass were added. Three monotonic and one cyclic shear tests were carried out and monitored with a stereovision system. Furthermore, the influence of the anti-buckling device was evaluated numerically by observing the contribution of friction to the calibrated plasticity parameters via Finite Element Model Updating (FEMU) [27] and to stress triaxiality fields. Last, friction was calibrated in addition to the kinematic hardening parameters of the investigated steel.

2 Modified Arcan fixture and tested samples

In this section, the modifications to the Arcan fixture are presented. They include increased thickness of the fixture, upgraded gripping system of the tested samples, and modular design of the fixture. Additionally, changes to the butterfly geometry are also presented.

2.1 Modified Arcan device

The Arcan fixture [20] was designed as two separate semi-circular symmetrical plates made of aluminum alloy. The butterfly samples were glued to the supporting plates, and subjected to in-plane shear loadings. For the present study, the Modified Arcan Fixture (MAF, see Figure 1) was designed to study the mechanical response of thin (*i.e.,* $\leq$ 5 mm in thickness) metal sheets subjected to in-plane tensile, simple shear and combined loadings with expected triaxiality values of 0.33, 0 and < 0.66 in the gauge areas, respectively. The main advantage of the MAF is an increased stiffness of the fixture to avoid out-of-plane bending, and a modular design to allow for varying sample thicknesses. Figure 1 shows the MAF that consists of two separate yet identical semi-circular 35-mm thick supporting plates (*i.e.,* rigs), two sets of gripping jaws, and two identical testing machine adapters.

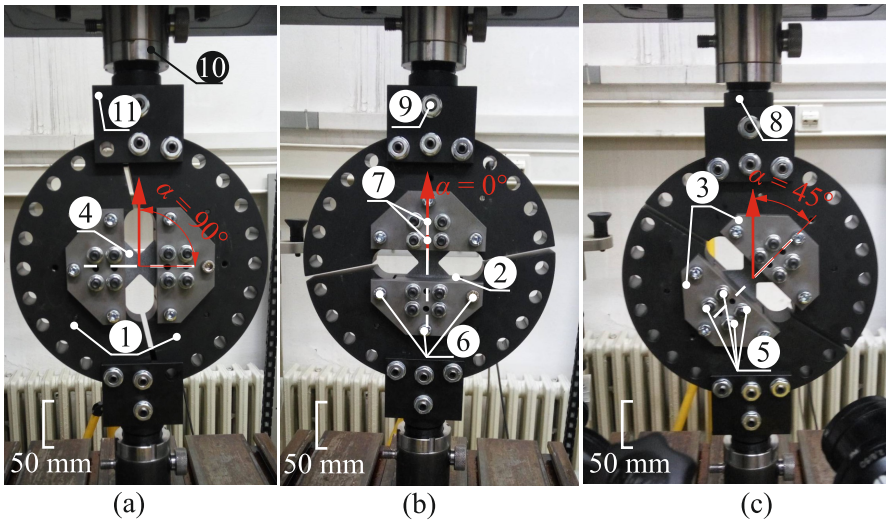

Fig. 1: Loading configurations of the Modified Arcan Fixture. (a) Simple shear configuration, (b) tensile loading configuration, and (c) combined shear/tensile loading configuration. See text for the description of the labels

The Arcan rig (1) (Figure 1) is made of M200 steel plates with a radius of 123.5 mm. The use of high strength steel (*i.e.,* $\sigma_y = 1000$ MPa) ensures that the fixture does not enter the plastic regime during tests. Near the peripheral area of the rigs, a series of twelve 13-mm in diameter holes was drilled $15°$ apart. The prescribed load onto the butterfly sample is selected by the loading holes. For example, pure tension ($\alpha = 0°$), simple shear ($\alpha = 90°$) and combined loadings ($0° < \alpha < 90°$) can be applied. The front central part of the rigs contains milled rectangular openings designed to hold the gripping jaws and the butterfly sample. The size of the rectangular openings is 75×35 mm with a depth of 25 mm from the front face. The rectangular openings result in asymmetric distributions of rig stiffness (*i.e.,* the rear side of the fixture is stiffer than the front side). This shortcoming manifested itself in the form of out-of-plane bending of the sample since the load distribution induced

spurious bending. The aforementioned imperfection was compensated with the appropriate design of the gripping jaws (2) and (3) (Figure 1).

The gripping jaw (2) serves as a placeholder to prevent any motion of the sample. The jaw (3) was designed with dual purpose. The primary purpose is to connect the sample (4) to the fixture via two sets of four M8 bolts (5). The secondary role is to increase the rigidity of the front side of the rigs, which is established by directly connecting jaw (3) to the front side via three additional M8 bolts (6). As a result, the rigs and griping jaws behave as a single solid part. Two additional pins (7) were added to prevent bolt shearing. Moreover, the gripping system was designed to ensure the coaxiality between the loading axis and that of the sample. To prevent slip of the sample, the contact surfaces on the gripping jaws were knurled.

The connection between the fixture and the testing machine is established via two adapters (8). They consist of a central shaft, which is fastened to the testing machine via a single 13-mm in diameter pin (9), the lock nut (10), and two tabs (11) on the sides of the shaft. Each tab consists of three loading holes equally spaced according to the layout on the rigs. The central shaft of the Arcan adapter was designed with a radius less than the machine connector slot. As a result, a clearance is present between the Arcan adapter and the machine slot. Since the Arcan fixture is connected to the machine with a single pin, a single rotational degree of freedom is allowed. During tests, the fixture has the ability for self-alignment. However, to compensate for the aforementioned clearance, the Arcan adapter was also threaded at the connection point with the machine. This modification allows for the use of lock nut (10). By tightening the nut, the adapter is firmly pushed into the connector slot of the machine, thereby increasing the preload on the sample.

2.2 Butterfly sample

The butterfly sample (Figure 2) was designed with two symmetric V notches for localizing the plastic strains in the narrow gauge area (*i.e.,* between the two V notches). The surface of the sample is divided into three regions, namely, the gripped area, the observable area during tests and the Region of Interest (ROI) for stereocorrelation analyses. The dimensions of the gripped area, shown as red hatched in Figure 2(a), correspond to those of the contact surfaces of gripping jaws (2) and (3). Since the gripped surfaces cannot be monitored during tests, only a 30×40-mm^2 surface area is visible. However, the chosen ROI, depicted by green hatches, was smaller than the observable area of the sample. This choice is justified by the fact that shear strains were concentrated in the gauge area close to the ligament.

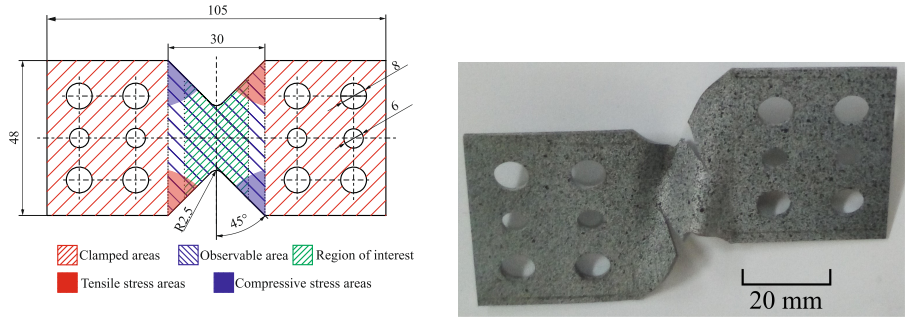

Fig. 2: (a) Butterfly geometry with characteristic regions (see text). The various stress areas are depicted for simple shear loading. Dimensions are in mm. (b) Buckled E1 sample under simple shear loading in the modified Arcan fixture

On each end of the sample, four 8-mm holes were drilled to allow the threaded M8 bolts to pass through to tighten the sample and the fixture together. Tightening the sample with

four bolts makes the contact pressure more uniform. Two additional holes for 6-mm pins were added to prevent bolt shearing.

3 Experimental investigation

The experimental investigation presented herein was performed with the MAF. The latter offers three main loading modes depending on the angle α of the fixture with respect to the loading axis of the testing machine (depicted by the red arrow in Figure 1). The first loading configuration (Figure 1(a)) induces simple shear stress states in the gauge area of the sample, whereas the second loading configuration (Figure 1(b)) corresponds to tensile loading where the expected triaxiality levels in the gauge area are around 0 and 0.33, respectively. Furthermore, the combination of both loading configurations (Figure 1(c)) enables for the application of combined shear/tensile loadings with expected triaxialities in the gauge area ranging from 0 to 0.66.

3.1 Buckling under shear loading

The accurate characterization of thin sheets subjected to shear loading is challenging [25, 4, 26]. The samples are generally thin with a large gauge width to thickness ratio inducing folding of the sample (Figure 2(b)). Saurupt et al. [25] concluded that the folding mechanism could be interpreted as buckling due to compressive stresses. Due to sample clamping, the material close to two diagonally opposed corners of the unclamped region is subjected to tension while the other corners are subjected to compression. Where compression occurs, buckling initiation was reported [4]. Such mechanism may be prevented using additional supports placed on the observed region of interest [28], or by changing the sample gauge width [4].

The butterfly sample subjected to shear loading on the MAF exhibited buckling. This phenomenon was observed for sample thicknesses less than 2 mm (Figure 2(b)). In the experimental investigations presented herein, the behavior of 1-mm thick butterfly samples, made of C60 high carbon steel, was sought. Therefore, in order to suppress the initiation of buckling, additional supports in the form of two transparent plates made of Poly methyl methacrylate (PMMA) were selected. Such configuration was already used to successfully mitigate wrinkling in 1D and 2D tests on sub-millimeter sheets [29, 30]. The dimensions of the PMMA plates (*i.e.,* 70×25 mm) were chosen with respect to the observable area (Figure 2(a)). Moreover, the transparency of PMMA allows optical measurement methods to be employed. Stereocorrelation was applied to measure displacement and strain fields of the ROI. The application of the supports is straightforward. Each plate was placed on the front and back surfaces of the sample and was connected via six M5 bolts.

3.2 Experimental setup

In order to determine the influence of the additional support on the mitigation of buckling, an appropriate experimental protocol had to be defined. The three configurations employed in this investigation are presented in Table 1. Furthermore, the influence of the stiffness of the connection between the MAF and the testing machine had to be studied. Pham et al [28] determined that clamping of the fixture (*i.e.,* increasing the stiffness of the fixture) resulted in stress perturbations in the sample, thereby leading to buckling initiation. Higher stiffnesses of the MAF are achieved by tightening the lock nut on the testing machine adapter. Consequently, additional tensile/compressive preloads could be applied to the tested samples.

Table 1: Experimental configurations (M: monotonic, C: cyclic)

Test	E1	E2	E3	E4
Configuration	#1	#2	#3	#3
Loading regime	M	M	M	C
Thickness of PMMA plates, mm	–	5	10	10
Preload, N	-39	-1000	-40	-35

The first configuration was characterized by a loosened connection between the MAF and the testing machine. Furthermore, no additional support was applied. However, even with the allowed self-alignment of the MAF, buckling of the sample occurred (Figure 2(b)). Therefore, in the second configuration, an additional support with 5-mm thick PMMA plates was employed. Higher stiffness of the MAF was achieved and the measured preload was equal to -1000 N (Table 1). Although the PMMA support was applied, buckling of the sample was observed, which fractured the plates. For that reason, the third configuration employed 10-mm thick plates, and a loosened connection between the MAF and the testing machine. The third configuration suppressed buckling initiation. An additional cyclic test was then performed with the third configuration for further validation purposes.

The shear tests were carried out on a uniaxial testing machine *Messphysik Beta* 50-5 in controlled displacement with a stroke rate of 1 mm/min. The material response in the observed ROI (Figure 2) was monitored by a stereovision system. The image acquisition rate for the monotonic (*i.e.,* E1, E2 and E3) experiments was 1 fps, whereas for the cyclic (*i.e.,* E4) test it was 0.3 fps. The hardware parameters of the optical setup are listed in Table 2.

Table 2: Hardware parameters of the stereovision system

Cameras	Dalsa Falcon 4M60
Definition	2358×1728 pixels (B/W images)
Color filter	none
Gray Levels rendering	8 bits
Lens	Titanar 50 mm
Aperture	f/2.8
Field of view	3,996 mm^2
Image scale	≈ 32 pixel/mm
Stereo-angle	25°
Stand-off distance	31.6 cm
Image acquisition rate	1 fps (0.3 fps for test E3)
Patterning technique	B/W paints
Pattern feature size	15 px

The experimental investigation employing the MAF (1) (Figure 3) was monitored by the optical setup (Figure 3) consisting of two vertically positioned Dalsa cameras (2) and (3) (Figure 3) and two light sources (4). The vertical layout of the cameras was chosen in order to achieve maximum spatial resolution for the ROI. The stereovision system captured the entire gauge area of the sample (5) *and* the additional PMMA supports (6).

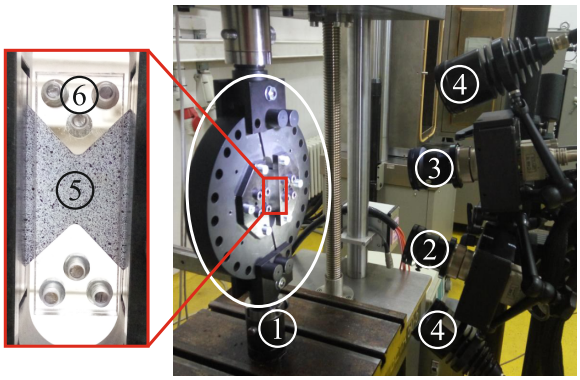

Fig. 3: Experimental and optical setups used for stereocorrelation measurements. See text for the description of the labels

For this study, FE-based stereocorrelation [31, 32, 33] was utilized for measuring displacement and strain fields in the region of interest (ROI). The aforementioned algorithm uses a continuous description of the observed surface discretized with triangular finite elements. The commercial code EikoTwin DIC [34] was used. The calibration was carried out in two steps. For the pre-calibration step, a first estimation of the projection matrix was sought for each camera. During this process, the scale factor (*i.e.,* conversion between pixel and mm) was set. An FE mesh was created, which corresponded to the nominal geometry of the sample *and* the fixture (Figure 4(a)) that were observed by both cameras. Since each camera was independent at this stage, different points were chosen for the left and right camera pictures. These points must be distributed in the entire 3D volume that is covered by each camera. A total of 8 points was chosen in two different planes and the first estimates of the projections matrices were obtained for this self-calibration route [35]. The pre-calibration step allows in particular for the verification of the reprojection of the measurement mesh (Figure 4(b)).

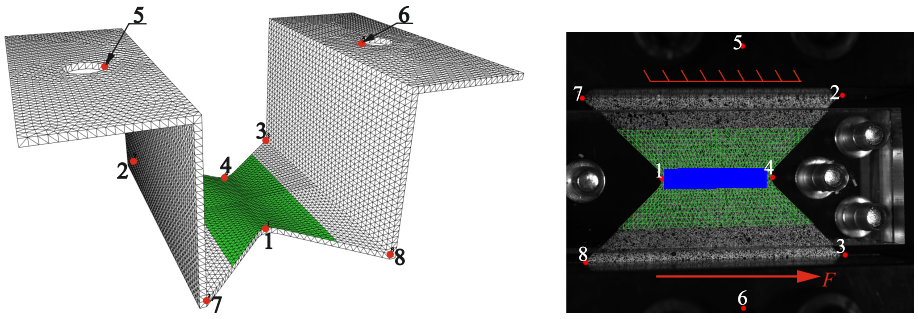

(a) (b)

Fig. 4: Chosen reference points on the FE mesh and one of the reference images for the pre-calibration step. (a) User defined points (*i.e.,* fiducials) on the FE mesh, and (b) on one of the reference pictures used in the pre-calibration step. The (green) mesh of the ROI is also shown in the 3D model and its reprojection in one of the reference pictures. The blue rectangle depicts the area over which the average strains were assessed

The calibration step was then performed to determine the best projection matrices via global registrations [35] of the two reference images based on the knowledge of the nominal geometry. It was initialized with the projection matrices determined during the pre-calibration step. Once the calibration step was carried out, shape corrections were performed for the actual ROI (Figure 4(b)) by running a second series of spatial registrations in which out-of-plane corrections were allowed [32].

Last, displacement fields were measured by performing temporal registrations in which the nodal displacements were determined [31, 36, 33]. The stereocorrelation parameters are listed in Table 3. The noise floor estimates were obtained by calculating the (temporal) standard deviations of the nodal displacements and strains from the registration of ten image pairs acquired in the unloaded states.

Table 3: Stereocorrelation analysis parameters

DIC software	EikoTwin DIC
Image filtering	none
Element length	1 mm
Shape functions	linear (T3 elements)
Mesh	see Figure 4
Matching criterion	penalized sum of squared differences
Regularization length	5 mm
Displacement noise floor for test E1 (x z y)	0.4 µm 0.2 µm 0.7 µm
Displacement noise floor for test E2 (x z y)	0.1 µm 0.2 µm 0.5 µm
Displacement noise floor for test E3 (x z y)	0.2 µm 0.1 µm 0.6 µm
Displacement noise floor for test E4 (x z y)	0.2 µm 0.2 µm 0.6 µm
Strain ϵ_{xz} noise floor for test E1	6×10^{-5}
Strain ϵ_{xz} noise floor for test E2	6×10^{-5}
Strain ϵ_{xz} noise floor for test E3	7×10^{-5}
Strain ϵ_{xz} noise floor for test E4	8×10^{-5}

Figure 5 displays the load histories of the four tests reported herein. For each test, six characteristic points were chosen for which the stereocorrelation results are discussed in the following subsections.

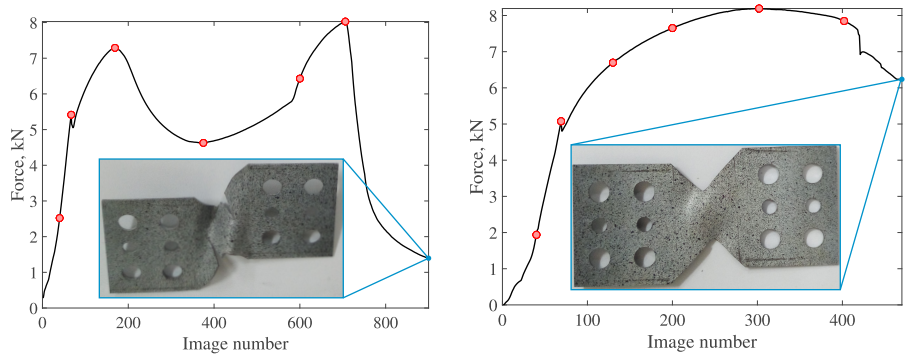

(a) E1

(b) E2

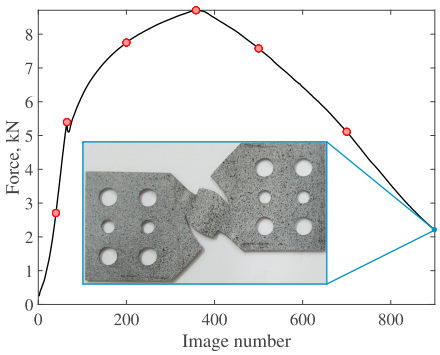

(c) E3

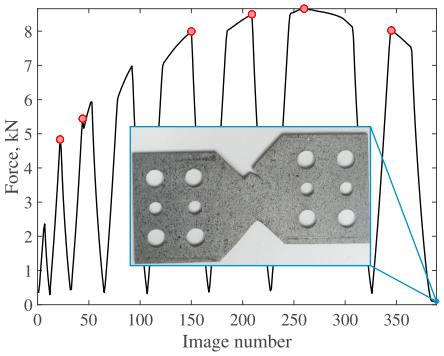

(d) E4

Fig. 5: Load histories for tests E1, E2, E3 and E4. Six characteristic points are outlined by red circles for each experiment for which the stereocorrelation results are discussed hereafter

3.3 Test E1

The loading history of test E1 (Figure 5(a)) displays a disrupted response. Since no PMMA support was utilized, buckling occurred (Figure 2(b)), thereby resulting in lower load levels. The first peak load was equal to 7.2 kN for a shear strain of 17.5%. The kinematic fields corresponding to the characteristic points shown in Figure 5(a) are reported in Appendix A.

3.4 Test E2

The loading history of test E2 shown in Figure 5(b) exhibited a more stable behavior compared to the E1 loading history (Figure 5(a)). This trend was due to the application of the 5-mm thick plates, which delayed buckling inception. However, since the stiffness of the connection between the MAF and the testing machine was high, buckling was not totally suppressed. This mechanism led to the failure of the PMMA supports and the test was interrupted. The kinematic fields corresponding to the characteristic points shown in Figure 5(b) are reported in Appendix A.

3.5 Test E3

Figure 5(c) shows the loading history of test E3. Compared to the loading histories of tests E1 (Figure 5(a)) and E2 (Figure 5(b)), the highest load level was reached in test E3. The 10-mm thick support did not fail. The connection stiffness between the MAF and the testing machine was loosened again. As a result, buckling was prevented, thus the material response could be observed more clearly.

Figure 6 displays the measured out-of-plane displacement fields for test E3. Since the 10-mm thick plates were employed, negligible amplitudes were measured throughout the experiment. This result proves that the plate thickness was sufficient to significantly lower the amplitudes of out-of-plane motions. In elasticity (Figure 6(a)) and early plasticity (Figure 6(b)), the displacements were of the same order of magnitude. Increases in magnitude observed in Figure 6(c) were due to the tendency toward buckling (as seen in test E1). However, the additional supports prevented further increases. The displacement fluctuations were attributed to buckling. Even for the highest achieved load (Figure 6(d)), the out-of-plane dis-

placements were considered negligible. However, after damage initiation and growth (Figure 6(e-f)), thinning of the sample was observed around the roots of the V notches.

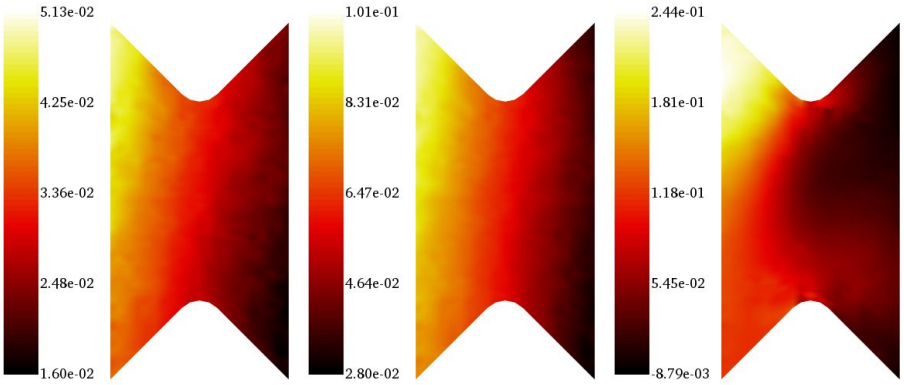

(a) $F = 2.7\text{kN}, \epsilon_{xz} = 0.12\%$ **(b)** $F = 5.4\text{kN}, \epsilon_{xz} = 0.37\%$ **(c)** $F = 7.75\text{kN}, \epsilon_{xz} = 22.7\%$

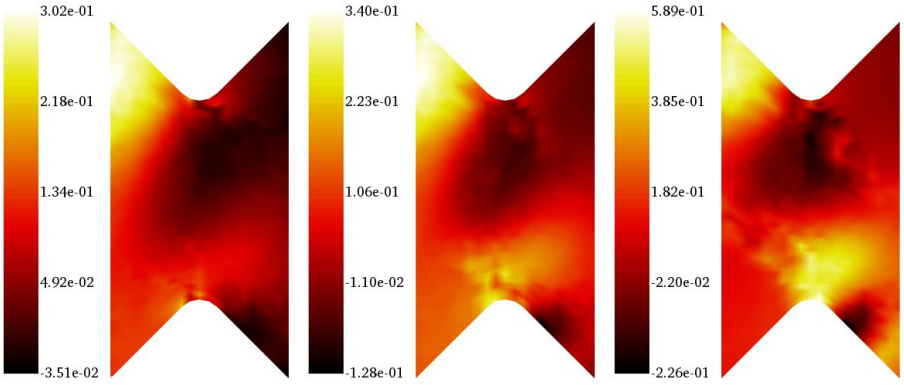

(d) $F = 8.71\text{kN}, \epsilon_{xz} = 48.7\%$ **(e)** $F = 7.6\text{kN}, \epsilon_{xz} = 70.82\%$ **(f)** $F = 5.1\text{kN}, \epsilon_{xz} = 92.2\%$

Fig. 6: Measured out-of-plane displacement fields for test E3. The displacements are expressed in mm

The analysis of the axial displacements (*i.e.,* perpendicular to the loading direction, see Figure 4(b)) revealed rotations of the ROI (Figure 7(a)). This trend also occurred in the plastic regime (Figure 7(b)). Furthermore, the axial displacements showed two emerging discontinuities, which are indicated by arrows in Figure 7(c). These “discontinuities” were

also observed in the strain (Figure 8(f)) and residual (Figure 9(c)) maps, and corresponded to two symmetrically propagating cracks.

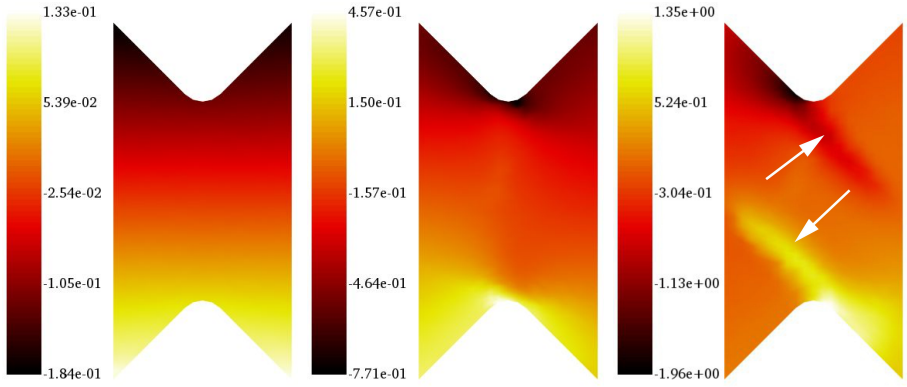

(a) $F = 5.4\text{kN}, \epsilon_{xz} = 0.37\%$ **(b)** $F = 8.71\text{kN}, \epsilon_{xz} = 48.7\%$ **(c)** $F = 5.1\text{kN}, \epsilon_{xz} = 92.2\%$

Fig. 7: Measured axial displacements for test E3. The arrows indicate the location of cracks. The displacements are expressed in mm

Figure 8 shows the measured shear strain fields. Similarly to the previous two tests, the strain distribution in elasticity (Figure 8(a)) and in the transition to plasticity (Figure 8(b)) was essentially uniform. Furthermore, the achieved strain levels were at least one order of magnitude higher than the noise floor levels (Table 3). No damage was detected in the correlation residual map (Figure 9(a)). Furthermore, a single strained band developed between the V notches (Figure 8(c)). Comparing the strain levels achieved for approximately equal loads, tests E3 (Figure 8(c)) and E2 (Figure 22(d)) led similar values, which further confirmed that no buckling occurred in test E2 at that point. Overall, larger strain levels were reached in test E3 in comparison to tests E1 and E2.

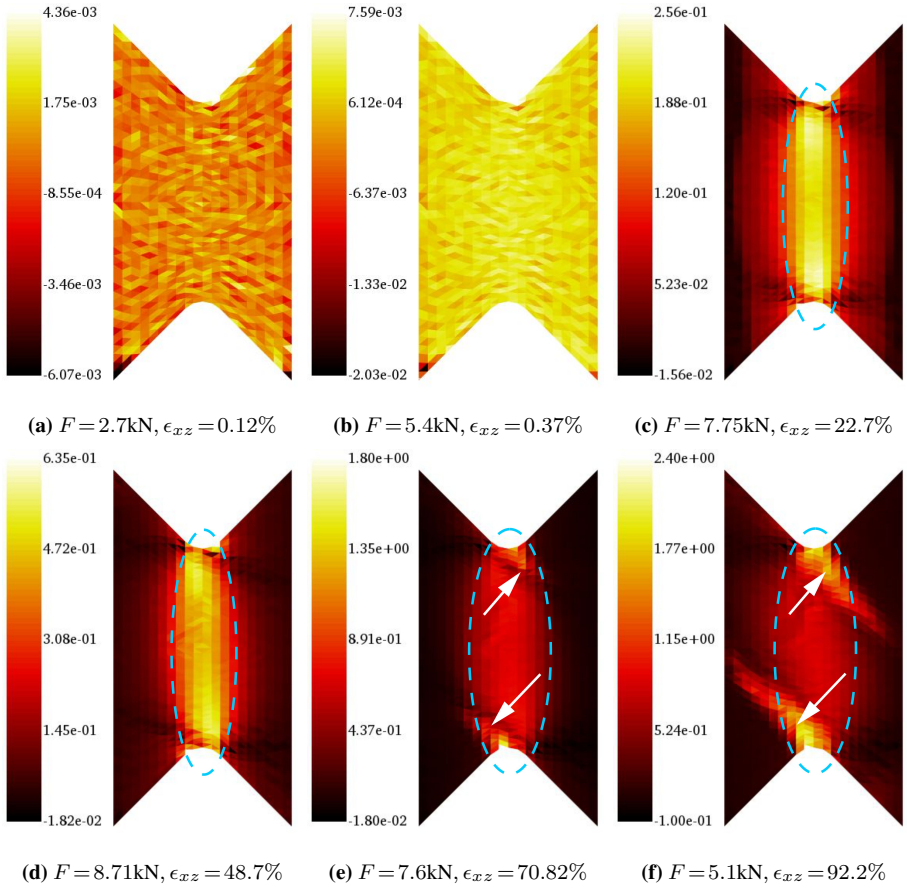

(a) $F = 2.7\text{kN}, \epsilon_{xz} = 0.12\%$ **(b)** $F = 5.4\text{kN}, \epsilon_{xz} = 0.37\%$ **(c)** $F = 7.75\text{kN}, \epsilon_{xz} = 22.7\%$

(d) $F = 8.71\text{kN}, \epsilon_{xz} = 48.7\%$ **(e)** $F = 7.6\text{kN}, \epsilon_{xz} = 70.82\%$ **(f)** $F = 5.1\text{kN}, \epsilon_{xz} = 92.2\%$

Fig. 8: Measured ϵ_{xz} strain fields for test E3. The strained band is outlined by dashed blue ellipses, whereas the location of the cracks are indicated by arrows

For the highest load level, the corresponding strain level was equal to 48.7% (Figure 8(d)). Very high gradients were observed in the strain fields (see Figures 8(e-f)), which were also present in axial displacement fields (Figure 7(c)) and correlation residual maps (Figure 9(b-c)). These "discontinuities" correspond to initiated and growing cracks. Since the sample had a tendency toward buckling, slight folding occurred in the center of the ROI, which caused changes in brightness (*i.e.,* shadows). These changes in brightness were

observed as an increase in the correlation residuals in the ROI center (Figure 9(b-c)). The correlation residuals are sensitive to damage initiation and growth [37]. Observing the correlation residual maps allowed mesocracks to be detected and quantified (*i.e.,* symmetric initiation and propagation of two cracks from each V-notch, see Figure 9(c)). Last, comparing the correlation residual maps with the final deformed shape of the sample (Figure 5(c)) shows a good agreement for the location and size of the cracks.

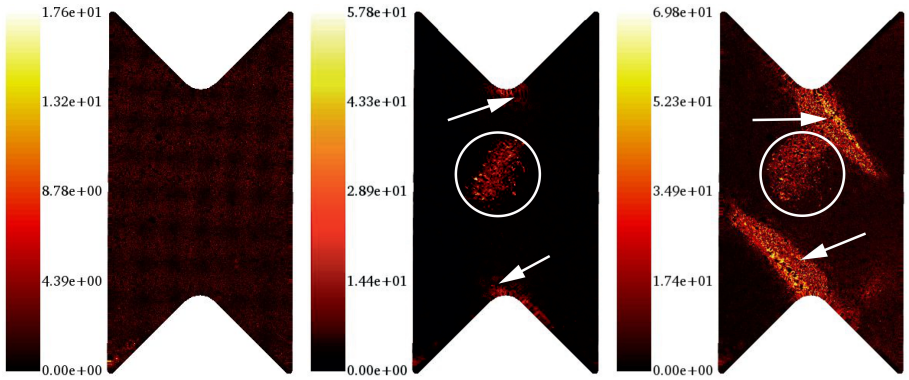

(a) $F = 5.4$kN, $\epsilon_{xz} = 0.37\%$ **(b)** $F = 8.71$kN, $\epsilon_{xz} = 48.7\%$ **(c)** $F = 5.1$kN, $\epsilon_{xz} = 92.2\%$

Fig. 9: Correlation residual maps for test E3. The residuals are expressed in % of the dynamic range of the reference pictures. The arrows indicate the location of propagating cracks, whereas the white circle outlines the change in brightness as a result of limited buckling

3.6 Test E4

Figure 5(d) shows the loading history of test E4. This test consisted of 8 loading/unloading cycles. The 10-mm thick supports were utilized in addition to a relaxed connection between the MAF and the testing machine since it allowed buckling of the sample to be avoided. Observing the final deformed shape (Figure 5(c)), it was concluded that the sample remained

flat throughout the whole experiment. This observation was an additional validation of the usefulness of the anti-buckling device used herein.

Figure 10 displays measured out-of-plane displacement fields for test E4. Since the same configuration (*i.e.,* PMMA supports and relaxed connection between the MAF and the testing machine) was employed in tests E3 and E4, it was expected (and confirmed) that no notable out-of-plane displacements occurred. Furthermore, the displacement levels in elasticity (Figure 10(a)) and early plasticity (Figure 10(b)) were very small as was the case in test E3. Moreover, negligible out-of-plane displacement amplitudes were observed in the whole experiment. However, as was also the case for test E3, the sample had a tendency toward buckling, which was prevented thanks to the additional supports. This phenomenon led to non-uniform distributions of out-of-plane displacements (Figures 10(c-f)).

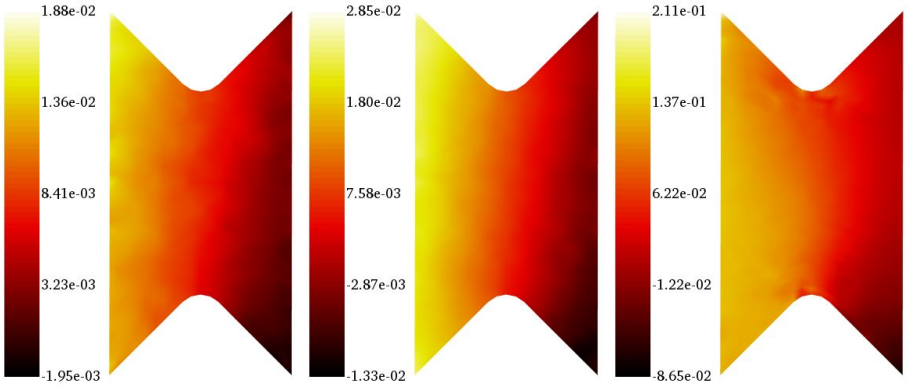

(a) $F = 4.83\text{kN}, \epsilon_{xz} = 0.25\%$ **(b)** $F = 5.44\text{kN}, \epsilon_{xz} = 0.3\%$ **(c)** $F = 8\text{kN}, \epsilon_{xz} = 26.5\%$

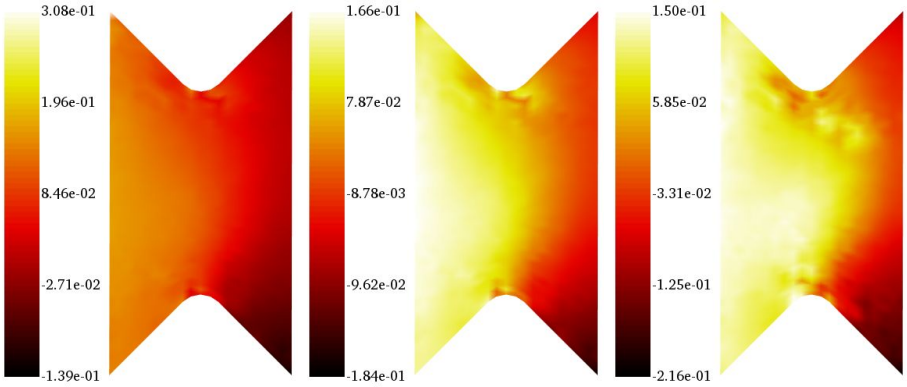

(d) $F = 8.55\text{kN}, \epsilon_{xz} = 39.8\%$ **(e)** $F = 8.65\text{kN}, \epsilon_{xz} = 47.4\%$ **(f)** $F = 8\text{kN}, \epsilon_{xz} = 68.1\%$

Fig. 10: Measured out-of-plane displacement fields for test E4. The displacements are expressed in mm

The measured axial displacement fields revealed the rotation of the ROI (Figure 11). Such rotation was also observed for test E3. Furthermore, the levels of axial displacements achieved in this test (Figure 11(a-b)) were comparable to those of test E3. Additionally, "discontinuities" arose at the roots of both V notches (Figure 11(c)). However, compared to test E3, the present discontinuities were of different sizes, which will be discussed in the sequel.

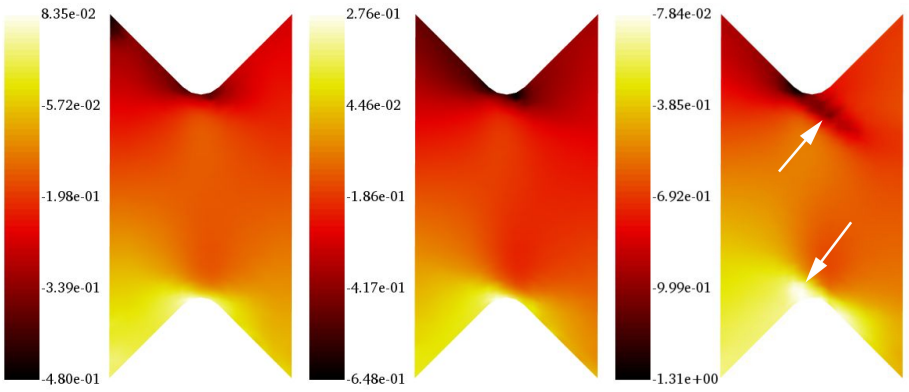

(a) $F = 8\text{kN}, \epsilon_{xz} = 26.5\%$ **(b)** $F = 8.65\text{kN}, \epsilon_{xz} = 47.4\%$ **(c)** $F = 8\text{kN}, \epsilon_{xz} = 68.1\%$

Fig. 11: Measured axial displacements for test E4. The arrows indicate the locations of the cracks. The displacements are expressed in mm

Figure 12 shows the measured shear strain fields. The shear strains were uniformly distributed at the peaks of the second and third cycles (Figure 12(a-b)). A strained band subsequently developed between the V-notches (Figures 12(c-e)) as in the previous tests. For approximately equal loads, the strain levels achieved for test E4 (Figure 12(c)) were comparable to those of tests E3 (Figure 8(c)) and E2 (Figure 22(d)), further substantiating that no buckling occurred at that point. The "discontinuity" observed in Figure 12(f) corresponded to the same phenomenon shown in Figures 11(c) and Figure 13(c), namely, the location of propagating cracks. Moreover, values for approximately equal loads (*i.e.,* 8 kN) for tests E4 (Figure 12(f)) and E3 (Figure 12(e)) were comparable.

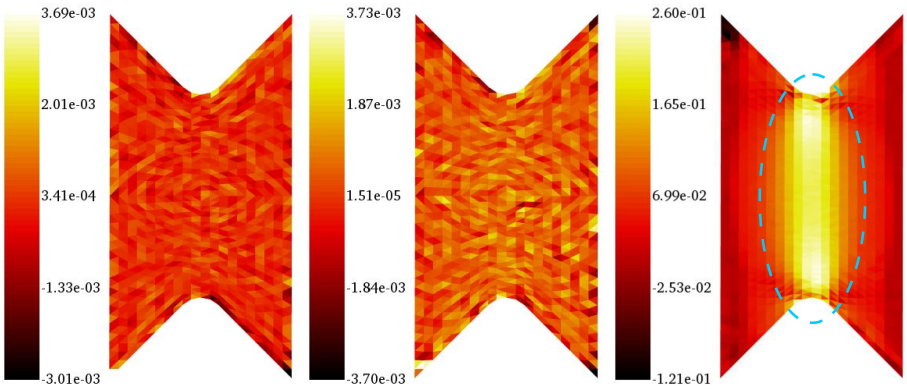

(a) $F = 4.83\text{kN}, \epsilon_{xz} = 0.25\%$ **(b)** $F = 5.44\text{kN}, \epsilon_{xz} = 0.3\%$ **(c)** $F = 8\text{kN}, \epsilon_{xz} = 26.5\%$

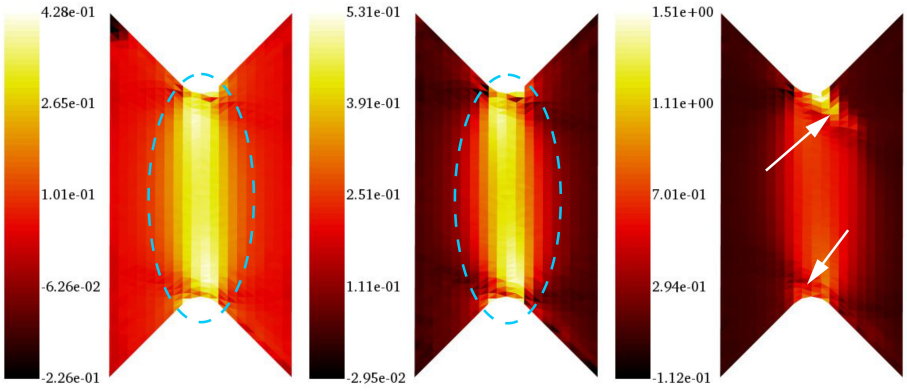

(d) $F = 8.55\text{kN}, \epsilon_{xz} = 39.8\%$ **(e)** $F = 8.65\text{kN}, \epsilon_{xz} = 47.4\%$ **(f)** $F = 8\text{kN}, \epsilon_{xz} = 68.1\%$

Fig. 12: Measured ϵ_{xz} strain fields for test E4. The strained band is outlined by blue ellipses, whereas the location of strain discontinuities (*i.e.,* cracks) are indicated by arrows

The rises in correlation residuals observed in Figure 13(a-b)) were attributed to speckle pattern smearing due to the motion of the PMMA supports with respect to the sample surface. Furthermore, the increase in correlation residuals on the edges of the ROI were attributed to speckle pattern smearing due to overly tightened PMMA plates. Since the sample exhibited a tendency toward buckling, the central part of the plates was subjected to bending thus increasing the contact pressure on the edges of the sample. For test E3, two cracks initi-

ated approximately at the same time and propagated symmetrically (Figure 9(c)). However, for test E4, the crack located at the top V-notch (Figure 13(c)) initiated earlier than that at the lower V-notch thus propagating farther.

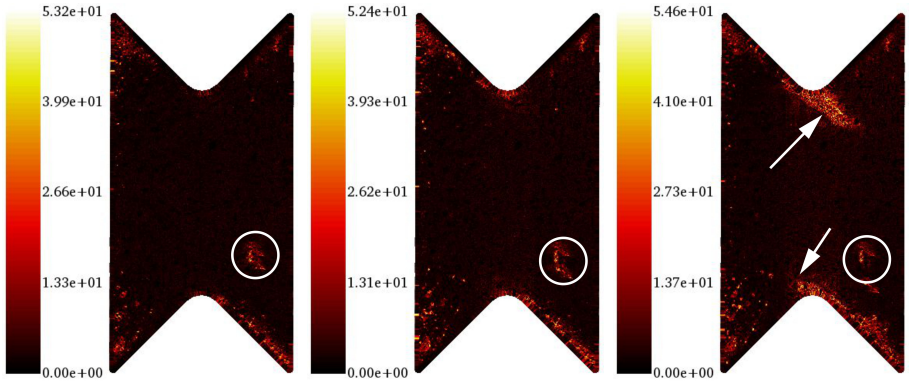

(a) $F = 8\text{kN}, \epsilon_{xz} = 26.5\%$ **(b)** $F = 8.65\text{kN}, \epsilon_{xz} = 47.4\%$ **(c)** $F = 8\text{kN}, \epsilon_{xz} = 68.1\%$

Fig. 13: Correlation residual maps for test E4. The residuals are expressed in % of the dynamic range of the reference pictures. The arrows indicate the location of propagating cracks. The white circles outline smearing of the speckle pattern on the surface due to relative motions of the sample surface with respect to the PMMA supports

3.7 Discussion

In this section, the global response is compared for each test presented in the previous sections. In order to calculate the engineering stress, the measured force for each experiment was divided by the initial cross-sectional area S_0 between the V notches of the corresponding sample. The respective stress-strain curves are shown in Figure 14.

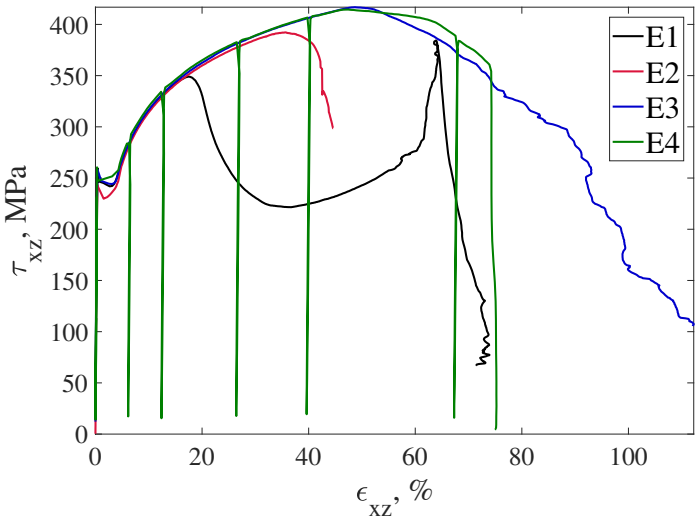

Fig. 14: Macroscopic stress/strain responses of the four analyzed tests

A good agreement in terms of global response is observed until instability inception due to buckling. Test E1 was stable up to 17% shear strain, which was proven by the measured out-of-plane displacement fields reported in Figure 19. Until this critical state, the magnitude of out-of-plane displacements was low. Since buckling occurred in test E1, additional supports were applied in test E2. A good reproducibility is observed for the global response between tests E2, E3 and E4 up to 34% shear strain. The instability in test E2 was due to the large level of preload (*i.e.,* the connection between the MAF and the test machine was very stiff). No instability was observed for tests E3 and E4 (*i.e.,* no buckling was noted when the connection between the MAF and the test machine was loosened and thicker supports were utilized). Furthermore, the agreement between tests E3 and E4 further validated the proposed setup for cyclic loadings.

Table 4 gathers characteristic values for each experiment. Similar yield stresses were observed regardless of the employed configuration. It was concluded that instability initiated

in the plastic regime. Furthermore, the highest ultimate load was achieved in tests E3 and E4 for a corresponding shear strain of 48%, and an ultimate shear strength of 417 MPa. A good reproducibility between the reported quantities for tests E3 and E4 was noted, which fully validated the third configuration. With the application of the PMMA plates onto sample E2, buckling was delayed, thereby leading to a 43 MPa higher ultimate shear strength compared to test E1. With thicker supports and loosened connection, the ultimate strength further increased by 25 MPa compared to test E2. The resulting shear strains at the ultimate load are 10-30% higher for tests E3 and E4 compared to tests E2 and E1, respectively.

Table 4: Characteristic values for the four shear tests on the Modified Arcan Fixture

Test	Yield stress, MPa	Ultimate shear strength, MPa	Ultimate load, kN	Shear strain at ultimate load, %
E1	259	349	7.3	17.5
E2	243	392	8.2	35.6
E3	258	417	8.71	48.7
E4	261	417	8.66	47.4

4 Analysis of friction between PMMA plates and the sample

In this section, the influence of friction between the PMMA plates and the sample surfaces is reviewed and discussed. It was assumed that the effect of friction was small since all experiments displayed identical responses before buckling occurred (Figure 5). Further, the speckle pattern did not degrade too much since sterecorrelation could be run until the end of each test. During the installation of the PMMA supports, the six M6 bolts were not tightened in order to minimize friction and contact pressure between the sample surface and the plates. In the following, a numerical study is presented for more quantitative evaluations of the effect of friction.

4.1 Parameter calibration

In order to numerically describe the material behavior during mechanical tests, reliable parameters are needed. FEMU was employed to calibrate the sought parameters for test E3. The material model used in the identification procedure was implemented in the commercial software *Abaqus*. Nonlinear kinematic hardening follows Armstrong-Frederick's model [38]. Thus, the sought parameters were the yield stress σ_y, hardening modulus C, and nonlinear coefficient c.

Within FEMU frameworks, differences between measured and computed quantities are minimized by iteratively updating the material parameters based on sensitivity fields [39]. If only the measured displacement fields are considered (*i.e.,* FEMU-U), the cost function is expressed as the squared error between measured $\{\mathbf{u}_m\}$ and computed $\{\mathbf{u}_c\}$ nodal displacements

$$\chi_u^2(\{\mathbf{p}\}) = \frac{1}{\gamma_u^2 N_u} \left\| \{\mathbf{u}_m\} - \{\mathbf{u}_c\} \right\|^2, \tag{1}$$

where $\{\mathbf{p}\}$ is the column vector gathering all unknown material parameters, γ_u the standard displacement uncertainty, and N_u the number of kinematic degrees of freedom [40]. With such setting, χ_u tends to 1 when the only source of error is due to measurement uncertainty. Any deviation from 1 is an indication of model error.

The identification procedure can also be conducted with respect to measured loads $\{\mathbf{F}_m\}$ and computed reaction forces $\{\mathbf{F}_c\}$ (FEMU-F) extracted from edges where Dirichlet boundary conditions are prescribed

$$\chi_F^2(\{\mathbf{p}\}) = \frac{1}{\gamma_F^2 N_F} \left\| \{\mathbf{F}_m\} - \{\mathbf{F}_c\} \right\|^2, \tag{2}$$

where γ_F is the standard uncertainty of the load cell, and N_F the number of load data.

The combination of the aforementioned cost functions (*i.e.,* FEMU-UF) is expressed as

$$\chi^2_{tot} = (1-\omega)\chi^2_u + \omega\chi^2_F, \tag{3}$$

where the parameter ω determines the contribution of each individual cost function. For the present study, the latter was set to $\omega = 0.5$, which endowed each cost function with equal weight.

The FE mesh used in the identification procedure was constructed from the measurement mesh (Figure 4). It was converted into four-noded quadrilateral (Q4) elements, and then extruded to obtain C3D8 elements with reduced integration (C3D8R). The measured displacements were prescribed along the stressed edges of the mesh as Dirichlet boundary conditions (Figure 16(a)). The elastic parameters (*i.e.,* Young's modulus E and Poisson's ratio ν) were kept constant and equal to their nominal values (Table 5). Only the aforementioned plastic parameters were calibrated.

Table 5: Identification results via FEMU-UF

	E, GPa	ν, -	σ_{Y}, MPa	C, GPa	c, -	χ_{U}	χ_{F}
Initial	210	0.25	250	6000	15	35	116
Identified	210	0.25	365	4635	13	23	11

Once calibrated, the parameters yielded significant decreases in both displacement and force residuals (Table 5). Furthermore, the identification resulted in a very good agreement between the global reaction forces extracted from the FE model and the measured forces (Figure 15), which led to residuals that were on average only 11 times the uncertainty level. However, in elasticity, the computed response was slightly offset from the measured curve. This trend is believed to be due to the fact that the Dirichlet boundary conditions had to

be extruded. The identified material parameters reported in Table 5 were used in further numerical simulations. The calibrated value of the yield stress was higher than the expected value estimated from the *macroscopic* stress-strain curve (Figure 14). This difference was due to the fact that even in the elastic regime, the stress state was not uniform in the ligament.

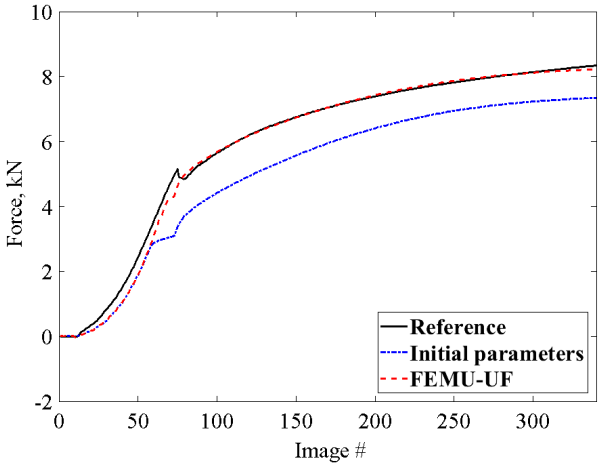

Fig. 15: Comparison between measured and resultant forces extracted from the FE model of test E3

4.2 Effect of friction

The effect of friction was studied via complete FE simulations of test E3 with the two PMMA plates. The sample was again discretized with C3D8R elements, and the PMMA plates with C3D4 tetrahedra. The boundary conditions on the model were the same as in the identification procedure. However, rigid body out-of-plane motions were eliminated. Bolts were replaced by a combination of kinematic coupling and connector elements (CONN3D2, type = beam). Bolt heads were replaced with kinematic couplings (Figure 16(b) depicted by blue lines) on the PMMA surfaces around the bolt holes, while the bolt shaft was simu-

lated with connector elements. The master nodes of the kinematic coupling were attached with the connector elements, which ensured stiff connections between nodes. Since the bolts were not pre-loaded, the bolt pretension was not simulated. All out-of-plane motions were disabled in the the master nodes of the kinematic couplings for both PMMA plates. Furthermore, for a single master node, the remaining displacements and all rotations (Figure 16(b) depicted by the red dot) were disabled to suppress the rigid body motions of the plates. The plates were assumed to remain elastic (with a 3 GPa Young's modulus and 0.3 Poisson's ratio). Between the sample and PMMA surfaces, general contact was defined with Coulomb friction [41]. Since damage initiation and growth was out of the scope of this work, the simulations were carried out only for the first 330 time steps (Figure 5(c)) of the experiment (*i.e.,* before damage occurred).

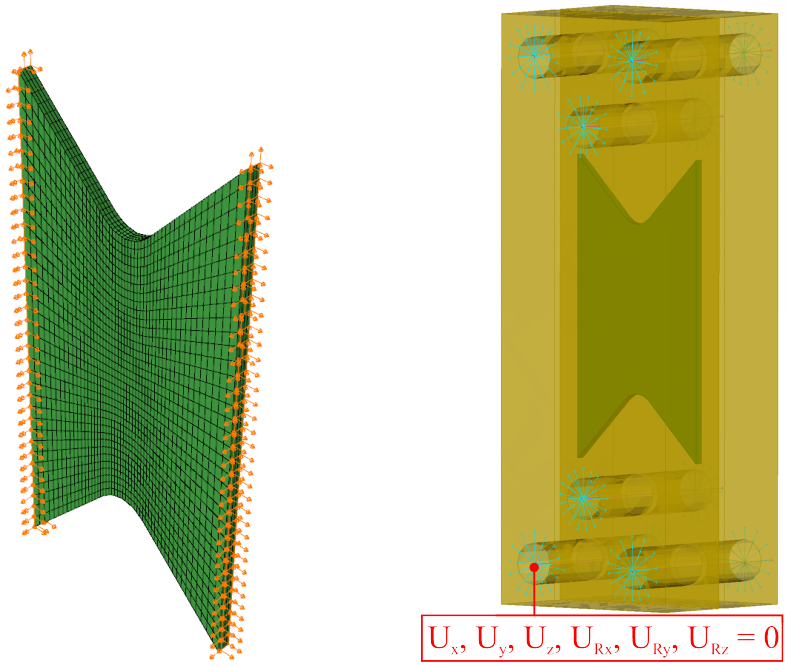

Fig. 16: FE model of test E3. (a) E3 sample with prescribed measured displacements as boundary conditions. (b) Assembly of sample E3 and PMMA plates

It was expected that the resultant forces extracted from the stressed edges of the model were sensitive to friction. In the available literature, the reported values of friction coefficient between PMMA and steel vary [42, 43, 44, 45]. However, the estimated levels generally range from 0.3 to 0.4. First, FEMU-UF was run to calibrate plastic parameters for a very low friction coefficient (*i.e.,* $\mu = 0.01$). The calibrated parameters are reported in Table 6; they were similar to those obtained previously even though the boundary conditions were different (Table 5). The calibrated material parameters were then used to initialize the second FEMU-UF analysis where, additionally, the friction coefficient was sought. The initial value was set to $\mu = 0.3$, which corresponded to the lower bound found in the surveyed

literature. The parameters calibrated along with μ all decreased (the hardening modulus C experienced the largest relative reduction). The global residual χ_{tot} (Equation (3)) only slightly decreased.

Table 6: Identification results for low friction value and calibrated material parameters and friction coefficient μ

	E, GPa	ν, -	σ_Y, MPa	C, MPa	c, -	χ_{tot}	$\delta\overline{\sigma}$, MPa
$\mu = 0.01$	210	0.25	365	4616	13.1	43	-
$\mu = 0.33$	210	0.25	357	3860	11.8	42.6	38

To further illustrate the effect of friction on the calibrated parameters, a uniaxial tensile loading was applied to a single C3D8R element. Dirichlet boundary conditions were prescribed on four surface nodes of the cube (denoted by arrows in Figure 17(a)), whereas on the opposite surface, both rigid body displacements and rotations were disabled. The prescribed displacements ranged from 0 to 0.47 times the element height with a step size of 0.001 (*i.e.,* corresponding to the strain levels obtained via the DIC virtual gauge before damage occurred). The differences between stresses for the frictionless (reference) case (*i.e.,* $\mu = 0.01$) and for the calibrated value ($\mu = 0.33$) were not monotonic with respect to the strain level. The mean stress difference $\delta\overline{\sigma}$ was equal to 38 MPa (Figure 17(b)), which indicated that friction had a non negligible effect on the calibrated kinematic hardening parameters.

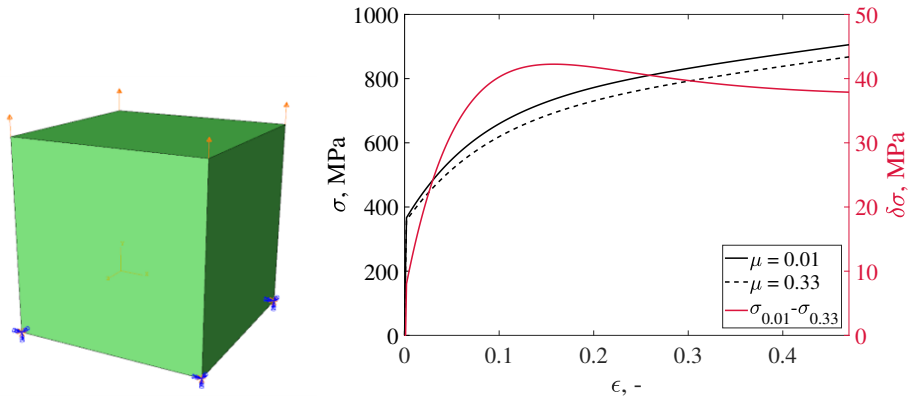

Fig. 17: (a) Cube element used for depicting the tensile response with the calibrated parameters (Table 6) and the corresponding boundary conditions. (b) Stress-strain curves calculated for $\mu = 0.01$ and $\mu = 0.33$ with the respective material parameters (black curves) and corresponding stress differences (red curve)

From the numerical simulation with the calibrated material parameters and friction coefficient, the stress triaxiality fields were evaluated. In Figure 18, the triaxiality field is displayed for the last analyzed image when $\mu = 0.33$. From the triaxiality field, it was concluded that the gauge area was predominantly subjected to shear stresses (*i.e.,* stress triaxialities close to zero). This result was observed for the central points through the thickness (*i.e.,* points 1,2 and 3), which displayed slight deviations in stress triaxialities yet close to zero. This trend was observed for all analyzed images. For the chosen points in the root of the V notch, the stress triaxiality changed significantly with the applied shear strain. For low shear strains, the stress triaxiality was closer to zero (*i.e.,* shear stress state). At the root of the V notch, complex stress states were expected, which were observed from the deviation of the middle point (*i.e.,* point 5), whereas the surface points had almost identical

levels. Moreover, the areas around the V notch where the material was subjected to tensile stresses (*i.e.,* stress triaxiality close to 0.33) corresponded to the locations of initiated cracks (Figure 5(c)).

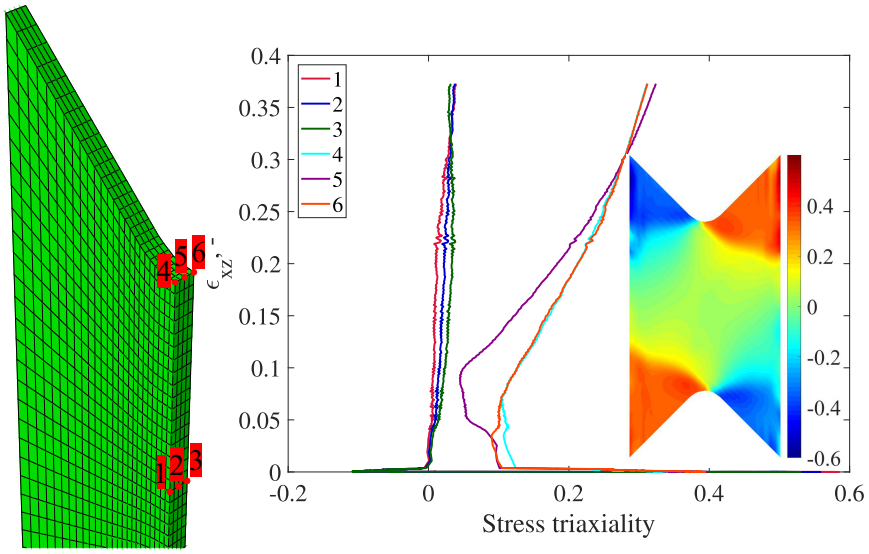

Fig. 18: Stress triaxiality history for six different points with respect to the calculated shear strain in the virtual gauge and the triaxiality field for the last computed image (*i.e.,* frame 330) when $\mu = 0.33$

5 Conclusion

The experimental campaign performed herein was aimed at preventing buckling to occur in thin (*i.e.,* 1 mm) butterfly samples under simple shear loading on a modified Arcan fixture (MAF). Three monotonic shear tests and one additional cyclic test were carried out. They were monitored with a stereovision system, and the kinematic fields were measured by means of FE-based stereocorrelation. Three different configurations of the experimental setup were studied considering anti-buckling devices and connection stiffness between the

MAF and the testing machine. Furthermore, friction between the anti-buckling device and the sample was evaluated and subsequently calibrated via FEMU-UF. The main results of this work are:

- shear buckling was successfully suppressed for Arcan butterfly samples with a large gauge area using the thickest anti-buckling device,
- FEMU using measured displacements prescribed as Dirichlet boundary conditions on the FE model was carried out to calibrate kinematic hardening parameters,
- the influence of the friction coefficient on the calibrated material parameters was studied using a numerical model of the sample and the anti-buckling device,
- the friction coefficient between the PMMA anti-buckling device and the sample surface could also be calibrated ($\mu = 0.33$).

Last, a detailed analysis of the prescribed boundary conditions on the FE model of the butterfly sample may provide optimal routes to avoid complex numerical simulations (*i.e.,* modeling of the sample and the anti-buckling device).

Acknowledgements

This work was performed within the FULLINSPECT project supported by the Croatian Science Foundation (UIP-2019-04-5460 Grant). The authors also acknowledge and thank EikoSim for providing the EikoTwin DIC software to conduct the stereocorrelation analyses reported herein.

6 Compliance with Ethical Standards

The authors have no conflict of interest to declare.

References

1. Tisza M (2005) Numerical modeling and simulation in sheet metal forming academic and industrial perspectives. Mater Sci Forum 473-474:407–414, 10.4028/www.scientific.net/MSF.473-474.407
2. Ghosh AK, Bae DG (2000) A planar simple shear test and flow behavior in a superplastic Al-Mg alloy. Metall Mater Trans 34(11):2465–2471, https://doi.org/10.1007/s11661-003-0006-3
3. Rauch EF (1998) Plastic anisotropy of sheet metals determined by simple shear tests. Mater Sci Eng A 241(1-2):179–183, https://doi.org/10.1016/S0921-5093(97)00486-3
4. Bouvier S, Haddadi H, Levée P, Teodosiu C (2006) Simple shear tests: Experimental techniques and characterization of the plastic anisotropy of rolled sheets at large strains. Journal of Materials Processing Technology 172(1):96–103, 10.1016/j.jmatprotec.2005.09.003
5. Abedini A, Noder J, Kohar CP, Butcher C (2020) Accounting for Shear Anisotropy and Material Frame Rotation on the Constitutive Characterization of Automotive Alloys using Simple Shear Tests. Mech Mater 148(April):103419, 10.1016/j.mechmat.2020.103419
6. Miyauchi K (1984) A proposal of a planar simple shear test in sheet metals. Sci Pap Inst Phys Chem Res 78(3):27–40
7. Peirs J, Verleysen P, Degrieck J (2012) Novel Technique for Static and Dynamic Shear Testing of Ti6Al4V Sheet. Exp Mech 52(7):729–741, 10.1007/s11340-011-9541-9
8. Roth CC, Mohr D (2016) Ductile fracture experiments with locally proportional loading histories. Int J Plast 79:328–354, 10.1016/j.ijplas.2015.08.004

9. ASTM (2005) ASTM B831-05, Standard Test Method for Shear Testing of Thin Aluminum Alloy Products, ASTM International, West Conshohocken, PA, 2005, https://doi.org/10.1520/B0831-05
10. Merklein M, Biasutti M (2011) Forward and reverse simple shear test experiments for material modeling in forming simulations. Special Edition: 10th International Conference on Technology of Plasticity, ICTP 2011 pp 702–707
11. Yin Q, Zillmann B, Suttner S, Gerstein G, Biasutti M, Tekkaya AE, Wagner MFX, Merklein M, Schaper M, Halle T, Brosius A (2014) An experimental and numerical investigation of different shear test configurations for sheet metal characterization. Int J Solids Struct 51(5):1066–1074, https://doi.org/10.1016/j.ijsolstr.2013.12.006
12. Bao Y, Wierzbicki T (2004) A comparative study on various ductile crack formation criteria. Journal of Engineering Materials and Technology, Transactions of the ASME 126(3):314–324, 10.1115/1.1755244
13. Reyes A, Eriksson M, Lademo OG, Hopperstad OS, Langseth M (2009) Assessment of yield and fracture criteria using shear and bending tests. Mater Des 30(3):596–608, 10.1016/j.matdes.2008.05.045
14. Roth CC, Mohr D (2018) Determining the strain to fracture for simple shear for a wide range of sheet metals. Int J Mech Sci 149:224–240, 10.1016/j.ijmecsci.2018.10.007
15. Roth CC, Mohr D (2015) Experimental investigation on shear fracture at high strain rates. EPJ Web Conf 94:3–6, 10.1051/epjconf/20159401078
16. Iosipescu N (1967) New Accurate Procedure for Single Shear Testing of Metals. J Mater 2(3):537–566
17. Mohr D, Henn S (2007) Calibration of stress-triaxiality dependent crack formation criteria: A new hybrid experimental-numerical method. Exp Mech 47(6):805–820, 10.1007/s11340-007-9039-7

18. Mohr D, Oswald M (2008) A new experimental technique for the multi-axial testing of advanced high strength steel sheets. Exp Mech 48(1):65–77, 10.1007/s11340-007-9053-9
19. Mohr D, Doyoyo M (2003) A new method for the biaxial testing of cellular solids. Exp Mech 43(2):173–182, https://doi.org/10.1007/BF02410498
20. Arcan M, Hashin Z, Voloshin A (1978) A method to produce uniform plane-stress states with applications to fiber-reinforced materials. Exp Mech 18(4):141–146, https://doi.org/10.1007/BF02324146
21. Dunand M, Mohr D (2011) Optimized butterfly specimen for the fracture testing of sheet materials under combined normal and shear loading. Eng Fract Mech 78(17):2919–2934, 10.1016/j.engfracmech.2011.08.008
22. Abedini A, Butcher C, Anderson D, Worswick M, Skszek T (2015) Fracture Characterization of Automotive Alloys in Shear Loading. SAE Int J Mater Manuf 8(3), 10.4271/2015-01-0528
23. Abedini A, Butcher C, Worswick MJ (2017) Fracture Characterization of Rolled Sheet Alloys in Shear Loading: Studies of Specimen Geometry, Anisotropy, and Rate Sensitivity. Exp Mech 57(1):75–88, 10.1007/s11340-016-0211-9
24. Peshekhodov I, Jiang S, Vucetic M, Bouguecha A, Berhens BA (2016) Experimental-numerical evaluation of a new butterfly specimen for fracture characterisation of AHSS in a wide range of stress states. IOP Conference Series: Materials Science and Engineering 159(1), 10.1088/1757-899X/159/1/012015
25. Boni S, G'Sell C, Weynant E, Haudin JM (1982) Microscopic in situ observation of the plastic deformation of polybutene-1 films under simple shear. Polym Test 3(1):3–24, https://doi.org/10.1016/0142-9418(82)90009-5

26. Pucillo GP, Grasso M, Penta F, Pinto P (2011) On the mechanical characterization of materials by Arcan-type specimens. Eng Fract Mech 78(8):1729–1741, https://doi.org/10.1016/j.engfracmech.2011.02.002
27. Grédiac M, Hild F (eds) (2012) Full-Field Measurements and Identification in Solid Mechanics. ISTE / Wiley, London (UK)
28. Pham CH, Adzima F, Coer J, Manach PY (2017) Anti-Buckling Device for Ultra-Thin Metallic Sheets Under Large and Reversed Shear Strain Paths. Exp Mech 57(4):593–602, https://doi.org/10.1007/s11340-017-0256-4
29. Bertin M, Hild F, Roux S (2017) On the identifiability of the Hill-1948 model with one uniaxial tensile test. Comptes Rendus Mécanique 345(6):363–369, https://doi.org/10.1016/j.crme.2017.04.001
30. Bertin M, Hild F, Roux S (2017) On the identifiability of Hill-1948 plasticity model with a single biaxial test on very thin sheet. Strain 53(5):e12233, https://doi.org/10.1111/str.12233
31. Dufour J, Beaubier B, Roux S, Hild F (2014) Displacement measurement using CAD-based stereo-correlation with meshes. In: ICEM conference, 10.1007/978-3-319-06986-9_34
32. Dubreuil L, Dufour JE, Quinsat Y, Hild F (2016) Mesh-based shape measurements with stereocorrelation. Experimental Mechanics 56(7):1231–1242, https://doi.org/10.1007/s11340-016-0158-x
33. Pierré JE, Passieux JC, Périé JN (2017) Finite Element Stereo Digital Image Correlation: Framework and Mechanical Regularization. Experimental Mechanics 57(3):443–456, https://doi.org/10.1007/s11340-016-0246-y
34. EikoSim Company (2020) EikoTwin DIC. https://eikosim.com/en/eikotwin-2/

35. Beaubier B, Dufour J, Hild F, Roux S, Lavernhe-Taillard S, Lavernhe-Taillard K (2014) CAD-based calibration of a 3D-DIC system: Principle and application on test and industrial parts. Experimental Mechanics 54(3):329–341, 10.1007/978-1-4614-4235-6_32
36. Dufour JE, Beaubier B, Hild F, Roux S (2015) CAD-based displacement measurements. Principle and first validations. Experimental Mechanics 55(9):1657–1668, https://doi.org/10.1007/s11340-015-0065-6
37. Hild F, Bouterf A, Roux S (2015) Damage Measurements via DIC. International Journal of Fracture 191(1-2):77–105, 10.1007/s10704-015-0004-7
38. Armstrong P, Frederick C (1966) A mathematical representation of the multiaxial bauschinger effect. CEGB Rep RD/B/N660
39. Tarantola A (1987) Inverse Problems Theory. Methods for Data Fitting and Model Parameter Estimation. Elsevier Applied Science, Southampton (UK)
40. Mathieu F, Leclerc H, Hild F, Roux S (2015) Estimation of elastoplastic parameters via weighted FEMU and integrated-DIC. Experimental Mechanics 55(1):105–119
41. Coulomb C (1821) Theorie des machines simples (in French). Bachelier, Paris (France)
42. Rabbe LM, Rieu J, Lopez A, Combrade P (1994) Fretting deterioration of orthopaedic implant materials: Search for solutions. Clin Mater 15:221–226, 10.1016/0267-6605(94)90049-3
43. Nuño N, Amabili M, Groppetti R, Rossi A (2001) Static coefficient of friction between Ti-6A1-4V and PMMA for cemented hip and knee implants. J Biomed Mater Res 59(1):191–200, 10.1002/jbm.1233
44. Lim A, Castagne S, Wong CC (2014) Effect of Friction Coefficient on Finite Element Modeling of the Deep - Cold Rolling Process. In: Int. Conf. Shot Peen., pp 376–380
45. Nuño N, Groppetti R, Senin N (2006) Static coefficient of friction between stainless steel and PMMA used in cemented hip and knee implants. Clin Biomech 21(9):956–

962, 10.1016/j.clinbiomech.2006.05.008

Appendix A

This appendix gathers stereocorrelation results of tests E1 and E2 that enabled for the improvements utilized in tests E3 and E4.

6.1 Test E1

Figure 19 shows out-of-plane displacement fields for different load levels (Figure 5(a)) and strain values. Positive displacements are oriented away from the reader. Low out-of-plane displacements were measured in the elastic regime of the sample (Figure 19(a)). Furthermore, the inception of plasticity (Figure 19(b)) was also characterized by small out-of-plane displacements. However, for the 7.2-kN load level (*i.e.,* the first peak on the load-time plot of Figure 5), the out-of-plane displacement amplitudes increased. This growing trend continued while further loading the sample. Furthermore, the out-of-plane displacement distribution was symmetric, which was also observed on the deformed sample in Figure 5(a). The aforementioned symmetry was observed in the displacement levels (*i.e.,* displacement amplitudes were similar in Figure 19(d-f)). Even though a stereovision system was employed, these high levels of measured displacement were not considered reliable since the out-of-plane rotation of the ROI caused some parts to be out of focus.

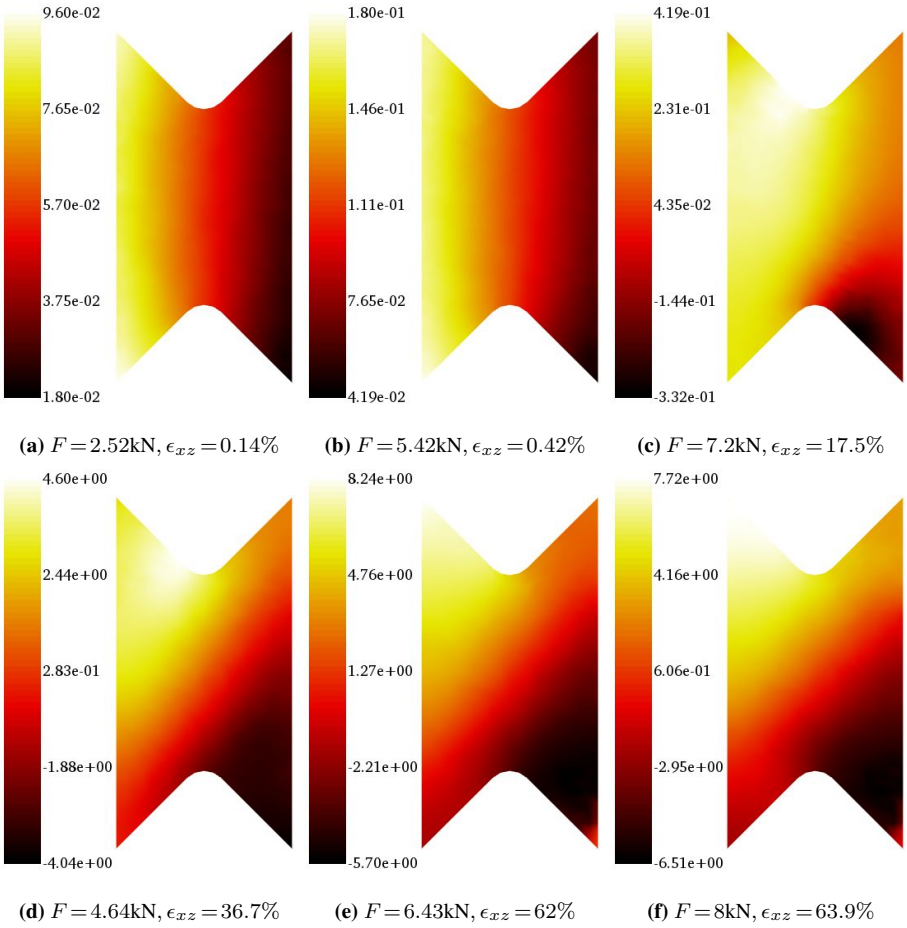

(a) $F = 2.52\text{kN}, \epsilon_{xz} = 0.14\%$ **(b)** $F = 5.42\text{kN}, \epsilon_{xz} = 0.42\%$ **(c)** $F = 7.2\text{kN}, \epsilon_{xz} = 17.5\%$

(d) $F = 4.64\text{kN}, \epsilon_{xz} = 36.7\%$ **(e)** $F = 6.43\text{kN}, \epsilon_{xz} = 62\%$ **(f)** $F = 8\text{kN}, \epsilon_{xz} = 63.9\%$

Fig. 19: Measured out-of-plane displacement fields for test E1. The displacements are expressed in mm. F denotes the applied load, and ϵ_{xz} the average shear strain calculated with the optical gauge

Figure 20 shows measured shear strain fields for different load levels (Figure 5(a)). The average strain levels in elasticity (Figure 20(a)) and at the inception of plasticity (Figure 20(b)) were low as expected. Furthermore, a single strained band developed between the V notches where the strain levels were one order of magnitude higher than on the edges of

the ROI (Figure 20(c)). The rotation of the ROI due to buckling is observed in Figure 20(d). Further measurements (Figure 20(e-f)) were deemed unreliable.

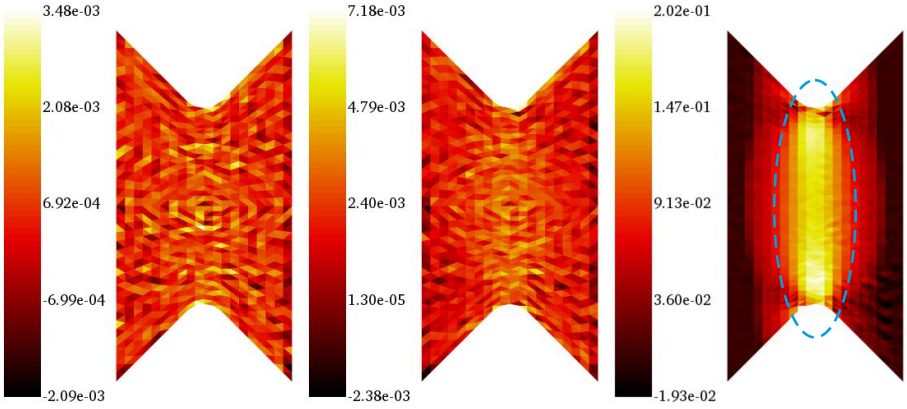

(a) $F = 2.52\text{kN}, \epsilon_{xz} = 0.14\%$ **(b)** $F = 5.42\text{kN}, \epsilon_{xz} = 0.42\%$ **(c)** $F = 7.2\text{kN}, \epsilon_{xz} = 17.5\%$

(d) $F = 4.64\text{kN}, \epsilon_{xz} = 36.7\%$ **(e)** $F = 6.43\text{kN}, \epsilon_{xz} = 62\%$ **(f)** $F = 8\text{kN}, \epsilon_{xz} = 63.9\%$

Fig. 20: Measured ϵ_{xz} strain fields for test E1. F denotes the applied load, and ϵ_{xz} the average shear strain calculated via the virtual sensor. The strained band is outlined by a dashed blue ellipse

Test E2

Figure 21 shows measured out-of-plane displacements for characteristic load levels (Figure 5(b)) and strain values. As for test E1, the out-of-plane displacements were very small in the elastic regime (Figure 21(a)) as well as for a large part of the plastic regime (Figure 21(b-d)). However, clear signs of buckling initiation were observed (Figure 21(e-f)). The displacements in the center of the sample were negative, whereas on the opposite corners they were positive. This result indicated that wrinkling had started, and was also observed from the shape of the deformed sample in (Figure 5(b)). The PMMA support fractured due to increased buckling. Thus, stereocorrelation results were no longer deemed reliable beyond this point.

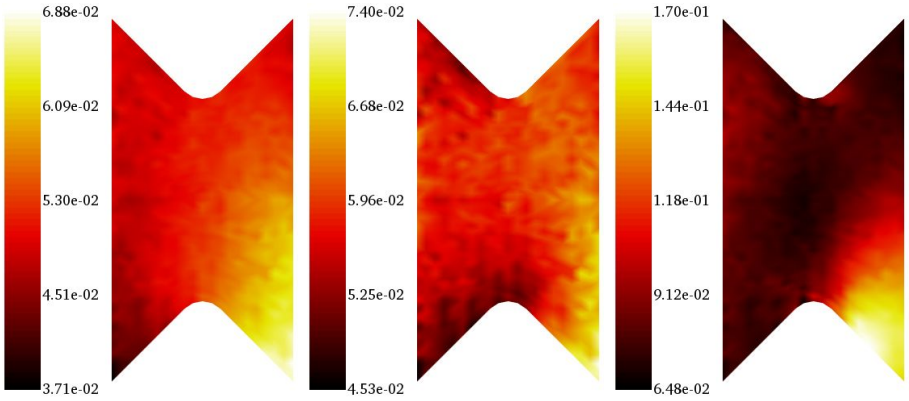

(a) $F = 1.94$kN, $\epsilon_{xz} = 0.09\%$ **(b)** $F = 5$kN, $\epsilon_{xz} = 0.34\%$ **(c)** $F = 6.7$kN, $\epsilon_{xz} = 11\%$

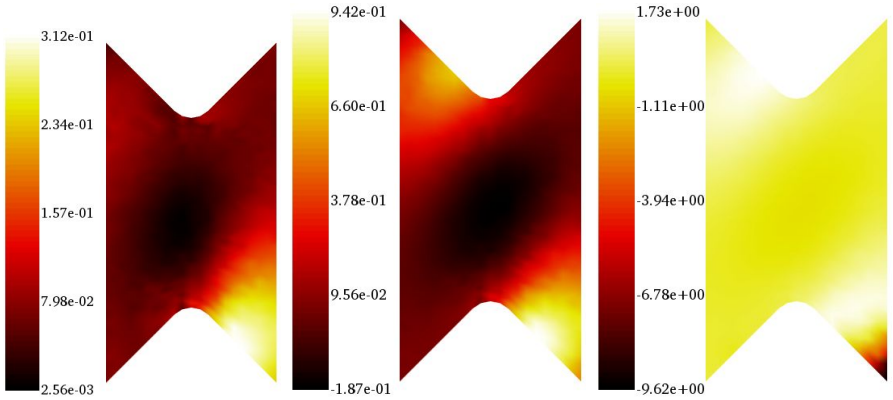

(d) $F = 7.6$kN, $\epsilon_{xz} = 22\%$ **(e)** $F = 8.2$kN, $\epsilon_{xz} = 35.5\%$ **(f)** $F = 7.85$kN, $\epsilon_{xz} = 41.4\%$

Fig. 21: Measured out-of-plane displacement fields for test E2. The displacements are expressed in mm

Figure 22 displays measured shear strain fields. Since buckling of the sample was delayed, the material response (*i.e.,* strain fields) was captured more reliably. Since only elastic strains were present in Figure 22(a-b), they were rather evenly distributed over the ROI, and were at least one order of magnitude higher than the noise floor levels (Table 3). Furthermore, a single strained band developed between the two V notches (Figure 22(c)) and was observed until the end of the test (Figure 22(d-e)). Comparing strains between tests E2 and

E1, higher levels were achieved due to the more stable material response thanks to the additional supports.

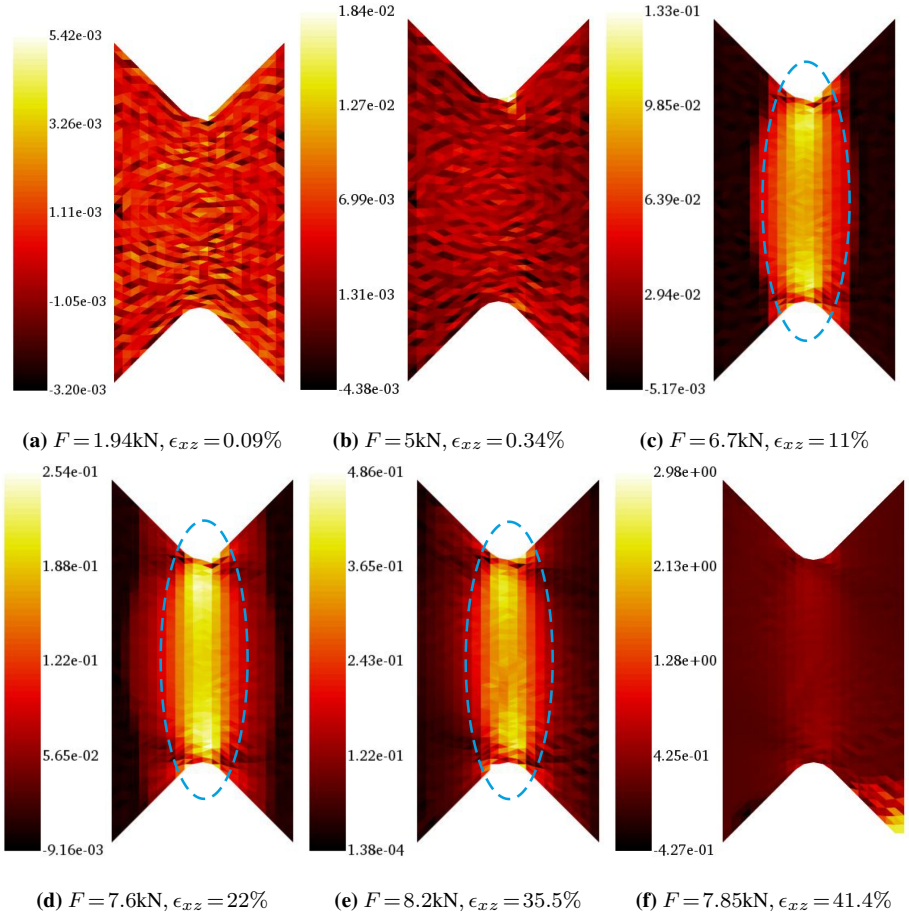

(a) $F = 1.94\text{kN}, \epsilon_{xz} = 0.09\%$ **(b)** $F = 5\text{kN}, \epsilon_{xz} = 0.34\%$ **(c)** $F = 6.7\text{kN}, \epsilon_{xz} = 11\%$

(d) $F = 7.6\text{kN}, \epsilon_{xz} = 22\%$ **(e)** $F = 8.2\text{kN}, \epsilon_{xz} = 35.5\%$ **(f)** $F = 7.85\text{kN}, \epsilon_{xz} = 41.4\%$

Fig. 22: Measured ϵ_{xz} strain fields for test E2. The strained band is outlined by dashed blue ellipses

Scientific paper 3

A. Zaplatić, A. Vrgoč, Z. Tomičević, and F. Hild, “Boundary condition effect on the evaluation of stress triaxiality fields,” Int J Mech Sci, vol. 246, May 2023, doi: 10.1016/j.ijmecsci.2023.108127.

Preprint of the published journal article.

Boundary condition effect on the evaluation of stress triaxiality fields

Andrija Zaplatić, Ana Vrgoč, Zvonimir Tomičević, François Hild

Boundary Condition Effect on the Evaluation of Stress Triaxiality Fields

Andrija Zaplatić[a,b], Ana Vrgoč[a,b], Zvonimir Tomičević[a,*], François Hild[b]

[a] *University of Zagreb, Faculty of Mechanical Engineering and Naval Architecture*
10002 Zagreb, Croatia
[b] *Université Paris-Saclay, CentraleSupélec, ENS Paris-Saclay, CNRS*
LMPS - Laboratoire de Mécanique Paris-Saclay, 91190 Gif-sur-Yvette, France

Abstract

A general framework is presented for evaluating stress triaxiality fields using five different configurations of Dirichlet boundary conditions. The latter ones were measured via stereocorrelation for a simple shear test on a thin sample where buckling was mitigated with an anti-buckling fixture. Friction and material parameters displayed negligible influence on the stress triaxiality fields. Accounting for the anti-buckling fixtures provided the most realistic stress triaxiality fields, but was computationally demanding. Prescribing all out-of-plane displacements, noisier but trustworthy stress triaxiality fields were also obtained by using much less computational resources.

Keywords: Buckling, Dirichlet boundary conditions, inverse problem, simple shear, stereocorrelation

1. Introduction

Thin sheets subjected to metal forming experience elastic springback after their deformation stages. Therefore, it is important to accurately predict reversible

*Corresponding author
Email address: zvonimir.tomicevic@fsb.hr (Zvonimir Tomičević)

deformations. Nowadays, the validity of forming processes is often controlled via Finite Element (FE) analyses that depend on how trustworthy material properties are. Furthermore, product optimization procedures are also governed numerically via FE approaches, thereby improving product design and subsequent manufacturing stages to reduce material waste [1]. Experimental investigations need to be carried out to determine the material response under simple or complex loading regimes. For metal forming, shear is an especially important stress state [2, 3, 4]. However, pure shear stress states cannot be easily achieved experimentally for sheets. As a result, mechanical tests considering simple shear are carried out on thin sheets instead.

Material characterization during mechanical tests where complex loading regimes are employed call for advanced measurement methods. The development of digital imaging provided an opportunity for the emergence of full-field measurement techniques. Digital Image Correlation (DIC) [5, 6, 7, 8, 9, 10] stands out as the most widely employed full-field measurement method due to its versatility and straightforward use. Moreover, the development of global DIC [11, 12, 13, 14] formulated within an FE framework resulted in simple and seamless couplings between experiments and FE simulations. Robust identification methods were designed to utilize this opportunity for the calibration of material parameters.

The resulting output of global DIC is nodal displacements from which strains are calculated. Although displacement and strain fields are readily available with DIC, stress fields cannot be directly measured. The stress fields may be used to evaluate stress triaxiality fields (written as the ratio between hydrostatic and von Mises equivalent stresses). Stress triaxiality plays an important role in damage and

fracture mechanics for predicting the type of failure (*i.e.*, ductile or brittle [15, 16, 17, 18, 19]). Combinations of DIC and X-ray diffraction (XRD) techniques may be used to measure both total and elastic strain fields [20, 21, 22, 23, 23]. The drawback is the required and expensive equipment, as well as the fact that the number of measurement points for XRD is generally limited, and as such, this method is not suited for industrial purposes.

The focus may then shift to analytical and numerical routes instead of experimental investigations to evaluate stress fields. In recent years, several approaches were proposed to assess stress and stress triaxiality fields from DIC measurements. Réthoré [24] developed the so-called Mechanical Image Correlation (MIC) method for evaluating stress fields without assuming any constitutive law. A similar approach where no constitutive laws were defined was used by Dalémat *et al.* [25] where DIC was coupled with a Data Driven Identification algorithm (DDI) for evaluating stress fields. Musiał *et al.* [26] presented an original proposition for evaluating stress fields from DIC data for uniaxial and simple shear tests by considering the measured displacement field gradient and a J_2-plasticity model. The DIC based stress fields gave more accurate results with respect to FE analyses since they accounted for all inaccuracies during experiments. Andrade *et al.* [27] proposed a method to estimate the stress triaxiality fields from DIC strain fields for Von Mises' and Hill's models. Furthermore, Brosius *et al.* [28] developed a similar semi-analytical approach where the stress fields were determined from DIC data. Lindner *et al.* [29] used Integrated DIC to evaluate stress triaxiality fields of a notched titanium alloy sample. It was concluded that even for thin samples, 3D meshes were required to analyze stress triaxiality fields. A similar 3D FE approach was used herein.

Abushawashi *et al.* [30] developed a novel method for constitutive modeling in plane strain conditions. Using DIC data, the authors determined equivalent stress and strain fields to run numerical simulations. From the numerical results, the stress triaxiality fields were evaluated since they display great influence on metal ductility [31, 32, 33]. Brünig *et al.* [34] also combined DIC data with numerical simulations to analyze a biaxial experiment on an H-specimen [35, 36, 37] covering a wide range of stress triaxialities and Lode parameters. Huang *et al.* [38] combined DIC results with computations to evaluate plastic strain and failure of Ti-6Al-4V alloys for specimens with different initial stress triaxialities. Wang *et al.* [39] coupled DIC data with FE runs to study Split Hopkinson Pressure Bar experiments. It was shown that the failure strain decreased with increasing stress triaxiality or strain rate. Peng *et al.* [40] coupled DIC with FE analyses to characterize the stress state of flat metal specimen with inclined notches to analyze the influence of stress triaxiality and Lode angle on failure modes. Pham *et al.* [41] developed a four-node quadrilateral plate element to analyze flexural and buckling responses of a functionally graded plate under different boundary conditions.

Advanced FE-DIC enables for straightforward couplings of measured data with numerical simulations in inverse problems aiming for material parameter calibration [42, 43, 44]. Finite Element Model Updating (FEMU) [45, 46, 47, 48] stands out as the most widely used algorithm for such purposes. With FEMU, the calculated displacement fields and resultant forces are compared to the measured quantities to determine the sensitivity matrices, *i.e.*, how the change in parameters affects them [49, 50, 51]. FEMU was employed for simple (*e.g.*, uniaxial [52]) and more complex (*e.g.*, biaxial [53]) mechanical tests. For identification purposes, the measured displacements were prescribed as Dirichlet boundary conditions on

the FE model. For thin samples, where plane stress states are expected, 2D DIC measurements may be sufficient. However, this approach may be limited when 3D effects cannot be neglected. Réthoré *et al.* [54] proposed a framework where the 3D displacement fields measured with stereocorrelation were used in an integrated procedure. Wang *et al.* [55] also coupled measured 3D displacements with FEMU to describe plastic anisotropy in the so-called Erichsen bulge test.

From the reviewed literature, it is concluded that very few studies combined DIC and FE simulations to assess stress triaxiality *fields* [56, 36, 57, 58]. One key question when coupling experimental and numerical tools is related to boundary conditions. Driving numerical simulations using DIC data for assessing stress triaxiality fields is the goal of this work. To be consistent with the experiment, measured displacements are utilized to drive FE analyses. For that purpose, a monotonic simple shear test was carried out with a Modified Arcan Fixture (MAF) on a 1 mm butterfly shaped specimen, which promoted uniform stress states in the gauge area, made of C60 steel. To measure the surface kinematics, a stereovision setup was used to capture both in-plane and out-of-plane components. Since thin samples subjected to simple shear loading are susceptible to buckling [59], additional supports made of transparent Poly methyl methacrylate (PMMA) were utilized to prevent sample buckling [60, 61, 59, 62]. The experimental setup analyzed herein was developed by Zaplatić *et al.* [63] where thin butterfly samples were subjected to simple shear. The friction coefficient between the PMMA plates and the sample was calibrated numerically via FEMU. To study the effect of prescribed boundary conditions, five test cases were defined, which differed in the definition of the applied kinematics. For each test case, FEMU was carried out to determine the influence of boundary conditions on the calibrated material pa-

rameters. In-depth analyses of the corresponding stress triaxiality fields were conducted for each test case. Such experimental and numerical framework provides a unique approach for analyzing the influence of the prescribed Dirichlet boundary conditions on stress triaxiality fields since the FE simulations were directly driven by experimentally measured DIC data.

2. Experimental protocol

In this section, the entire experimental protocol involving the Modified Arcan Fixture and stereovision system are presented. The stereocorrelation results are then analyzed and discussed.

The experiment presented herein was aimed at preventing buckling of thin sheet samples under simple shear loading. The mechanical test was carried out on a Modified Arcan Fixture (Figure 1), which enables for three loading regimes, namely, shear, tensile and combinations thereof. The MAF employs butterfly shaped samples with two V notches in the middle of the gauge section to promote uniform strain distributions. The expected triaxiality levels in the gauge area (*i.e.*, between the V notches) for the aforementioned loading regimes are 0, 0.33 and 0.66, respectively [63]. The 1-mm thick butterfly sample made of high carbon C60 steel was subjected to simple shear (Figure 1). The experiment was performed on a uniaxial testing machine *Messphysik Beta* 50-5 in displacement control mode with a stroke rate of 1 mm/min. The standard force uncertainty γ_F of the load cell was equal to 10 N.

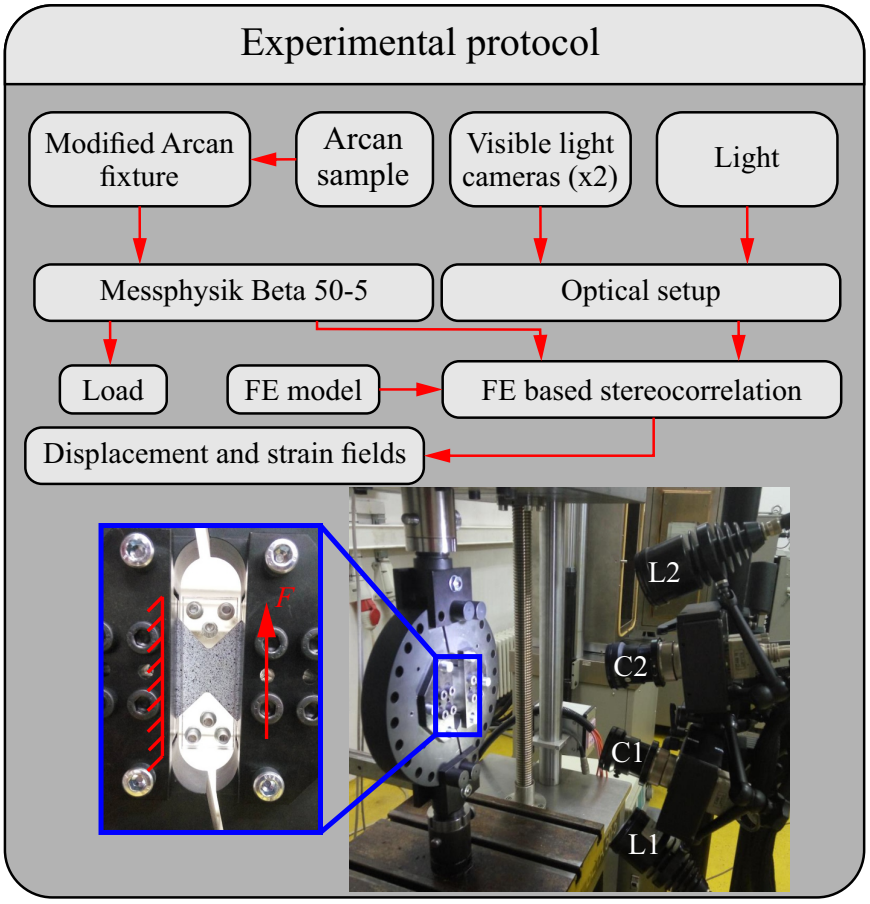

Fig. 1: Experimental workflow with the experimental and optical setup consisting of two vertically positioned visible light cameras (C1 and C2) and two light sources (L1 and L2). On the extracted detail, the Region Of Interest (for stereocorrelation purposes) is depicted on the butterfly sample with the positioned PMMA plates.

Since a thin sample was subjected to simple shear, buckling was expected to occur. In order to mitigate shear buckling, an anti-buckling fixture was designed, which was composed of two 10-mm thick (PMMA) plates. The use of PMMA for the material of the anti-buckling fixture was due to its transparency thus allowing optical measurement methods to be used. Similar setups were employed to minimize buckling and wrinkling of sub-millimeter thick sheets [60, 61, 59]. The

dimensions of the two PMMA plates (*i.e.*, 70×25 mm) were defined with respect to the observable area of the butterfly sample (Figure 1). The plates around both lateral surfaces were connected with a total of six M5 bolts, which were not tightened to reduce the influence of the anti-buckling fixture on the stress triaxiality fields. The material response in the Region Of Interest (ROI) was captured with the stereovision system detailed in Table 1. A total of 900 images was acquired by each camera, where the first ten image pairs corresponded to the unloaded state.

Table 1: Hardware parameters of the stereo-system

Cameras	Dalsa Falcon 4M60
Definition	2358×1728 pixels (B/W images)
Color filter	none
Gray Levels rendering	8 bits
Lens	Titanar 50 mm
Aperture	f/2.8
Field of view	3,996 mm^2
Image scale	≈ 32 pixel/mm
Stereo-angle	25°
Stand-off distance	31.6 cm
Image acquisition rate	1 fps
Patterning technique	B/W paints
Pattern feature size	15 px

The displacement and strain fields of the ROI were measured via FE-based stereocorrelation [64, 65, 66]. The employed software (EikoTwin DIC) consid-

ers a continuous description of the ROI discretized with triangular T3 finite elements [67]. The aforementioned algorithm uses the known geometry of the sample and setup, as observed from the reference images, for calibration purposes. Following the calibration step, shape corrections of the chosen ROI were performed by running a second series of spatial registrations in which out-of-plane corrections were allowed [65]. The stereocorrelation analysis parameters are reported in Table 2. The listed noise floor estimates were determined by calculating the mean temporal standard deviations of each nodal displacement and element strains from the registration of the ten reference image pairs.

Table 2: Stereocorrelation analysis parameters

DIC software	EikoTwin DIC
Image filtering	none
Element length	1 mm
Shape functions	linear (T3 elements)
Mesh	see Figure 3
Matching criterion	penalized sum of squared differences
Regularization length	5 mm
Displacement noise floor (x z y)	0.2 µm 0.1 µm 0.6 µm
Strain ε_{12} noise floor	7×10^{-5}

The global stress/strain response of the sample is shown in Figure 2. The engineering shear stress was calculated by dividing the measured force by the initial cross-sectional area S_0 between the V notches (*i.e.*, 21×1 mm). The strain levels were evaluated by averaging the measured strains within the virtual gauge located

between the V notches of the DIC mesh (Figure 3(c)). The yield stress was approximately equal to 248 MPa (for an offset strain of 0.4%). For the highest load level (*i.e.*, 8.7 kN), the ultimate shear strength was equal to 417 MPa, and the corresponding shear strain 48.7%. From the deformed sample, two distinct symmetric cracks were observed (Figure 2). The initial location of the cracks correlated with tensile stress areas (*i.e.*, with expected stress triaxiality of 0.33). Slight buckling of the central region was also distinguished, especially where compressive stress states were expected (depicted by green rectangles in Figure 2).

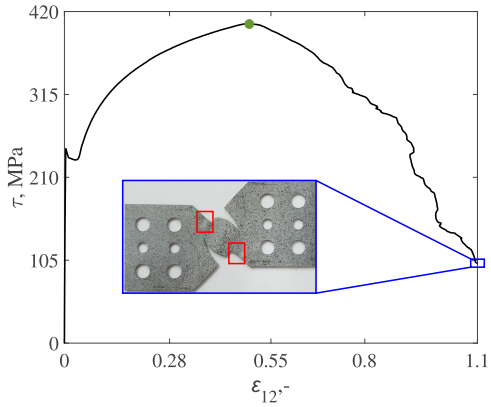

Fig. 2: Macroscopic shear stress/strain response. The green point indicates time step 340 (*i.e.*, strain level of 44%). The analyses reported herein were carried out up to this point. On the deformed sample, the locations of buckling onset are highlighted by red rectangles, which corresponded to areas subjected to compression.

The carried out experiment with the anti-buckling fixture mostly resulted in negligible to small out-of-plane displacements. In Figure 3, out-of-plane displacement, residual and strain fields are reported for time step 340 before damage inception (Figure 2). The measured out-of-plane displacement field revealed a heterogeneous distribution, which indicated a tendency toward buckling. The area

of increased displacements denoted by the blue rectangle corresponds to zones where negative triaxialities were expected (*i.e.*, approximately -0.33, which indicates compressive stresses). The same area is not highlighted in the correlation residual map (Figure 3(b)), thus proving the trustworthiness of the measurements. Increased residuals were visible in the central part of the ROI (highlighted by the green rectangle). Due to the tendency toward buckling, minor wrinkling of the central part of the ROI occurred, which led to changes in brightness (*i.e.*, shadows). The strain map (Figure 3(c)) revealed that a single shear strain band developed between the V notches where the expected triaxiality was 0.

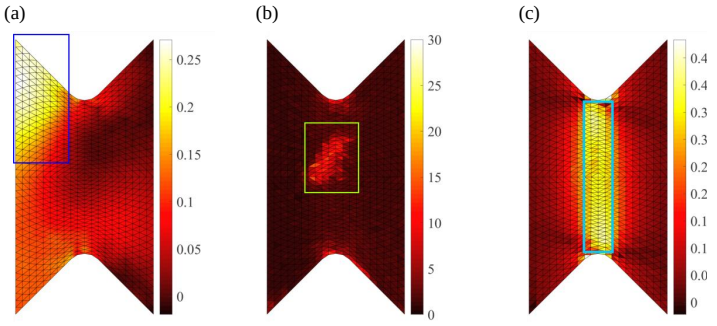

Fig. 3: (a) Out-of-plane Displacement (expressed in mm), (b) gray level residual (in % of the dynamic range of the reference images), and (c) ε_{12} strain fields for time step 340 (*i.e.*, before damage occurred). Positive displacements are oriented toward the reader. The blue box highlights localized increases in out-of-plane displacements where limited buckling initiated. The green box shows increased residuals where a slight change in brightness occurred. The cyan box depicts the location and size of the virtual strain gauge. Negligible out-of-plane displacements were measured and a uniform shear strain band developed.

3. Numerical protocol

In this section, the entire numerical protocol is presented. First, the FE models of the sample and the PMMA plates is introduced. Second, the five analyzed test

cases are defined. Last, the FEMU identification procedure is summarized. The numerical investigation presented herein dealt with the influence of the prescribed boundary conditions (BCs) on the predictions of the FE model, specifically the stress triaxiality fields. To evaluate the latter ones, the material parameters were calibrated via weighted Finite Element Model Updating (FEMU).

In the present analyses, the numerical simulations were driven by *experimentally measured* displacements prescribed as Dirichlet BCs. The goal was to analyze the influence of the BCs on the stress triaxiality fields. Yang *et al.* [68] introduced bifurcation analyses in FE simulations to analyze wrinkling of the modified Yoshida buckling test (YBT). Even though the numerical analyses closely followed the experiments, the BCs on the gripped part could not describe slip between the specimen and the grips in a straight forward manner. Using DIC measured data, there is no need to model the grips. Chen *et al.* [69] analyzed the influence of a disturbance force on buckling of YBT specimens. The simulation of thin sheet buckling was challenging, and imperfections had to be introduced in the numerical model. In the present study, the imperfections were included through the measured BCs. No geometrical imperfections were added [70]. All the reported simulations were performed with the implicit version of Abaqus [71], and no advanced tools (*e.g.*, arc length method or explicit schemes) were needed.

3.1. Test cases

Five distinct test cases (Figure 4) were defined for which the influence of BCs was evaluated on the stress triaxiality fields and sample buckling modeling (Table 3). For each studied case, the FE model of the sample was discretized with C3D8R elements.

3.1 Test cases

Table 3: Test cases with their boundary conditions

Test case	Description
T1	Measured U_x and U_y displacements on stressed surfaces and U_z displacements on the stressed edges of Surface 1 + PMMA plates ($\mu = 0.33$) (Figure 4(a) and (b) - R and Y)
T2	Measured U_x and U_y displacements on stressed surfaces and U_z displacements on the stressed edges of Surface 1 + PMMA plates ($\mu = 0.01$)
T3	Measured U_x and U_y displacements on stressed surfaces (Figure 4(b) - R)
T4	T3 and U_z displacements on stressed edges (Figure 4(b) - R and Y)
T5	T3 and U_z displacements on Surface 1 (Figure 4(b) - R, Y and B)

In test case T1 (Figure 4(a)), the assembly of the butterfly sample and the PMMA plates was modeled with defined interactions between the two parts. The measured displacements were prescribed on the stressed surfaces of the sample mesh as Dirichlet BCs. Out of plane (z) displacements were prescribed only along the stressed edges of Surface 1 whose normal was along negative z. Conversely, pure (*i.e.*, 2D) DIC displacements x and y were extruded through the thickness of the mesh (*i.e.*, along the z direction Figure 4(b) - denoted in Red and Yellow color).

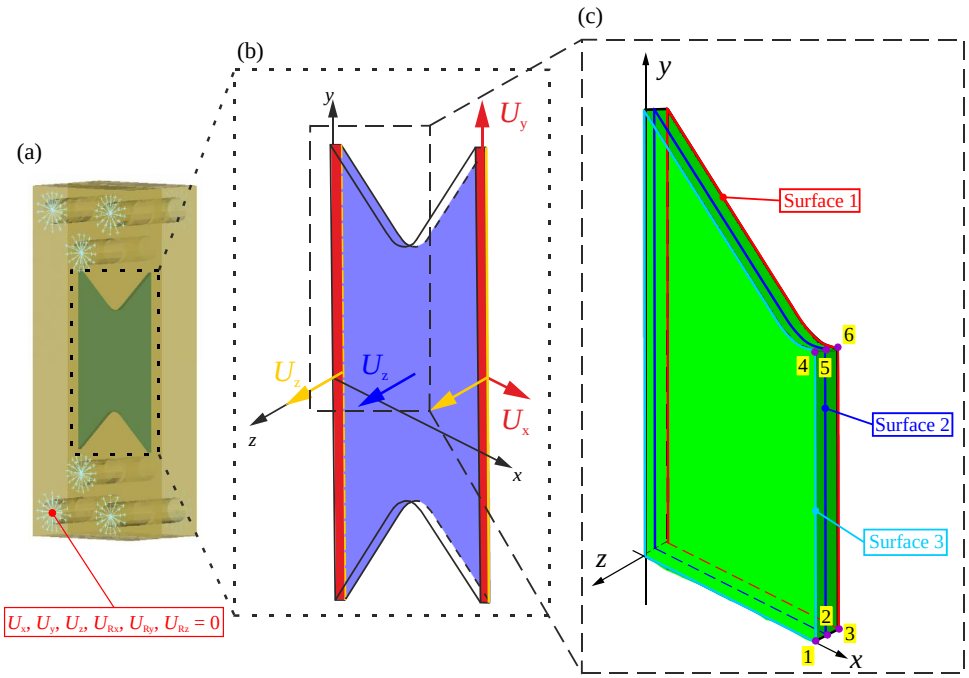

Fig. 4: (a) FE model with the PMMA plates. (b) Different sets of boundary conditions. Red (R) - in-plane displacements (U_x, U_y) on entire surfaces, yellow (Y) - out-of-plane displacements U_z on the edges and blue (B) - out-of-plane displacements U_z on the entire surface. (c) Detail of a quarter of the FE model where six points and three surfaces are defined, which are used for further analyses.

The second test case T2 was identical to T1 regarding the prescribed BCs and numerical model. However, the friction coefficient was set to $\mu = 0.01$ to probe the influence of negligible friction on the numerical model. For test case T3, only 2D displacements (*i.e.*, along x and y directions) were prescribed on the stressed surface (Figure 4(b) - denoted in Red color) as if they had been measured via 2D-DIC. This test case was not deemed eligible to simulate buckling as an idealized configuration was defined (*i.e.*, no imperfections in terms of out-of-plane displacements were introduced).

In test case T4, out-of-plane displacements were prescribed along the stressed edges of Surface 1, identical to T1 and T2, but the PMMA plates were not modeled (Figure 4(b) - denoted in Red and Yellow color). For the last test case (T5), the entire Surface 1 was further constrained with the measured out-of-plane-displacements (Figure 4(b) -denoted in Red, Yellow and Blue color). This choice was made due to the inaccurate description of buckling with case T4. To further probe the simulation validity regarding buckling, the out-of-plane displacements were prescribed on the entire surface. Each analysis performed herein was run for the first 340 time steps (*i.e.*, until the shear strain reached $\varepsilon_{12} = 0.44$, see Figure 2).

For the first two test cases, the interaction between the sample and the PMMA plates needed to be defined. General contact was introduced with Coulomb friction [72], where two different friction coefficients were considered. The plates were discretized with C3D4 tetrahedra. In the mechanical test, they were connected with six bolts that were not tightened. The numerical model was simplified to avoid modeling bolt pretension. The bolts were replaced by a combination of kinematic couplings and connector elements (CONN3D2, type = beam). Kinematic couplings were used to replace bolt heads on the surfaces around the holes (depicted by cyan lines in Figure 4(a)), whereas the connector elements represented the bolt shank and thread. Connector elements were used to link the master nodes of the kinematic coupling, thereby ensuring stiff connections between the plates. To prevent rigid body motions of the plates, for a single master node, all displacements and rotations were disabled (red dot in Figure 4(a)). For all other master nodes, only out-of-plane displacements were disabled. Elastic properties (*i.e.*, 3 GPa Young's modulus and 0.3 Poisson's ratio) were assigned to the PMMA

plates.

3.2. Parameter calibration

The extraction of stress triaxiality fields depends on material parameters. FEMU was employed as the identification procedure. To describe the nonlinear behavior, Armstrong-Frederick's kinematic hardening model [73] was selected. The sought parameters were the yield stress σ_y, hardening modulus C, and nonlinear coefficient c. FEMU minimizes differences between experimentally measured and numerically calculated quantities. The minimization procedure iteratively updates the sought parameters by calculating Hessian matrices based on sensitivity fields [49, 74] (*i.e.*, changes of each considered quantity for a small variation of the parameters). In the present cases, the differences between measured and computed displacement fields, as well as measured load and global reaction forces extracted from the numerical model were considered.

If the minimization procedure were to take into account only measured displacement fields (*i.e.*, FEMU-U), the cost function would be formulated as the sum of squared differences between measured $\{\mathbf{u}_m\}$ and computed $\{\mathbf{u}_c\}$ nodal displacements

$$\chi_u^2(\{\mathbf{p}\}) = \frac{1}{\gamma_u^2 N_u} \left\| \{\mathbf{u}_m\} - \{\mathbf{u}_c\} \right\|_2^2, \tag{1}$$

where $\{\mathbf{p}\}$ is the column vector gathering all sought material parameters, γ_u the standard displacement uncertainty, and N_u the number of kinematic degrees of freedom [74]. When the only source of error is due to the measurement uncertainty, χ_u tends to 1. Therefore, any deviation from 1 implies model errors.

FEMU may also be utilized to minimize the differences between the measured forces $\{\mathbf{F}_m\}$ and calculated reaction forces $\{\mathbf{F}_c\}$ (*i.e.*, FEMU-F) extracted from

the stressed edges of the FE model where Dirichlet BCs were prescribed

$$\chi_F^2(\{\mathbf{p}\}) = \frac{1}{\gamma_F^2 N_F} \left\| \{\mathbf{F}_m\} - \{\mathbf{F}_c\} \right\|_2^2, \tag{2}$$

where γ_F is the standard uncertainty of the load cell, and N_F the number of load data.

The identification procedure can be enhanced by combining the aforementioned cost functions

$$\chi_{tot}^2 = (1-\omega)\chi_u^2 + \omega\chi_F^2, \tag{3}$$

where the factor ω weighs the contribution of each individual cost function. In this work, ω was set to 0.5 to give equal weight to both cost functions.

4. Numerical results

In this section, the numerical results for each test case are presented and compared. First, FEMU was carried out to determine the optimal set of material parameters for each individual test case. For the identification procedure and further numerical analyses, the triangular T3 mesh used for stereocorrelation measurements (Figure 3) was converted into four-noded quadrilateral (Q4) elements. The 2D Q4 mesh was then extruded to construct the 3D mesh composed of linear brick elements with reduced integration (C3D8R).

4.1. FEMU identification results

The calibrated material parameters, their initial value and converged cost functions are gathered in Table 4. The parameters calibrated for test case T1 were used as initial guess for the other cases. For each test case, the elastic parameters (*i.e.*,

Young's modulus E and Poisson's ratio ν) were kept constant and set to 210 GPa and 0.25, respectively.

Table 4: FEMU results for all test cases. The calibrated parameters of case T1 were used as initial guess for all other test cases. Values of χ_U, χ_F and χ_{tot} are displayed for initial and converged solutions. The standard parameter uncertainties ($\pm$) are also indicated.

Parameter	σ_y, MPa	C, MPa	c	χ_U		χ_F		χ_{tot}	
				Initial	Converged	Initial	Converged	Initial	Converged
T1	360 ± 15	3860 ± 640	12 ± 1.7	60	59.6	40.4	9.3	51.2	42.6
T2	380 ± 9	3920 ± 460	11 ± 1.7	59.4	59.5	43.9	10.5	52.5	42.7
T3	380 ± 9	3920 ± 460	11 ± 1.7	34	33	44.4	10.4	32	24.5
T4	380 ± 10	3910 ± 510	11 ± 2	69	71	47	10.5	59	51
T5	380 ± 13	3890 ± 660	11 ± 2.4	7.8	7	45.8	10.7	32.9	9

The calibration procedure yielded parameters that provided good agreement between the measured load and the global reaction forces. Each calibration resulted in lowered global residual χ_{tot}. For case T1, the calibrated yield stress σ_y and hardening coefficient C were the lowest, except for the nonlinear coefficient c, which was the highest of all test cases. Furthermore, the converged global residual χ_{tot} and the force residual χ_F were lower compared to test cases T2 and T4.

The second test case T2 experienced an increase in yield stress σ_y by 6% and hardening coefficient C by 1%, whereas c was reduced by 7%. The global residual at convergence was only slightly higher than for T1. The displacement residuals for the initial parameters and at convergence displayed slightly lower values than their T1 counterpart. However, for T1 the force residuals were lower. Since friction was negligible, higher values of σ_y and C were calibrated to compensate for the additional force due to friction [63].

The third test case T3, where only in-plane measurements were prescribed,

yielded the second lowest global residual. This result was due to the lack of prescribed out-of-plane displacements that were affected by higher measurement uncertainties (Table 2). Furthermore, with this approach, buckling of the sample was not possible to simulate since no imperfections were considered. This observation highlights the significance of enriching the FE model with measured out-of-plane displacements for buckling simulation. Although only in-plane measurements were prescribed, it was decided to include out-of-plane displacements in the calculation of χ_{tot}, which was significantly lower than for test cases T1 and T2. This observation shows that prescribing only in-plane measurements was not sufficient to describe any out-of-plane motion. This test case cannot be considered representative of the real experiment since it was idealized. The identified values of the sought parameters were essentially the same as for test case T2 since no friction was included in the numerical model.

Even though the identification procedure converged, the global residual was the highest of all proposed FE modeling strategies for test case T4. Both displacement and force residuals for the first iteration and at convergence were greater than those for T1 and T2. Furthermore, the displacement residual experienced a slight increase at convergence due to higher out-of-plane displacements (*i.e.*, buckling, which could not be accurately described). It was concluded that 3D measurements prescribed as Dirichlet BCs were sufficient to simulate buckling. However, due to the complexity of the material behavior, buckling for case T4 was not fully controlled (*i.e.*, restricted by the PMMA plates). The deviation of the calculated out-of-plane displacements from the measured counterparts resulted in increased displacement residual χ_U. The initial and converged force residuals χ_F also displayed higher values than the previous test cases, except for T2 where the same

level was reached.

For the final test case T5, the measured out-of-plane displacements were prescribed over the entire Surface 1 to drive the numerical simulation toward limited buckling with Dirichlet BCs. The calculation of χ_U considered only stereocorrelation measurements. The lowest χ_{tot} was reached with this approach since out-of-plane displacements were accounted for and controlled. This last case resulted in approximately eight times lower displacement residuals than for T1. By constraining the entire Surface 1, buckling could be triggered with stereocorrelation data. The drawback of this approach is the introduction of additional measurement uncertainties in the prescribed out-of-plane displacements (Table 2). An additional cost function regarding the reaction forces extracted from the constrained surface was defined in the FEMU algorithm. The goal was to minimize these reaction forces to be as close as possible to zero. The identification procedure yielded the highest value of σ_y compared to all other test cases, which increased by approximately 7%, whereas C changed only slightly from its initial value (*i.e.*, 0.7%). The nonlinear coefficient c experienced the highest relative change (ca. 8%).

The standard uncertainty of the calibrated parameters was also calculated to determine the influence of the prescribed Dirichlet BCs. For the yield stress σ_y, the highest uncertainty was reached for test cases T1 and T5, *i.e.*, the more complex cases. The parameter uncertainties for the other three cases were similar. For test cases T1 and T5, the highest uncertainty for C was also observed, whereas for T2 and T3 they were similar. The highest uncertainty for c was obtained for case T5. From these results, it was concluded that the prescribed BCs had an influence on the calibrated material parameters. The most complex test cases T1 and T5 yielded the highest parameter uncertainties. For case T1, the cause was

friction, whereas for T5 it was due to the prescribed out-of-plane displacement on the entire measurement surface.

To illustrate the effect of friction, a *unique* set of material parameters was selected (*i.e.*, those of case T1, see Table 4) and computations were run with the five BCs. From each simulation, the reaction forces were extracted and are displayed in Figure 5(a). All test cases yielded lower reaction forces compared to T1. This trend was explained by the fact that all of them were frictionless (*i.e.*, for case T2 friction was approximately zero and for the other three it was not modeled). The influence of friction cannot be deemed negligible, which is further supported by the calibrated material parameters (Table 2). For the last four test cases, friction was neglected, and the FEMU procedure yielded higher values for σ_y and C compared to T1 to compensate for the absence of friction. This effect was especially apparent for the first two test cases T1 and T2 where the same numerical model was employed.

Cases T1 and T2 were very close in terms of numerical model. Their reaction force differences were the lowest of all the reported differences (Figure 5(b)), which was further substantiated by the lowest mean. The highest differences were observed between cases T1 and T4. Overall, the root mean square differences were about 33 times the standard force uncertainty γ_F. These results highlight the consequence of not including friction in the identification procedure.

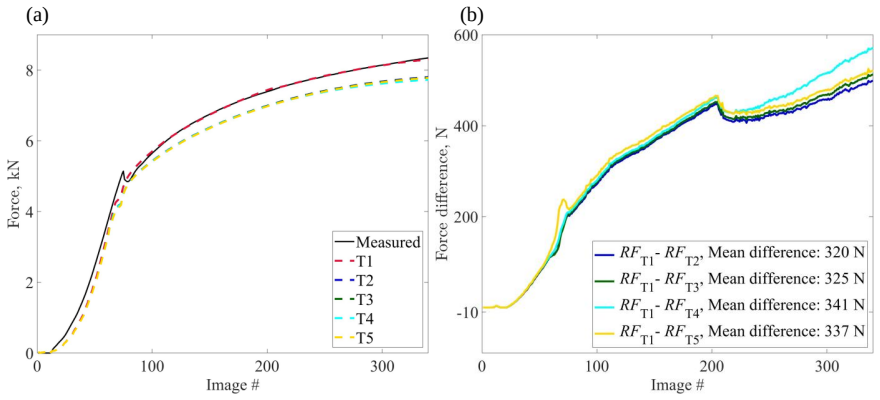

Fig. 5: (a) Comparison of global reaction forces extracted from the FE models for the material parameters calibrated for case T1. (b) Differences in global reaction forces with respect to T1. The mean reaction force differences were on average 33× higher than the standard force uncertainty γ_F ($i.e.$, $\chi_F \approx 33$). These results show the consequence of not including friction in the identification procedure (*i.e.*, lower reaction forces since the material parameters were not properly calibrated in the absence of friction).

4.2. *Stress triaxiality fields*

In the following, the influence of different BC prescriptions on stress triaxiality fields is studied, both surface-wise and node-wise (Figure 4(c)). Three surfaces were chosen to evaluate them, namely, the back Surface 1, middle Surface 2 and front Surface 3. Moreover, in total six nodes were chosen for the evaluation of the corresponding triaxialities. The three nodes in the middle (*i.e*, nodes 1, 2 and 3) of the FE model were chosen to asses the stress state in the gauge area (*i.e*, between the V notches) since the butterfly sample was designed to promote uniform stress states in the gauge region. The sample was subjected to simple shear, thus uniform shear stress states were expected (*i.e.*, the stress triaxiality should vanish). Furthermore, three points were chosen in the root of the V notch (*i.e*, nodes 4, 5 and 6) to evaluate the stress state in that area. All test cases

displayed similar distributions of stress triaxialities on the chosen sample planes (Figures 6-10). The locations of the initiated cracks in the sample (see inset of Figure 2) coincided with the areas of positive stress triaxialities (*i.e.*, ≈ 0.33) where tensile stresses occurred.

From the stress triaxiality fields shown in Figure 6 for test case T1, identical distributions are observed on all three surfaces. The stress triaxiality fields were generally divided into three main parts, namely, areas with positive (red) tensile, negative (blue) compressive, and approximately zero (green) shear parts. Small fluctuations in terms of increased stress triaxiality values occurred on the edges of the surfaces. This effect was attributed to the prescribed BCs, which introduced additional random fluctuations due to measurement uncertainties. Furthermore, no severe wrinkling was caused by sample buckling since it was prevented with this numerical model.

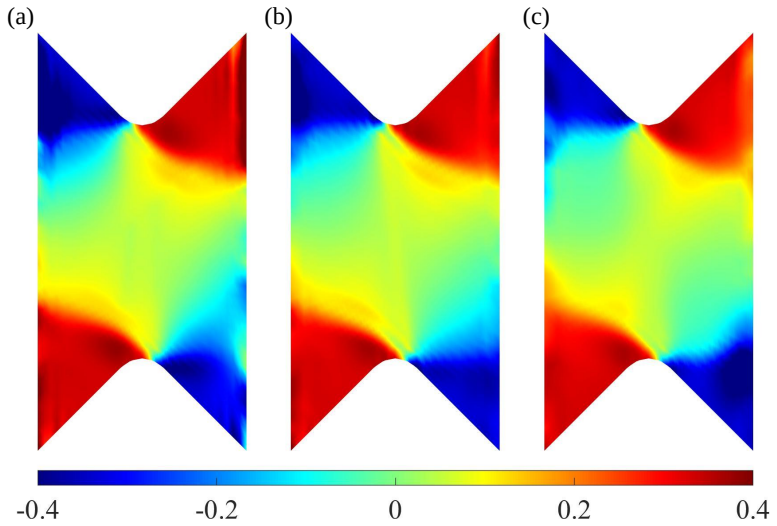

Fig. 6: Stress triaxiality fields for time step 340 (test case T1), for the front surface (a), the mid-thickness surface (b) and back surface (c). Almost identical fields are observed for the three analyzed surfaces.

Test case T2 (Figure 7) displayed identical triaxiality distributions as T1 since the numerical model was the same, except for the value of the friction coefficient. As in the previous case, increased stress triaxiality levels were observed on the boundaries of the FE model where Dirichlet BCs were prescribed. The stress triaxiality in the middle of the gauge area was also close to zero. From the stress triaxiality fields, it was concluded that the influence of friction remained very limited.

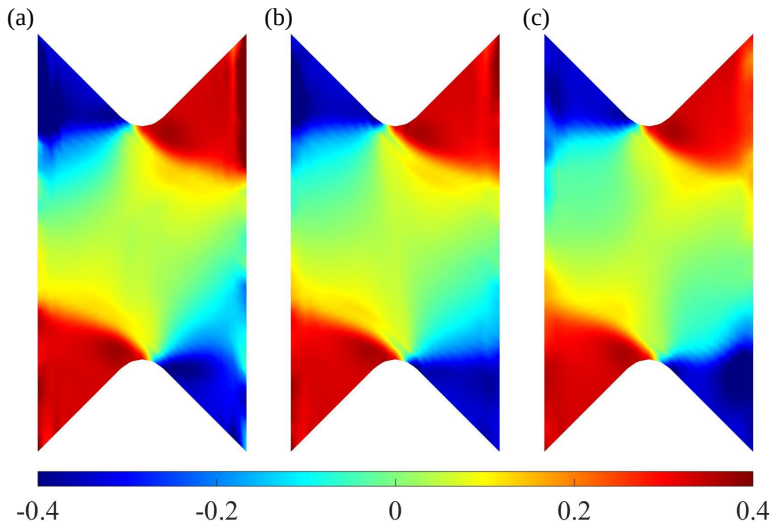

Fig. 7: Stress triaxiality fields for time step 340 (test case T2), for the front surface (a), the mid-thickness surface (b) and back surface (c). Almost identical fields are observed for the three analyzed surfaces.

Test case T3 differed from other ones as it was the only configuration where no out-of-plane displacements were prescribed to the FE model. No buckling developed in the numerical simulations since they were idealized (*i.e.*, there were no imperfections in terms of out-of-plane displacement). All three surfaces displayed identical stress triaxiality distributions. The stress triaxiality levels in the middle of the gauge area were close to zero (*i.e.*, a shear stress state developed). Similar

distributions of stress triaxialities were observed compared to cases T1 and T2, and the constrained edges of the FE model displayed lower fluctuations since no out-of-plane displacements were prescribed.

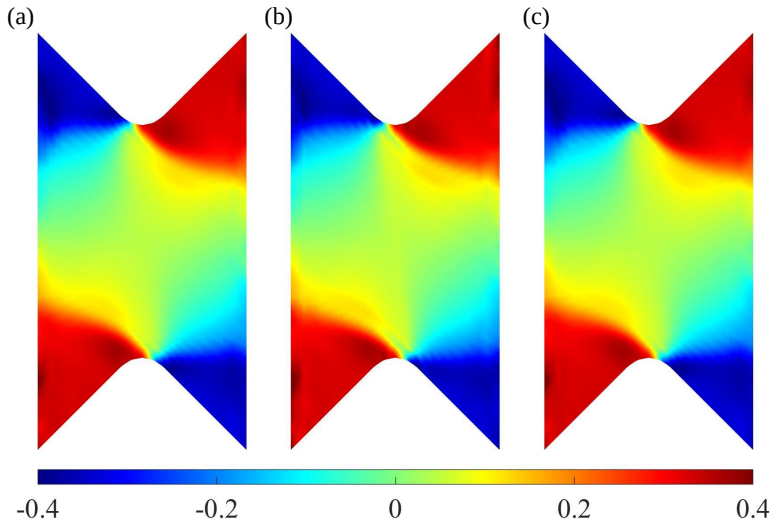

Fig. 8: Stress triaxiality fields for time step 340 (test case T3), for the front surface (a), the mid-thickness surface (b) and back surface (c). Almost identical fields are observed for the three analyzed surfaces.

For test case T4, the fluctuations in the stress triaxiality fields on Surfaces 1 and 3 (Figure 9) were more marked. The middle Surface 2 was similar to the previous test cases and no significant fluctuations occurred. However, Surface 1 suffered from more important variations in the stress triaxiality field in the middle of the gauge section, where zero levels were expected. This effect was attributed to buckling, which was triggered by introducing out-of-plane displacements in the Dirichlet BCs. Even though buckling developed, it was not severe. Its influence on the stress triaxiality fields was not negligible since additional stresses were induced. From the stress triaxiality fields, the effect of limited buckling was seen. The gauge area on Surface 1 was subjected to tensile stresses, whereas the same

area on Surface 3 was compressed. From this observation, it was concluded that buckling was oriented away from the reader.

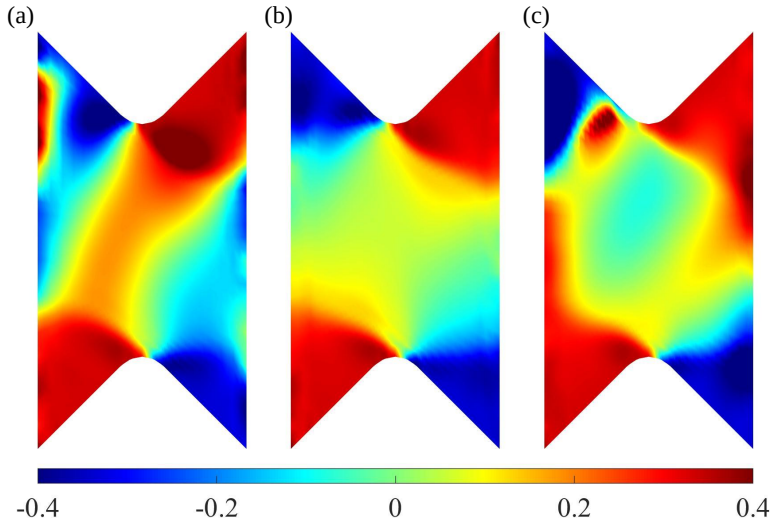

Fig. 9: Stress triaxiality fields for time step 340 (test case T4), for the front (a) and back (c) surfaces where the influence of buckling is more pronounced than for the mid-thickness surface (b).

Since the entire Surface 1 was constrained by the prescribed out-of-plane displacements, test case T5 was the most sensitive to measurement uncertainties. Triaxiality fluctuations were observed on all three surfaces in Figure 10, and as expected, Surface 1 was most affected. The stress triaxiality distribution on all three surfaces was still close to the previous cases. For test case T4, where buckling was also simulated, similar distributions of stress triaxialities in the gauge region were distinguished. The stress triaxiality values for the red areas ranged from 0.3 to approximately 0.5, which was similar to the levels obtained for cases T1 and T2. In the gauge area, they were higher than for T1. This trend was attributed to buckling inception since out-of-plane displacements were prescribed on Surface 1.

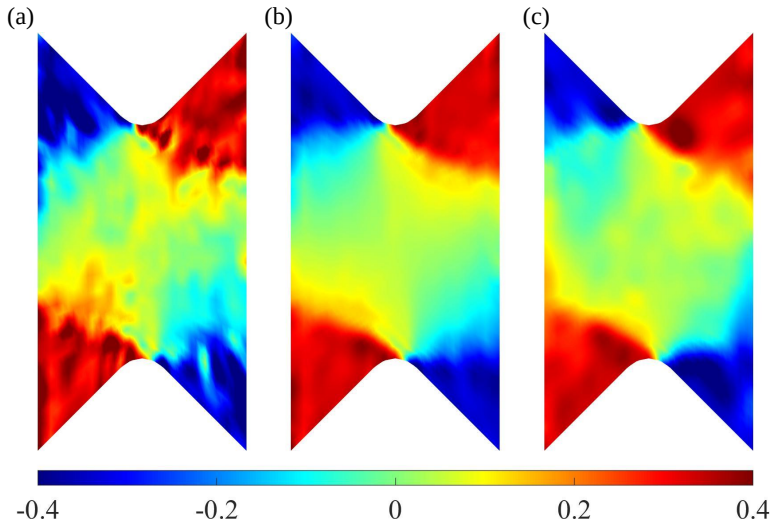

Fig. 10: Stress triaxiality fields for time step 340 (test case T5). For the front surface (a), the influence of the measurement uncertainties is more important than for the back surface (c); for the mid-thickness surface (b) it is minimal.

The stress triaxiality history for the six chosen nodes (Figure 4(c)) is plotted against the average shear strain calculated from the virtual gauge (Figure 3(c)) and reported in Figure 11. From the analysis of the stress triaxiality fields, it was concluded that the gauge area was subjected to predominantly shear stresses (*i.e.*, with stress triaxiality approximately equal to zero). The middle nodes 1, 2 and 3 (Figure 3(a)) for case T1 (Figure 11(a)) displayed small deviations through the thickness in the middle of the sample with an increase of the mean shear strain. However, the mean values for time step 300 were equal to 0.03 for all three nodes (Table 5). The second set of nodes (*i.e.*, 4, 5 and 6) experienced notable fluctuations. However, their levels all converged toward 0.33 (*i.e.*, tensile stress state) for the final time step.

Table 5: Mean nodal stress triaxiality for each test case in the plastic regime (*i.e.*, from time step 100 to 340)

Node	1	2	3	4	5	6
T1	0.01	0.02	0.03	0.20	0.19	0.20
T2	0.01	0.02	0.03	0.20	0.19	0.20
T3	0.02	0.02	0.02	0.20	0.19	0.20
T4	-0.01	0.02	0.06	0.20	0.20	0.25
T5	0.01	0.02	0.04	0.20	0.25	0.50

Test case T2 was essentially identical to T1 with regards to nodal stress triaxiality history, thereby indicating negligible influence of friction on the stress triaxiality (Figure 11(b)). Furthermore, similarities were also observed for the mean levels (Table 5); for cases T1, T2 and T3, they were identical. Test case T3, where only in-plane displacements were prescribed on the stressed edges, did not exhibit any buckling, which was further illustrated by the indistinguishable stress triaxiality histories for nodes 1, 2 and 3 and 4 and 6 (Figure 11(c)). Node 5 displayed an identical history as cases T1 and T2.

Test case T4, where the FE model was enriched with out-of-plane displacements, exhibited more pronounced buckling compared to the first two cases (Figure 11(d)). Therefore, the previously commented trend for nodes 1,2 and 3 was no longer observed. A divergence of nodal stress triaxialities occurred (Figure 11(d)). This phenomenon was attributed to buckling since Surface 3 (Node 1) was subjected to compression and Surface 1 (Point 3) to tension according to the stress triaxiality fields (Figure 9). The middle point 2 displayed the same response as in

previous test cases. Nodes 4 and 6 also experienced higher divergence compared to the other test cases. Nodes 2 and 5 located on the middle plane (*i.e.*, Surface 2) did not exhibit any dependence on buckling as the levels and histories were equivalent to case T1.

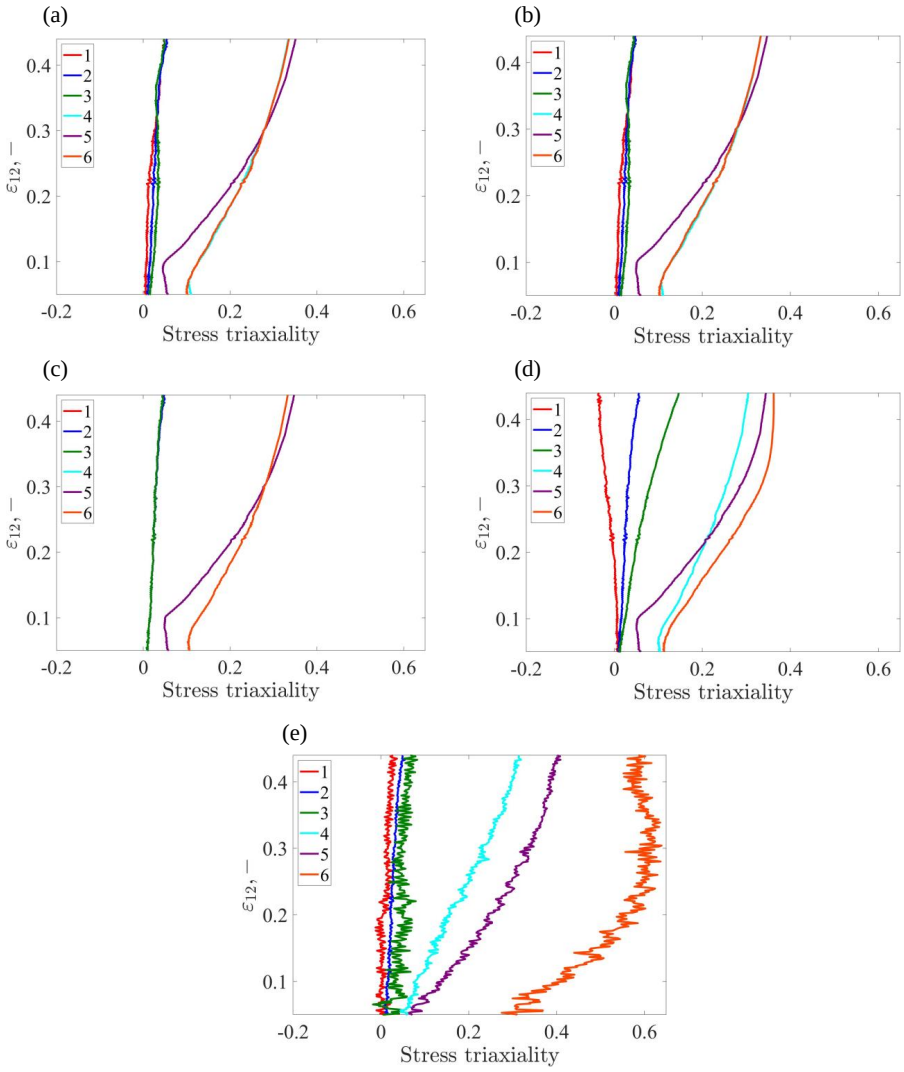

Fig. 11: Nodal stress triaxiality history vs. mean shear strain (in the optical gauge) for test cases T1 (a), T2 (b), T3 (c), T4 (d) and T5 (e). For the middle nodes 1,2 and 3, the trend is similar for all cases, except T4 where buckling developed. For nodes 4, 5 and 6 the trend is similar for each test case.

The introduction of measured out-of-plane displacements on Surface 1 resulted in noisier stress triaxialities (Figure 11(e)). Although all nodes were affected, nodes 3 and 6 suffered the most since they were located on the constrained surface, thus displaying higher sensitivity to measurement uncertainties. The influence of the latter ones was also observed from the mean values of all nodes as they showed slight deviations from the previous test cases, especially for node 6, which was two times higher than for the other cases (Table 5).

Figure 12 reports the mean stress triaxiality differences for Surface 2 with respect to test case T1 since for the chosen plane all cases displayed similar results. The mean stress triaxiality differences for test cases T2 and T4 showed similar trends. For the first one hundred images (in elasticity) the differences were insignificant, whereas in the plastic regime they were several orders of magnitude larger. Conversely, test cases T3 and T5 exhibited much larger differences than T2 and T4 in elasticity. However, T3 did not display any distinct change in the difference levels, whereas T5 showed a gradual decrease of the differences with increased load levels. This trend was attributed to a better description of sample buckling, thus better simulating the complex stress states in the material. Although additional measurement uncertainties were introduced in test case T5, no severe anomalies were observed. In plasticity, the mean differences for all test cases were of similar order of magnitude.

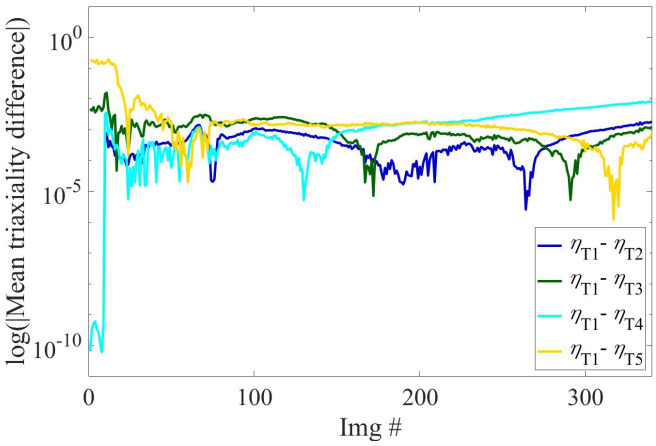

Fig. 12: Comparison of mean stress triaxiality differences for Surface 2 between all test cases with respect to T1. Highest differences are reported in elasticity, whereas for plasticity the differences are of similar orders of magnitude. Slightly higher differences are observed between test cases T1 and T4 thereby confirming that for the stress triaxiality fields it is necessary to use a 3D model.

5. Discussion

In this section, the influence of the calibrated parameters on the stress triaxiality fields is studied for each test case. The converged solution for the stress triaxiality fields was subtracted to that for which a single parameter was changed by 1%. The standard differences per image are displayed for all three surfaces to study the influence of the considered parameter through the sample thickness.

By observing the standard sensitivity to the yield stress σ_y (Figure 13), a sudden increase to stress triaxiality differences occurred in the early stages of yielding as seen on the force curve. This trend was similar in all test cases. For cases T1 and T5, the increase was more pronounced than for the other ones. In the middle of the sample (*i.e.*, Surface 2) the highest difference was observed for T1, whereas on Surface 3 it was for cases T5 and T1. This trend was attributed to the complex-

ity of the numerical models. After the initial stages of yielding, the calculated differences were lower and stable until the end of the numerical analysis.

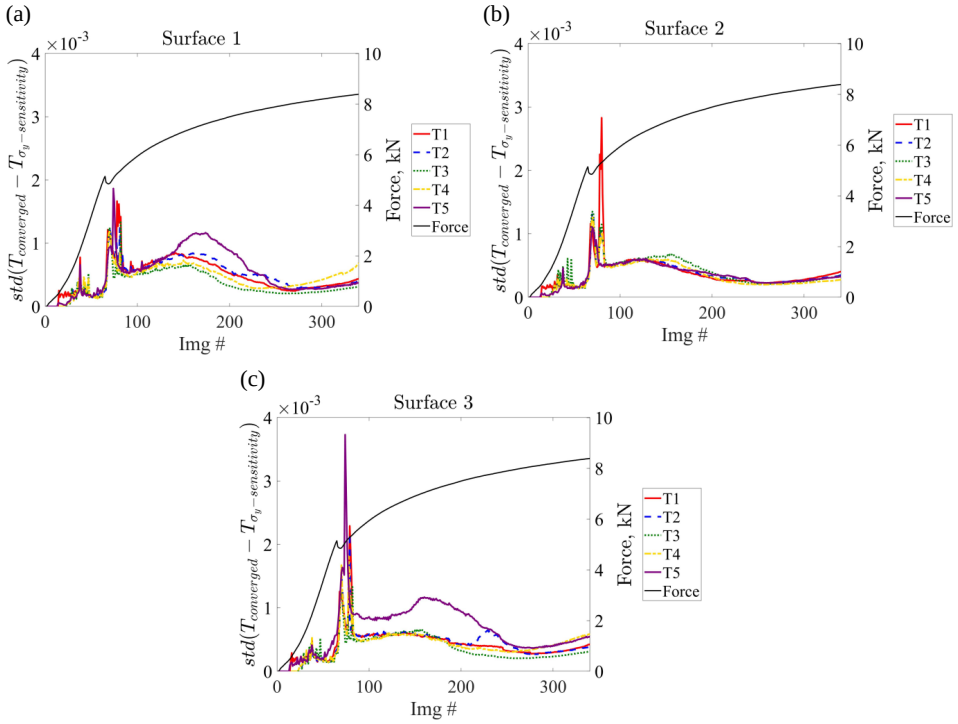

Fig. 13: Standard sensitivity of stress triaxiality fields to σ_y for each test case for (a) Surface 1, (b) Surface 2 and (c) Surface 3. A sudden increase in standard sensitivity occurred in the early stages of yielding for each test case. These changes are negligible since they were two orders of magnitude lower than the actual stress triaxiality levels.

The standard sensitivity of the stress triaxiality fields to parameter C (Figure 14) was the highest in the early stages of hardening. In elasticity and early plasticity, they were negligible and after yielding they began to rise. After the maximum point, the values decreased and remained low until the end of the numerical simulations. For case T5, the highest level was reached for Surfaces 1 and 3. For Surface 2, all test cases displayed similar values. However, for Surfaces 1 and 3, T4 was an outlier since toward the end of the simulation the stress

triaxiality differences did not follow the same trend as the other test cases.

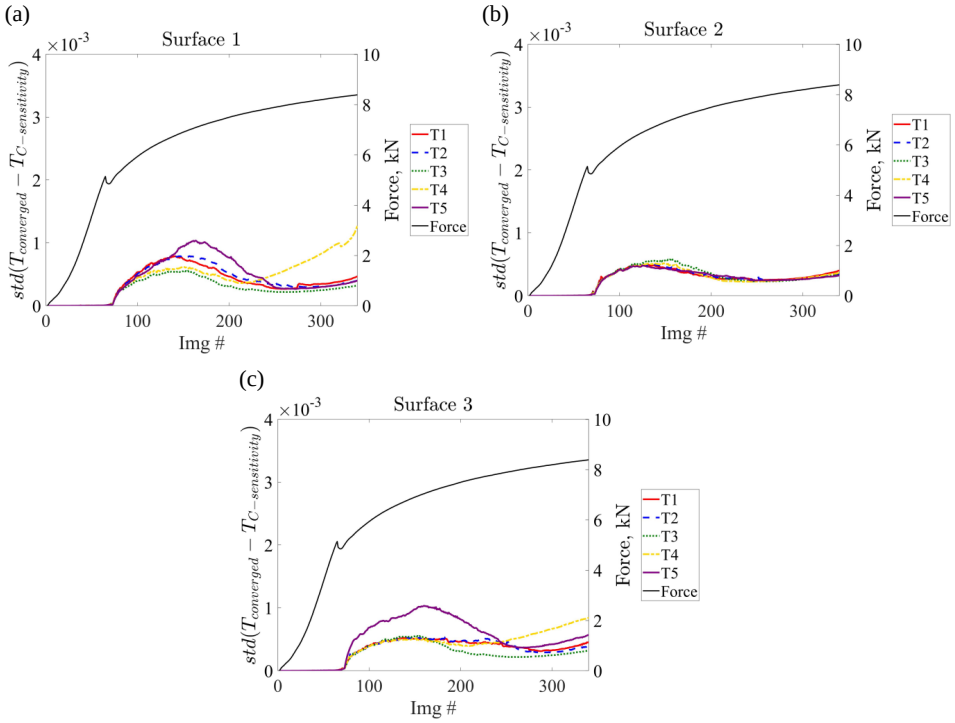

Fig. 14: Standard sensitivity of stress triaxiality fields to parameter C for each test case for (a) Surface 1, (b) Surface 2 and (c) Surface 3. The standard sensitivities were higher in early plasticity. Such changes are negligible since they are approximately three orders of magnitude lower than the actual stress triaxiality levels.

For all test cases, the change in parameter c (see Figure 15) displayed an influence on the stress triaxiality differences at the very end of the numerical simulations (*i.e.*, when approaching the ultimate load). In elasticity and early plasticity, the differences were negligible. During the early stages of hardening the influence was more noticeable. Yet, it was still limited in comparison to later stages. On Surface 1, case T4 displayed much higher values than the other ones due to buckling initiation.

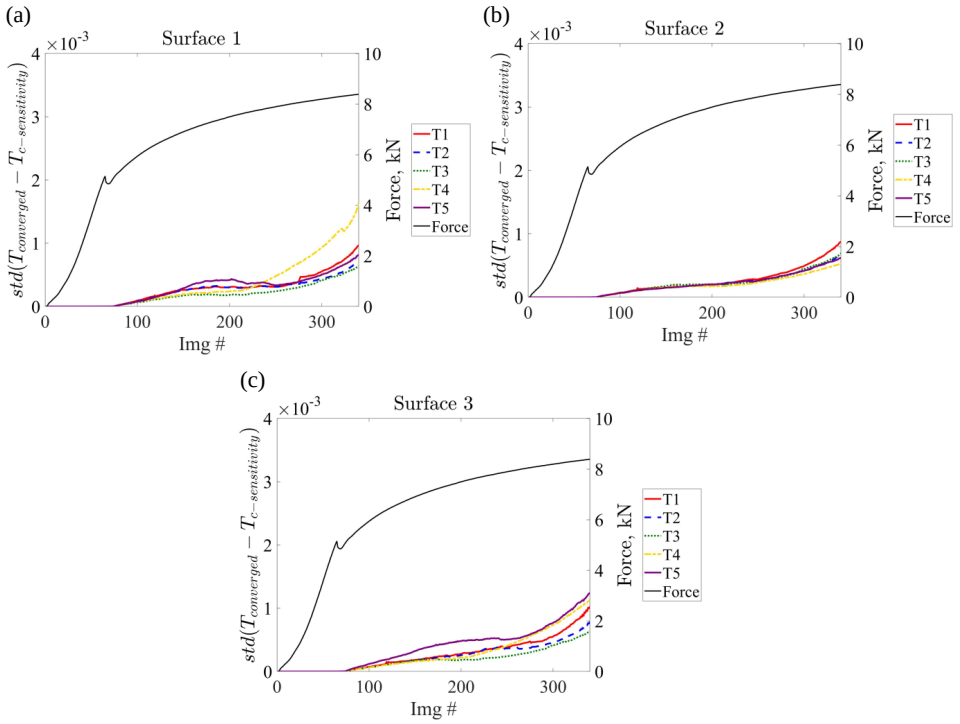

Fig. 15: Standard sensitivity of stress triaxiality fields to parameter c for each test case for (a) Surface 1, (b) Surface 2 and (c) Surface 3. The standard sensitivities are more pronounced at the very end of the numerical simulations. These changes are negligible (three orders of magnitude lower) compared to the actual triaxiality levels.

From Figures 13-15 it was concluded that the change in triaxiality fields remained very limited as the standard variations were of the order of 10^{-3}. These differences were ten times lower than the parameter changes. It is worth noting that for Surface 2, for each parameter, the stress triaxiality differences were minimal and the curves for each test case were in good agreement. For the yield stress σ_y, the differences were higher in amplitude than for the hardening parameters C and c for each test case and surface.

Table 6 gathers the mean sensitivities calculated from image 150 until the end of the analysis for each surface and test case observed in Figures 13-15. For Sur-

faces 1 and 3, larger fluctuations were observed, where T5 displayed the highest sensitivity to material parameter changes. Conversely, for Surface 2, the change of material parameters induced similar influences on the stress triaxiality changes for each test case. These values were two orders of magnitude lower than the parameter change (1%).

Table 6: Mean standard sensitivities to parameter changes for the three considered surfaces

	$\overline{std(\sigma_y)} \times 10^{-4}$			$\overline{std(C)} \times 10^{-4}$			$\overline{std(c)} \times 10^{-4}$		
	S1	**S2**	**S3**	**S1**	**S2**	**S3**	**S1**	**S2**	**S3**
T1	3.9	3.1	4.4	4.2	3.1	4.2	4.3	3.5	4.2
T2	4.3	3.2	4.9	4.1	3.1	4.5	3.7	3.1	3.7
T3	3.1	3.4	3.1	3	3.2	3	2.9	3.1	2.9
T4	4.2	2.9	4.4	5.4	3	6.2	4.7	2.7	5.8
T5	6.7	3.2	5.8	6.2	3	5.3	6.1	3	4.4

Last, the comparison between all test cases is analyzed. Test case T5 was taken as reference and the stress triaxiality fields were subtracted to each previous test case only for Surface 1. This choice was made as measured out-of-plane displacements were prescribed on the aforementioned surface. Root mean square (RMS) differences were calculated and are displayed in Figure 16. It was observed that in elasticity, the RMS differences were about eight times higher than in the hardening stages of the sample (Figure 16(a)). In the semi-logarithmic plot (Figure 16(b)) this trend becomes clearer. In elasticity, each type of BC had a strong influence on the stress triaxiality levels and distributions. As plasticity set in, the displacement levels became higher. Therefore, when comparing these computations, the results

in elasticity were discarded.

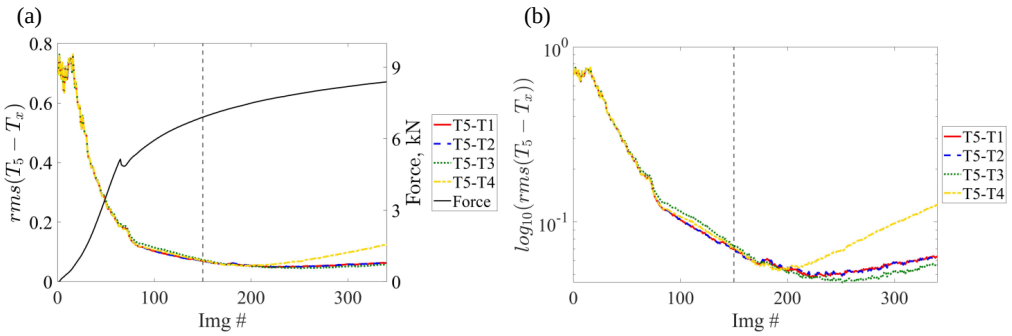

Fig. 16: Root mean square differences in stress triaxiality fields with respect to test case T5 for Surface 1. (a) RMS difference vs. image number. (b) Semi-logarithmic plot of the previous differences. The dashed vertical line depicts the beginning of the computations reported in Table 7. The highest differences are for case T4 where buckling developed whereas for other cases they remained of same order of magnitude.

In Table 7, the mean values of the RMS differences are gathered from image 150 until the final one. It was observed that the lowest value was for T3. Since T1 and T2 were similar, except for the consideration of friction, the mean differences were close. The highest difference was for case T4, where significant and unphysical buckling occurred. Although there was a visible influence of different BCs, they remained low.

Table 7: Mean RMS differences in stress triaxiality fields with respect to T5 for Surface 1

Case	$\overline{RMS}$
T5-T1	0.0561
T5-T2	0.0563
T5-T3	0.0528
T5-T4	0.0768

6. Conclusions and outlook

In this study, an extensive analysis was carried out to evaluate the effect of different Dirichlet BCs on the evaluation stress triaxiality fields. The prescribed displacements were measured via FE-based stereocorrelation for a simple shear test on a 1 mm thick sample. To evaluate stress triaxiality fields, the constitutive equation and its parameters had to be identified. Armstrong-Frederick's kinematic hardening model was selected and calibrated via weighted FEMU.

First, the five investigated cases led to different sets of material parameters. Yet, negligible influence was evidenced on the stress triaxiality fields. A very fine calibration of the material response was thus not required in the studied test.

Second, when modeling the anti-buckling fixture, the friction coefficient was considered as an additional parameter to be calibrated. Compared to the predictions with a very small value, the stress triaxiality fields were very close even though the calibrated material responses were different. Such simulations were very costly, therefore three other cases were also investigated.

Third, by prescribing only in-plane displacements measured on the stressed surfaces of the FE model, limited wrinkling was not accounted for. Interestingly, the stress triaxiality fields were close to the previous estimates and constituted a first estimate if wrinkling had been fully prevented.

Fourth, by also considering the out-of-plane displacements on the stressed edges of the sample, buckling was observed in the simulations. The resulting deformed shape was not consistent with the measured one. Different stress triaxiality fields were observed and it was concluded that they were not physical.

Fifth, prescribing all out-of-plane displacements as BCs on the sample surface,

limited buckling was accurately simulated. The drawback was the inclusion of additional measurement uncertainties through such BCs. As a result, the stress triaxiality fields were more fluctuating, yet close to the levels observed when modeling the anti-buckling fixture. This case provided, by construction, accurate deformed shapes in a less computationally demanding manner than the first one.

The framework presented herein is not limited to the specific experiment where simple shear was applied to an Arcan sample. The procedure is generic and may also be applied to simpler or more complex experimental investigations and for other materials.

Acknowledgements

This work was performed within the FULLINSPECT project supported by the Croatian Science Foundation (UIP-2019-04-5460 Grant). The authors also acknowledge and thank EikoSim for providing the EikoTwin DIC software to perform the stereocorrelation analysis reported herein.

Compliance with Ethical Standards

The authors have no conflict of interest to declare.

References

[1] Tekkaya AE, Allwood JM, Bariani PF, Bruschi S, Cao J, Gramlich S, Groche P, Hirt G, Ishikawa T, Löbbe C, Lueg-Althoff J, Merklein M, Misiolek WZ, Pietrzyk M, Shivpuri R, Yanagimoto J (2015) Metal forming beyond shaping: Predicting and setting product properties. CIRP Ann - Manuf Technol 64(2):629–653, 10.1016/j.cirp.2015.05.001

[2] Bae DG, Ghosh AK (2000) A planar simple shear test and flow behavior in a superplastic Al-Mg alloy. Metall Mater Trans A 34:2465–2471

[3] Driemeier L, Brünig M, Micheli G, Alves M (2010) Experiments on stress-triaxiality dependence of material behavior of aluminum alloys. Mech Mater 42:207–217, 10.1016/j.mechmat.2009.11.012

[4] Zhang K, Badreddine H, Hfaiedh N, Saanouni K, Liu J (2021) Enhanced CDM model accounting of stress triaxiality and Lode angle for ductile damage prediction in metal forming. Int J Damage Mech 30(2):260–282, 10.1177/105678952095804

[5] Sutton M, Wolters W, Peters W, Ranson W, McNeill S (1983) Determination of displacements using an improved digital correlation method. Image Vis Comput 1(3):133–139, 10.1016/0262-8856(83)90064-1

[6] Sutton M, McNeill S, Helm J, Chao Y (2000) Advances in two-dimensional and three-dimensional computer vision. In: Rastogi P (ed) Photomechanics, Springer, Berlin (Germany), vol Topics in Appl. Phys., 77, pp 323–372

[7] Hild F, Roux S (2006) Digital image correlation: From measurement to identification of elastic properties - a review. Strain 42:69–80

[8] Pan B, Qian K, Xie H, Asundi A (2009) Two-dimensional digital image correlation for in-plane displacement and strain measurement: a review. Measurement Science and Technology 20(6):062001, 10.1088/0957-0233/20/6/062001

[9] Sutton M (2013) Computer vision-based, noncontacting deformation measurements in mechanics: A generational transformation. Applied Mechanics Reviews 65(AMR-13-1009):050802

[10] Sutton M, Hild F (2015) Recent advances and perspectives in digital image correlation. Experimental Mechanics 55(1):1–8

[11] Sun Y, Pang J, Wong C, Su F (2005) Finite-element formulation for a digital image correlation method. Applied Optics 44(34):7357–7363

[12] Besnard G, Hild F, Roux S (2006) "Finite-element" displacement fields analysis from digital images: Application to Portevin-Le Chatelier bands. Experimental Mechanics 46:789–803

[13] Hild F, Roux S (2012) Comparison of Local and Global Approaches to DIC. Exp Mech 52(9):1503–1519, 10.1007/s11340-012-9603-7

[14] Wang B, Pan B (2016) Subset-based local vs. finite element-based global digital image correlation: A comparison study. Theor Appl Mech Lett 6(5):200–208, 10.1016/j.taml.2016.08.003

[15] Lou Y, Chen L, Clausmeyer T, Tekkaya A, Whan Yoon J (2017) Modeling of ductile fracture from shear to balanced biaxial tension for sheet metals. Int J Solids Struct 112:169–184, 10.1016/j.ijsolstr.2016.11.034

[16] Yu F, Ben Jar P, Hendry M (2018) Constitutive analysis of pressure-insensitive metals under axisymmetric tensile loading: A stress triaxiality-dependent plasticity damage model. Int J Mech Sci 142–143:21–32, 10.1016/j.ijmecsci.2018.04.035

[17] Peng J, Wang Y, Dai Q, Liu Y, Liu L, Zhang Z (2019) Effect of Stress Triaxiality on Plastic Damage Evolution and Failure Mode for 316L Notched Specimen. Metals 9(1067):1–18, 10.3390/met9101067

[18] Rickhey F, Hong S (2022) Stress Triaxiality in Anisotropic Metal Sheets—Definition and Experimental Acquisition for Numerical Damage Prediction. Materials 15(11):3738, 10.3390/ma15113738

[19] Wang S, Wang Y, Yu L, Ji K, Liu X, Lou Y (2022) Failure Modeling for QP980 Steel by a Shear Ductile Fracture Criterion. Metals 12(452):1–18, 10.3390/met12030452

[20] Djaziri S, Renault P, Hild F, Le Bourhis E, Goudeau P, Thiaudière D, Faurie D (2011) Combined synchrotron x-ray and image-correlation analyses of biaxially deformed w/cu nanocomposite thin films on kapton. J Appl Crystallogr 44:1071–1079, 10.1107/S0021889811030226

[21] Djaziri S, Faurie D, Le Bourhis E, Goudeau P, Renault P, Mocuta C, Thiaudière D, Hild F (2013) Deformation modes of nanostructured thin film under controlled biaxial deformation. Thin Solid Films 530:30–34, 10.1016/j.tsf.2012.05.051

[22] Güner A, Zillmann B, Lampke T, Tekkaya AE (2014) In-situ Measurement of Loading Stresses with X-ray Diffraction for Yield Locus Determination. Int J Automot Technol 15(2):303–316, 10.1007/s12239-014-0031-9, http://link.springer.com/article/10.1007/s12239-012-0027-2

[23] Voillot B, Lebrun JL, Billardon R, Hild F (2018) Validation of registration

techniques applied to XRD signals for stress evaluations in titanium alloys. Experimental Mechanics 58(8):1265–1280, 10.1007/s11340-018-0391-6

[24] Réthoré J (2017) Computational measurements of stress fields from digital images. Int J Numer Methods Eng 113(12):1810–1826, https://doi.org/10.1002/nme.5721

[25] Dalémat M, Coret M, Leygue A, Verron E (2019) Measuring stress field without constitutive equation. Mech Mater 136, 10.1016/j.mechmat.2019.103087

[26] Musiał S, Nowak M, Maj M (2019) Stress field determination based on digital image correlation results. Arch Civ Mech Eng 19(4):1183–1193, 10.1016/j.acme.2019.06.007

[27] Andrade F, Conde S, Feucht M, Helbig M, Haufe A (2019) Estimation of Stress Triaxiality from optically measured Strain Fields. In: 12th European LS-DYNA Conference, 1

[28] Brosius A, Küsters N, Lenzen M (2018) New method for stress determination based on digital image correlation data. CIRP Ann 67(1):269–272, 10.1016/j.cirp.2018.04.026

[29] Lindner D, Mathieu F, Hild F, Allix O, Minh CH, Paulien-Camy O (2015) On the evaluation of stress triaxiality fields in a notched titanium alloy sample via integrated digital image correlation. J Appl Mech Trans ASME 82(7):1–10, 10.1115/1.4030457

[30] Abushawashi Y, Xiao X, Astakhov V (2013) A novel approach for determining material constitutive parameters for a wide range of triaxiality under plane strain loading conditions. Int J Mech Sci 73:133–142, 10.1016/j.ijmecsci.2013.05.007

[31] Barsoum I, Faleskog J, Pingle S (2012) The effect of stress state on ductility in the moderate stress triaxiality regime of medium and high strength steels. Int J Mech Sci 65:203–212, 10.1016/j.ijmecsci.2012.10.003

[32] Anderson D, Winkler S, Bardelcik A, Worswick M (2014) Influence of stress triaxiality and strain rate on the failure behavior of a dual-phase DP780 steel. Mater Des 60:198–207, 10.1016/j.matdes.2014.03.073

[33] Brünig M, Brenner D, Gerke S (2015) Stress state dependence of ductile damage and fracture behavior: Experiments and numerical simulations. Eng Frac Mech 141:152–169, 10.1016/j.engfracmech.2015.05.022

[34] Brünig M, Gerke S, Zistl M (2019) Experiments and numerical simulations with the H-specimen on damage and fracture of ductile metals under non-proportional loading paths. Eng Frac Mech 217:106531, 10.1016/j.engfracmech.2019.106531

[35] Gerke S, Adulyasak P, Brünig M (2017) New biaxially loaded specimens for the analysis of damage and fracture in sheet metals. Int J Solids Struct 110–111:209–218, 10.1016/j.ijsolstr.2017.01.027

[36] Brünig M, Zistl M, Gerke S (2020) Biaxial experiments on characterization of stress-state-dependent damage in ductile metals. Prod Eng 14:87–93, 10.1007/s11740-019-00930-2

[37] Zistl M, Brünig M, Gerke S (2022) Analysis of damage and fracture behavior in ductile metal sheets undergoing compression and shear preloading. Int J Mater Form 15(59):1–14, 10.1007/s12289-022-01705-4

[38] Huang J, Guo Y, Qin D, Zhou Z, Li D, Li Y, Li Y (2018) Influence of stress triaxiality on the failure behavior of Ti-6Al-4V alloy under a broad range of strain rates. Theor Appl Fract Mech 97:48–61, 10.1016/j.tafmec.2018.07.008

[39] Wang B, Xiao X, Astakhov V, Liu Z (2019) The effects of stress triaxiality and strain rate on the fracture strain of Ti6Al4V. Eng Frac Mech 219:106627, 10.1016/j.engfracmech.2019.106627

[40] Peng J, Zhou P, Wang Y, Dai Q, Knowles D, Mostafavi M (2021) Stress Triaxiality and Lode Angle Parameter Characterization of Flat Metal Specimen with Inclined Notch. Metals 10(11):1627, 10.3390/met11101627

[41] Pham VV, Nguyen VC, Tounsi A (2022) Static bending and buckling analysis of bi-directional functionally graded porous plates using an improved first-order shear deformation theory and FEM. Eur J Mech A/Solids 96:104743, 10.1016/j.euromechsol.2022.104743

[42] Avril S, Bonnet M, Bretelle A, Grédiac M, Hild F, Ienny P, Latourte F, Lemosse D, Pagano S, Pagnacco E, Pierron F (2008) Overview of identification methods of mechanical parameters based on full-field measurements. Experimental Mechanics 48(4):381–402

[43] Grédiac M, Hild F (eds) (2012) Full-Field Measurements and Identification in Solid Mechanics. ISTE / Wiley, London (UK)

[44] Pierron F, Grédiac M (2021) Towards Material Testing 2.0. A review of test design foridentification of constitutive parameters from full-field measurements. Strain 57:e12370, 10.1111/str.12370

[45] Kavanagh KT, Clough RW (1971) Finite element applications in the characterization of elastic solids. Int J Solids Struct 7(1):11–23, 10.1016/0020-7683(71)90015-1

[46] Kavanagh KT (1972) Extension of classical experimental techniques for characterizing composite-material behavior. Exp Mech 12(1):50–56, 10.1007/BF02320791

[47] Pagnacco E, Caro-Bretelle A, Ienny P (2012) Parameter identification from mechanical field measurements using finite element model updating strategies. In: Grédiac M, Hild F (eds) Full-Field Measurements and Identification in Solid Mechanics, ISTE / Wiley, London (UK), pp 247–274

[48] Prates PA, Pereira AF, Sakharova NA, Oliveira MC, Fernandes JV (2016) Inverse Strategies for Identifying the Parameters of Constitutive Laws of Metal Sheets. Adv Mater Sci Eng 2016(Dic):1–18, 10.1155/2016/4152963

[49] Tarantola A (1987) Inverse Problems Theory. Methods for Data Fitting and Model Parameter Estimation. Elsevier Applied Science, Southampton (UK)

[50] Bertin M, Hild F, Roux S, Mathieu F, Leclerc H, Aimedieu P (2016) Integrated digital image correlation applied to elasto-plastic identification in a biaxial experiment. J Strain Anal Eng Des 51(2):118–131, 10.1177/0309324715614759

[51] Prates PA, Pereira AF, Oliveira MC, Fernandes JV (2019) Analytical sensitivity matrix for the inverse identification of hardening parameters of metal sheets. Eur J Mech A/Solids 75:205–215, 10.1016/j.euromechsol.2019.01.010

[52] Tomičević Z, Kodvanj J, Hild F (2016) Characterization of the nonlinear behavior of nodular graphite cast iron via inverse identification–Analysis of uniaxial tests. Eur J Mech A/Solids 59:140–154, 10.1016/j.euromechsol.2016.02.010

[53] Tomičević Z, Kodvanj J, Hild F (2016) Characterization of the nonlinear behavior of nodular graphite cast iron via inverse identification: Analysis of biaxial tests. Eur J Mech A/Solids 59:195–209, 10.1016/j.euromechsol.2016.03.006

[54] Réthoré J, Muhibullah ET, Coret M, Chaudet P, Combescure A (2013) Robust identification of elasto-plastic constitutive law parameters from digital images using 3D kinematics. Int J Solids Struct 50(1):73–85, 10.1016/j.ijsolstr.2012.09.002

[55] Wang Y, Coppieters S, Lava P, Debruyne D (2016) Anisotropic yield surface identification of sheet metal through stereo finite element model updating. J Strain Anal Eng Des 51(8):598–611, 10.1177/0309324716666437

[56] Lindner D, Mathieu F, Hild F, Allix O, Ha Minh C, Paulien-Camy O (2015) On the evaluation of stress triaxiality fields in a notched titanium alloy sample via integrated DIC. Journal of Applied Mechanics 82(7):071014

[57] Panwitt H, Heyer H, Sander M (2020) Experimental and Numerical Investigation of the Fracture Behavior of Welded Aluminum Cross Joints under Axial Compression. Materials 13(4310):1–23, 10.3390/ma13194310

[58] Brünig M, Zistl M, Gerke S (2021) Numerical Analysis of Experiments on Damage and Fracture Behavior of Differently Preloaded Aluminum Alloy Specimens. Metals 11(381):1–22, 10.3390/met11030381

[59] Pham CH, Adzima F, Coer J, Manach PY (2017) Anti-Buckling Device for Ultra-Thin Metallic Sheets Under Large and Reversed Shear Strain Paths. Exp Mech 57(4):593–602, 10.1007/s11340-017-0256-4

[60] Bertin M, Hild F, Roux S (2017) On the identifiability of the Hill-1948 model with one uniaxial tensile test. Comptes Rendus Mécanique 345(6):363–369, https://doi.org/10.1016/j.crme.2017.04.001

[61] Bertin M, Hild F, Roux S (2017) On the identifiability of Hill-1948 plasticity model with a single biaxial test on very thin sheet. Strain 53(5):e12233, https://doi.org/10.1111/str.12233

[62] Zhang P, Pereira M, Abeyrathna B, Rolfe B, Wilkosz D, Weiss M (2019) Improving the shear test to determine shear fracture limits for thin stainless steel sheet by shape optimisation. Int J Mech Sci 164:105116, 10.1016/j.ijmecsci.2019.105116

[63] Zaplatić A, Tomičević Z, Čakmak D, Hild F (2022) Improvement of the Arcan setup for the investigation of thin sheet behavior under shear loading. Exp Mech 62:313–332, 10.1007/s11340-021-00762-1

[64] Dufour J, Beaubier B, Roux S, Hild F (2014) Displacement measurement using CAD-based stereo-correlation with meshes. In: ICEM conference, 10.1007/978-3-319-06986-9_34

[65] Dubreuil L, Dufour JE, Quinsat Y, Hild F (2016) Mesh-based shape measurements with stereocorrelation. Exp Mech 56(7):1231–1242, 10.1007/s11340-016-0158-x

[66] Pierré JE, Passieux JC, Périé JN (2017) Finite Element Stereo Digital Image Correlation: Framework and Mechanical Regularization. Exp Mech 57(3):443–456, 10.1007/s11340-016-0246-y

[67] Dufour JE, Beaubier B, Hild F, Roux S (2015) CAD-based displacement measurements. Principle and first validations. Exp Mech 55(9):1657–1668, 10.1007/s11340-015-0065-6

[68] Yang DY, Kim JB, Yoon JW (2000) Wrinkling initiation and growth in modified Yoshida buckling test: Finite element analysis and experimental comparison. Int J Mech Sci 42:1683–1714, 10.1016/S0020-7403(99)00046-6

[69] Chen J, Yuan W, Wu W, Yang C (2020) Numerical simulation of wrinkling behavior for the tin plate. In: Procedia Manuf., vol 50, pp 429–432, 10.1016/j.promfg.2020.08.078

[70] Alimirzaei S, Mohammadimehr M, Tounsi A (2019) Nonlinear analysis of viscoelastic micro-composite beam with geometrical imperfection using FEM: MSGT electro-magneto-elastic bending, buckling and vibration solutions. Struct Eng Mech 71(5):485–502, 10.12989/sem.2019.71.5.485

[71] Pham DK, Pham CH, Hancock GJ (2022) Explicit approach for elastic local buckling analysis of thin-walled channels under combined bending and shear. Thin-Walled Struct 173:108925, 10.1016/j.tws.2022.108925

[72] Coulomb C (1821) Théorie des machines simples (in French). Bachelier, Paris (France)

[73] Armstrong PPJ, Frederick C (1966) A mathematical representation of the multiaxial bauschinger effect. CEGB Rep RD/B/N660 24:1–26

[74] Mathieu F, Leclerc H, Hild F, Roux S (2015) Estimation of elastoplastic parameters via weighted FEMU and integrated-DIC. Exp Mech 55(1):105–119, 10.1007/s11340-014-9888-9

Scientific paper 4

A. Zaplatić, Z. Tomičević, X. Chang, I. Skozrit, S. Roux, and F. Hild, “Hybrid infrared-visible multiview correlation to study damage in a woven composite complex-shaped specimen,” Coupled Systems Mechanics, vol. 12, no. 5, pp. 445–459, 2023, doi: 10.12989/csm.2023.12.5.445.

Preprint of the published journal article.

Coupled Systems Mechanics, *Vol. 12, No. 5 (2023) 445-459*
https://doi.org/10.12989/csm.2023.12.5.445

Hybrid infrared-visible multiview correlation to study damage in a woven composite complex-shaped specimen

Andrija Zaplatić[1,2a], Zvonimir Tomičević*[1], Xuyang Chang[2b], Ivica Skozrit[1c], Stephane Roux[2d] and François Hild[2e]

[1]*Faculty of Mechanical Engineering and Naval Architecture, University of Zagreb, 10002 Zagreb, Croatia*
[2]*Université Paris-Saclay, CentraleSupélec, ENS Paris-Saclay, CNRS, LMPS, 91190 Gif-sur-Yvette, France*

(Received May 28, 2023, Revised July 10, 2023, Accepted July 29, 2023)

Abstract. In this study, a cyclic tensile test on a notched butterfly specimen made of woven glass fiber composite was performed on a modified Arcan fixture. During the mechanical test, the sample was monitored with a hybrid stereoscopic system comprised of two visible lights and one infrared camera. The visible light cameras were employed for kinematic measurements using a finite-element-based multiview correlation technique. A semi-hybrid correlation approach was followed, providing Lagrangian temperature fields of the Region of Interest. Due to the complex composite architecture and specimen shape, localized shearing was observed during the tensile loading. Furthermore, asymmetrical damage developed around the notches as revealed by localized strains and thermal hot spots.

Keywords: Arcan fixture; damage; full-field measurements; stereocorrelation; woven composite

1. Introduction

The growing industry standards impose strict requirements for modern materials. Nowadays, conventional engineering materials are substituted with fiber-reinforced polymer matrix composites, especially in high-tech engineering. Composites are lightweight materials, and their architecture can be finely tailored to specific loading conditions. By predicting the loading regimes of in-service conditions, their mass and manufacturing cost are then reduced. However, since composite architectures are complex (Vrgoč *et al.* 2021), extensive mechanical investigations are required for a comprehensive characterization of their degradation under different loading conditions.

Since composite materials are subjected to complex loading regimes during their operational

*Corresponding author, Associate Professor, E-mail: zvonimir.tomicevic@fsb.hr
[a]Ph.D. Student, E-mail: andrija.zaplatic@fsb.hr
[b]Post-doctoral Student, E-mail: xuyang.chang@ens-paris-saclay.fr
[c]Associate Professor, E-mail: ivica.skozrit@fsb.hr
[d]Research Professor, E-mail: Stephane.roux@ens-paris-saclay.fr
[e]Research Professor, E-mail: Francois.HILD@ens-paris-saclay.fr

http://www.techno-press.org/?journal=csm&subpage=8 ISSN: 2234-2184 (Print), 2234-2192 (Online)

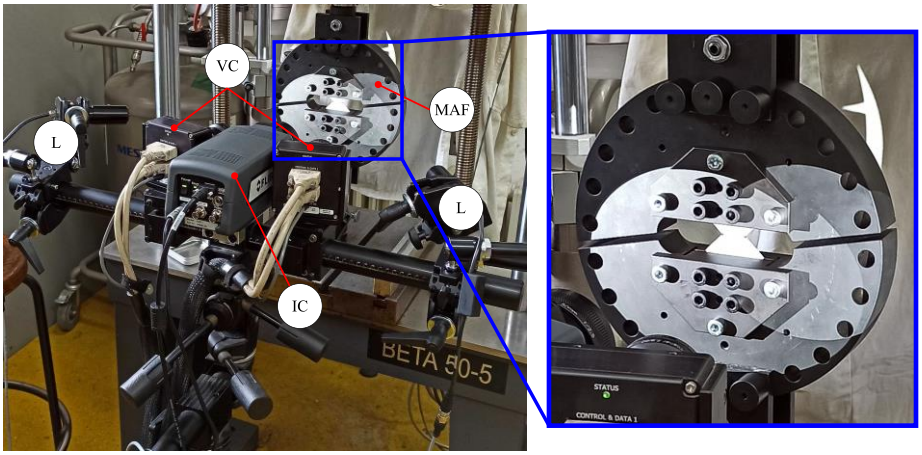

(a) (b)

Fig. 1 (a) Test setup with the modified Arcan fixture and cameras; see text for description of the labels (b) Modified Arcan fixture

time, it is necessary to carry out mechanical tests that simulate realistic working conditions. Tensile tests are the most common due to their simplicity and availability. To simulate different loading types, composite samples are cut at different angles (Vrgoč *et al.* 2021). However, using special loading devices, different loading types can be prescribed to the sample. The modified Arcan fixture or MAF (Zaplatić *et al.* 2022) is a well-established loading apparatus, which provides a wide range of loading types by simply rotating the device. The MAF was used for a variety of materials such as metals (Zaplatić *et al.* 2022, Zaplatić *et al.* 2023), composites (de Sousa Junior *et al.* 2017, Hao *et al.* 2019, Ud Din *et al.* 2020, Holmes *et al.* 2023), adhesive joints (Benelli *et al.* 2023), or wood (Xavier *et al.* 2009). However, advanced measurement protocols are necessary for the full-field characterization of Arcan samples.

The development of visible light cameras prompted the emergence of contactless full-field measurement methods where Digital Image Correlation (DIC) stands out as the most used tool (Sutton *et al.* 2009). In its fundamental form, DIC discretizes the observed region of interest (ROI) into a number of subsets (or facets) and measures the displacements of the center of each facet independently. The drawback of such approaches is the independently measured kinematics, which results in discontinuities, thus requiring additional post-processing interpolation/smoothing. This step can be avoided by using finite element (FE) based DIC, which assumes the continuity of the displacement field over the entire ROI (Hild and Roux 2012). For complex sample geometries, Multiview Correlation or MC (aka stereocorrelation) may be used. MC may also exploit FE meshes (Berny *et al.* 2021). Furthermore, the optical setup can be enriched by adding an infrared camera in so-called hybrid environments (Charbal *et al.* 2016, Wang *et al.* 2020). With hybrid setups, displacements and temperatures are measured simultaneously using hybrid multiview correlation (HMC) algorithms (Dufour *et al.* 2015, Charbal *et al.* 2016, Wang *et al.* 2020).

The aim of this paper is to characterize the response of a woven glass fiber sample under tensile loading. The MAF is used to load the butterfly specimen. A hybrid stereoscopic setup consisting of two visible light and one infrared cameras is employed. FE-based MC is used for displacement and strain measurements. Moreover, a semi-hybrid algorithm is implemented in order to obtain Lagrangian temperature fields using the measured displacement fields.

Table 1 Hardware parameters of the hybrid system

Cameras	2×Dalsa Falcon 4M60	Flir A6751
Definition	2358×1728 px	640×512 px
Digitization	8-bits	16-bits
Lens	Titanar 50 mm	Flir 50 mm
Distance ring	7 mm	6.35 mm
Aperture	f/5.6	-
Stereo-angle	25°	0°
Stand-off distance	260 mm	265 mm
Camera distance	88 mm	-
Image acquisition rate	1 fps	1 fps
Patterning technique	B/W paint	-

2. Experimental investigation

In this research, a cyclic tensile test was carried out with the MAF. The 3-mm thick butterfly specimen was made of woven glass fibers infused with a vinylester resin. The yarns were oriented at 0°/90° along the loading direction. Two notches were cut with a band saw in the central gauge area of the sample. The length of the notches was approximately 2 mm long and 1 mm wide. The speckle pattern on the sample was created by spraying a thin layer of white paint on the surface, and then fine black speckles were applied using a paintbrush. The speckle pattern was not visible in the IR spectrum, hence uniform emissivity ($\varepsilon = 0.96$ (Leistner *et al.* 2019)) was assumed over the observed Region of Interest (ROI). The sample was loaded with a 0.24 mm/min rate in displacement control mode. The experimental and optical setups are shown in Fig. 1. The sample surface was monitored by a stereo-optical camera pair (VL) and one infrared camera (IC) with two light sources (L). In this work, only visible light cameras were used for displacement measurements. The hardware parameters of the optical setup are listed in Table 1.

3. Multiview calibration and correlation

In this section, the FE-based MC algorithm is presented. It is based on the pinhole camera model, which allows any 3D point to be projected onto 2D image planes of each camera *c*

$$s^c \cdot \begin{Bmatrix} x^c \\ y^c \\ 1 \end{Bmatrix} = \left[\mathbf{\Pi}^c \right] \begin{Bmatrix} X \\ Y \\ Z \\ 1 \end{Bmatrix}, \tag{1}$$

where $[\mathbf{\Pi}^c]$ is the projection matrix, s^c the scale factor, x^c and y^c the projected image coordinates of the FE nodal coordinates *X, Y* and *Z*. The projection matrix $[\mathbf{\Pi}^c]$ is calculated by multiplying the intrinsic $[\mathbf{K}^c]$ and extrinsic $[\mathbf{T}^c]$ matrices

$$\left[\mathbf{\Pi}^c\right]=\left[\mathbf{K}^c\right]\left[\mathbf{T}^c\right]=\begin{bmatrix} f_x & \xi & c_x \\ 0 & f_y & c_y \\ 0 & 0 & 1 \end{bmatrix}\begin{bmatrix} r_{11} & r_{12} & r_{13} & t_x \\ r_{21} & r_{22} & r_{23} & t_y \\ r_{31} & r_{32} & r_{33} & t_z \end{bmatrix}. \tag{2}$$

where f_x and f_y are the horizontal and vertical scale factors expressed in pixels, c_x and c_y the positions of the optical center, and ξ is the skew angle which is often disregarded since the horizontal and vertical scale factors are similar. The parameters r_{ij} in the extrinsic matrix $[\mathbf{T}^c]$ refer to three Euler angles ψ, φ and θ and their combinations. Finally, the last three parameters of the extrinsic matrix $[\mathbf{T}^c]$ are three translations t_x, t_y and t_z in x, y and z directions, respectively. During the calibration procedure, the extrinsic and intrinsic parameters are determined for each camera to construct the projection matrices $[\mathbf{\Pi}^c]$.

3.1 Camera calibration procedure

The calibration procedure was initialized by *Point and Perspective* (PnP) solutions (Lepetit *et al.* 2009) solutions to obtain initial guesses of the extrinsic and intrinsic parameters from which the initial projection matrices $[\mathbf{\Pi}^c]$ are constructed for each camera c. At least 6 points are chosen on the FE mesh ($\mathbf{X}$), and their respective positions in the images are selected ($\boldsymbol{x}^c$). For calibration, gray level conservation is assumed such that the pictures captured by the left $f^1(\boldsymbol{x}^1)$ and right $f^2(\boldsymbol{x}^2)$ cameras (where $\boldsymbol{x}^c = (x^c, y^c)$ and c=1 or 2) satisfy

$$f^1\left(\boldsymbol{x}^1\right)= f^2\left(\boldsymbol{x}^2\right) \tag{3}$$

Eq. (3) is only valid if the calibration parameters are properly determined without any acquisition noise. Therefore, a global formulation is performed where the Sum of Squared Differences (SSD)

$$\rho^2\left(\{\mathbf{P}\}\right)=\left\| f^1\left(\boldsymbol{x}^1\left(\mathbf{X},\left[\mathbf{\Pi}^1\right]\right)\right)- f^2\left(\boldsymbol{x}^2\left(\mathbf{X},\left[\mathbf{\Pi}^2\right]\right)\right)\right\|^2 \tag{4}$$

is minimized over the chosen ROI where ρ denotes the calibration residuals and $\{\mathbf{P}\}$ collects the intrinsic and extrinsic parameters of the two cameras. For this integrated approach, the intrinsic and extrinsic parameters are first calibrated, and from which the projection matrices $[\mathbf{\Pi}^{1,2}]$ are then obtained. The sensitivity fields with respect to each parameter are computed via finite differences. The small parameter variations lead to pseudo-displacement fields in the 2D camera planes for each 3D point from $\boldsymbol{x}^c$ to $\boldsymbol{x}^c + \delta\boldsymbol{x}^c$ from which the sensitivity field for each camera is expressed as

$$\mathbf{S}_\mathbf{P}^c = \frac{\delta \boldsymbol{x}^c}{\delta \mathbf{P}^c} \tag{5}$$

which is a 2D vector field defined at each evaluation point $\mathbf{X}$. In the calibration procedure, the intrinsic and extrinsic parameters are progressively updated to minimize the cost function (4) via Gauss-Newton iterations. After computing the sensitivity fields, the Hessian $[\mathbf{H}^c]$ for each camera is computed as

$$\left[\mathbf{H}^c\right]=\sum_{ROI}\left[\nabla f^c\left(\boldsymbol{x}^c\left(\mathbf{X},\left[\mathbf{\Pi}^c\right]\right)\right)\cdot\mathbf{S}_\mathbf{P}^c\right]^\mathrm{T}\left[\nabla f^c\left(\boldsymbol{x}^c\left(\mathbf{X},\left[\mathbf{\Pi}^c\right]\right)\right)\cdot\mathbf{S}_\mathbf{P}^c\right] \tag{6}$$

All camera-wise Hessian matrices are gathered in the global Hessian matrix [**C**]

$$\left[\mathbf{C}\right]=\begin{bmatrix}\left[\mathbf{H}^1\right] & 0\\ 0 & \left[\mathbf{H}^2\right]\end{bmatrix} \tag{7}$$

Next, the camera parameter-based second member $\{\mathbf{b}^c\}$ is expressed as

$$\begin{aligned}\left\{\mathbf{b}^1\right\}&=\sum_{ROI}\left[\mathbf{S}_\mathbf{P}^1\cdot\nabla f^1\left(\boldsymbol{x}^1\right)\right]^T\cdot\left(f^1\left(\boldsymbol{x}^1\left(\mathbf{X},\left[\boldsymbol{\Pi}^1\right]\right)\right)-f^2\left(\boldsymbol{x}^2\left(\mathbf{X},\left[\boldsymbol{\Pi}^2\right]\right)\right)\right)\\ \left\{\mathbf{b}^2\right\}&=\sum_{ROI}\left[\mathbf{S}_\mathbf{P}^2\cdot\nabla f^2\left(\boldsymbol{x}^2\right)\right]^T\cdot\left(f^2\left(\boldsymbol{x}^2\left(\mathbf{X},\left[\boldsymbol{\Pi}^2\right]\right)\right)-f^1\left(\boldsymbol{x}^1\left(\mathbf{X},\left[\boldsymbol{\Pi}^1\right]\right)\right)\right)\end{aligned} \tag{8}$$

and are gathered in the global second member

$$\left\{\mathbf{B}\right\}=\begin{Bmatrix}\left\{\mathbf{b}^1\right\}\\ \left\{\mathbf{b}^2\right\}\end{Bmatrix} \tag{9}$$

At each iteration step the corrections to the sought parameters for each camera are calculated

$$\left\{\delta\mathbf{P}\right\}=\left[\mathbf{C}\right]^{-1}\left\{\mathbf{B}\right\} \tag{10}$$

until the convergence criterion over the stationarity of the residuals, expressed in gray levels, is satisfied

$$\Delta\rho=\rho^n-\rho^{n-1}<10^{-5} \tag{11}$$

where n is the number of the current iteration.

3.2 Kinematic measurements

After calibrating the cameras, the nodal-wise kinematic field **U**(**X**) is measured at any given time t. The new SSD cost function considers the reference images f^c and corrected deformed image $\tilde{g}^c(t)$ at time t for each respective camera

$$\mathbf{U}(\mathbf{X},t)=\min\sum_{1}^{c=Nc}\sum_{ROI}\left(\tilde{g}^c_{\mathbf{U}(\mathbf{X},t)}\left(\boldsymbol{x}^c\left(\mathbf{X},\left[\boldsymbol{\Pi}^c\right]\right),t\right)-f^c\left(\boldsymbol{x}^c\left(\mathbf{X},\left[\boldsymbol{\Pi}^c\right]\right)\right)\right)^2 \tag{12}$$

where $\tilde{g}^c_{\boldsymbol{U}(\boldsymbol{X},t)}(x^c(\boldsymbol{X},[\boldsymbol{\Pi}^c]),t)$ represents the deformed image acquired by camera c at time t corrected by the displacement field $\boldsymbol{U}(\boldsymbol{X},t)$ and N_c the number of cameras. The regularity of the kinematic field $\boldsymbol{U}(\boldsymbol{X},t)$ in space, is ensured using a set of spatial shape functions $\boldsymbol{\Phi}$(**X**)

$$\mathbf{U}\left(\mathbf{X},t\right)=\sum_{1}^{i=N_{DOF}}u_i\left(t\right)\boldsymbol{\Phi}_i\left(\mathbf{X}\right) \tag{13}$$

where N_{DOF} is the number of degrees of freedom, u_i the nodal displacements determined at each step t. In the present case, three-noded (T3) elements were considered (Berny *et al.* 2021). An iterative Gauss-Newton scheme was employed for the FE-based MC procedure. Therefore, the Hessian matrix [$\mathbf{H}_U$] and second member vector {$\mathbf{B}_U$} need to be computed

$$\left[\mathbf{H}_{\mathrm{U}}\right]=\sum_{1}^{c=N_c}\sum_{ROI}\left(\boldsymbol{\Phi}(\mathbf{X})\cdot\frac{\partial \boldsymbol{x}^c}{\partial \mathbf{X}}\cdot\nabla f^c\left(\boldsymbol{x}^c\left(\mathbf{X},\left[\boldsymbol{\Pi}^c\right]\right)\right)\right)^{\mathrm{T}}\left(\boldsymbol{\Phi}(\mathbf{X})\cdot\frac{\partial \boldsymbol{x}^c}{\partial \mathbf{X}}\cdot\nabla f^c\left(\boldsymbol{x}^c\left(\mathbf{X},\left[\boldsymbol{\Pi}^c\right]\right)\right)\right) \tag{14}$$

and

$$\left\{\mathbf{B}_{\mathrm{U}}\right\}=\sum_{1}^{c=N_c}\sum_{ROI}\left(\boldsymbol{\Phi}(\mathbf{X})\cdot\frac{\partial \boldsymbol{x}^c}{\partial \mathbf{X}}\cdot\nabla f^c\left(\boldsymbol{x}^c\left(\mathbf{X},\left[\boldsymbol{\Pi}^c\right]\right)\right)\right)^{\mathrm{T}}\cdot\left(\tilde{g}^c_{\mathbf{U}(\mathbf{X},t)}\left(\boldsymbol{x}^c\left(\mathbf{X},\left[\boldsymbol{\Pi}^c\right]\right),t\right)-f^c\left(\boldsymbol{x}^c\left(\mathbf{X},\left[\boldsymbol{\Pi}^c\right]\right)\right)\right) \tag{15}$$

where $\frac{\partial \boldsymbol{x}^c}{\partial \mathbf{X}}$ is the displacement sensitivity. The nodal displacement amplitude corrections are calculated

$$\left\{\delta \boldsymbol{u}\right\}=\left[\mathbf{H}_{\mathrm{U}}\right]^{-1}\left\{\mathbf{B}_{\mathrm{U}}\right\} \tag{16}$$

and the nodal displacement vector is updated

$$\left\{\boldsymbol{u}(t)\right\}=\left\{\boldsymbol{u}(t)\right\}+\left\{\delta \boldsymbol{u}(t)\right\}. \tag{17}$$

The camera-wise gray-level residuals $\boldsymbol{\varphi}^{\boldsymbol{c}}$ are computed for each evaluation point

$$\varphi^c\left(\boldsymbol{x}^c\right)=\tilde{g}^c_{\mathbf{U}(\mathbf{X},t)}\left(\boldsymbol{x}^c\left(\mathbf{X},\left[\boldsymbol{\Pi}^c\right]\right),t\right)-f^c\left(\boldsymbol{x}^c\left(\mathbf{X},\left[\boldsymbol{\Pi}^c\right]\right)\right) \tag{18}$$

3.3 IR camera

It should be noted that, since the speckle pattern was not visible in IR images, the IR camera could not be calibrated with the approach presented in Section 3.1. Hence only the PnP solution of the projection matrix [$\boldsymbol{\Pi}^3$] was used. Furthermore, no prior IR camera calibration for the tested sample surface was performed and a uniform emissivity $\varepsilon = 0.96$ was assumed over the entire ROI. The measured displacements $\boldsymbol{U}(\boldsymbol{X},t)$ need to be transformed from the FE mesh perspective to the camera plane. The nodal displacements in the IR camera plane $\boldsymbol{u}^{IR}$ are defined

$$\mathbf{u}^{IR}(t)=\mathbf{x}_g^{IR}-\mathbf{x}_f^{IR}(t) \tag{19}$$

where $\boldsymbol{x}_f^{IR}$ is the position of any projected FE node onto the IR camera plane in the reference configuration, and $\boldsymbol{x}_g^{IR}(t)$ that in the deformed configuration. The next step was to determine the projector matrix [**p**], which is used to interpolate nodal values to pixel positions. With the known nodal displacements, it is possible to compute the displacement fields for any pixel position

$$\begin{aligned}\left\{\mathbf{u}_x^{px}(t)\right\}&=\left[\mathbf{p}\right]\cdot\left\{\mathbf{u}_x^{IR}(t)\right\}\\ \left\{\mathbf{u}_y^{px}(t)\right\}&=\left[\mathbf{p}\right]\cdot\left\{\mathbf{u}_y^{IR}(t)\right\}\end{aligned} \tag{20}$$

where $\boldsymbol{u}^{px}$ are the pixel-wise displacements of the ROI. Finally, the IR images were then corrected using the pixel-wise displacements

$$T(\mathbf{x},t)=g^{IR}\left(\mathbf{x}+\mathbf{u}^{px}(\mathbf{x},t),t\right) \tag{21}$$

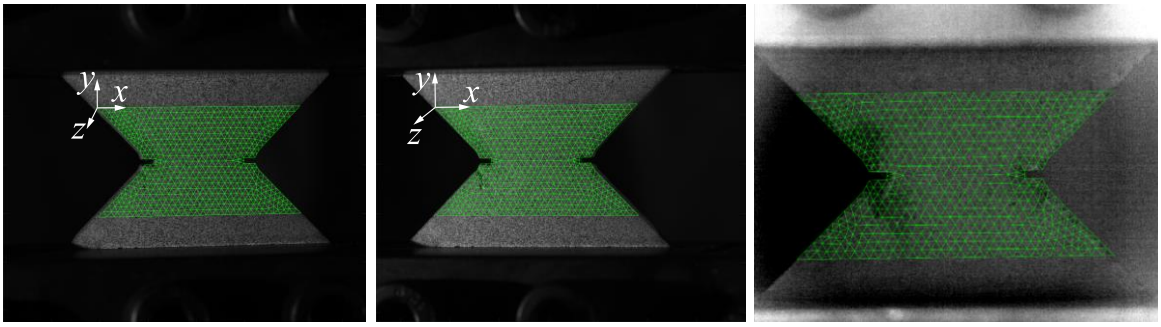

(a) (b) (c)

Fig. 2 Projected 3D mesh with the calibrated projection matrices [$\mathbf{\Pi}^c$] on the image plane of the first (a) and second (b) visible light cameras as well as the IR camera (c)

Table 2 Hybrid multiview analysis parameters

DIC software	Correli 3.0			
Image filtering	None			
Average element length	0.7 mm			
Shape functions	Linear (T3 elements)			
Matching criterion	Sum of squared differences			-
Temperature noise floor	-			0.05°C
Displacement noise floor	U_x	U_y	U_z	-
	0.3 μm	0.4 μm	2 μm	
Strain noise floor	ε_x	ε_y	γ_{xy}	
	5×10^{-4}	6×10^{-4}	4×10^{-4}	

where $T(\boldsymbol{x}, t)$ is the pixel-wise Lagrangian temperature field of the ROI. Since the displacement fields were obtained via FE-based MC performed with images acquired with visible light cameras, it is a semi-hybrid procedure (in contrast with a full hybrid that would include the IR images in the determination of the displacement field (Wang *et al.* 2020).

4. Experimental results

In this section, the multimodal results are discussed. Before the experiment, a set of 10 images was captured in the unloaded state for each camera, which were used for the calculation of measurements uncertainties (Table 2). A single pair of visible light images was used for the full calibration of the projection matrices. The geometry of the sample and its relation to the MAF was known a priori. Hence, characteristic points related to the sample and MAF were used to initialize the calibration procedure. The final projection matrices [$\mathbf{\Pi}^c$] provided good results for the 3D mesh, once projected onto each image plane of the three cameras (Fig. 2). Moreover, a calibration object may be desirable given the planar shape of the sample.

The tensile test consisted of eight loading/unloading cycles. In Fig. 3, the mean net section stress is displayed, which was calculated by dividing the measured force with the initial ligament

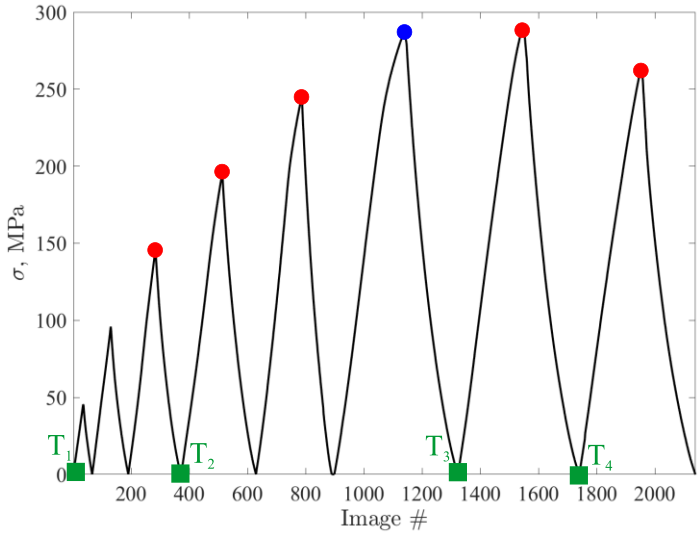

Fig. 3 Loading history of the tensile test. Five characteristic points are outlined by red circles for which kinematic and temperature measurements are reported hereafter. The chosen net section stress levels are 145, 196, 245, 289 and 262 MPa. The blue point denotes 99% of the ultimate tensile strength (289 MPa). The results for this level are not displayed since they were very close to the next one. The green rectangles denote the first image of each loading cycle between CT scans

(a) (b) (c)

Fig. 4 Measured displacement fields expressed in mm for the first cycle peak (145 MPa). Components U_x (a), U_y (b) and U_z (c)

area. The cycles were defined *a priori* by conducting a monotonic tensile test with the same experimental setup and same material. The sample was removed five times from the MAF during the test in order to access any microstructural changes via X-ray computed tomography (CT) (Bartulović *et al.* 2022). The effects of unmounting and remounting of the sample are discussed hereafter. The presented IR images are corrected by subtracting the current temperature field T with the first image of the corresponding loading cycle (Fig. 3). This operation is possible thanks to the fact that Lagrangian fields were obtained.

The first results are for the images captured for the peak of the elastic regime of the material. The displacements for a stress level of 145 MPa are displayed in Fig. 4. The tensile loading axis corresponds to the y-direction (vertical direction in Fig. 2). The largest displacements are reported for the top left and right parts of the ROI. This is due to the geometry of the sample where the central part exhibited higher stiffness than the peripheral zones of the ROI. Displacement gradients are detected in a narrow zone around the notches as well as along vertical lines emanating from the notches. These phenomena are also observed in Fig. 5 and Fig. 6.

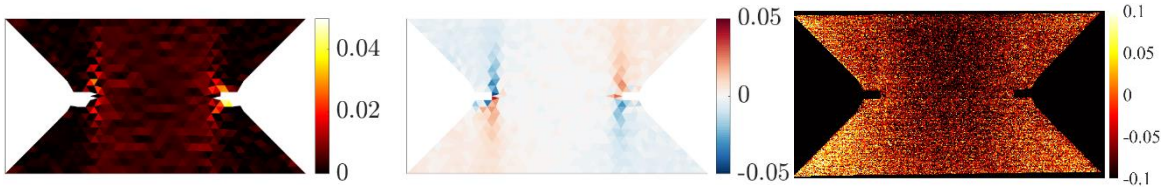

(a) (b) (c)

Fig. 5 Measured strain and temperature fields for the first cycle peak (145 MPa). (a) ε_{yy}, (b) ε_{xy} and (c) ΔT=T-T_1 (in °C)

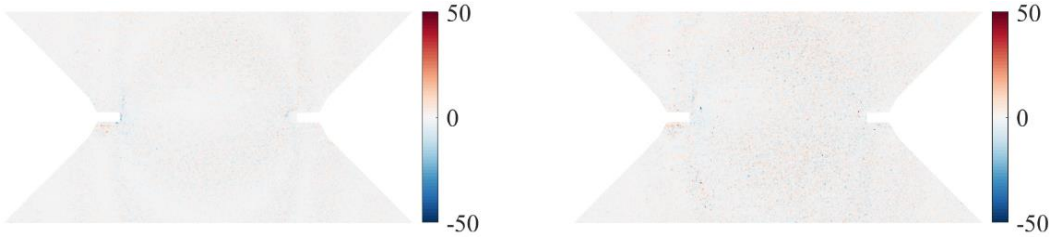

(a) (b)

Fig. 6 Gray level residuals for the first cycle peak (145 MPa) for the first (a) and second (b) cameras

(a) (b) (c)

Fig. 7 Measured displacement fields expressed in mm for the second cycle peak (196 MPa). Components U_x (a), U_y (b) and U_z (c)

The highest strain levels (Fig. 5) are concentrated in small zones around the notches. On both longitudinal (Fig. 5(a)) and shear (Fig. 5(b)) strain fields, two bands oriented along the loading direction are observed. The strain levels on both fields are of the same order of magnitude. Furthermore, the temperature field (Fig. 5(c)) reveals slight decreases in temperature in the center of the sample between the notches, which correspond to thermoelastic effects (Crupi *et al.* 2015).

The correlation residuals (Fig. 6) for this stage between the reference and corrected deformed images reveal very small differences, which may be safely attributed to acquisition noise thereby indicating full convergence of the FE-based MC algorithm.

The second set of results (Figs. 7 and 8) correspond to early onset of mechanical nonlinearity. Increased out-of-plane z displacements is noted (Fig. 7(c)). The rise of these displacements was caused by the first unmounting and remounting of the sample. These perturbations caused rigid body motions, which do not influence the strain fields. The displacements in the y-direction indicate high gradients due to shear bands.

Strained bands are observed on both longitudinal (Fig. 8(a)) and shear (Fig. 8(b)) strain fields. Higher strain levels are reported for the left notch. The temperature field (Fig. 8(c)) still reveals thermoelastic effects in in the entire area between the notches.

(a) (b) (c)

Fig. 8 Measured strain and temperature fields for the second cycle peak (196 MPa). (a) ε_{yy}, (b) ε_{xy} and (c) ΔT=T-T_2 (in °C)

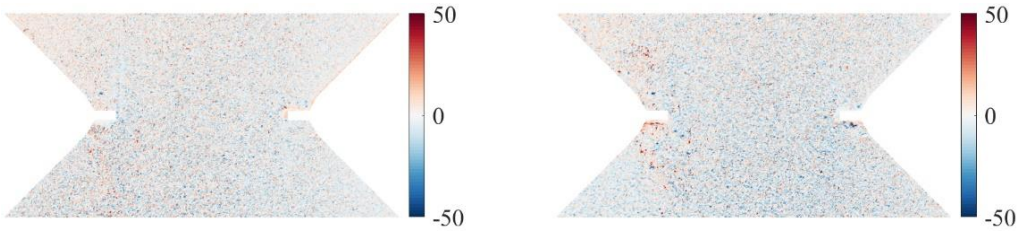

(a) (b)

Fig. 9 Gray level residuals for the second cycle peak (196 MPa) for the first (a) and second (b) cameras

(a) (b) (c)

Fig. 10 Measured displacement fields expressed in mm for the third cycle peak (245 MPa). Components U_x (a), U_y (b) and U_z (c)

The correlation residual levels (Fig. 9) increased overall. The main cause is attributed to changes in brightness and contrast (BC) compared to the reference states, which is seen in the residual levels between the left and right images. It is especially apparent for the second camera. Such a uniform change may result from a rotation of the sample surface with regards to the lighting sources, due to non-Lambertian surface reflectivity/diffusivity. The highest residuals occurred on the left peripheral part of the sample where BC changed the most for both cameras.

Increasing the applied stress by 50 MPa, the displacement fields in the *y*-direction (Fig. 10(b)) experienced the largest change. The displacements in the *y*-direction display much higher gradients due to shear than in Fig. 7(b). Moreover, the displacement fields in *x* and *z*-directions (Fig. 10(a), (c)) experienced very small changes. The high gradients observed in the *x*-direction for U_y displacement field are not observed in the *x* and *z* displacement fields.

The gradients observed in the previous figure have a direct signature in the strain fields shown in Fig. 11. Strain (shear) bands are visible in both longitudinal (Fig. 11(a)) and shear (Fig. 11(b)) strain fields. They are more pronounced than for the previous load level. Both longitudinal and shear strains have similar levels. Increased temperatures are noted in the lower right corner of the ROI (see Fig. 11(c)) and the same localization is present in the strain fields, but not in the residual

(a) (b) (c)

Fig. 11 Measured strain and temperature fields for the third cycle peak (245 MPa). (a) ε_{yy}, (b) ε_{xy} and (c) ΔT=T-T_2 (in °C)

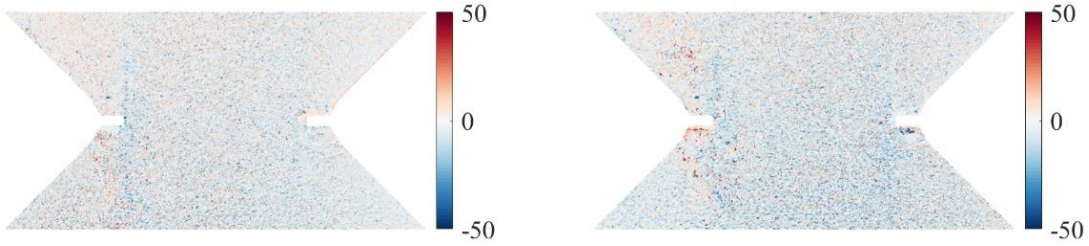

(a) (b)

Fig. 12 Gray level residuals for the third cycle peak (245 MPa) for the first (a) and second (b) cameras

(a) (b) (c)

Fig. 13 Measured displacement fields expressed in mm for the fourth cycle peak (289 MPa). Components U_x (a), U_y (b) and U_z (c)

fields (Fig. 12). Since the increase temperature is minimal, it is attributed to artefactual heating originating from the testing machine and lighting.

The gray level residual fields (Fig. 12) were similar to the previous cycle (Fig. 9), thereby indicating that the BC conditions did not change much during one further unmounting/remounting step. However, increased residuals are noted perpendicular to the left notch, oriented along the loading direction. This location matches that of the shear strain bands. Moreover, below the right hand side notch, the increased residuals coincide with the highest strains (Fig. 11).

The next step corresponds to the ultimate tensile load level tested to investigate whether any damage initiated on the monitored surface. Before this cycle, the sample was removed and mounted again. Rigid body motions are observed from the displacement fields in x and z-directions (Fig. 13(a, c)). High gradients are detected in the displacement field in the y-direction (Fig. 13(b)) between the center and peripheral parts of the sample.

Several shear bands are observed in the strain fields shown in Fig. 14. As seen from the high gradients in Fig. 13, increased strains occurred around the notches. The highest strain levels were reached above the left notch where also a faint variation in temperature is observed indicating that the strain levels were reached earlier, leading to lower temperature and a more diffuse signature.

(a) (b) (c)

Fig. 14 Measured strain and temperature fields for the fourth cycle peak (289 MPa). (a) ε_{yy}, (b) ε_{xy} and (c) ΔT=T-T_3 (in °C)

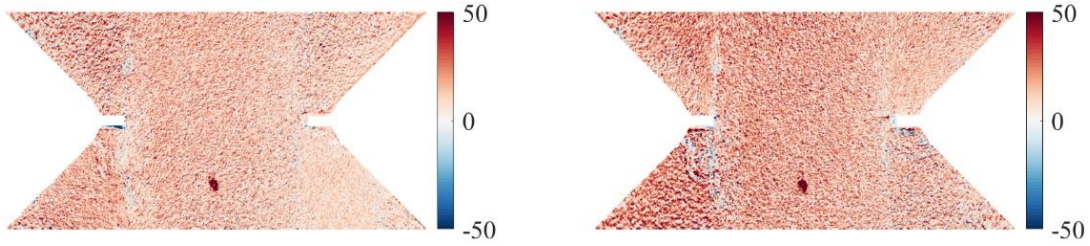

(a) (b)

Fig. 15 Gray level residuals for the fourth cycle peak (289 MPa) for the first (a) and second (b) cameras

(a) (b) (c)

Fig. 16 Measured displacement fields expressed in mm for the fifth cycle peak (262 MPa). Components U_x (a), U_y (b) and U_z (c)

Above the right notch, increased strain levels are also present. This is also observable in the IR image (Fig. 14(c)) where increased changes in temperature are present due to energy dissipation during damage initiation.

The correlation residuals (Fig. 15) reveal changes in BC conditions as for the previously discussed results. For the second camera, the overall residuals are higher than for the first one. Increased residuals are located around the notches. On the notch roots, small areas with higher levels indicate the presence of initiated cracks as was observed in the strain and displacement fields. Furthermore, below the right notch, higher residuals correspond to the shear band that propagated on its edge. A spot with high residuals is also present in the lower central part of the ROI. This was caused by a damaged speckle pattern, which was not related to the loading of the sample but due to its mounting/unmounting.

For the final loading step, the maximum load was lower than the previous one, thus indicating that damage further developed in the sample. Severe gradients are detected in the displacement fields (Fig. 16), especially around the right notch root from which another strain band emanated (Fig. 17). The sample was removed from the testing machine before this last cycle, which caused rigid body motions seen in the *y* and *z*-directions (Fig. 17(a-c)).

(a) (b) (c)

Fig. 17 Measured strain and temperature fields for the first cycle peak (262 MPa). (a) ε_{yy}, (b) ε_{xy} and (c) ΔT=T-T_4 (in °C)

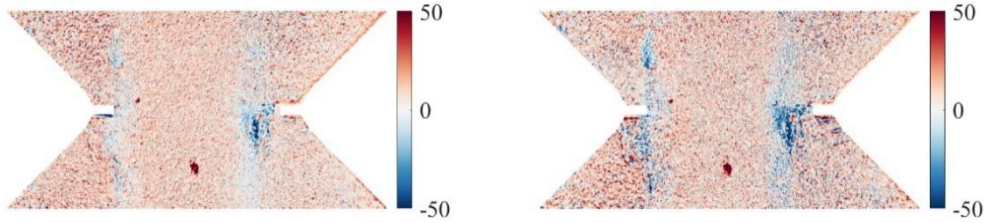

(a) (b)

Fig. 18 Gray level residuals for the fifth cycle peak (262 MPa) for the first (a) and second (b) cameras

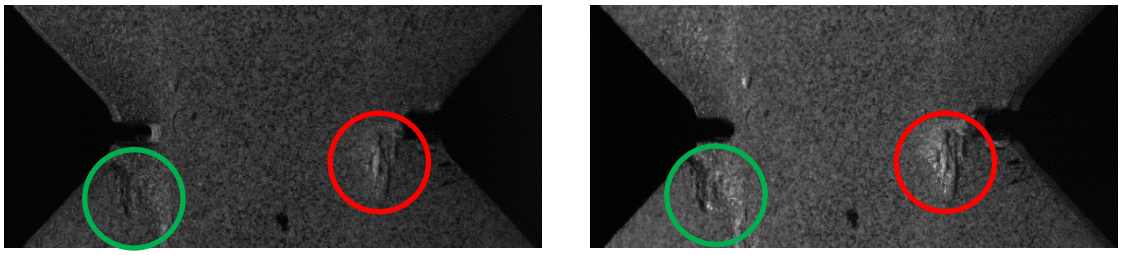

(a) (b)

Fig. 19 Images of the damaged sample acquired by the first (a) and second (b) visible light cameras at the fifth cycle peak. The red circle indicates surface damage. The green circle indicates the surface deformity, which originates from the manufacturing process

The strain fields reveal several shear bands, with two in the vicinity of the right notch where severe damage occurred. In all strain fields (Fig. 17 (a, b)), the bands around the right notch are visible. Moreover, higher changes in temperature are observed in that area, highlighting energy dissipation due to damage. A change in temperature also occurred around the left notch in the same location as high strain levels are reported.

The correlation residuals (Fig. 18) also reveal high levels in the same locations as the strain bands evidenced in the displacement and strain fields. The highest residuals are located under the right notch. Damage also occurred above the left notch, which is clearer for the second camera.

The gray level residuals are compared to the raw images (Fig. 19). The increased residuals correspond to damage observed on the images. Due to differences in BC between images, the residual fields are also slightly different. Moreover, the peripheral areas of the ROI exhibit increased residuals for both cameras. The underlying damage caused the speckled surface to break, hence the FE-based MC algorithm could not converge between the reference and the deformed image since the gray level conservation was violated. From Fig. 19, it is confirmed that damage

was more extensive in the vicinity of the right notch (Fig. 19 red circle).

5. Conclusions

In this study, a cyclic tensile test was performed on a notched glass fiber woven composite with an MAF. A hybrid optical setup with two visible light and one infrared cameras was used to monitor the surface motion of the sample. An FE-based multiview correlation algorithm was employed to measure displacement, strain and temperature fields. The main results of this work are:

- A semi-hybrid multiview procedure was implemented in which Lagrangian temperature fields could be reported over the investigated ROI *in addition to* displacement and strain fields using the exact same spatial coordinates.
- Although unidirectional tensile load was applied on the sample, shear strain bands emanated from the two notches because of the sample geometry and the underlying woven architecture.
- Damage initiated and developed asymmetrically around both notches, which indicates a significant influence of the woven fabric.

Improvements to the experimental setup could enable for a complete multiview and hybrid analysis to be performed. Last, brightness and contrast corrections could be implemented.

Acknowledgments

This work was performed within the FULLINSPECT project supported by the Croatian Science Foundation (UIP-2019-04-5460 Grant). AZ was also supported through the Incoming International Scholarship Program of ENS Paris-Saclay. This work was also partially supported by the European Union through the European Regional Development Fund, Operational Programme "Competitiveness and Cohesion" 2014-2020 of the Republic of Croatia, project "Improvement of high-efficiency welding technology" (ImproWE, KK.01.1.1.07.0076).

References

Bartulović, A., Tomičević, Z., Bubalo, A. and Hild, F. (2022), "Assessment of DVC measurement uncertainty on GFRPs with various fiber architectures", *Coupled Syst. Mech.*, **11**(1), 15-32. https://doi.org/10.12989/csm.2022.11.1.015.

Benelli, A., Ciardiello, R., Boursier Niutta, C. and Goglio, L. (2023), "Experimental and numerical characterization of adhesive joints with composite substrates by means of the Arcan test", *Int. J. Adhes. Adhesiv.*, **122**, 103321. https://doi.org/10.1016/j.ijadhadh.2022.103321.

Berny, M., Archer, T., Beauchêne, P., Mavel, A. and Hild, F. (2021), "Displacement uncertainty quantifications in T3-stereocorrelation", *Exp. Mech.*, **61**(5), 771-790. https://doi.org/10.1007/s11340-021-00690-0.

Berny, M., Archer, T., Hild, F., Mavel, A., Beauchêne, P., Herb, V. and Lacombe, B. (2019), "On performing spatiotemporal stereocorrelation at very high temperatures", *Conference Proceedings of the Society for Experimental Mechanics Series*, **12**, 181-183. https://doi.org/10.1007/978-3-319-97481-1_24.

Berny, M., Archer, T., Mavel, A., Beauchêne, P., Roux, S. and Hild, F. (2018), "On the analysis of heat haze effects with spacetime DIC", *Opt. Laser. Eng.*, **111**, 135-153. https://doi.org/10.1016/j.optlaseng.2018.06.004.

Charbal, A., Dufour, J.E., Hild, F., Poncelet, M., Vincent, L. and Roux, S. (2016), "Hybrid stereocorrelation using infrared and visible light cameras", *Exp. Mech.*, **56**(5), 845-860. https://doi.org/10.1007/s11340-016-0127-4.

Crupi, V., Guglielmino, E., Risitano, G. and Tavilla, F. (2015), "Experimental analyses of SFRP material under static and fatigue loading by means of thermographic and DIC techniques", *Compos. Part B: Eng.*, **77**, 268-277. https://doi.org/10.1016/j.compositesb.2015.03.052.

de Sousa Junior, R.R., Gouveia, J.R., Ito, N.M. and dos Santos, D.J. (2017), "Failure prediction of hybrid composite using Arcan's device and Drucker-Prager model", *Polym. Test.*, **58**, 256-261. https://doi.org/10.1016/j.polymertesting.2017.01.001.

Dufour, J.E., Hild, F. and Roux, S. (2015), "Shape, displacement and mechanical properties from isogeometric multiview stereocorrelation", *J. Strain Anal. Eng. Des.*, **50**(7), 470-487. https://doi.org/10.1177/0309324715592530ï.

Hao, P., Din, I.U. and Panier, S. (2019), "Development of modified Arcan fixture for biaxial loading response of fiber-reinforced composites", *Polym. Test.*, **80**, 106148. https://doi.org/10.1016/j.polymertesting.2019.106148.

Hild, F. and Roux, S. (2012), "Comparison of local and global approaches to digital image correlation", *Exp. Mech.*, **52**(9), 1503-1519. https://doi.org/10.1007/s11340-012-9603-7.

Holmes, J., Sommacal, S., Das, R., Stachurski, Z. and Compston, P. (2023), "Digital image and volume correlation for deformation and damage characterisation of fibre-reinforced composites: A review", *Compos. Struct.*, **315**, 116994. https://doi.org/10.1016/j.compstruct.2023.116994.

Leistner, C., Löffelholz, M. and Hartmann, S. (2019), "Model validation of polymer curing processes using thermography", *Polym. Test.*, **77**, 105893. https://doi.org/10.1016/j.polymertesting.2019.05.009.

Lepetit, V., Moreno-Noguer, F. and Fua, P. (2009), "EPnP: An accurate O(n) solution to the PnP problem", *Int. J. Comput. Vision*, **81**(2), 155-166. https://doi.org/10.1007/s11263-008-0152-6.

Sutton, M.A., Orteu, J.J. and Schreier, H. (2009), *Image Correlation for Shape, Motion and Deformation Measurements: Basic Concepts, Theory and Applications*, Springer Science & Business Media.

Ud Din, I., Hao, P., Panier, S., Khan, K.A., Aamir, M., Franz, G. and Akhtar, K. (2020), "Design of a new arcan fixture for in-plane pure shear and combined normal/shear stress characterization of fiber reinforced polymer composites", *Exp. Techniq.*, **44**(2), 231-240. https://doi.org/10.1007/s40799-019-00353-9.

Vrgoč, A., Tomičević, Z., Smaniotto, B. and Hild, F. (2021), "Damage characterization in fiber reinforced polymer via Digital Volume Correlation", *Coupled Syst. Mech.*, **10**(6), 545-560. https://doi.org/10.12989/csm.2021.10.6.545ï.

Vrgoč, A., Tomičević, Z., Zaplatić, A. and Hild, F. (2021), "Damage analysis in glass fibre reinforced epoxy resin via digital image correlation", *Trans. FAMENA*, **45**(2), 1-12.

Wang, Y., Charbal, A., Dufour, J.E., Hild, F., Roux, S. and Vincent, L. (2020), "Hybrid multiview correlation for measuring and monitoring thermomechanical fatigue test", *Exp. Mech.*, **60**(1), 13-33. https://doi.org/10.1007/s11340-019-00500-8.

Wang, Y., Charbal, A., Hild, F., Roux, S. and Vincent, L. (2019), "Crack initiation and propagation under thermal fatigue of austenitic stainless steel", *Int. J. Fatig.*, **124**, 149-166. https://doi.org/10.1016/j.ijfatigue.2019.02.036.

Xavier, J., Oliveira, M., Morais, J. and Pinto, T. (2009), "Measurement of the shear properties of clear wood by the Arcan test", *Holzforschung*, **63**(2), 217-225. https://doi.org/10.1515/HF.2009.034.

Zaplatić, A., Tomičević, Z., Čakmak, D. and Hild, F. (2022a), "Identifiability of Ludwik's law parameters depending on the sample geometry via inverse identification procedure", *Coupled Syst. Mech.*, **11**(2), 133-149. https://doi.org/10.12989/csm.2022.11.2.133.

Zaplatić, A., Tomičević, Z., Čakmak, D. and Hild, F. (2022b), "Improvement of the Arcan setup for the investigation of thin sheet behavior under shear loading", *Exp. Mech.*, **62**(2), 313-332. https://doi.org/10.1007/s11340-021-00762-1.

Zaplatić, A., Vrgoč, A., Tomičević, Z. and Hild, F. (2023), "Boundary condition effect on the evaluation of stress triaxiality fields", *Int. J. Mech. Sci.*, **246**, 108127. https://doi.org/10.1016/j.ijmecsci.2023.108127.

Scientific paper 5

A. Zaplatić, Z. Tomičević, F. Hild, “Characterization of woven composite material under multiaxial loading regimes using FE-based stereocorrelation”, Acta Polytechnica CTU Proceedings, vol. 48, pp. 56-60., 2024, doi: 10.14311/APP.2024.48.0056

Preprint of the published journal article.

Acta Polytechnica CTU Proceedings **48**:56–60, 2024
https://doi.org/10.14311/APP.2024.48.0056

Published by the Czech Technical University in Prague

CHARACTERIZATION OF WOVEN COMPOSITE MATERIAL UNDER MULTIAXIAL LOADING REGIMES USING FE-BASED STEREOCORRELATION

Andrija Zaplatić[a,b], Zvonimir Tomičević[a,*], François Hild[b]

[a] *University of Zagreb, Faculty of Mechanical Engineering and Naval Architecture, 10002 Zagreb, Croatia*

[b] *Université Paris-Saclay, CentraleSupélec, ENS Paris-Saclay, CNRS, LMPS – Laboratoire de Mécanique Paris-Saclay, 91190 Gif-sur-Yvette, France*

[*] corresponding author: zvonimir.tomicevic@fsb.unizg.hr

Abstract. In this paper, woven glass fiber composite samples were subjected to three different cyclic loading histories (i.e., tensile, shear and combined loading at 45° via the Modified Arcan Fixture. During the experiments, the samples were monitored by a stereovision system. Finite Element based stereocorrelation was used to measure the displacement and strain fields. The analysis of the experiments revealed different damage mechanisms. Furthermore, for the 45° experiment, the highest strain levels were reached, whereas for the tensile test, the highest stress levels were achieved.

Keywords: Stereocorrelation, woven composite, Arcan fixture, multiaxial loading.

1. Introduction

The mechanical characterization of various materials is essential for designing and optimizing engineering components. In modern engineering, traditional materials like steel and alloys are increasingly being replaced by fiber-reinforced polymer (FRP) composites [1]. These composites are highly sought after for their excellent strength-to-weight ratio. An additional advantage of FRPs is their customizable architecture, which can be tailored to meet specific workload conditions. However, predicting the ultimate failure and degradation of these components remains challenging due to their complex architecture. Predicting their lifetime is also challenging due to their heterogeneity, which makes composites susceptible to various damage mechanisms that may degrade their stability [2]. Therefore, extensive experimental investigations are necessary to study the composite behavior under different loading regimes [3]. Since uniaxial mechanical tests do not adequately simulate real-world conditions, more complex loading configurations are required. However, these tests often demand high-cost and specialized testing machines, which may not be readily available.

To address this issue, specially designed loading apparatuses for uniaxial testing machines have been developed. One popular setup is the Modified Arcan Fixture (MAF) [4–6], which applies three distinct loading regimes (i.e., tensile, shear, and their varied combinations at several angles) to butterfly-shaped specimens. The MAF allows for testing a variety of materials, including wood [7] and composite joints [8], although it was originally designed for composite materials [9].

Due to the complex geometry of the Arcan samples, which features two V-notches in the ligament area, classical contact measurement equipment is highly impractical. As a result, contactless optical measurement methods like Digital Image Correlation (DIC) are more suited [10, 11]. DIC utilizes visible light cameras to perform full-field measurements, and in recent years, the global DIC approach has gained popularity [12]. This approach incorporates Finite Element (FE) features in such a way that displacement measurements are performed on meshes. Consequently, the resulting outputs are nodal displacements, from which strain fields are determined. Additionally, this method provides correlation residuals, which highlight damaged areas during the experiment [13]. An added advantage of FE-based approaches is the continuity assumption of the displacement fields, eliminating the need for interpolation as required in local approaches [14].

If out-of-plane motions are expected or a complex 3D sample is being tested, multiple cameras are employed within a stereovision framework [15, 16]. The finite element method has also been integrated into stereocorrelation environments [17–19]. By utilizing the known FE geometry of the observed object, it is possible to perform camera calibration directly on the object itself [19, 20] and then measure 3D surface displacements.

2. Materials and methods

In this section, the woven composite samples, experimental setup, and investigation are presented. Additionally, the FE-based stereocorrelation method is briefly introduced.

2.1. Material

The investigated composite samples were manufactured by reinforcing a vinylester resin with woven glass fibers. The 3 mm thick samples were composed

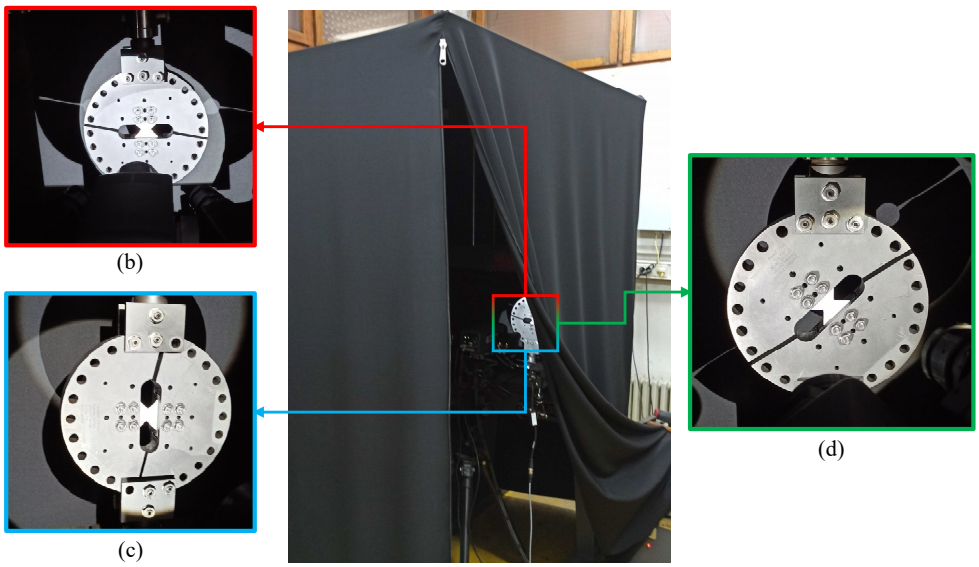

FIGURE 1. Experimental setup. (a) Testing machine and optical system protected by black fabric. Loading configurations: (b) tension, (c) shear and (d) combined tension and shear at 45°.

of 7 layers of woven fabric, where the yarns were 0°/90° oriented. Additionally, the fabric layers were stacked identically on top of each other.

Due to the complex geometry of the samples and the use of glass fibers, conventional machining methods were sub-optimal for processing the composite plates. Therefore, water jet technology was used to cut the samples from the composite plates. To ensure sample failure during the experiment, two additional V-notches were cut for each sample. These additional notches were 2 mm long and 0.5 mm wide, thereby reducing the net section area to approximately 48 mm^2.

2.2. Experimental investigation

The experimental setup (Figure 1a) consisted of the MAF and the optical system. The MAF allows for different loading conditions to be applied to the Arcan sample by rotating the fixture relative to the loading axis. In this research, three Arcan specimens were tested and three loading configurations were prescribed, namely tension (WF00) (Figure 1b), shear (WF90) (Figure 1c), and their combination at 45° (WF45) (Figure 1d). For each experiment, the sample was loaded at a velocity of 2 $\mu\mathrm{m\,s}^{-1}$ in displacement control mode on the Messphysik Beta 50-5 uniaxial testing machine, each experiment consisting of eight loading/unloading cycles. The testing speed was chosen according to previous research [13, 20]. The samples were intermittently taken out of the MAF to perform X-ray computed tomography scanning to obtain any micro-structural changes inside of the material. Therefore, cyclic loading regimes were defined.

To minimize external lighting influences that could affect brightness and contrast conditions, the experimental and optical setups were covered with black fabric (Figure 1a). The optical system included two identical visible light cameras that monitored the surfaces of the samples during the experiments. Furthermore, two light sources were employed to illuminate the sample surface.

2.3. FE based stereocorrelation

In this work, FE-based stereocorrelation [5, 21] was performed to measure 3D surface displacement fields using FE meshes [17–19], which correspond to the observed sample geometry. Additionally, strain fields were calculated from the measured displacement fields.

Stereocorrelation consists of two main steps, namely, calibration and correlation. In the calibration step, the projection matrix $[\pi]$ for each camera is determined, allowing the FE mesh to be projected onto both camera images, defining the same Region of Interest (ROI). The projection matrix $[\pi]$ can be built if the intrinsic and extrinsic camera parameters are known. However, usually they are unknown and are determined with the calibration. The calibration can be defined as a least square minimization between the two camera images

$$\rho^2(\{\mathbf{P}\}) = \sum_{ROI} \left\| f_1\left(\mathbf{x}_1\right) - f_2(\mathbf{x}_2) \right\|^2, \tag{1}$$

where $\{\mathbf{P}\}$ is a vector that gathers all the sought intrinsic and extrinsic parameters, $\mathbf{x}_\mathrm{c}$ are the projected physical points defined over the FE mesh $\mathbf{X}$

$$\mathbf{x}_\mathrm{c} = \mathbf{x}_\mathrm{c}\left(\mathbf{X}, [\pi_\mathrm{c}]\right). \tag{2}$$

In the correlation step, the nodal-wise displacement field $\mathbf{U}(\mathbf{X}, t)$ is measured for any given time-step t. The new cost function can be written as

$$\mathbf{U}(\mathbf{X}, t) = \arg\min \sum_{\mathrm{c}=1}^{N_\mathrm{c}} \sum_{ROI} \left(\tilde{g}_\mathrm{c}\left(\mathbf{x}_\mathrm{c}, t\right) - f_\mathrm{c}\left(\mathbf{x}_\mathrm{c}\right)\right)^2, \tag{3}$$

where f_c are the respective camera reference images, $\tilde{g}_c$ the corrected deformed image at time t by the kinematic field $\mathbf{U}(\mathbf{X}, t)$ for each respective camera and N_c is the camera number. The regularity of the kinematic field $\mathbf{U}(\mathbf{X}, t)$ in space is ensured by using a set of spatial shape functions $\psi_{\mathrm{i}}(\mathbf{X})$

$$\mathbf{U}(\mathbf{X}, t) = \sum_{\mathrm{i}=1}^{DOF} u_{\mathrm{i}}(t)\boldsymbol{\psi}_{\mathrm{i}}(\mathbf{X}), \tag{4}$$

where DOF is the number of degrees of freedom, $u_{\mathrm{i}}(t)$ are the nodal displacements for the time t. In these analyses, the FE meshes consisted of three-noded elements (T3) [19]. Furthermore, the camera-wise gray level residuals ϕ_{c} can be computed for each physical point x_{c}

$$\phi_{\mathrm{c}} = \tilde{g}_{\mathrm{c}}\left(\mathbf{x}_{\mathrm{c}}, t\right) - f_{\mathrm{c}}\left(\mathbf{x}_{\mathrm{c}}\right). \tag{5}$$

Both the calibration and correlation are performed by resorting to the iterative Gauss-Newton scheme. For more detailed information, the reader is referred to Zaplatić et al. [20], Chang et al. [16, 21].

3. Results

In this section, the stereocorrelation results are presented for all three experiments. The major principal strain (Figure 2) and stereocorrelation residual (Figure 3) fields are displayed for the maximum achieved stress level $\sigma_{\max}$ for each experiment respectively (Table 1). From Table 1, it is concluded that the highest stress level was achieved for the tensile test (WF00), whereas the lowest was reached for the shear test (WF90).

In Figure 2 the major principal strain fields are displayed for all three experiments for the maximum stress levels (Table 1). First, for the tensile test (Figure 2a), two concentrated strained bands emanating from the notches are observed. Furthermore, four additional strain concentrations are distinguished on the peripheral areas of the sample. Since the yarns were parallel to the tensile load, the middle part was the most rigid part of the sample, whereas the peripheral areas were not. Hence, they were more prone to damage.

In the shear experiment (Figure 2b), a single strained band is visible in the gauge region, parallel to the loading direction. At the roots of the notches, the strain levels were the highest, whereas the top and bottom parts exhibited very small strain values.

For the WF45 experiment, a single strained band developed between the V notches (Figure 2c), similarly to WF90 test. However, it was slightly inclined compared to the WF90 strained band. Two strain concentrations are visible at diagonal peripheral areas of the sample, depicted by the green circles.

Using the stereocorrelation residuals, it is possible to reveal if surface damage developed. For the tensile test (Figure 3a), three cracks formed around the root of the left notch. Four cracks also developed in peripheral areas, which were also visible in the corresponding strain field (Figure 2a). Several small horizontal cracks are observed on the surface of the sample, which corresponded to surface matrix cracks [20].

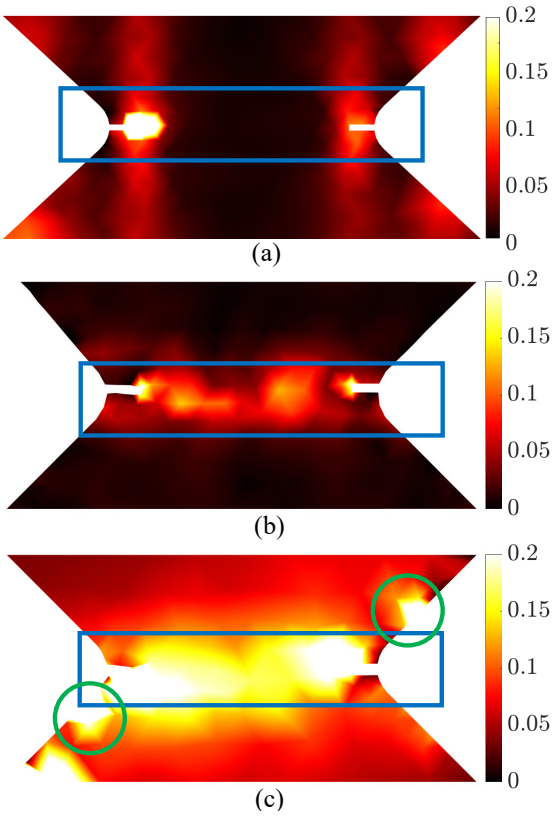

Figure 2. Major principal strain fields for (a) test WF00, (b) test WF90 and (c) test WF45 at the ultimate stress. The blue squares depict the virtual gauges where the nodal strain values were extracted and averaged. The green circles highlight strain concentrations outside of the virtual gauge.

Experiment	$\sigma_{\max}$
WF00	300 MPa
WF90	78 MPa
WF45	178 MPa

Table 1. Ultimate stress levels for each experiment.

In the residual field of the shear experiment (Figure 3b), a major crack is distinguished, which emanated from the root of the left notch. The entire gauge region displayed increased residuals, which further indicated damage on the surface.

Last, for the 45° experiment, increased residuals are present across the entire middle gauge region of the sample (Figure 3c). The residual levels are higher than in the previous two experiments (Figure 3a, b). Similarly to the strain field, increased residuals spread out diagonally on the opposite ends of the gauge area.

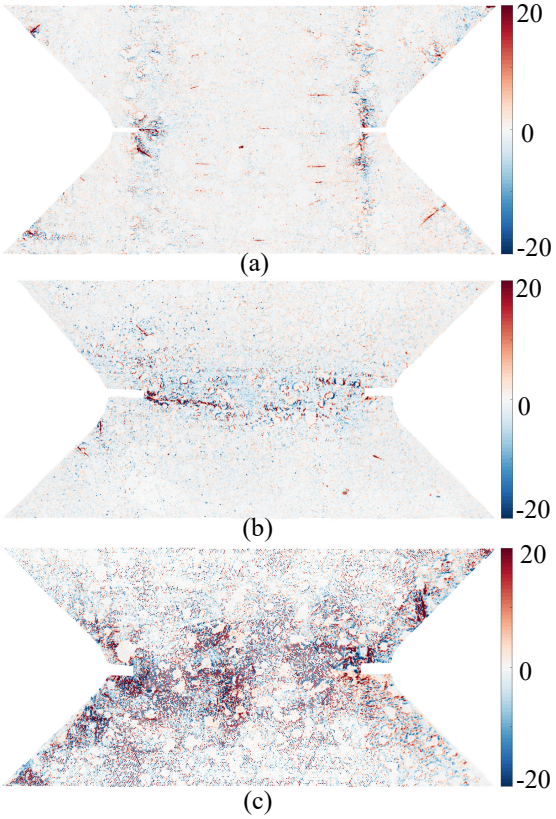

FIGURE 3. Stereocorrelation residual fields for (a) WF00, (b) WF90 and (c) WF45 tests for the ultimate stress. The residuals are expressed as a percentage of the dynamic range of the camera reference images.

4. DISCUSSION

In this section, the stress-strain responses (Figure 4) of the three experiments are compared and discussed. The stresses were calculated as the applied force divided by the net section area of each sample. The average strain levels were determined from virtual strain gauges defined for each experiment in Figure 2.

As previously noted, the tensile test exhibited the highest stress levels, while the shear experiment showed the lowest. When examining the stress-strain curves, it is observed that the tensile test resulted in the lowest strain levels, whereas the combined tensile and shear experiment achieved the highest strain levels. This difference is attributed to the orientation of yarns with respect to the loading direction. The tensile test corresponded to the highest rigidity due to the aligned yarn orientation, whereas shear exhibited the lowest rigidity. The WF45 experiment had yarns oriented at 45° with respect to the loading direction; thus it had increased rigidity compared to the shear experiment.

5. CONCLUSION

In this work, FE based stereocorrelation was applied to characterize the mechanical response and behavior of woven glass fiber composite samples under three

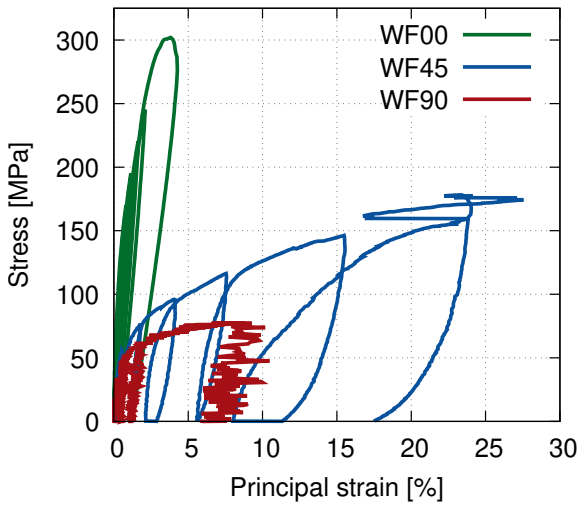

FIGURE 4. Stress-major principal strain curves for all three experiments.

distinct loading configurations. The main conclusion are as follows:

- The sample orientation with respect to the loading direction had a major influence on the stress-strain response, in particular its rigidity.
- The tensile test reached the highest stress level, whereas the shear experiment achieved the lowest.
- The highest strain and stereocorrelation residual levels were reached for the 45° experiment, thereby indicating the most accumulated damage on the investigated surfaces.

The experimental setup presented herein is not limited to composite materials. It was designed to be robust and versatile. Since the experimental protocol was established for different loading regimes, it is possible to introduce additional modalities in the stereocorrelation procedure, such as infrared and X-ray spectra for a more comprehensive material characterization.

ACKNOWLEDGEMENTS

This work was performed within the FULLINSPECT project supported by the Croatian Science Foundation (UIP-2019-04-5460 Grant). AZ was also supported through the Incoming International Scholarship Program of ENS Paris-Saclay.

REFERENCES

[1] R. Hsissou, R. Seghiri, Z. Benzekri, et al. Polymer composite materials: A comprehensive review. *Composite Structures* **262**:113640, 2021. https://doi.org/10.1016/j.compstruct.2021.113640

[2] A. Vrgoč, Z. Tomičević, B. Smaniotto, F. Hild. Application of different imaging techniques for the characterization of damage in fiber reinforced polymer. *Composites Part A: Applied Science and Manufacturing* **150**:106576, 2021. https://doi.org/10.1016/j.compositesa.2021.106576

[3] Q. Guo, Y. Zhang, D. Li, et al. Experimental characterization of the compressive properties and failure mechanism of novel multiaxial 3D woven composites. *Composites Communications* **28**:100905, 2021. https://doi.org/10.1016/j.coco.2021.100905

[4] M. Arcan, Z. Hashin, A. Voloshin. A method to produce uniform plane-stress states with applications to fiber-reinforced materials. *Experimental Mechanics* **18**(4):141–146, 1978. https://doi.org/10.1007/BF02324146

[5] A. Zaplatić, Z. Tomičević, D. Čakmak, F. Hild. Improvement of the Arcan setup for the investigation of thin sheet behavior under shear loading. *Experimental Mechanics* **62**(2):313–332, 2022. https://doi.org/10.1007/s11340-021-00762-1

[6] A. Zaplatić, A. Vrgoč, Z. Tomičević, F. Hild. Boundary condition effect on the evaluation of stress triaxiality fields. *International Journal of Mechanical Sciences* **246**:108127, 2023. https://doi.org/10.1016/j.ijmecsci.2023.108127

[7] J. Xavier, M. Oliveira, J. Morais, T. Pinto. Measurement of the shear properties of clear wood by the Arcan test. *Holzforschung* **63**(2):217–225, 2009. https://doi.org/10.1515/HF.2009.034

[8] A. Benelli, R. Ciardiello, C. B. Niutta, L. Goglio. Experimental and numerical characterization of adhesive joints with composite substrates by means of the Arcan test. *International Journal of Adhesion and Adhesives* **122**:103321, 2023. https://doi.org/10.1016/j.ijadhadh.2022.103321

[9] T. Laux, K. W. Gan, J. M. Dulieu-Barton, O. T. Thomsen. A simple nonlinear constitutive model based on non-associative plasticity for UD composites: Development and calibration using a Modified Arcan Fixture. *International Journal of Solids and Structures* **162**:135–147, 2019. https://doi.org/10.1016/j.ijsolstr.2018.12.004

[10] G. Besnard, H. Leclerc, F. Hild, et al. Analysis of image series through global digital image correlation. *Journal of Strain Analysis for Engineering Design* **47**(4):214–228, 2012. https://doi.org/10.1177/0309324712441435

[11] F. Hild, A. Bouterf, S. Roux. Damage measurements via DIC. *International Journal of Fracture* **191**(1-2):77–105, 2015. https://doi.org/10.1007/s10704-015-0004-7

[12] A. Zaplatić, Z. Tomičević, D. Čakmak, F. Hild. Identifiability of Ludwik's law parameters depending on the sample geometry via inverse identification procedure. *Coupled Systems Mechanics* **11**(2):133–149, 2022. https://doi.org/10.12989/csm.2022.11.2.133

[13] A. Vrgoč, Z. Tomičević, A. Zaplatić, F. Hild. Damage analysis in glass fibre reinforced epoxy resin via digital image correlation. *Transactions of FAMENA* **45**(2):1–12, 2021. https://doi.org/10.21278/TOF.452024020

[14] F. Hild, S. Roux. Comparison of local and global approaches to digital image correlation. *Experimental Mechanics* **52**(9):1503–1519, 2012. https://doi.org/10.1007/s11340-012-9603-7

[15] R. Fouque, R. Bouclier, J.-C. Passieux, J.-N. Périé. Stereo digital image correlation: formulations and perspectives. *Comptes Rendus Mécanique* **349**(3):453–463, 2021. https://doi.org/10.5802/crmeca.93

[16] X. Chang, C. L. Gourriérec, L. Turpin, et al. Proper Generalized Decomposition stereocorrelation to measure kinematic fields for high speed impact on laminated glass. *Computer Methods in Applied Mechanics and Engineering* **415**:116217, 2023. https://doi.org/10.1016/j.cma.2023.116217

[17] L. Dubreuil, J.-E. Dufour, Y. Quinsat, F. Hild. Mesh-based shape measurements with stereocorrelation. principle and first results. *Experimental Mechanics* **56**:1231–1242, 2016. https://doi.org/10.1007/s11340-016-0158-x

[18] J.-E. Pierré, J.-C. Passieux, J.-N. Périé. Finite Element Stereo Digital Image Correlation: Framework and mechanical regularization. *Experimental mechanics* **57**:443–456, 2017. https://doi.org/10.1007/s11340-016-0246-y

[19] M. Berny, T. Archer, P. Beauchêne, et al. Displacement uncertainty quantifications in T3-stereocorrelation. *Experimental Mechanics* **61**(5):771–790, 2021. https://doi.org/10.1007/s11340-021-00690-0

[20] A. Zaplatić, Z. Tomičević, X. Chang, et al. Hybrid infrared-visible multiview correlation to study damage in a woven composite complex-shaped specimen. *Coupled Systems Mechanics* **12**(5):445–459, 2023. https://doi.org/10.12989/csm.2023.12.5.445

[21] X. Chang, C. L. Gourriérec, F. Hild, S. Roux. Brightness and contrast corrections for stereocorrelation. Global and instantaneous formulation with spatial regularization. *Mechanical Systems and Signal Processing* **208**:111057, 2024. https://doi.org/10.1016/j.ymssp.2023.111057

Scientific paper 6

A. Zaplatić, X. Chang, Z. Tomičević, S. Roux, F. Hild, “Hybrid infrared and visible light correlation for woven composite samples subjected to three in-plane loadings”

Preprint of the submitted journal article.

Hybrid infrared and visible light correlation for woven composite samples subjected to three in-plane loadings

Andrija Zaplatić[a,b], Xuyang Chang[c], Zvonimir Tomičević[a,*], Stéphane Roux[b], François Hild[b]

[a] *University of Zagreb, Faculty of Mechanical Engineering and Naval Architecture 10002 Zagreb, Croatia*
[b] *Université Paris-Saclay, CentraleSupélec, ENS Paris-Saclay, CNRS LMPS - Laboratoire de Mécanique Paris-Saclay, 91190 Gif-sur-Yvette, France*
[c] *University of Science and Technology Beijing, School of Physics and mathematics 100030 Beijing, China*

Abstract

This paper presents a detailed analysis of woven glass fiber composite samples subjected to complex in-plane loading regimes. Three butterfly shaped samples, each with two V notches in the gauge region, were tested under tensile, simple shear, and combined tensile/ shear loading at 45° angle using a modified Arcan fixture. An advanced optical setup, consisting of two visible-light cameras and one infrared camera, was utilized. Hybrid multiview correlation was employed to measure surface displacement, strain, and Lagrangian temperature fields.

Highest stress levels were achieved for the tensile loading configuration. On the other hand, for the combined tensile/simple shear loading configuration, the highest strain levels were reached. The combined loading exhibited features of both tensile and simple shear loadings. The findings revealed the presence of a thermoelastic effect during tensile and combined loadings, but not in the shear-only case. Additionally, during combined loading, the shear strains were dominant until significant damage occurred, after which the strains in the loading direction took over. A linear relationship between temperature changes and shear strain was also observed in the simple shear experiment.

Keywords: woven composite, thermography, multiview correlation, multimodality, Arcan rig

*Corresponding author
Email address: zvonimir.tomicevic@fsb.unizg.hr (Zvonimir Tomičević)

1. Introduction

The rapid advancement and evolution of manufacturing industries, particularly, for aeronautical [1] and automotive [2] applications, require equally advanced materials. This role particularly suits fiber reinforced polymer (FRP) composites as their utilization increased rapidly over the recent years [3]. FRP composites are highly sought after due to their adaptability to various working conditions. By customizing the architecture and the geometry of these composites, it is possible to adapt the composite components to specific loading regimes. Their intricate and heterogeneous architecture makes FRP composites more difficult to characterize compared to traditional homogeneous engineering materials, such as metals and alloys. Furthermore, an additional advantage of FRP composites is their lower weight to strength ratio. Such advantage is important for manufacturing since less material is needed to provide the required strength to the components. However, due to such complex architectures, extensive experimental investigations need to be carried out under complex loading regimes that simulate real life working conditions [4, 5, 6].

During the design stage, it is crucial to predict when the component will fail. For homogeneous materials, various models exist. Predicting the behavior and ultimate failure of FRP composites remains challenging due to their inherent heterogeneity. For instance, FRP composites may be vulnerable to various damage mechanisms, including fiber/matrix interface debonding, fiber breakage, matrix microcracking, fiber pull-out, all of which contributing to the ultimate strength and structural stability [7, 8, 9]. Simple experiments such as uniaxial tensile test are not sufficient. By characterizing a heterogeneous material under 1D loading, it is not possible to predict the FRP component behavior under in-service workload scenarios. Therefore, multiaxial experiments need to be carried out [10]. The high cost and limited availability of testing machines capable of prescribing such complex loading regimes impose practical constraints [11]. To avoid such costly testing equipment, it is possible to change the geometry of the samples [12, 13, 14] to introduce complex strain/stress states in the material. One step further is to develop specialized apparatuses which are employed alongside uniaxial testing machines. Among

those, the Arcan fixture [15] stands out. Using a modified Arcan fixture (MAF) [16], a spectrum of in-plane loading regimes can be applied to samples, namely, tensile, simple shear and their various combinations. Furthermore, specially developed butterfly sample with two V notches ensure damage and strain localization in the middle of the gauge region. Despite these advancements, obtaining accurate material responses during testing remains challenging when relying on contact-based measurement systems like extensometers and strain gauges, particularly for samples with complex geometries and mesostructures. This issue is alleviated by the development of optical methods, which allow for full-field measurements. Among them, digital image correlation (DIC), utilizing visible light cameras [17], has emerged as one of the most versatile technique for full-field kinematic measurement [18]. In addition, advanced methods such as infrared (IR) thermography [19, 20] and X-ray computed tomography (XCT) [21, 22, 23] are gaining interest for their ability to provide deeper insights into the internal structure and failure mechanisms of composites.

Nowadays, 2D-DIC [24] is commonly used due to its simplicity and versatility from macro to micro scale [25]. DIC can be formulated in two ways. The first, the commonly referred to as local DIC [26, 24] discretizes the sample surface into a set number of facets. The algorithm measures the local displacements for each facet individually with no regards to any neighboring facets. The counterpart to local DIC, *i.e.* global DIC [27] ensures the continuity of the displacement fields by utilizing, for instance, a Finite Element (FE) mesh defined over the image thus avoiding additional interpolation [28], albeit at a higher computational cost. However, 2D-DIC is unsuitable for non-planar geometries or scenarios involving out-of-plane displacements [29]. In such cases, stereocorrelation [30] can be utilized, leveraging image pairs for shape measurements [26, 31, 32] and displacement analysis [24, 33]. When using a single digital camera, mirrors can be implemented in the optical setup [34, 35], thus obtaining image pairs from different angles. The conventional stereovision system consists of two or more digital cameras [24, 16, 36]. Similar to global 2D-DIC, global stereocorrelation can also incorporate FE meshes [31, 33, 37].

The calibration of the stereovision system may exploit the known geometry of CAD models [38] or FE meshes [31, 33]. In ideal scenarios, when capturing image pairs of the same object, the camera modalities are identical and lighting should be uniform during the observation period. Achieving such ideal conditions may be challenging even with identical cameras and lighting, surface rotation with regards to the camera may induce changes in the gray level. Therefore, brightness and contrast corrections should be implemented within the stereocorrelation algorithm to enhance robustness and accuracy [39, 40]. While FE-based stereocorrelation is a powerful technique akin to 2D-DIC, both methods are limited to surface descriptions (*e.g.*, only surface-level damage can be captured). For multiple layered composites, that observation is not sufficient to fully characterize damage accumulating within the material. For this reason, additional measurement methods may be integrated in the measurement protocol to enable for more comprehensive analyses. In recent decades, infrared thermography proved to be efficient at detecting and evaluating damage of the composite materials [41]. Infrared thermography is a powerful measurement technique for quantifying temperature fields and detecting heat-related phenomena in composite materials [42, 43]. It is widely used to assess structural integrity and detect defects [44, 45], particularly in applications such as aircraft components [46] and cars [47]. Additionally, IR thermography enables for the monitoring of materials under mechanical loading [48].

A hybrid framework combining IR thermography and DIC in a hybrid multiview setting maximizes the potential of both modalities [49, 50, 51, 40]. This framework ensures the simultaneous measurement of displacement, strain, and temperature fields within a unified Lagrangian reference frame. For instance, Wang *et al.* [52] demonstrated the efficacy of this hybrid approach in analyzing thermomechanical fatigue tests, revealing crucial insights into material damage under cyclic loadings. However, integrating IR and visible-light modalities presents unique challenges, particularly digital level variations caused by thermomechanical couplings [53] or damage-induced effects in composites [41]. These variations may introduce significant biases. To address these challenges,

brightness and contrast corrections are to be applied to IR images [54, 39, 40], thereby ensuring that temperature variations are accounted for. Corrected temperature variations are then analyzed alongside strain measurements, enabling for the assessment of localized thermal changes within the same Lagrangian frame. This hybrid implementation captures both surface (via DIC) and subsurface (via IR thermography) phenomena, providing a more comprehensive analysis of dissipation effects and temperature variations in relation to strain fields [55]. By correlating these datasets, researchers can investigate mechanisms of material degradation, damage propagation, and structural performance. Ultimately, this approach enhances the understanding of the thermomechanical behavior of composites and offers a robust tool for assessing their integrity under complex loading conditions.

Within this research, a hybrid multiview correlation (HMC) framework is presented and employed for a woven composite. Three samples made of a vynilester resin reinforced with woven glass fibers (0°/90°) were subjected to in-plane multiaxial cyclic loadings, namely, tensile, simple shear and a combination thereof. First, the hybrid optical setup is presented, followed by the FE-based multiview correlation principles. The next sections present the results for the three experiments that are subsequently compared.

2. Experimental protocol

Arcan butterfly samples [16] with two V notches in the gauge region were subjected to three different types of loadings. The Arcan samples were water jet cut out of 3 mm thick woven composite plates. The composite plates were made of a vinylester resin reinforced with seven woven glass fabric plies, where all yarns were oriented at 0° /90° with respect to each other. Two additional 2 mm long and 0.5 mm wide notches were cut in the roots of the V notches, thereby reducing the net section area to approximately 48 mm^2.

Conventionally, composite samples are cut at different angles and loaded in uniaxial tension to simulate complex loadings [56]. In the present work, the composite samples were cut so that the yarns were at 0° /90° with respect to the longitudinal axis of the

sample. Using a MAF, different types of load regimes can be applied to such samples, by rotating it with angles ranging from 0° to 90° with steps of 15°. In this research, three types orientations were chosen, namely, tensile (at 0°), simple shear (at 90°), and combined tensile/shear (at 45°).

The MAF configurations are displayed in Figure 1. The MAF and the optical setup (Figure 1(a)) were entirely covered with black fabric to minimize any light disturbances that could have an impact on the IR images. The optical setup consisted of two identical visible light cameras (C1 and C2) and one infrared camera (C3). Such a hybrid optical setup is beneficial since *all* three cameras observe the same region of Interest (ROI). The cameras were rotated alongside the MAF so that, for each experiment, the hybrid optical setup observed the same ROI and in the same orientation. Hence, for the WF90 and WF45 configurations, the optical setup had to be rotated by 90° and 45°, respectively. For all three loading configurations, the samples were loaded with a 0.24 mm/min velocity in a displacement controlled mode.

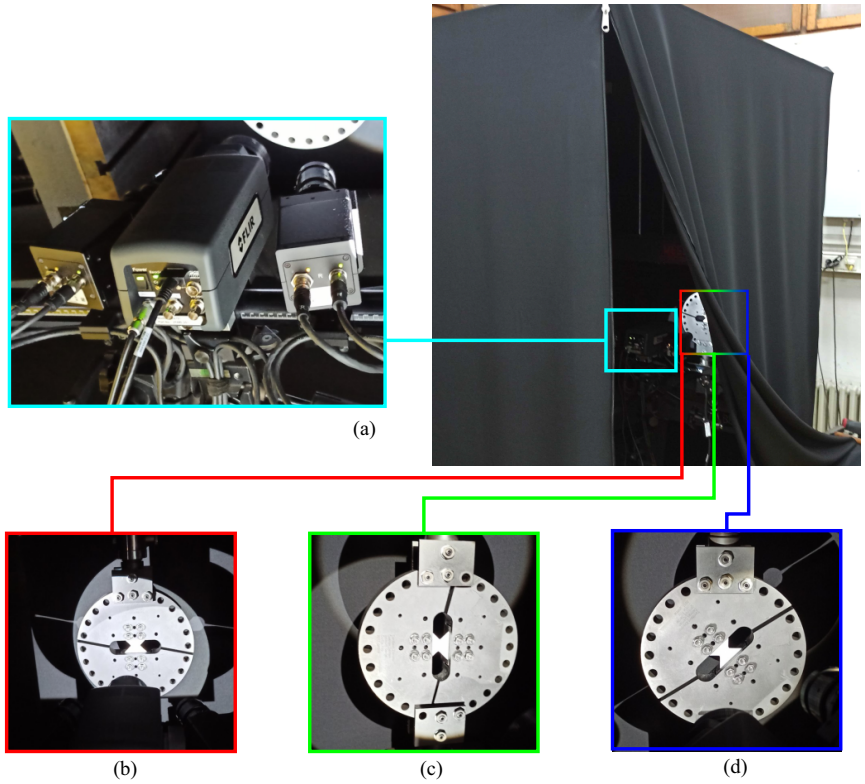

Fig. 1: Experimental setup. (a) Optical multiview system consisting of two visible light cameras (C1 and C2) and one infrared camera (C3). (b) MAF tensile configuration (WF00), (c) simple shear configuration (WF90), and (d) combined tension/shear (45°) configuration (WF45).

The parameters of the hybrid optical setup are listed in Table 1. These parameters did not change between the three experiments. The standard black speckles used for DIC were invisible to the IR camera due to their similar emissivity. Therefore, a specialized graphite spray was applied in the form of coarse black speckles on the surface. Before each experiment, 20 images were captured in the unloaded state to evaluate the measurement uncertainties.

Table 1: Hardware parameters of the hybrid multiview system

Setup	Visible light cameras	IR camera
Camera	$2\times$ Dalsa Falcon 12M	Flir A6751
Definition	4096×3068 px	640×512 px
Gray/digital levels rendering	8 bit	16 bit
Lens	Titanar B75	Flir 50 mm
Distance ring	-	6.35 mm
Aperture	f/5.6	-
Field of view	82×61 mm	64×51.2 mm
Image scale	0.02 mm/px	0.1 mm/px
Stereo angle	$25°$	$0°$
Stand-off distance	326 mm	320 mm
Camera center proximity	44 mm	0
Image acquisition rate	1 fps	
Patterning technique	B/W paints + black graphite speckles	

The experimental protocol was identical for all three experiments. It consisted of total of nine loading/unloading cycles with intermittent X-ray computed tomography scanning (Figure 2). Before the experiments, three CT scans were acquired in the unloaded state to evaluate the measurement uncertainties assocaited with digital volume correlation. Although the results from the CT scanning and digital volume correlation are not the topic of the research reported herein, it is important to note the impact of *ex-situ* scanning. Since the samples had to be removed and mounted back in the MAF, it induced large rigid body motions. Hence, a stereo optical setup was mandatory. In Figure 2(a-c), surface slices of the samples are displayed to highlight the differences of the underlying meso-architecture. Each sample had four whole yarns between the notches, but the horizontal notches were not distributed the same way. Only for the WF00 and WF45 configurations were the notches cut within the yarn itself, which may lead to intra-yarn debonding.

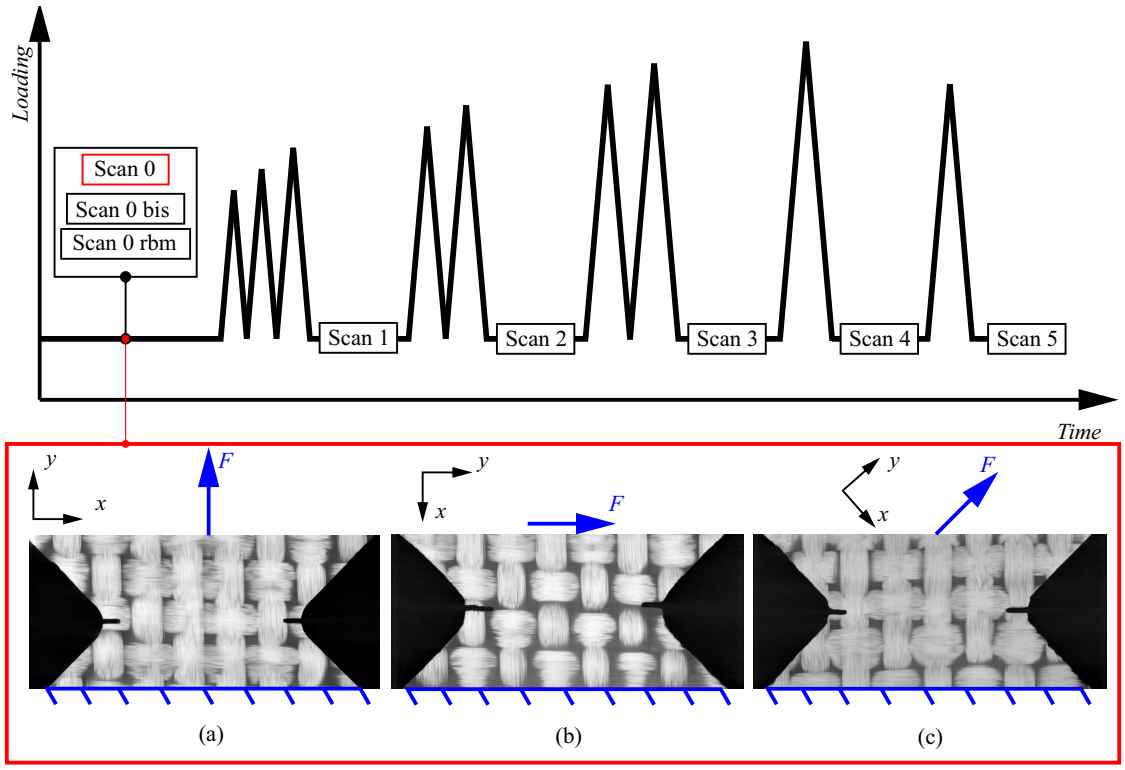

Fig. 2: Experimental *Ex-situ* protocol concerning the loading history with Scan 0 sections (red box). (a) WF00, (b) WF90 and (c) WF45 configurations. A visual representation is added to clarify the loading directions.

3. Global formulation of hybrid multiview correlation

This section first recalls the basic principles of hybrid multiview calibration and correlation. Then, the implementation of brightness and contrast corrections (BCCs) is introduced. The interested reader may refer to Refs. [57, 58, 51, 39, 40] for further details.

3.1. Calibration

By combining two different modalities (*i.e.*, visible light and infrared images), it is necessary to first perform image normalization. The normalization is performed in two steps. First, the image gray level distribution is translated and set the mean to zero. Secondly, the new image histogram is scaled by the standard deviation. For each camera c, the normalized image $\widetilde{f}^c$ reads

$$\widetilde{f}^{(c)} = \frac{f^{(c)} - \mu(f^{(c)})}{\mathrm{std}\,(f^{(c)})} \tag{1}$$

where $\mu(\bullet)$ denotes the average, $\mathrm{std}(\bullet)$ the standard deviation. For the speckled surface, it is assumed that the images captured by the different cameras originate from the same gray-level patterns. Hence, an "intrinsic pattern" $\widehat{F}$ is defined as the average of all reference images

$$\widehat{F}(\mathbf{X}) = \frac{1}{N_c}\sum_{c=1}^{N_c} \widetilde{f}^{(c)}(\mathbf{x}^{(c)}, t=0) \tag{2}$$

where N_c defines the total number of cameras. The $\mathbf{x}^c$ represents the projected physical points, which depend on the 3D positions in the FE mesh $\mathbf{X}$ and the corresponding projection matrices $[\mathbf{\Pi}^{(c)}]$ for the c-th camera

$$\mathbf{x}^c = \mathbf{x}^c\left([\mathbf{\Pi}^{(c)}], \mathbf{X}\right). \tag{3}$$

The general philosophy of the global formulation in hybrid multiview calibration is to use the "intrinsic texture" as the master information to describe the speckled surface, and all cameras are calibrated with respect to the projection of this "intrinsic texture" onto each image plane [57, 51, 32]. Thus, the calibration of each camera c consists in finding the (extrinsic and intrinsic) parameters of its projection matrix $[\mathbf{\Pi}^{(c)}(\{\mathbf{P}^{(c)}\})]$, which are collected in a column vector, $\{\mathbf{P}\}^\top = \{\{\mathbf{P}^{(1)}\}^\top, \{\mathbf{P}^{(2)}\}^\top, \cdots, \{\mathbf{P}^{(N_c)}\}^\top\}$. The minimization of the following cost function

$$\rho^2(\{\mathbf{P}\}) = \sum_{c=1}^{N_c}\int_{\mathrm{ROI}} \left(\widetilde{f}^{(c)}(\mathbf{x}^{(c)}, t=0) - \widehat{F}(\mathbf{X})\right)^2 d\mathbf{X} \tag{4}$$

is performed via an integrated approach [39]. When lightning and perspective differences for each camera are negligible or non-existent, the gray level conservation between each reference image $\widetilde{f}^c(\mathbf{x}^c)$ and the intrinsic texture $\widehat{F}(\mathbf{X})$ is satisfied [39]. Otherwise, such conditions may impact the stability of HM algorithms since the gray level conservation between cameras is no longer fulfilled, especially when the IR camera is included. Using brightness and contrast corrections (BCCs) for each camera c, the corrected reference

image $\widehat{f^c}(\mathbf{X})$ is built for each camera

$$\widehat{f}^{(c)}(\mathbf{X}) = (1 + c^c(\mathbf{x}^{(c)}))\widetilde{f}^c(\mathbf{x}^{(c)}, t = 0) + b^c(\mathbf{x}^{(c)}) \tag{5}$$

where $b^c\left(\mathbf{x}^{(c)}\right)$ and $c^c\left(\mathbf{x}^{(c)}\right)$ represent the 2D brightness and contrast correction fields for camera c. The new cost function then reads

$$\xi^2(b, c) = \sum_{c=1}^{N_c} \int_{\text{ROI}} \left((1 + c^c(\mathbf{x}^{(c)}))\widetilde{f}^c(\mathbf{x}^{(c)}, t = 0) + b^c(\mathbf{x}^{(c)}) - \widehat{F}(\mathbf{X})\right)^2 d\mathbf{X} \tag{6}$$

3.2. Hybrid multiview correlation

Following the calibration step, the measured displacement field $\mathbf{U}_m(\mathbf{X}, t)$ for each time t (*i.e.*, instantaneous registrations) minimizes the following cost function

$$\mathbf{U}_m = \underset{\mathbf{U}}{\text{argmin}} \sum_{c=1}^{N_c} \int_{\text{ROI}} \left(\widetilde{f}^{(c)}(\mathbf{x}^{(c)}, 0) - \widetilde{f}^{(c)}_{\mathbf{U}}(\widetilde{\mathbf{x}}^{(c)}, t)\right)^2 d\mathbf{X} \tag{7}$$

where $\widetilde{f}^{(c)}_{\mathbf{U}}(\widetilde{\mathbf{x}}^{(c)}(\mathbf{X}), t)$ is the corrected deformed image acquired by the c-th camera at time t, namely,

$$\widetilde{f}^{(c)}_{\mathbf{U}}(\widetilde{\mathbf{x}}^{(c)}, t) = \widetilde{f}^{(c)}_{\mathbf{U}}(\mathbf{x}^{(c)}(\mathbf{X} + \mathbf{U}_m(\mathbf{X}, t)), t) \tag{8}$$

The displacement field is written as

$$\mathbf{U}(\mathbf{X}) = \sum_{i=1}^{N_s} \alpha_i(t)\mathbf{\Phi}_i(\mathbf{X}) \tag{9}$$

where $\alpha_i(t)$ is the nodal displacement to be determined at each time instant t, and $\mathbf{\Phi}_i(\mathbf{X})$ the corresponding vectorial shape function. A Gauss-Newton algorithm is implemented to minimize the above cost functions [57]. It is worth noting that the initial shape is defined with the same mesh as that used to measure the displacement and temperature fields.

3.3. Brightness and Contrast Corrections

As in the calibration step, BCCs have to be implemented for the registration of IR images. These corrections are then used to evaluate the nodal temperatures. Global BCCs were carried out [39], so that the gray-level conservation is recovered by applying brightness and contrast corrections to the corrected deformed images

$$\widetilde{f}^{(c)}_{(\mathbf{U},\mathbf{BCC})}(\widetilde{\mathbf{x}}^{(c)},t) = (1 + c^{(c)}(\mathbf{x}^{(c)},t)\widetilde{f}^{(c)}(\widetilde{\mathbf{x}}^{(c)},t) + b^{(c)}(\mathbf{x}^{(c)},t) \tag{10}$$

where $b^{(c)}$ and $c^{(c)}$ stand for brightness and contrast corrections for the c-th camera. For the IR (C3) camera, using the brightness and contrast fields, the local temperature variations during the experiment are obtained in the reference (Lagrangian) frame.

4. Results

In this section, the results for the three experiments are reported. For each experiment, the major eigenstrain, residual and radiometric temperature fields (expressed in digital levels - DL) are analyzed. The temperature fields were obtained via Equation (10). The instantaneous correlation residuals are defined as

$$\varphi_{instant}(t,\mathbf{X}) = \sqrt{\frac{1}{N_c}\sum_{c=1}^{N_c}\left(\frac{\widetilde{f}^{(c)}_{(\mathbf{U},\mathbf{BCC})}(\widetilde{\mathbf{x}}^{(c)}(\mathbf{X}),t) - \widetilde{f}^{(c)}(\mathbf{x}^{(c)}(\mathbf{X}),0)}{\max\left(\widetilde{f}^{(c)}\right) - \min\left(\widetilde{f}^{(c)}\right)}\right)^2} \tag{11}$$

Table 2 lists the HMC parameters. For the three analyses, linear 2D triangular elements were employed. The mean element lengths were approximately the same, except for the test WF45 due to the quality of the speckle pattern. Therefore, a higher number of evaluation points was defined for that FE mesh compared to those of experiments WF00 and WF90 since the same discretization method was used.

Table 2: Correlation parameters

Experiment	WF00	WF90	WF45
Software	Correli 3.0		
Mean element length	≈ 1.1 mm	≈ 1.1 mm	≈ 1.45 mm
Shape functions	Linear (T3)		
Meshes	Unstructured (Figure 3)		
Matching criterion	Sum of squared differences		
Gray level interpolation	Linear		
Evaluation points (per element)	435	435	561

Table 3 collects the measurement uncertainties for displacements, strains and temperature. For all three experiments, the out-of-plane displacement U_z exhibited the highest uncertainty compared to in-plane displacements U_x and U_y, due to lower placement sensitivities in the out-of-plane direction compared to those in the in-plane directions [37]. The in-plane displacement uncertainties were similar except for test WF90, where the U_y uncertainty was higher than for the other two experiments due to slightly worse speckle pattern. All the strain uncertainties had similar levels. Lastly, the lowest temperature uncertainty, expressed in digital levels, is reported for WF90, due to a larger graphite speckle pattern.

Table 3: Standard nodal displacement, strain and temperature uncertainties for the three tests

Experiment	WF00	WF90	WF45
U_x, μm	0.4	0.7	0.42
U_y, μm	0.7	1	0.45
U_z, μm	1	2.3	1.6
ε_{xx}	10^{-4}	1.5×10^{-4}	1.2×10^{-4}
ε_{yy}	1.1×10^{-4}	1.5×10^{-4}	1.8×10^{-4}
ε_{xy}	10^{-4}	1.1×10^{-4}	1.1×10^{-4}
T, DL	1.6	0.8	1.8

In Figure 3 the strain history for each experiment is shown. The strain history was obtained by averaging the nodal strains inside the virtual gauge defined over the FE mesh (Figure 3 - red boxes). The mean strains ε_{xx}, ε_{yy}, ε_{xy} and ε_1 are compared. In each diagram, four points are depicted for which the thermomechanical and residual fields will be displayed. Point P1 denotes the peak of the third cycle (*i.e.*, late stages of linear elas-

ticity). Next, point P2 refers to the peak of the seventh cycle (or late nonlinear behavior). The last two points P3 and P4 are related to the peaks of the final two cycles where significant damage developed on the surfaces of the samples. From all three diagrams, it is observed that the lowest strain levels were reached in tension (WF00), and the highest for the combined loading (WF45).

For the WF00 experiment (Figure 3(a)), the strains in the y direction (Figure 2(a)) are the highest, aside from the major eigenstrains. Furthermore, it is observed that both shear ε_{xy} and transverse ε_{xx} strains contribute to the major eigenstrain levels. Until the last cycle, the ε_{xx} strains were more prominent that the shear strains.

In the simple shear WF90 test, the shear strains ε_{xy} were the highest, as expected. However, the strains in the longitudinal direction (Figure 2(b)) increased from the second cycle onward after damage developed on the surface.

In the WF45 configuration, for the first seven cycles, the shear strain ε_{xy} was the most prominent although the sample was subjected to a combined loading. Only after the eighth cycle did the strain in longitudinal direction (Figure 2(c)) become dominant with respect to the shear strain. In the final cycle, they became prevalent. Furthermore, the transverse strains were not negligible. The ε_{xx} strain levels were comparable to those of ε_{yy} in test WF00 in the final cycle.

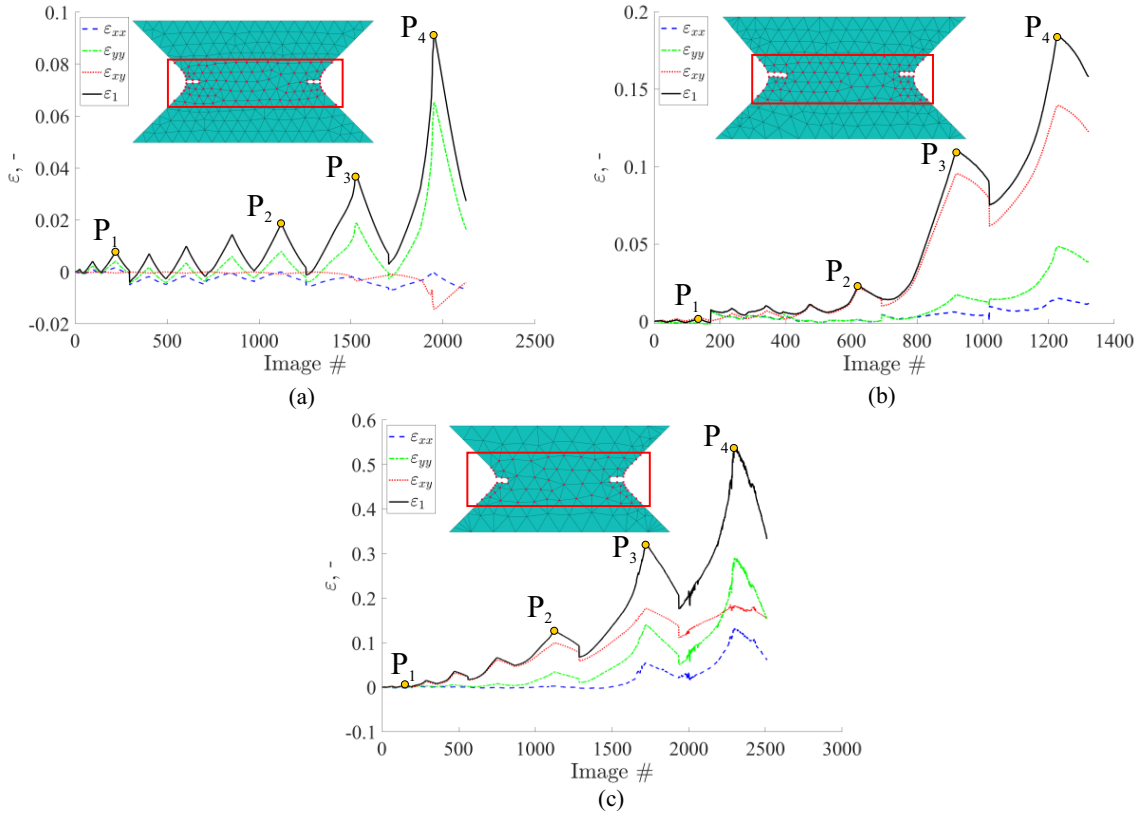

Fig. 3: Strain histories with the virtual gauges (red boxes) for tests WF00 (a), WF90 (b) and WF45 (c). Points P1-4 represent key stages during the loading process: the late phase of linear elasticity, the late phase of nonlinear behavior, the point of maximum load, and the peak of the final cycle.

4.1. *Thermomechanical results for test WF00*

The WF00 thermomechanical results, including the major eigenstrain, correlation residual and temperature fields are presented hereafter. In Figure 4 the load curve is presented with denoted points for which the results are analyzed. Furthermore, the loading is divided in five loading blocks as was explained in Figure 2.

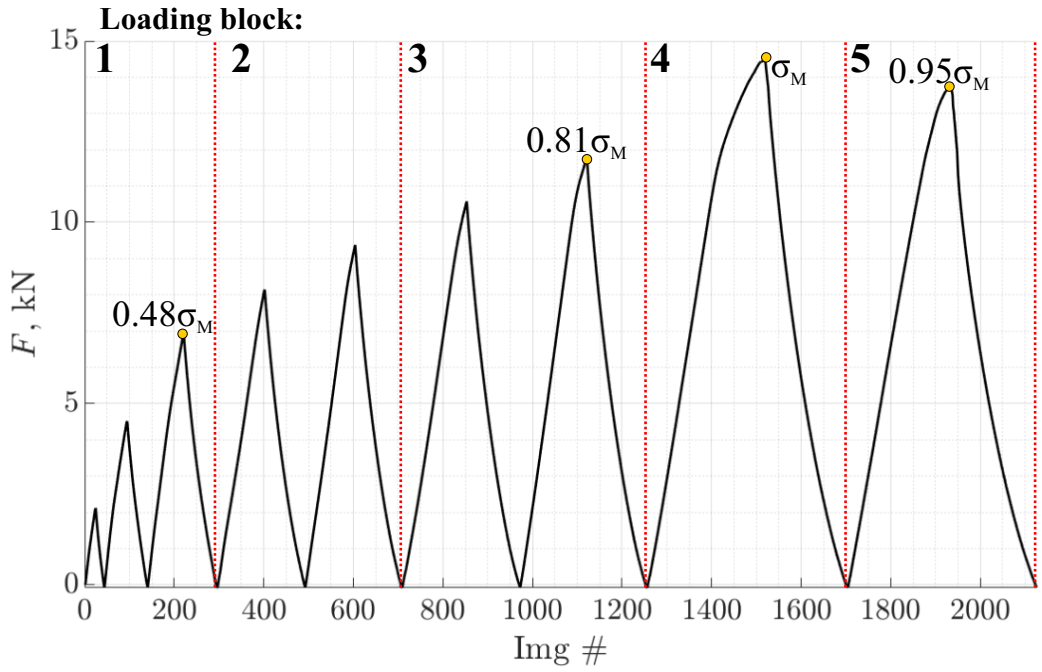

Fig. 4: Load curve for WF00 with denoted ultimate strength values for each observed point.

Four stages (Figure 3(a)) of the major eigenstrain fields are analyzed. In the late stages of elastic behavior (Figure 5(a), $0.48\sigma_M$) two strain bands are visible. Both bands emanated from the notch roots. These bands were active throughout the entire experiment. Larger strain levels were detected around the left notch. At later stages of the nonlinear response (Figure 5(b), $0.81\sigma_M$), the two bands were still present and higher levels were reached. For point P_3 (Figure 3(c), σ_M), *i.e.* for the highest force, four additional strain concentrations appeared at peripheral areas, which indicated damage. For the last point P_4 (Figure 5(d), $0.95\sigma_M$), no new localizations are observed but the existing ones are more pronounced.

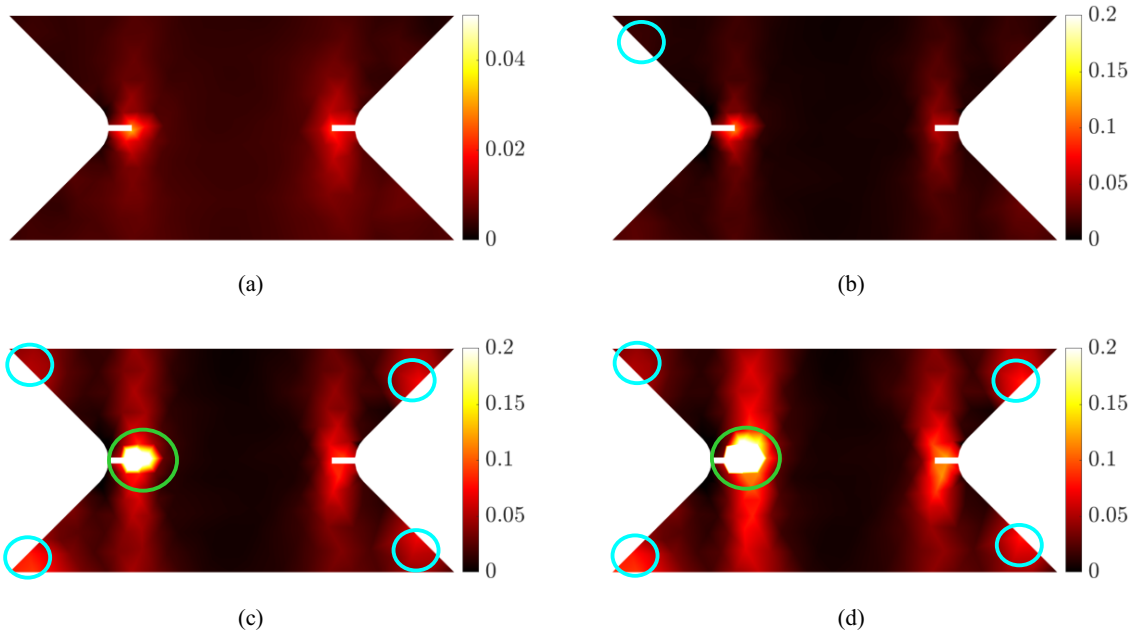

Fig. 5: Major eigenstrain fields of test W00 for points P_1 (a), P_2 (b) , P_3 (c) and P_4 (d).

In the stereocorrelation residuals (Figure 6(a), $0.48\sigma_M$) of WF00 for step P_1, a small line is observed at the root of the left notch. Alongside the strain concentrations, the correlation residuals indicate that damage occurred. As reported in the strain fields for point P_2 (Figure 5(b), $0.81\sigma_M$), identical localized areas are obtained in the correlation residual field (Figure 6(b)). Two new cracks initiated around the root of the left notch (green circle in Figure 6). Moreover, vertical residual bands corresponding to the strain bands are visible and indicate damage of the speckle pattern. Several horizontal cracks developed, which indicate cracking of the surface matrix (purple arrows in Figure 6). For the step P_3 (Figure 6(c), σ_M), the aforementioned residuals are present with higher levels. Additionally, four new cracks initiated on the peripheral areas (denoted by cyan circles) due to the differences in rigidity of the material caused by the sample geometry. For the last loading point P_4 (Figure 6(d), $0.95\sigma_M$), highest residuals are observed at the root of the left notch alongside much more pronounced vertical residual bands.

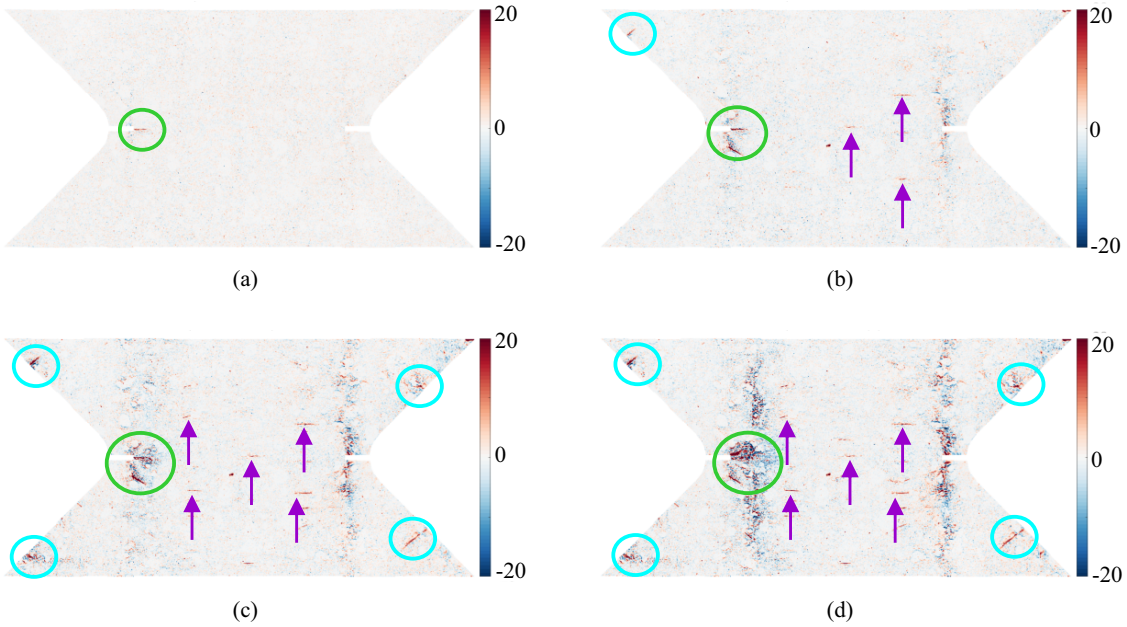

Fig. 6: WF00 C1 stereocorrelation residual fields expressed as percentage of the dynamic range of the reference image for points: a) P1, b) P2, c) P3 and d) P4. Green circles denote damage to the yarns, whereas purple arrows denote damage to the surface matrix.

The radiometric temperature fields are now studied. For the first point P_1 (Figure 7(a), $0.48\sigma_M$), no significant changes in the temperature are detected. For the point P_2 (Figure 7(a)), the temperature field indicates that the middle part of the ROI exhibited a drop in temperature (*i.e.*, thermoelastic effect). This observation was expected for the linear elastic regime. It is worth noting that the rigidity of the sample is not uniform across the ROI (Figure 2(a)). In simpler terms, the middle section of the ROI is more rigid than the peripherals. At the highest loading level P_3 (Figure 7(c), σ_M), change in the temperature field was captured, corresponding to damage initiation at the root of the left notch, and propagation is observed as well. For the last step P_4 (Figure 7(d), $0.95\sigma_M$), change in the temperature field was once again captured at the left notch, thereby indicating that damage further developed. Additionally, a weaker signal is observed at the root of the right notch.

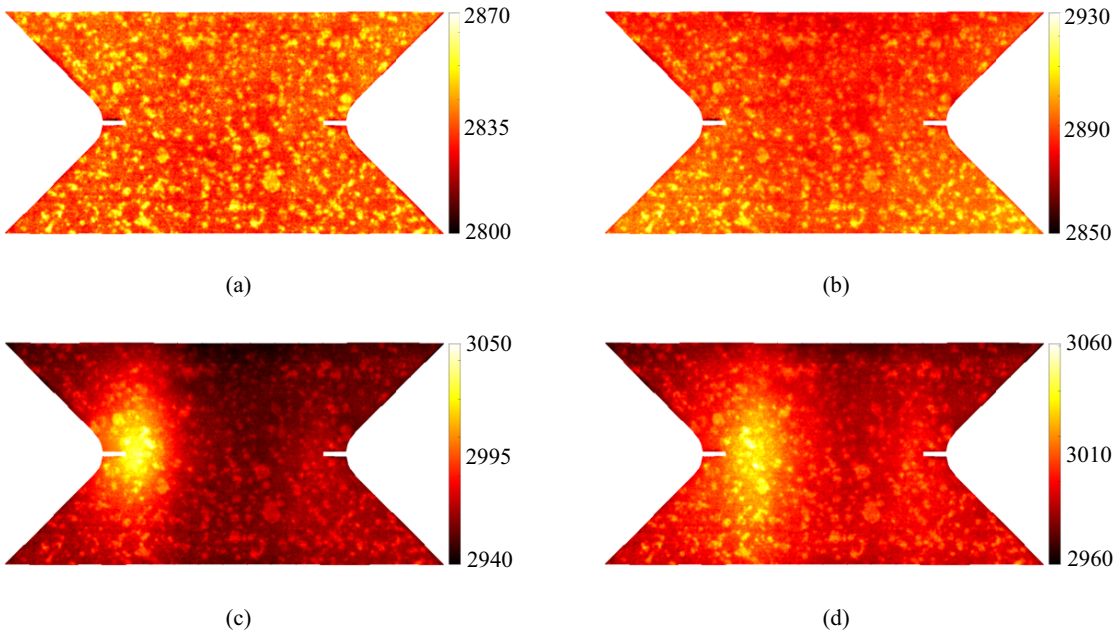

Fig. 7: Radiometric temperature fields (expressed in digital levels) of test W00 for points P_1 (a), P_2 (b), P_3 (c) and P_4 (d).

4.2. *Thermomechanical results for experiment WF90*

During the simple shear experiment, the loading direction was perpendicular to the longitudinal axis of the sample. The reported stages were chosen in an identical manner as for test WF00 and the corresponding ultimate strength values are reported in Figure 8.

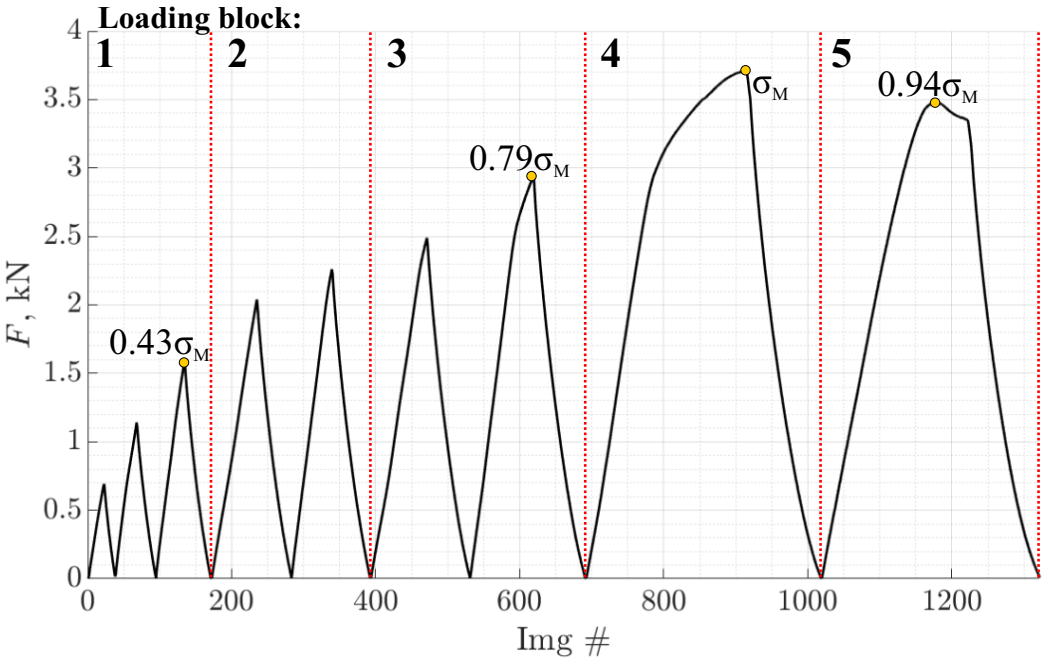

Fig. 8: Load curve for WF90 with denoted ultimate strength values for each observed point.

In Figure 9 (a) ($0.43\sigma_M$), the major eigenstrain field for step P_1 is displayed. A single strain band is discerned between the two notches. With further increase in the load level (Figure 9(b), $0.79\sigma_M$), the strain band developed more. No additional strain localization is observed on the strain field apart from the zone between the two notches. At the peak of applied load (Figure 9(c), σ_M), the strain band is no longer entirely localized between the notches, it also expanded outward and a greater area is affected. The average levels in the strain band are greater than in the WF00 test. Last, Figure 9(d) ($0.94\sigma_M$) shows that the strain levels further increased and remained localized in the same strain band.

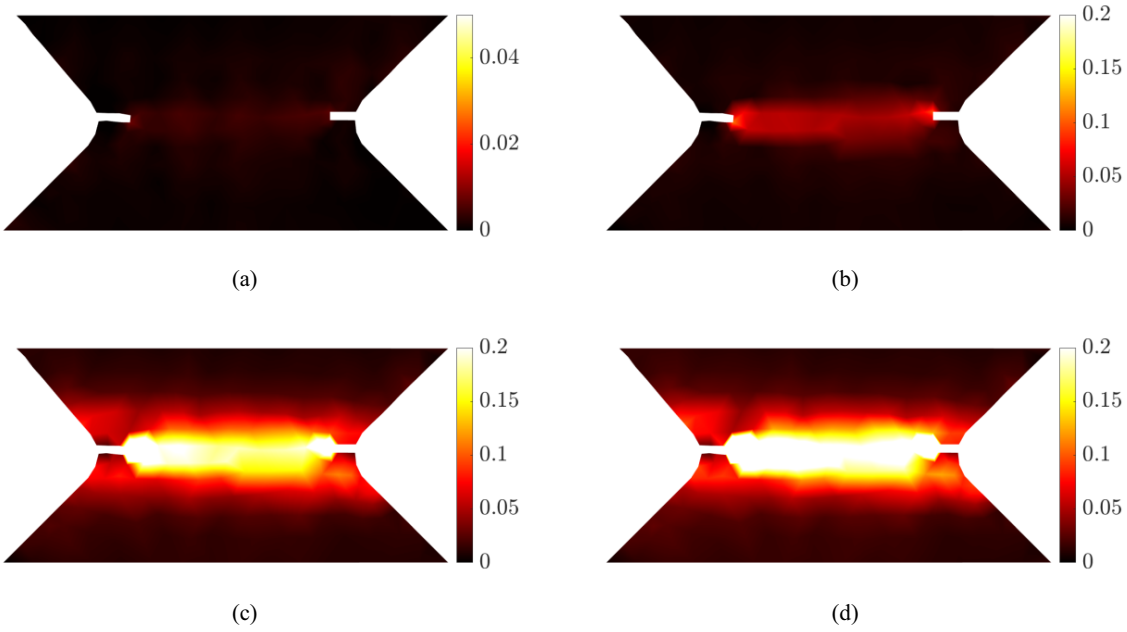

Fig. 9: Major eigenstrain fields of test W90 for points P_1 (a), P_2 (b) , P_3 (c) and P_4 (d).

From the correlation residuals of step P_1 (Figure 10(a), $0.43\sigma_M$), no damage is detected. For step P_2 (Figure 10(b), $0.79\sigma_M$), some slight damage is visible in the vicinity of the notches toward the center of the sample. These increased residuals were due to small cracks developing on the surface of the specimen. Moreover, the same areas are visible in the strain field (Figure 9 (b)). The small areas in the lower part of the sample were due to the damaged speckle pattern, which likely occurred during the un-mounting and re-mounting of the sample and they are not visible in the strain fields. For the highest force (Figure 10(c), σ_M), the crack that initiated on the left notch further propagated

toward the center of the sample. By comparing the crack path with the surface CT slice (Figure 2(b)), it is concluded that intra-yarn debonding occurred near the edge of the middle yarn (green ellipses in Figure 10). Furthermore, higher strains can be observed following the crack path (Figure 9 (c)). Increased residuals were also observed for the entire middle part of the sample, due to speckle pattern degradation resulting from material wrinkling in that area. For the last cycle (Figure 10(d), $0.94\sigma_M$), the crack that initiated on the left notch further propagated. This phenomenon is also observed on the corresponding strain field (Figure 9(d)) where increased strain levels emanating from both notches (Figure 10(c)) merge between the notches.

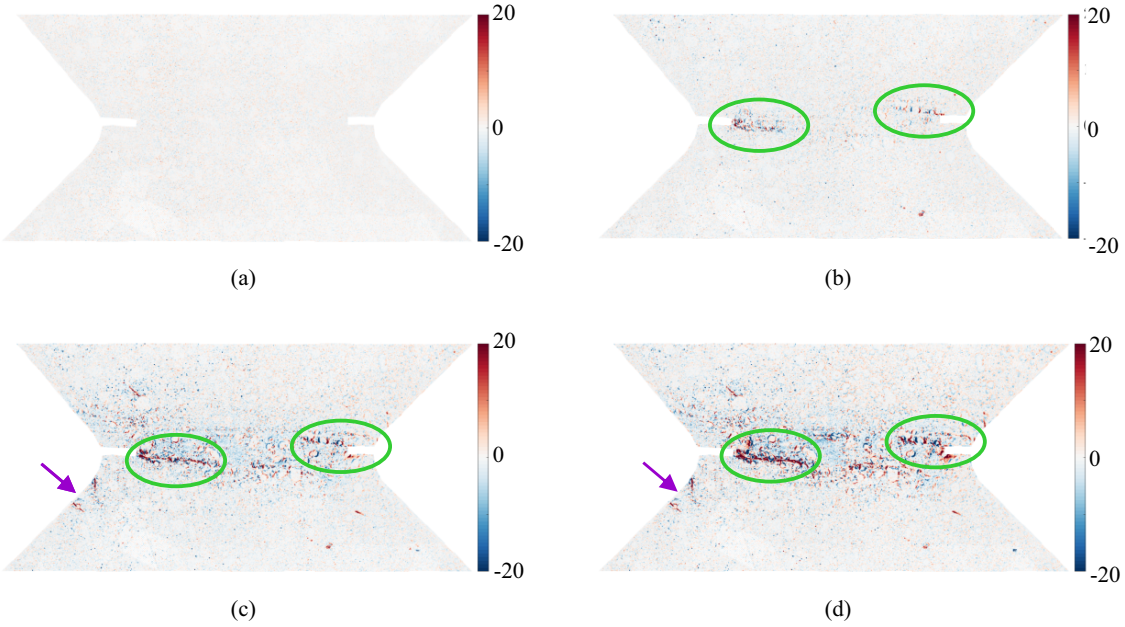

Fig. 10: Correlation residual fields of test W90 for points P_1 (a), P_2 (b) , P_3 (c) and P_4 (d). The green ellipses denote longitudinal damage to the fibers.

The temperature fields of test WF90 (Figure 11) are mostly different from those of test WF00 (Figure 7). The exception is step P_1 (Figure 11(a), $0.43\sigma_M$) where no significant changes in temperature were discerned. For the first experiment, *i.e.* WF00, changes in temperature were due to damage occurring inside the material (*e.g.* fibers breakage) or at its surface. For the WF90 experiment, a single thermal band was present since step P_2 (Figure 11(b), $0.79\sigma_M$) and throughout the end of the experiment (Figure 11(c-d)). Such a temperature distribution may be caused by inner friction between the yarns and their

interplay with the matrix inside the material [59] and plastic deformation [60].

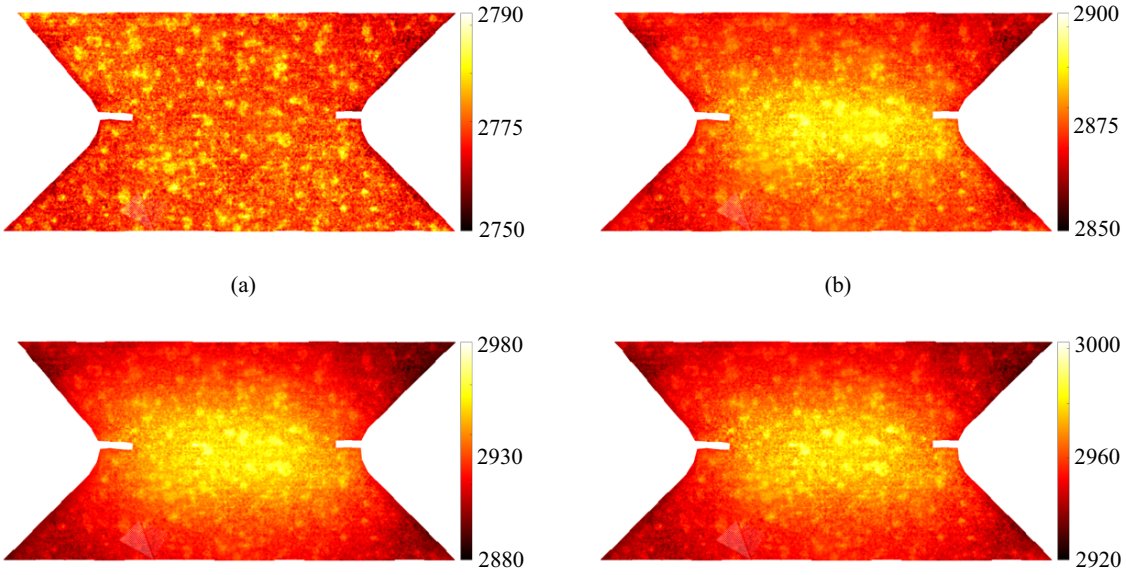

Fig. 11: Radiometric temperature fields (expressed in digital levels) of test W90 for points P_1 (a), P_2 (b), P_3 (c) and P_4 (d).

4.3. Thermomechanical results for test WF45

The last experiment WF45 was analyzed in a similar manner as WF00 and WF90. In Figure 12 the loading history is displayed with the denoted loading blocks and corresponding ultimate strenght values for the chosen points.

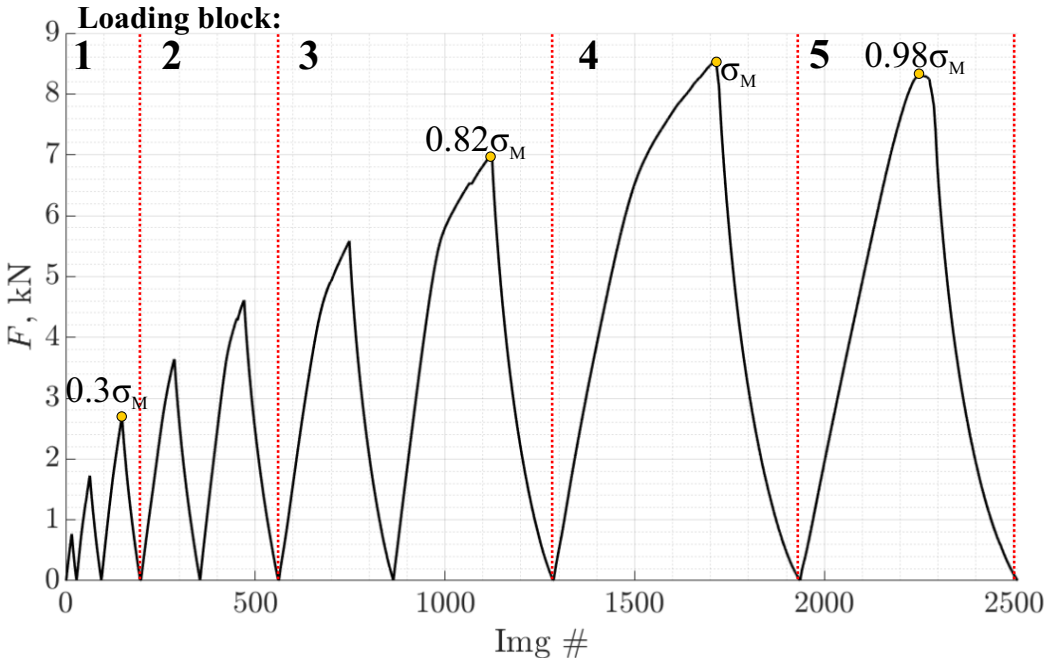

Fig. 12: Load curve for WF45 with denoted ultimate strength values for each observed point.

In the first stage P_1 of the combined tensile/simple shear test, a strained band is detected, which spans across the entire ROI at an angle (Figure 13(a), $0.3\sigma_M$). The strains are more discernible than for the WF90 experiment and are not localized in the middle of the sample. The strain levels are similar to those of WF00 test. In the strain field for the step P_2 (Figure 13(b), $0.82\sigma_M$), the strain band between the notches is the most distinguishable. When compared to the strain gauge data (Fig 3(c), σ_M), it can be concluded that shear is dominant strain. The strain levels are the highest of the three experiments. For step P_3 (Figure 13(c)), the middle strain band is still present, and four more concentrated areas on the opposite end of the peripheral edges are observed. The strain distribution aligns with the loading direction. For the last step (Figure 13(d), $0.98\sigma_M$), the aforementioned localized regions increased in level and expanded. At the upper left corner, low strain values were obtained. This phenomenon is explained by the inability of the algorithm to properly converge in that area due to severe damage to the speckle pattern (Figure 14(d)).

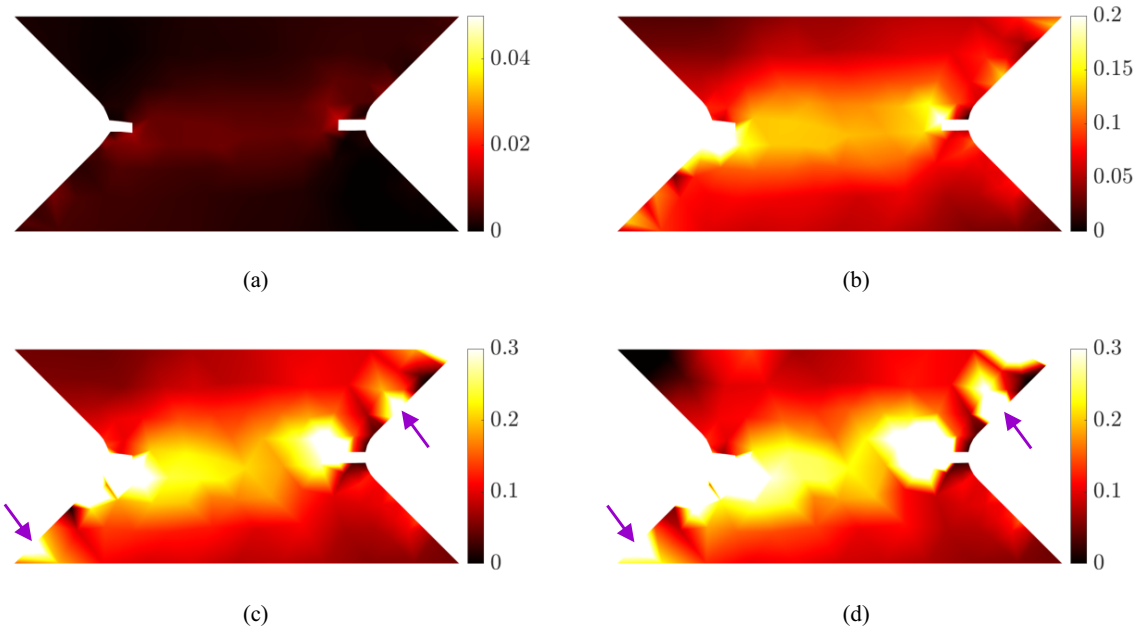

Fig. 13: Major eigenstrain fields of test W45 for points P_1 (a), P_2 (b) , P_3 (c) and P_4 (d).

The correlation residuals are uniform and no damage is observed for step P_1 (Figure 14(a), $0.3\sigma_M$). With load increase until step P_2 (Figure 14(b), $0.82\sigma_M$), the correlation residuals degraded over the ROI, mostly between the notches. At the highest force (Figure 14(c), σ_M), the residuals increased even more across the 45° region. Several damage zones are identified, namely, below the left notch top, the middle of the ROI and above the right notch root. Furthermore, on the lower left and upper right edges, several cracks are detected. The damage occurring at the roots of the notches are attributed to intra-yarn debonding (green ellipses in Figure 14), since the notches were cut directly into the middle yarn (Figure 2(c)). After this stage, the sample rigidity was reduced due to extensive damage. For the final step (Figure 14(d), $0.98\sigma_M$), damage further developed and the crack at the peripheral areas opened more. The combination of tension and shear impacting the damage evolution can be deduced. Due to shear, the middle crack initiated at the notch roots. Tension further opened the cracks and led to the initiation of the middle crack. Damage in the peripheral areas was also due to tension (as seen in Section 4.1).

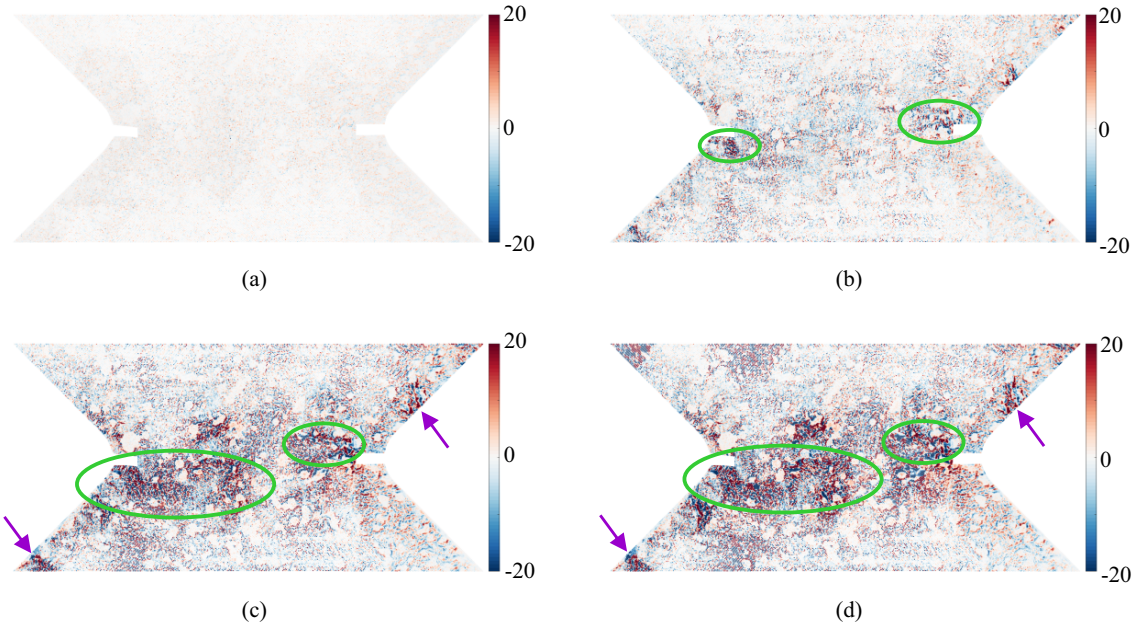

Fig. 14: Correlation residual fields of test W45 for points P_1 (a), P_2 (b) , P_3 (c) and P_4 (d). The green ellipses denote longitudinal damage to the fibers.

The temperature fields are similar to those observed in test WF90, where inner friction of the yarns, damage and plasticity in the matrix have played a key role in generating heat. In elasticity (Figure 15(a), $0.3\sigma_M$), no significant temperature changes are observed. For the second step (Figure 15(b), $0.82\sigma_M$), increased temperatures are observed spanning across the ROI between the notches. However, the corresponding area does not entirely lie between the notches, it is slightly tilted at an angle due to the nature of the mechanical loading. It is observed that the highest temperature level is reached in the middle of the sample. For the force peak (Figure 15(c), σ_M), the highest temperature level is reached at the right notch root. The distribution of temperature is similar to test WF90 and was inclined due to tension. For the last step (Figure 15(d), $0.98\sigma_M$), the temperature distribution is similar to the previous stage. However, the recorded temperature was slightly lower, indicating that most damage occurred at the maximum force and by further increasing the stroke, damage only expanded slightly.

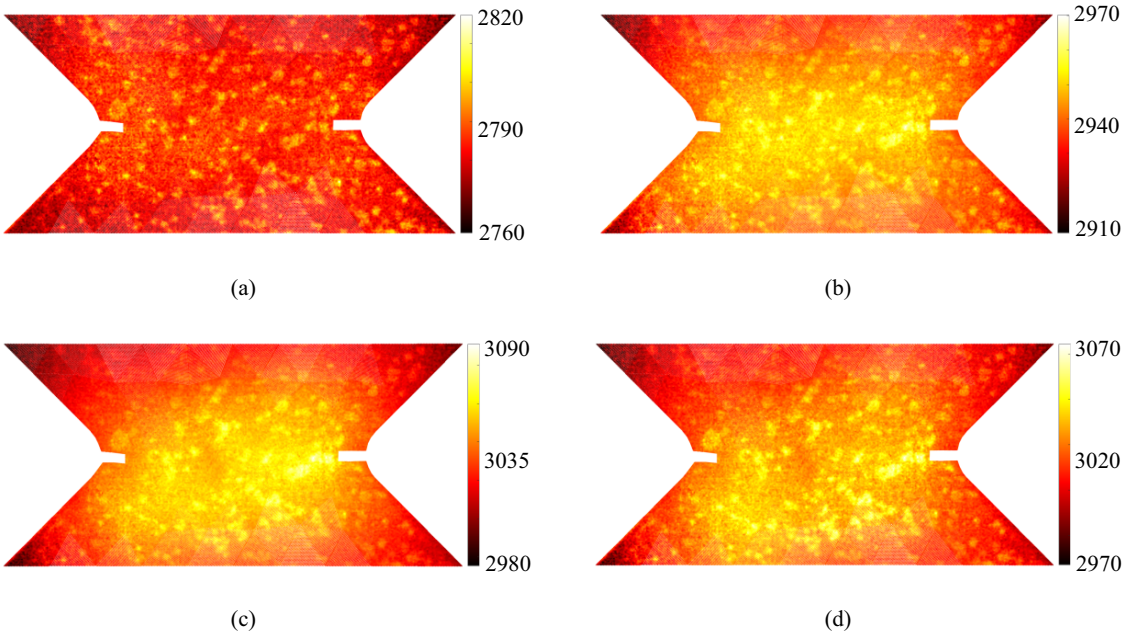

Fig. 15: Radiometric temperature fields (expressed in digital levels) of test W45 for points P_1 (a), P_2 (b), P_3 (c) and P_4 (d).

5. Discussion

In this section, the results of the three experiments are further compared and discussed. First, the net section stress-mean strain ($\sigma - \varepsilon_1$) diagrams are displayed. Next, the temperature change versus strain ($\Delta T - \varepsilon_1$) diagrams are discussed. The strains were calculated using the virtual gauges defined over the ROIs (Figure 3). Only the major eigenstrain ε_1 was taken into consideration to make the comparisons easier. The net section stress was calculated using the measured load divided by the area between the two notches, which was approximately equal to 48 mm^2.

In Figure 16 the stress-strain responses of the three experiments are displayed and in Figure 17 the stereocorrelation residuals are overlayed with the surface CT slices. The highest stress levels were achieved for the tensile test (WF00). During this experiment, the sample exhibited the highest rigidity due to the loading in the direction of the longest yarns in the material architecture (Figure 17(a)). The yarns perpendicular to the loading direction were essentially pulled apart by the loading and the structure of the interwoven yarns caused intra-yarn debonding which can be seen as the cracks at the left notch tip in

the stereocorrelation residuals (Figure 17(a)). Although the highest stress was achieved, the lowest strain levels were observed among the three experiments. Conversely, the shear experiment (WF90) led to the lowest stress levels, but higher strain levels than test WF00. Lower stresses were due to the composite architecture (Figure 17(b)) and the nature of loading. The highest strain levels were reached during the combined tensile/shear test (WF45). Since the loading was a combination of tension and simple shear, due to the tensile component, much higher stress levels were achieved compared to test W90. The combination of the aforementioned loadings proved to be beneficial to the integrity of the sample as higher strains were reached. Compared to test WF00, the strains were about 10 times higher, and compared to test WF90 almost 3 times higher. The maximum stress level was 2 times lower than for test WF00, and approximately 2 times higher than experiment WF90.

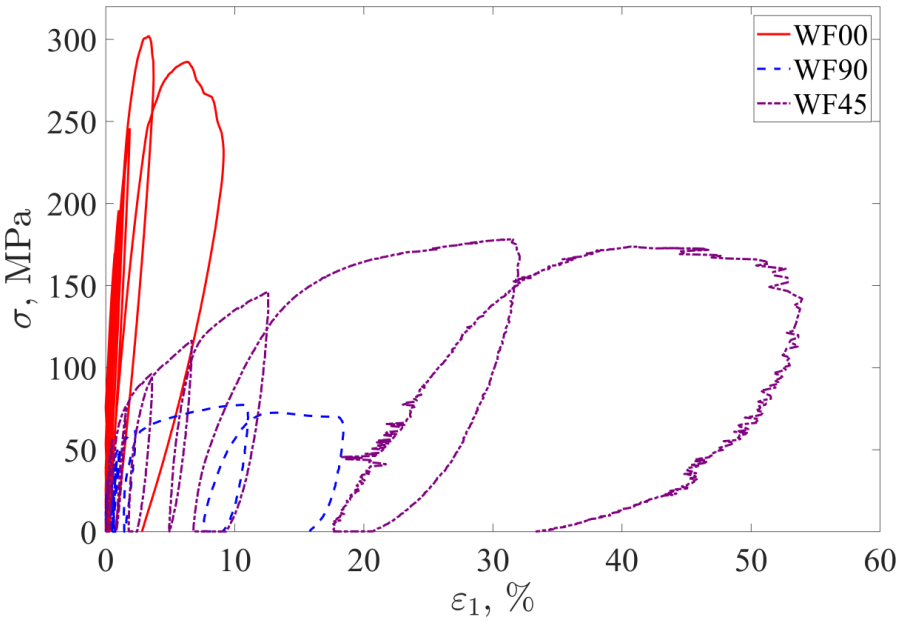

Fig. 16: Net section stress - main major eigenstrain ($\sigma - \varepsilon_1$) curves for all three experiments

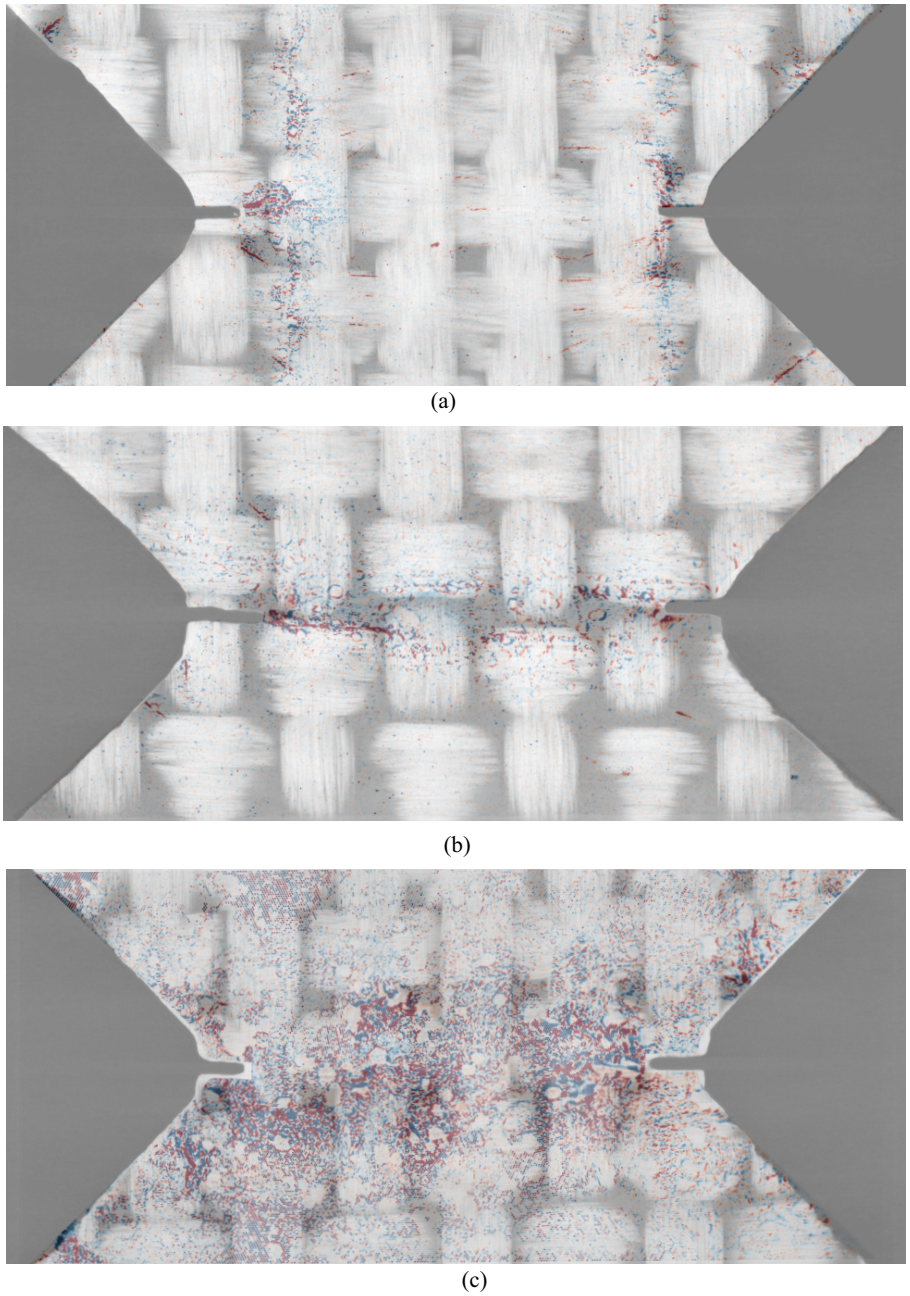

Fig. 17: Stereocorrelation residuals overlayed over the CT surface slices for: (a) WF00, (b) WF90 and (c) WF45

Figure 18 displays the relationship between the change in temperature and the strain obtained from the virtual gauge (Figure 3). The change in temperature ΔT was calculated as the difference between the reference temperature and each subsequent field. Next, using the same virtual gauge as for the strain fields, the nodal temperatures were averaged. By comparing the three experiments, it is observed that the highest change in temperature

was achieved by tensile loading (WF00), while the lowest with the simple shear experiment (WF90). The curves in Figure 18 display fluctuations during the experiment, which are attributed to temperature and strain uncertainties (Table 3) and errors introduced by brightness and contrast corrections.

During the WF00 experiment (Figure 18(a)), in the first three loading blocks (Figure 4), *i.e.* until step P_3, a drop in temperature was detected. For the first three blocks, the temperature lowers with the increase of strain. However, since the relationship between the temperature change and strains is not linear, the thermoelastic effect can be ruled out. After reaching the highest force, the onset of damage occurred, and the temperature increased rapidly with the strain levels. The same effect is also observed for the final loading block.

For the WF90 experiment (Figure 18(b)), the temperature changed slightly for the first two loading blocks (Figure 8). The strain levels were very low. During the third loading block, the temperature experienced a bigger increase. A linear relationship between the strains and temperature is observed. During the fourth and fifth loading blocks, the temperature increased substantially as the strains augmented. As soon as the loading peak was passed and unloading started, the temperature lowered rapidly with a small change in strain. Near the ends of the loading blocks, the temperature stabilized as the strains decreased.

The combined tensile and shear experiment (WF45) (Figure 18(c)) exhibits the characteristics of both WF00 and WF90 experiments. First, a decrease in temperature was detected for the first two loading blocks (Figure 12), and less so for the third. Furthermore, similar relationship between temperature change and strain is observed as for test WF90. The second and third loading blocks display a quasi linear relationship between strains and temperature changes. At the beginning of the fourth block, the change in temperature is comparable to that of test WF90 (Figure 18(b)). After reaching the maximum load, *i.e.* ultimate strength, and as the strains in the loading direction ε_{yy} are prevalent, the unloading stage is similar to that of test WF90. Near the end of the unloading, the

temperature remained constant for a longer range of strains compared to test WF90. The dominance of ε_{yy} becomes apparent after reaching the peak of the final loading block in the temperature change vs average strains (Figure 3(c)). The curve angle is not as steep as for experiment WF90, but less inclined than test WF00.

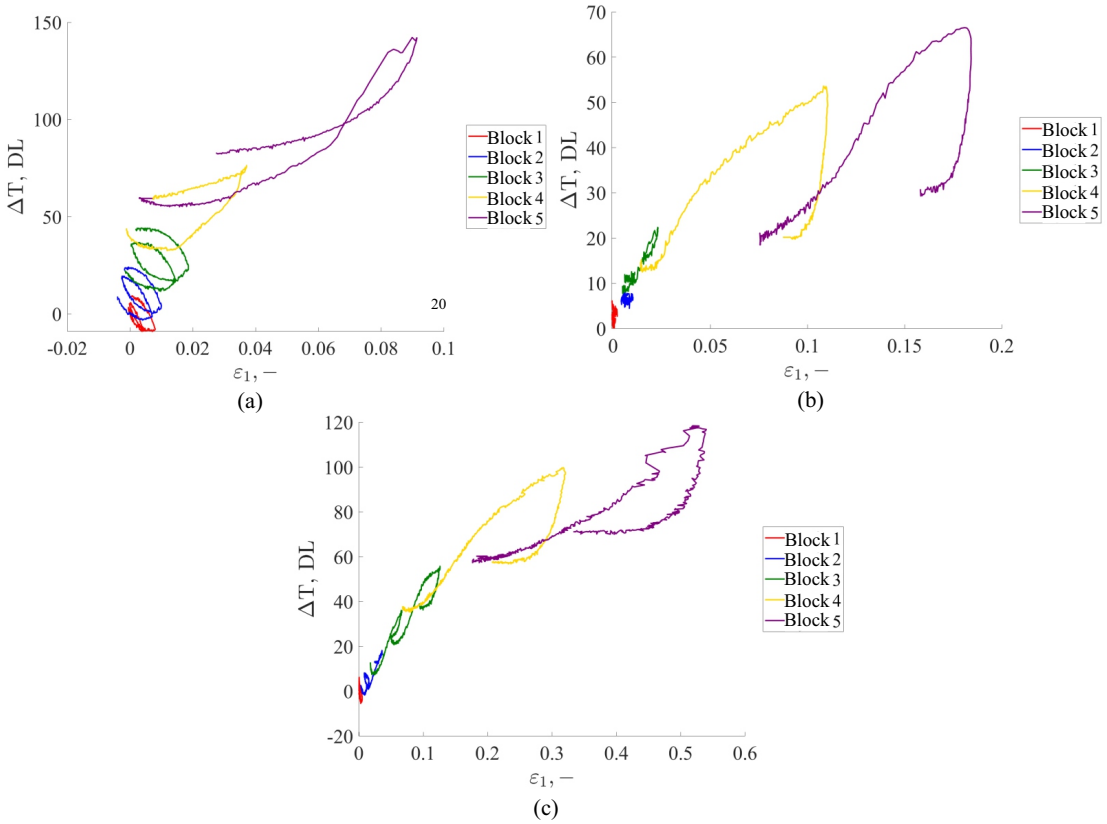

Fig. 18: Change in temperature (with respect to the reference image) vs. major eigenstrain ($\Delta T - \varepsilon_1$) curves for all three experiments.

6. Conclusion and outlook

In this study, three multiaxial experiments were performed on woven glass fiber samples with two notches using a modified Arcan fixture. The samples were subjected to three different loading conditions, namely, tensile, simple shear, and a combination of the last two. A hybrid optical setup comprising two visible-light cameras and one infrared camera, was employed. Hybrid multiview correlation was used to measure thermomechanical fields.

The key findings are as follows:

- The tensile test produced the highest stress, while the combined tensile/simple shear loading resulted in the highest strain levels.
- Under combined loading, shear strains dominated until significant damage occurred, after which strains in the loading direction became predominant.
- For the combined loading, the temperature-strain behavior reflected features of both tensile and simple shear experiments.
- For the tensile test, two strain bands were observed emanating from the notches parallel to the loading, for the simple shear a single strain band was captured between the notches and for the combined loading a single strain band was also captured between the notches, however, it was oriented at an angle.
- The damage mechanisms were detected by combining the surface CT slices and stereocorrelation residuals. During the simple shear and combined loading, intra-yarn debonding was captured emanating from the notches towards the sample center and the damage development was symmetrical, whereas for the tensile test yarn breakage, intra-yarn debonding and surface matrix cracking were captured.
- The temperature fields were similar for the simple shear and combined loading, *i.e.* a single area of increased temperature between the notches due to the yarn inner friction, whereas for the tensile the changes in the temperature were localized around the tips of the notches.

The hybrid correlation approach presented herein was designed to be robust and versatile. Future research should incorporate digital volume correlation analyses of reconstructed volumes from CT scans to further analyze damage growth and interactions within the material bulk.

Acknowledgements

This work was performed within the FULLINSPECT project supported by the Croatian Science Foundation (UIP-2019-04-5460 Grant). This work was also co-funded by the European Union and National Recovery and Resilience Plan Project, reference number: NPOO.C3.2.R3-I1.04.0121. AZ was also supported through the Incoming International Scholarship Program of ENS Paris-Saclay.

CRediT author statement

Zaplatić, A. - Conceptualization, Methodology, Software, Formal analysis, Investigation, Data Curation, Writing - Original Draft

Chang, X. - Software, Writing - Review & Editing

Tomičević, Z. - Conceptualization, Methodology, Data Curation, Project administration, Funding acquisition, Supervision, Writing - Review & Editing

Roux, S. - Conceptualization, Writing - Review & Editing

Hild, F. - Conceptualization, Methodology, Investigation, Supervision, Writing - Review & Editing

Declaration of competing interest

The authors have no conflict of interest to declare.

Declaration of generative AI in scientific writing

The authors declare that no generative AI was employed.

References

[1] M. E. Torbali, A. Zolotas, N. P. Avdelidis, A state-of-the-art review of non-destructive testing image fusion and critical insights on the inspection of aerospace composites towards sustainable maintenance repair operations, Applied Sciences 13 (2023) 2732. doi:10.3390/app13042732.

[2] F. Khan, N. Hossain, J. J. Mim, S. M. Rahman, M. J. Iqbal, M. Billah, M. A. Chowdhury, Advances of composite materials in automobile applications – a review, Journal of Engineering Research (2024). doi:10.1016/j.jer.2024.02.017.

[3] R. Hsissou, R. Seghiri, Z. Benzekri, M. Hilali, M. Rafik, A. Elharfi, Polymer composite materials: A comprehensive review, Composite Structures 262 (2021) 113640. doi:10.1016/j.compstruct.2021.113640.

[4] F. Schmidt, M. Rheinfurth, P. Horst, G. Busse, Multiaxial fatigue behaviour of gfrp with evenly distributed or accumulated voids monitored by various ndt methodologies, International Journal of Fatigue 43 (2012) 207–216. doi:10.1016/j.ijfatigue.2012.03.013.

[5] J. Choi, H. Lee, H. Lee, N. Kim, A methodology to predict the fatigue life under multi-axial loading of carbon fiber-reinforced polymer composites considering anisotropic mechanical behavior, Materials 16 (2023) 1952. doi:10.3390/ma16051952.

[6] A. Zaplatić, Z. Tomičević, F. Hild, Characterization of woven composite material under multiaxial loading regimes using fe-based stereocorrelation, Acta Polytechnica CTU Proceedings 48 (2024) 56–60. doi:10.14311/APP.2024.48.0056.

[7] A. Vrgoč, Z. Tomičević, B. Smaniotto, F. Hild, Application of different imaging techniques for the characterization of damage in fiber reinforced polymer, Composites Part A: Applied Science and Manufacturing 150 (11 2021). doi:10.1016/j.compositesa.2021.106576.

[8] J. Du, H. Wang, C. Chen, M. Ni, C. Guo, S. Zhang, H. Ding, H. Wang, Y. Bi, Damage classification and evolution in composite under low-velocity impact using acoustic emission, machine learning and wavelet packet decomposition, Engineer-

ing Fracture Mechanics 306 (2024) 110238. doi:10.1016/j.engfracmech.2024.110238.

[9] N. Li, Y. Zhou, Failure mechanism analysis of fiber-reinforced polymer composites based on multi-scale fracture plane angles, Thin-Walled Structures 158 (2021) 107195. doi:https://doi.org/10.1016/j.tws.2020.107195.

[10] N. Tableau, Z. Aboura, K. Khellil, F. Laurin, J. Schneider, Multiaxial loading on a 3d woven carbon fiber reinforced plastic composite using tensile-torsion tests : Identification of the first damage envelope and associated damage mechanisms, Composite Structures 227 (2019) 111305. doi:10.1016/j.compstruct.2019.111305.

[11] Q. Guo, Y. Zhang, D. Li, X. Sun, M. Li, L. Chen, Experimental characterization of the compressive properties and failure mechanism of novel multiaxial 3d woven composites, Composites Communications 28 (2021) 100905. doi:10.1016/j.coco.2021.100905.

[12] Q. Yin, B. Zillmann, S. Suttner, G. Gerstein, M. Biasutti, A. E. Tekkaya, M. F. Wagner, M. Merklein, M. Schaper, T. Halle, A. Brosius, An experimental and numerical investigation of different shear test configurations for sheet metal characterization, International Journal of Solids and Structures 51 (2014) 1066–1074. doi:10.1016/j.ijsolstr.2013.12.006.

[13] M. Gorji, D. Mohr, Micro-tension and micro-shear experiments to characterize stress-state dependent ductile fracture, Acta Materialia 131 (2017) 65–76. doi:10.1016/j.actamat.2017.03.034.

[14] A. Zaplatić, Z. Tomičević, D. Čakmak, F. Hild, Identifiability of ludwik's law parameters depending on the sample geometry via inverse identification procedure, Coupled Systems Mechanics 11 (2022) 133–149. doi:10.12989/csm.2022.11.2.133.

[15] M. Arcan, Z. Hashin, A. Voloshin, A method to produce uniform plane-stress states with applications to fiber-reinforced materials, Experimental Mechanics 18 (1978) 141–146. doi:10.1007/BF02324146.

[16] A. Zaplatić, Z. Tomičević, D. Čakmak, F. Hild, Improvement of the arcan setup for the investigation of thin sheet behavior under shear loading, Experimental Mechanics 62 (2022) 313–332. doi:10.1007/s11340-021-00762-1.

[17] M. A. Sutton, Computer vision-based, noncontacting deformation measurements in mechanics: A generational transformation, Applied Mechanics Reviews 65 (2013). doi:10.1115/1.4024984.

[18] J. Holmes, S. Sommacal, R. Das, Z. Stachurski, P. Compston, Digital image and volume correlation for deformation and damage characterisation of fibre-reinforced composites: A review, Composite Structures 315 (2023) 116994. doi:10.1016/j.compstruct.2023.116994.
URL https://linkinghub.elsevier.com/retrieve/pii/S0263822323003380

[19] C. Ibarra-Castanedo, J. R. Tarpani, X. P. V. Maldague, Nondestructive testing with thermography, European Journal of Physics 34 (2013) S91. doi:10.1088/0143-0807/34/6/S91.

[20] J. Zalameda, W. Winfree, Detection and characterization of damage in quasi-static loaded composite structures using passive thermography, Sensors 18 (2018) 3562. doi:10.3390/s18103562.

[21] A. Buljac, C. Jailin, A. Mendoza, J. Neggers, T. Taillandier-Thomas, A. Bouterf, B. Smaniotto, F. Hild, S. Roux, Digital volume correlation: Review of progress and challenges, Experimental Mechanics 58 (2018). doi:10.1007/s11340-018-0390-7.

[22] L. Mao, H. Liu, Y. Zhu, Z. Zhu, R. Gue, F. Chiang, 3d strain mapping of opaque materials using an improved digital volumetric speckle photography technique with x-ray microtomography, Applied Sciences 9 (2019) 1418. doi:doi.org/10.3390/app9071418.

[23] A. Vrgoč, Z. Tomičević, B. Smaniotto, F. Hild, Damage characterization in fiber reinforced polymer via digital volume correlation. coupled systems mechanics, Coupled System Mechanics 10 (2021) 545–560. doi:10.12989/csm.2021.10.6.545.
URL https://hal.science/hal-03482350

[24] H. Schreier, J. J. Orteu, M. A. Sutton, Image correlation for shape, motion and deformation measurements: Basic concepts, theory and applications, Springer US, 2009. doi:10.1007/978-0-387-78747-3.

[25] M. Mehdikhani, E. Steensels, A. Standaert, K. A. Vallons, L. Gorbatikh, S. V. Lomov, Multi-scale digital image correlation for detection and quantification of matrix cracks in carbon fiber composite laminates in the absence and presence of voids controlled by the cure cycle, Composites Part B: Engineering 154 (2018) 138–147. doi:https://doi.org/10.1016/j.compositesb.2018.07.006.

[26] M. Sutton, J. Yan, V. Tiwari, H. Schreier, J. Orteu, The effect of out-of-plane motion on 2d and 3d digital image correlation measurements, Optics and Lasers in Engineering 46 (2008) 746–757. doi:10.1016/j.optlaseng.2008.05.005.

[27] G. Besnard, F. Hild, S. Roux, "finite-element" displacement fields analysis from digital images: Application to portevin-le châtelier bands, Experimental Mechanics 46 (2006) 789–803. doi:10.1007/s11340-006-9824-8.

[28] F. Hild, S. Roux, Comparison of local and global approaches to digital image correlation, Experimental Mechanics 52 (2012) 1503–1519. doi:10.1007/s11340-012-9603-7.

[29] M. Flores, D. Mollenhauer, V. Runatunga, T. Beberniss, D. Rapking, M. Pankow, High-speed 3d digital image correlation of low-velocity impacts on composite plates, Composites Part B: Engineering 131 (2017) 153–164. doi:https://doi.org/10.1016/j.compositesb.2017.07.078.

[30] R. Fouque, R. Bouclier, J.-C. passieux, J.-N. ël Périé, Stereo digital image correlation: formulations and perspectives, Comptes Rendus. Mécanique 349 (2021) 453–463. doi:https://doi.org/10.5802/crmeca.93.

[31] L. Dubreuil, J.-E. Dufour, Y. Quinsat, F. Hild, Mesh-based shape measurements with stereocorrelation principle and first results, Experimental Mechanics 56 (2016) 1231–1242. doi:10.1007/s11340-016-0158-.

[32] X. Chang, C. L. Gourriéreca, L. Turpin, M. Berny, F. Hild, S. Roux, Proper generalized decomposition stereocorrelation to measure kinematic fields for high speed impact on laminated glass, Computer Methods in Applied Mechanics and Engineering 415 (2023) 116217. doi:10.1016/j.cma.2023.116217.

[33] J.-E. Pierré, J.-C. Passieux, J.-N. ël Périé, Finite element stereo digital image correlation: Framework and mechanical regularization, Experimental mechanics 57 (2017) pages443–456. doi:10.1007/s11340-016-0246-y.

[34] G. Besnard, J.-M. Lagrange, F. Hild, S. Roux, C. Voltz, Characterization of necking phenomena in high speed experiments by using a single camera, EURASIP Journal on Image and Video Processing 2010 (2010) 215956.
URL https://hal.science/hal-00497354

[35] L. Yu, B. Pan, Single-camera stereo-digital image correlation with a four-mirror adapter: optimized design and validation, Optics and Lasers in Engineering 87 (2016) 120–128. doi:10.1016/j.optlaseng.2016.03.014.

[36] A. Zaplatić, Z. Tomičević, X. Chang, I. Skozrit, S. Roux, F. Hild, Hybrid infrared-visible multiview correlation to study damage in a woven composite complex-

shaped specimen, Coupled Systems Mechanics 12 (5 2023). doi:doi.org/10.12989/csm.2023.12.5.000.

[37] M. Berny, T. Archer, P. Beauchêne, A. Mavel, F. Hild, Displacement uncertainty quantifications in t3-stereocorrelation, Experimental Mechanics 61 (2021) 771–790. doi:10.1007/s11340-021-00690-0.

[38] B. Beaubier, J.-E. Dufour, F. Hild, S. Roux, S. Lavernhe, K. L. Taillard, Cad-based calibration and shape measurement with stereodic principle and application on test and industrial parts, Experimental Mechanics 54 (2014) 329–341. doi:ff10.1007/s11340-013-9794-6ff.ffhal-00974363.

[39] X. Chang, C. L. Gourriérec, F. Hild, S. Roux, Brightness and contrast corrections for stereocorrelation global and instantaneous formulation with spatial regularization, Mechanical Systems and Signal Processing 208 (2024) 111057. doi:doi.org/10.1016/j.ymssp.2023.111057.

[40] A. Zaplatić, Z. Tomičević, X. Chang, P. Kosec, S. Roux, F. Hild, Advanced fe-based multimodal correlation analyses for the characterization of woven composite, Mechanical Systems and Signal Processing 224 (2024) 112079. doi:10.1016/j.ymssp.2024.112079.

[41] M. Gao, Z. Zhou, K. Ding, X. Wang, Detection of crack defects in carbon fiber composites using passive infrared thermography, Ferroelectrics 607 (2023) 154–172. doi:10.1080/00150193.2023.2198383.

[42] K. S.A., F. Brachelet, F. Breaban, D. Defer, Defect detection in cfrp by infrared thermography with co2 laser excitation compared to conventional lock-in infrared thermography, Composites Part B: Engineering 69 (2015) 1–5. doi:https://doi.org/10.1016/j.compositesb.2014.09.018.

[43] F. Ciampa, P. Mahmoodi, F. Pinto, M. Meo, Recent advances in active infrared

thermography for non-destructive testing of aerospace components, Sensors 18 (2) (2018). doi:10.3390/s18020609.

[44] V. Munoz, B. Valès, M. Perrin, M. L. Pastor, H. Welemane, A. Cantarel, M. Karama, Damage detection in cfrp by coupling acoustic emission and infrared thermography, Composites Part B: Engineering 85 (2016) 68–75. doi:10.1016/j.compositesb.2015.09.011.

[45] C. Maierhofer, M. Röllig, M. Gower, M. Lodeiro, G. Baker, C. Monte, A. Adibekyan, B. Gutschwager, L. Knazowicka, A. Blahut, Evaluation of different techniques of active thermography for quantification of artificial defects in fiber-reinforced composites using thermal and phase contrast data analysis, International Journal of Thermophysics 39 (2018). doi:10.1007/s10765-018-2378-z.

[46] S. Farmaki, D. A. Exarchos, I. K. Tragazikis, T. E. Matikas, K. G. Dassios, A novel infrared thermography sensing approach for rapid, quantitative assessment of damage in aircraft composites, Sensors (Switzerland) 20 (2020) 1–16. doi:10.3390/s20154113.

[47] M. A. Farooq, W. Shariff, D. O'callaghan, A. Merla, P. Corcoran, On the role of thermal imaging in automotive applications: A critical review, IEEE Access 11 (2023) 25152–25173. doi:10.1109/ACCESS.2023.3255110.

[48] J. Zalameda, W. Winfree, Passive thermography measurement of damage depth during composites load testing, Frontiers in Mechanical Engineering 7 (2021) 651149. doi:10.3389/fmech.2021.651149.

[49] A. Charbal, J. E. Dufour, F. Hild, M. Poncelet, L. Vincent, S. Roux, Hybrid stereocorrelation using infrared and visible light cameras, Experimental Mechanics 56 (2016) 845–860. doi:10.1007/s11340-016-0127-4.

[50] N. Cholewa, P. Summers, S. Feih, A. Mouritz, B. Lattimer, S. Case, A technique for coupled thermomechanical response measurement using infrared thermography

and digital image correlation (tdic), Experimental Mechanics 56 (2016) 145–164. doi:10.1007/S11340-015-0086-1.

[51] Y. Wang, A. Charbal, J. E. Dufour, F. Hild, S. Roux, L. Vincent, Hybrid multiview correlation for measuring and monitoring thermomechanical fatigue test, Experimental Mechanics 60 (2020) 13–33. doi:10.1007/s11340-019-00500-8.

[52] Y. Wang, A. Charbal, F. Hild, S. Roux, L. Vincent, Crack initiation and propagation under thermal fatigue of austenitic stainless steel, International Journal of Fatigue 124 (2019) 149–166. doi:10.1016/j.ijfatigue.2019.02.036.

[53] A. Charbal, S. Roux, F. Hild, L. Vincent, Spatiotemporal regularization for digital image correlation: Application to infrared camera frames, International Journal for Numerical Methods in Engineering 114 (2018) 1331–1349. doi:10.1002/nme.5788.

[54] A. Charbal, S. Roux, F. Hild, L. Vincent, Regularised digital-level corrections for infrared image correlation, Quantitative InfraRed Thermography Journal 15 (2018) 172–193. doi:10.1080/17686733.2018.1425955.

[55] M. Stamm, P. Krüger, H. Pfeiffer, B. Köhler, J. Reynaert, M. Wevers, In-plane heat-wave thermography as digital inspection technique for fasteners in aircraft fuselage panels, Applied Sciences 11 (2021) 132. doi:10.3390/app11010132.

[56] Multiaxial Fatigue and Deformation: Testing and Prediction, ASTM International, 2000. doi:10.1520/STP1387-EB.

[57] J.-E. Dufour, F. Hild, S. Roux, Shape, displacement and mechanical properties from isogeometric multiview stereocorrelation, The Journal of Strain Analysis for Engineering Design 50 (2015) 470–487. doi:10.1177/0309324715592530.
URL https://hal.archives-ouvertes.fr/hal-01198921

[58] A. Charbal, L. Vincent, F. Hild, M. Poncelet, J. E. Dufour, S. Roux, D. Farcage, Characterization of temperature and strain fields during cyclic laser shocks, Quantitative InfraRed Thermography Journal 13 (2016) 1–18. doi:10.1080/17686733.2015.1077544.

[59] Z. Pan, Z. Wu, J. Xiong, Localized temperature rise as a novel indication in damage and failure behavior of biaxial non-crimp fabric reinforced polymer composite subjected to impulsive compression, Aerospace Science and Technology 103 (2020) 105885. doi:10.1016/j.ast.2020.105885.

[60] P. S. Singh, R. Narayan, I. Sen, D. Hofmann, U. Ramamurty, Effect of strain rate and temperature on the plastic deformation behaviour of a bulk metallic glass composite, Materials Science and Engineering A-structural Materials Properties Microstructure and Processing 534 (2012) 476–484. doi:10.1016/J.MSEA.2011.11.096.

Scientific paper 7

A. Zaplatić, Z. Tomičević, X. Chang, P. Kosec, S. Roux, F. Hild, “Advanced FE-based multimodal correlation analyses for the characterization of woven composite”, Mechanical systems and signal processing, vol. 224, no. 24, pp. 112079, 2025, doi: 10.1016/j.ymssp.2024.112079

Preprint of the published journal article.

Advanced FE-based multimodal correlation analyses for the characterization of woven composite

Andrija Zaplatić[a,b], Zvonimir Tomičević[a,*], Xuyang Chang[c], Petar Kosec[d], Stéphane Roux[b], François Hild[b]

[a] *University of Zagreb, Faculty of Mechanical Engineering and Naval Architecture 10002 Zagreb, Croatia*
[b] *Université Paris-Saclay, CentraleSupélec, ENS Paris-Saclay, CNRS LMPS - Laboratoire de Mécanique Paris-Saclay, 91190 Gif-sur-Yvette, France*
[c] *University of Science and Technology Beijing, School of Physics and mathematics 100030 Beijing, China*
[d] *Neo Dens d.o.o., Fallerovo šetalište 22, 10000 Zagreb, Croatia*

Abstract

This paper presents a comprehensive characterization of a woven glass fiber composite sample with two notches in the gauge area subjected to cyclic tension using an Arcan fixture. An advanced optical setup was developed, comprising two visible light cameras and an infrared camera. Additionally, an X-ray scanner was employed to examine *ex-situ* the bulk for microstructural changes during the experiment. A multimodal correlation method is introduced that combines hybrid (infrared-visible) multiview correlations and Digital Volume Correlation to measure displacement, strain, and temperature fields within the *same* Lagrangian framework. The strain fields obtained from both algorithms are consistent. The findings reveal the presence of asymmetric shear bands and damage originating from the notch roots due to the underlying woven architecture. Several damage mechanisms are identified from both frameworks.

Keywords: Arcan fixture, woven composite, tomography, thermography, hybrid multiview correlation

*Corresponding author
Email address: zvonimir.tomicevic@fsb.hr (Zvonimir Tomičević)

1. Introduction

Industries, particularly aerospace engineering [1], constantly evolve and demand advanced materials. As a result, the utilization of fiber-reinforced polymer (FRP) composites is experiencing exponential growth [2]. FRPs are highly sought-after due to their ability to customize architecture and geometry for specific loading regimes. While conventional engineering materials, like metals, share some similarities, FRPs surpass them by offering superior strength-to-weight ratios. This advantage arises from the lower weight of FRPs despite their high strength. Yet, FRP architectures are more intricate and heterogeneous. Thus, comprehensive experimental investigations are essential for accurately predicting FRP degradations and ultimate failure under prescribed workloads.

Predicting the behavior and ultimate failure of FRP architectures is challenging due to their pronounced heterogeneity. FRPs are susceptible to multiple damage mechanisms, including fiber/matrix interface debonding, fiber breakage, matrix microcracking, fiber pull-out, and delamination of individual layers, all affecting the material stability [3]. Uniaxial tensile tests alone are insufficient for characterizing FRPs. More comprehensive experimental investigations are necessary [4]. The availability and high cost of testing machines capable of prescribing complex loading regimes induce constraints. In such cases, specialized loading apparatuses may be used parallel to uniaxial testing machines. One such setup is the Modified Arcan Fixture (MAF) [5], specifically designed to apply a wide range of in-plane loads, including uniaxial tension, simple shear, and their various combinations. It is then more complicated to obtain material responses during loading via classical contact measurement equipment such as extensometers and strain gauges due to the complex geometry of the samples. This difficulty is mitigated by developing optical methods in experimental mechanics, which provide means for contactless full-field measurements [6]. Digital Image Correlation (DIC) utilizing visible light cameras is widely recognized as the most versatile and user-friendly full-field measurement method [7]. Its adaptability and ease of use make it a popular choice. In recent years, other techniques such as infrared (IR) thermography [8, 9] and X-ray computed tomography

(XCT) [10, 11] have gained increased interest in the field of composite characterization.

2D-DIC is most often used due to its simplicity. Today, Finite element (FE) based DIC [12, 13, 14] is gaining attraction. The main difference with its local counterpart is that using FE meshes ensures continuity of the displacement fields with no additional interpolation [15]. However, the computational cost is higher. In cases of non-planar geometry or if out-of-plane displacements are expected, 2D DIC is not suitable [16]. It is possible to consider stereocorrelation [17] where image pairs are used for shape measurements [18, 19], calibration [20] and displacement measurements [21, 22]. The image pair can be obtained with one (utilizing a set of mirrors [23, 24]) or more cameras [21]. Similarly to global 2D DIC, it is also possible to utilize FE meshes in global stereocorrelation [25]. For the calibration of the stereovision system, the known geometry of the CAD model [26] or FE mesh [27, 28] are exploited. Although FE-based stereocorrelation is powerful, only surface kinematics and surface damage are observed and estimated. Additional measurement methods should be coupled for a more comprehensive material analysis.

IR thermography enables for the quantification of temperature fields and the detection of heat-related phenomena in composites [29]. It is beneficial for assessing thermal properties, detecting defects [30, 31], and monitoring changes in material behavior during mechanical loading [32]. IR thermography by itself is well-known and used. However, its potential is even more exploited when combined with DIC into a hybrid multiview framework [33]. In such a framework, it is possible to measure displacement and strain fields from the visible light cameras and the temperature fields, all expressed within the *same* Lagrangian frame. Such hybrid approaches were used by Wang *et al.* [34, 35] to analyze thermomechanical fatigue tests. The main difficulty when including IR images in DIC schemes is related to digital-level variations. This phenomenon happens as a result of thermomechanical couplings [36] (active thermography) or, in the case of composite materials, due to damage [37]. This effect is alleviated by implementing brightness and contrast corrections [38, 39]. In the present case, the calculated brightness and contrast

corrections are used to assess the local temperature variations over the Lagrangian frame. Using IR thermography, surface and sub-surface phenomena [40] are captured and analyzed by observing the effect of dissipation on temperature fields and comparing it to strain fields. However, damage within the bulk of the material is still unknown. Therefore, 3D imaging may also be used.

X-ray computed tomography (CT) offers valuable insights into the internal structure of composite materials [41, 42]. CT provides 3D images based on X-ray attenuation, revealing fiber orientations and internal defects [43]. It even provides quantitative measurements of porosity and fiber volume fraction [44]. Like DIC, CT scans are registered via Digital Volume Correlation, from which 3D displacement and strain fields are measured. Furthermore, the 3D volumes can also be discretized by FE meshes [45]. Mechanical regularization [46] was also implemented in some DVC algorithms [47], which introduces additional constraints to the measured displacement fields.

Both IR thermography and X-ray computed tomography contribute to a comprehensive understanding of composite materials by providing complementary information to (stereo)DIC. These techniques offer unique capabilities for studying the thermal behavior, internal structure, and defect analyses, enhancing the overall characterization process. This paper aims to establish a robust and reliable methodology for FRP characterization by utilizing *three* different imaging modalities within a *single* framework. Such an approach provides an extensive information pool on material behavior. Combining FE-based stereocorrelation, IR thermography, and X-ray imaging in the same Lagrangian framework is beneficial since the relationship between the released heat on the surface or in the bulk of the material and damage can be established. Furthermore, assessing the 3D kinematics within the material bulk further enriches the mechanical characterization. The literature survey did not yield with any previous studies where such framework was established. Furthermore, according to the existing literature, the hybrid IR and visible light correlation was not applied to FRPs.

The paper is organized as follows. A woven glass fiber composite [48] was subjected

to cyclic tension with intermittent unloadings to perform *ex-situ* CT scanning. The multimodal experimental setup and protocol are first defined, followed by the basic principles of FE-based stereocorrelation. The next section presents hybrid multiview correlation and DVC results, which are subsequently compared.

2. Experimental protocol

In this section, the experimental protocol is presented. A so-called Arcan notched specimen [5] was subjected to cyclic tension. The 3 mm thick sample was made of woven glass fibers infused with a vinylester resin, where the yarns were oriented at 0°/90°along the loading direction. Two notches were cut in the roots of both V sections. The notches were 2 mm long and 0.5 mm wide, reducing the net section area to approximately 48 mm^2. The sample was loaded with a 0.24 mm/min velocity in a displacement control mode.

The experimental and optical setup was entirely covered by black fabric (Figure 1(a)) to prevent any outside lighting perturbations that would impact the brightness and contrast conditions of the visible light cameras during the experiment. The MAF (Figure 1(b)) was configured for tensile loading. The hybrid multiview optical setup (Figure 1(c)) monitoring the sample surface consisted of two identical visible light cameras (VL) and one infrared camera (IR). All three cameras observed the same Region of Interest (ROI) from different angles.

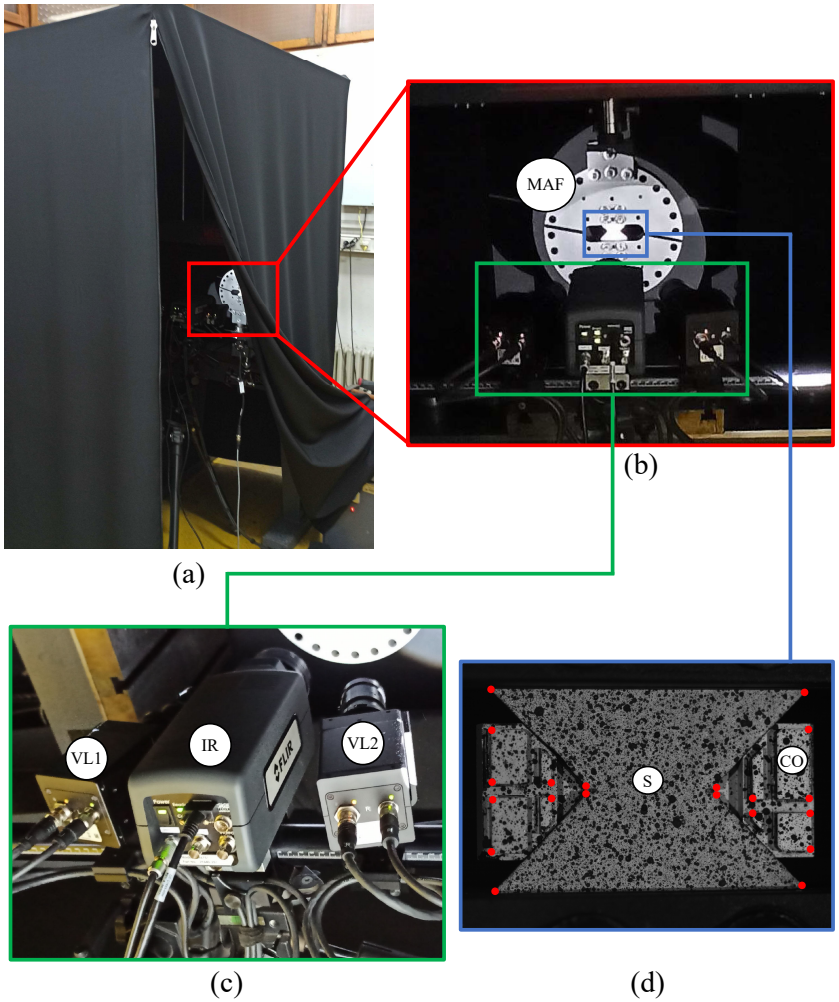

Fig. 1: Experimental setup. (a) Black fabric protection over the experimental and optical setup. (b) MAF. (c) Hybrid optical setup. (d) Arcan sample (S) with the 3D calibration object (CO) and highlighted pre-calibration points.

The parameters of the hybrid optical setup are listed in Table 1. Since the black and white speckles used had similar emissivity as the composite sample, they were invisible to the IR camera. Coarse graphite speckles were also deposited onto the sample surface to be visible by all three cameras (Figure 1(d)). Before the beginning of the experiment, 20 images were captured in the unloaded state using the hybrid optical setup to quantify measurement uncertainties. Images were also acquired with the 3D calibration object mounted on the sample surface.

Table 1: Hardware parameters of the multiview and multimodal system

Setup	Visible light cameras	IR camera
Camera	$2\times$ Dalsa Falcon 12M	Flir A6751
Definition	4096×3068 px	640×512 px
Gray Levels rendering	8 bit	16 bit
Lens	Titanar B75	Flir 50 mm
Distance ring	-	6.35 mm
Aperture	f/5.6	-
Field of view	82×61 mm	64×51.2 mm
Image scale	0.02 mm/px	0.1 mm/px
Stereo angle	$25°$	$0°$
Stand-off distance	326 mm	320 mm
Camera center proximity	44 mm	0
Image acquisition rate	1 fps	
Patterning technique	B/W paints + black graphite speckles	

The tensile experiment consisted of nine loading/unloading cycles (Figure 2). The prescribed loading was interrupted to acquire *ex-situ* CT scans of the unloaded state. The hardware parameters of the CT scanner and the captured scans are listed in Table 3. Before starting the experiment, three scans were captured, namely **Scan 0**, **Scan 0-bis**, and **Scan 0-rbm**. **Scan 0-bis** was acquired immediately after **Scan 0**. These two scans were used to evaluate the displacement and strain resolutions. The third, **Scan 0-rbm**, was performed to evaluate the influence of rigid body motions (rbm) on the DVC uncertainties since the sample was periodically mounted and unmounted from the CT scanner. Only **Scan 0** was High-Quality (HQ), whose parameters are reported in Table 4, whereas all other scans were of Low-quality (LQ).

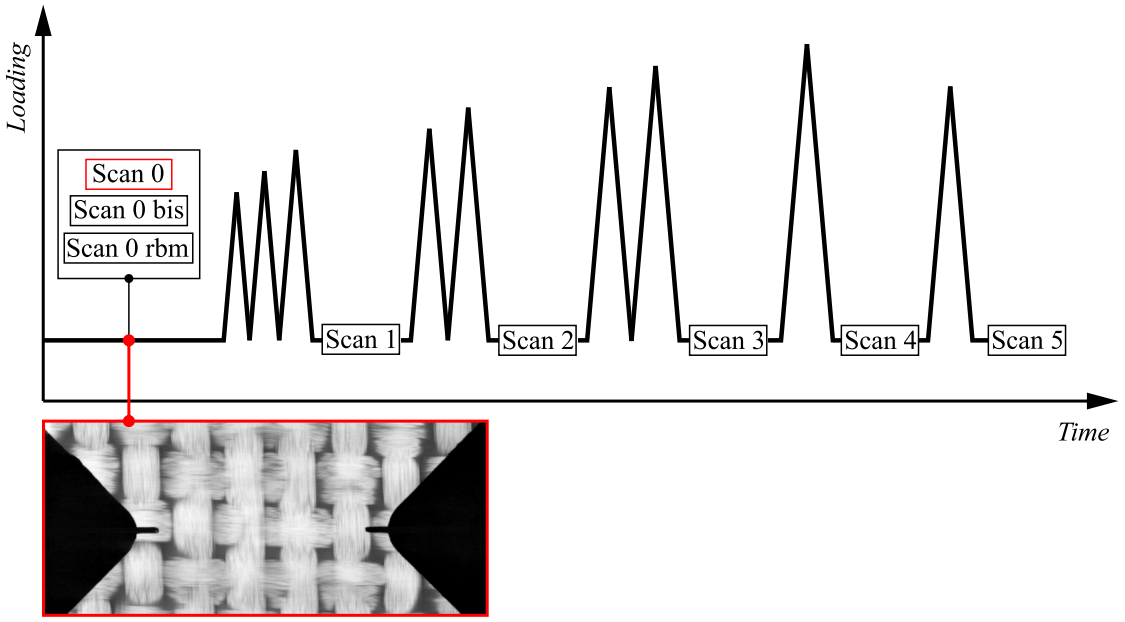

Fig. 2: *Ex-situ* scanning protocol concerning the loading history with a section of **Scan 0** (red box).

3. Global formulation of hybrid multiview correlation

This section introduces the formulation of Hybrid Multiview (HM) Calibration and subsequent correlation. Brightness and Contrast Corrections (BCCs) were applied for both HM calibration and correlation analyses. First, the projection transform, derived from the pinhole camera model [21], relates the 3D world coordinates to those of the 2D image plane

$$s^c \begin{Bmatrix} x^c \\ y^c \\ 1 \end{Bmatrix} = [\mathbf{P}^c] \begin{Bmatrix} X \\ Y \\ Z \\ 1 \end{Bmatrix} \tag{1}$$

where $\{X\ Y\ Z\ 1\}^\top$ are the homogeneous coordinates of any surface point (belonging to the FE mesh), $[\mathbf{P}^c]$ the (3×4) projection matrix of camera c, $\{x^c\ y^c\ 1\}^\top$ the homogeneous coordinates of the projected points in the camera c plane, and s^c the scale factor. The projection matrices $[\mathbf{P}^c]$ are built from the unknown intrinsic $[\mathbf{N}^c]$ (3×3) and extrinsic

$[\mathbf{E}^c]$ (3×4) matrices

$$[\mathbf{P}^c] = [\mathbf{N}^c]\,[\mathbf{E}^c] \tag{2}$$

with

$$[\mathbf{N}^c] = \begin{bmatrix} f_x^c & \zeta^c & c_x^c \\ 0 & f_y^c & c_x^c \\ 0 & 0 & 1 \end{bmatrix} \tag{3}$$

where f_x^c and f_y^c represent the focal lengths, c_x^c and c_y^c the optical centers, ζ^c the skew factor, which was assumed to be equal to zero. The extrinsic matrix describes the geometrical relationship between the sample frame (*i.e.* that of the nominal FE model) and that of camera c. It consists of a rotation matrix $[\mathbf{R}^c]$ (3×3) and translation vector $\{\mathbf{T}^c\}$ (3×1)

$$[\mathbf{E}^c] = [[\mathbf{R}^c]\,\{\mathbf{T}^c\}] \tag{4}$$

The rotation matrix $[\mathbf{R}^c]$ is generally written in terms of Euler angles $\alpha^c, \beta^c, \gamma^c$ for each camera independently, and the translation vector is also written camera-wise.

3.1. FE-based hybrid multiview calibration

The hybrid multiview calibration procedure is a critical step, especially in the presence of an IR camera. A robust initial guess of the projection matrices is mandatory. This estimate was obtained by resorting to a Point-*n*-Perspective (PnP) [49] solution in which specific nodes of the FE mesh were selected together with the corresponding pixels in each camera image (Figure 1(d)). With the known 2D and 3D coordinates, the projection matrices $[\mathbf{P}^c]$ were extracted via Direct Linear Transform [50]. Concerning PnP, utilizing a calibration object with an a priori known geometry for which the FE mesh was designed is desirable. In the following, it will be assumed that the PnP solution providing the intrinsic parameters was satisfactory. Thus, only the extrinsic parameters $\{\mathbf{p}^c\}$

$$\{\mathbf{p}^c\} = \left\{\alpha^c, \beta^c, \gamma^c, t_x^c, t_y^c, t_z^c\right\}^\top \tag{5}$$

were determined. Due to the different modalities, the digital levels of the IR camera could not be directly compared to 8-bit visible light images (Table 1). Therefore, it was necessary to perform histogram normalizations to cancel out the mean gray levels of all cameras, and to set the standard deviation to unity. The normalization procedure was performed in two steps, namely, (i) centering the gray level distribution around zero, (ii) scaling the new image histogram with the standard deviation

$$\tilde{f}^c = \frac{f^c - \mu(f^c)}{\mathrm{std}\,(f^c)} \tag{6}$$

The gray levels should be identical for all camera images in ideal conditions with no brightness and contrast variations. An *intrinsic texture* $\hat{f}(\mathbf{X})$ of the visible speckle pattern was constructed as the average of the gray levels at the projected physical points $\mathbf{x}^c$ for all cameras [26]

$$\hat{f}(\mathbf{X}) = \frac{1}{Nc} \sum_{c=1}^{Nc} \left(\tilde{f}^c \left(\mathbf{x}^c \right) \right) \tag{7}$$

where $\mathbf{x}^c$ represents the projected physical points, which depend on the 3D positions in the FE mesh $\mathbf{X}$ and the corresponding projection matrices $[\mathbf{P}^c]$

$$\mathbf{x}^c = \mathbf{x}^c \left(\mathbf{X}, [\mathbf{P}^c] \right) \tag{8}$$

The hybrid calibration then reduces to calibrating all three cameras with a unique reference image $\hat{f}(\mathbf{X})$. This calibration procedure is written as a least squares minimization of

$$\rho^2(\{\mathbf{p}^c\}) = \sum_{c=1}^{Nc} \sum_{ROI} \left\| \tilde{f}^c \left(\mathbf{x}^c \right) - \hat{f}(\mathbf{X}) \right\|^2 \tag{9}$$

where the parameters of interest $\{\mathbf{p}^c\}$, and hence the projection matrix $[\mathbf{P}^c]$, are iteratively updated. It should be noted that the initial image $\hat{f}(\mathbf{X})$ is constructed using the initial projection matrices. Hence, this unique reference image should also be iteratively reconstructed. The calibration cost function is Taylor-expanded in each parameter and minimized using a Gauss-Newton scheme [25].

When lightning and perspective differences for each camera are negligible and non-existent, the gray level conservation between each reference image $\tilde{f}^c(\mathbf{x}^c)$ and the intrinsic texture $\hat{f}(\mathbf{X})$ is satisfied [51]. Otherwise, such conditions may impact the stability of HM algorithms since the gray level conservation between cameras is no longer satisfied, especially when the IR camera is included. Using brightness and contrast corrections (BCCs) for each camera c, the corrected reference image $\hat{f}^c(\mathbf{x}^c)$ is built

$$\hat{f}^c(\mathbf{x}^c) = (1 + c^c(\mathbf{x}^c))\,\tilde{f}^c(\mathbf{x}^c) + b^c(\mathbf{x}^c) \tag{10}$$

where $b^c(\mathbf{x}^c)$ and $c^c(\mathbf{x}^c)$ represent the brightness and contrast correction fields for each camera. Equation (10) corresponds to an affine correction where b^c is the brightness field, and $(1 + c^c)$ the contrast field. The corresponding cost function reads

$$\xi^2(b, c) = \sum_{c=1}^{Nc} \sum_{ROI} \left\| (1 + c^c(\mathbf{x}^c))\,\tilde{f}^c(\mathbf{x}^c) + b^c(\mathbf{x}^c) - \hat{f}(\mathbf{X}) \right\|^2 \tag{11}$$

Both $b^c(\mathbf{x}^c)$ and $c^c(\mathbf{x}^c)$ fields are defined over the 2D image plane. However, they are rewritten in the 3D space of the sample surface $b^c(\mathbf{x}^c(\mathbf{X}))$ and $c^c(\mathbf{x}^c(\mathbf{X}))$ to be consistent for all cameras. The BC fields are decomposed over the FE mesh using a set of spatial shape functions ψ_i

$$b^c(\mathbf{X}) = \sum_{i=1}^{DOF} b_i^c \psi_i(\mathbf{X}) \quad , \quad c^c(\mathbf{X}) = \sum_{i=1}^{DOF} c_i^c \psi_i(\mathbf{X}) \tag{12}$$

3.2. FE-based hybrid multiview correlation

After convergence of the calibration algorithm, the next step is to measure displacement fields $\mathbf{U}(\mathbf{X}, t)$ at each time t. Hybrid multiview correlation consists in minimizing the sum of squared differences in which the normalized reference images $\tilde{f}^c$ and the normalized corrected deformed images $\tilde{g}^c_{\mathbf{U}}(\tilde{\mathbf{x}}^c, t)$ are considered

$$\mathbf{U}(\mathbf{X}, t) = \arg\min \sum_{c=1}^{N_c} \sum_{ROI} \left(\tilde{g}^c_{\mathbf{U}}(\tilde{\mathbf{x}}^c, t) - \tilde{f}^c(\mathbf{x}^c) \right)^2 \tag{13}$$

where $\mathbf{U}(\mathbf{X},t)$ is the measured displacement field, and the normalized corrected deformed images are computed as

$$\tilde{g}^c_{\mathbf{U}}\left(\tilde{\mathbf{x}}^c,t\right)=\tilde{g}^c\left(\mathbf{x}^c(\mathbf{X}+\mathbf{U}(\mathbf{X},t)),t\right) \tag{14}$$

The continuity of the displacement field $\mathbf{U}(\mathbf{X},t)$ is ensured by using a set of spatial shape functions $\boldsymbol{\psi}_i(\mathbf{X})$

$$\mathbf{U}(\mathbf{X},t)=\sum_{i=1}^{DOF}u_i(t)\boldsymbol{\psi}_i(\mathbf{X}) \tag{15}$$

where $\{\mathbf{u}(t)\}$ gathers all nodal displacements $u_i(t)$ of the FE mesh made of 3 noded triangles [25]. The nodal displacements are determined via a Gauss-Newton algorithm.

Because of the difference in image modality in a hybrid stereocorrelation system, Brightness and Contrast Corrections are mandatory for kinematic measurements and the computation of apparent temperature field when handling IR images. The gray-level conservation between the intrinsic texture and corrected deformed image read as,

$$\tilde{g}^c_{\mathbf{U}}\left(\tilde{\mathbf{x}}^c,t\right)=(1+c(\mathbf{x}^c,t))\tilde{f}^c\left(\mathbf{x}^c\right)+b(\mathbf{x}^c,t) \tag{16}$$

where $c(\mathbf{x}^c,t)$ and $b(\mathbf{x}^c,t)$ characterize the local brightness and contrast variations. For IR images (*i.e.*, $c=3$), the temperature fields $\tilde{g}^c_{\mathbf{T}}\left(\tilde{\mathbf{x}}^c,t\right)$ are obtained via Equation (16), which gives access to the local temperature variations during the experiment in the reference (Lagrangian) frame.

Hence, by using HM correlation (HMC), kinematic and temperature fields are measured [33], and the cost function to be minimized is written as

$$\eta^2=\sum_{c=1}^{N_c}\sum_{ROI}\left(\left(1+c^c(\mathbf{X},t)\right)\tilde{f}^c\left(\mathbf{x}^c\right)+b^c\left(\mathbf{X},t\right)-\tilde{g}^c_{\mathbf{U}}\left(\tilde{\mathbf{x}}^c,t\right)\right)^2 \tag{17}$$

Brightness and contrast fields are determined camera-wise at each time step. The corrected deformed camera images are updated with the respective brightness $b^c(\mathbf{X},t)$ and

contrast $c^c(\mathbf{X}, t)$

$$\tilde{g}^c_{\mathbf{U},BCC}(\tilde{\mathbf{x}}^c, t) = \frac{\tilde{g}^c_{\mathbf{U}}(\tilde{\mathbf{x}}^c, t) - b^c(\mathbf{X}, t)}{1 + c^c(\mathbf{X}, t)} \tag{18}$$

A staggered scheme (U-BCC-U) was implemented, and the registration was performed in three consecutive steps for each image set. First, pre-convergence was sought with the first U step, followed by a BCC step. In the last step, the kinematic field was recomputed with an initial guess corresponding to the pre-converged estimate and corrected with the determined B and C fields.

4. Results

In this section, all the obtained results are displayed and discussed. First, the calibration is reported. Next, the kinematic/thermal measurements, specifically the displacement, strain, correlation residuals, and IR temperature fields, are analyzed. Last, the *ex-situ* DVC results are presented. Figure 3 shows the applied load history. Specific instants of interest are marked, corresponding to results that will be discussed hereafter.

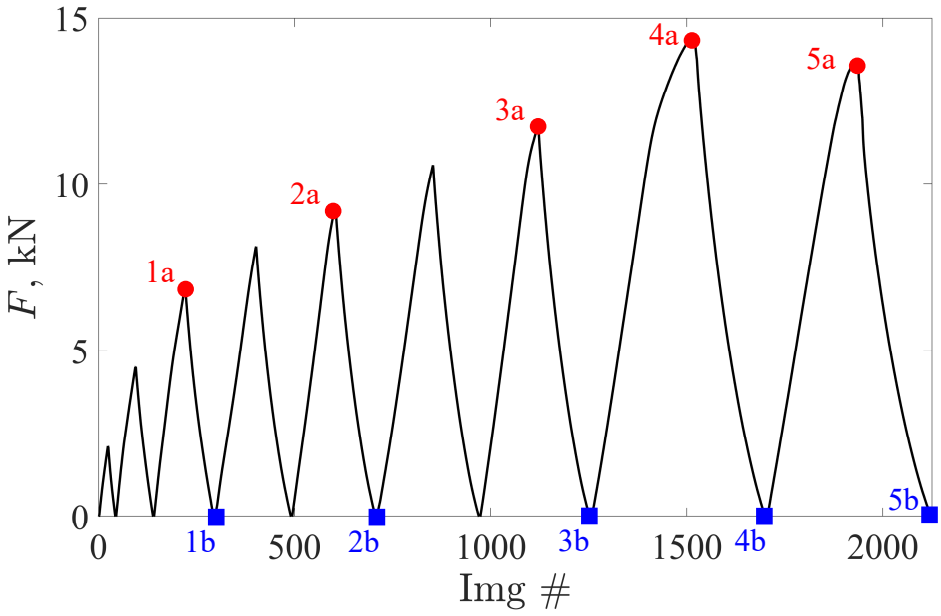

Fig. 3: Force history of the analyzed experiments. The key points in the loading history are marked with red dots for hybrid multiview correlation results and blue rectangles for DVC analyses.

Table 2 lists the HMC and DVC parameters. For both techniques, an *identical* FE

discretization was used where for the former, 2D triangular elements were employed and for the latter, 3D four-noded tetrahedron elements were used, and the average element length was kept the same (equal to 1.1 mm).

Table 2: Correlation parameters

Registration	HMC	DVC
Software	Correli 3.0	
Element size	≈ 1.1 mm	
Shape functions	Linear (T3)	Linear (T4)
Mesh	Unstructured	
Matching criterion	Sum of squared differences	
Regularization length	-	256 vx
Interpolation	Linear	
Evaluation points (per element)	435	-

4.1. Calibration

The calibration of the hybrid optical system commenced with the initialization via the PnP [49] procedure. A finite number of points was selected across the entire FE mesh of the visible sample surface and the calibration object (Figure 1(d)). The corresponding points were carefully chosen in all three camera images, providing initial projection matrices. The designed calibration object (Figure 1(d)) was ideal for the PnP step. However, the object was too large and the peripheral areas were outside of camera focus and thus were blurred. This effect proved to be a setback during the calibration step. Therefore, only the ROI was utilized instead of the entire FE mesh.

As two types of speckles were applied to the sample surface, the calibration protocol had to be slightly adapted. Since only the graphite speckles were visible on IR images, the calibration was performed in two steps:

1. The visible light cameras (1 and 2) were calibrated separately, where both types of speckle patterns were visible. The objective was to achieve convergence for the projection matrices to construct the intrinsic texture $\hat{f}$.
2. Then, all three cameras were calibrated simultaneously using the intrinsic texture $\hat{f}$ constructed from the visible light images. Although the initial projection matrices

were close to the solution, additional calibration was required, particularly for the IR camera. The visible light images were slightly blurred to filter out the very fine speckles, which were not visible in the IR images.

The calibration residuals are displayed in Figure 4 before and after BCCs. For the first two visible light cameras VL1 and VL2 (Figure 4(a-d)), similar patterns are observed. The surface of the sample was not completely flat as first assumed. Minor geometric imperfections were present due to the woven pattern underneath the speckle pattern. After BCCs, the pattern vanished, thereby proving the robustness of the algorithm. The calibration residuals decreased substantially. For the IR camera (Figure 4(e,f)), the initial residuals were very high. After BCC implementation, the residuals decreased, though they remained approximately $10\times$ higher compared to the visible light images. This difference is mainly due to two types of speckle patterns, one of which is invisible to the IR camera, hence increasing the calibration residuals.

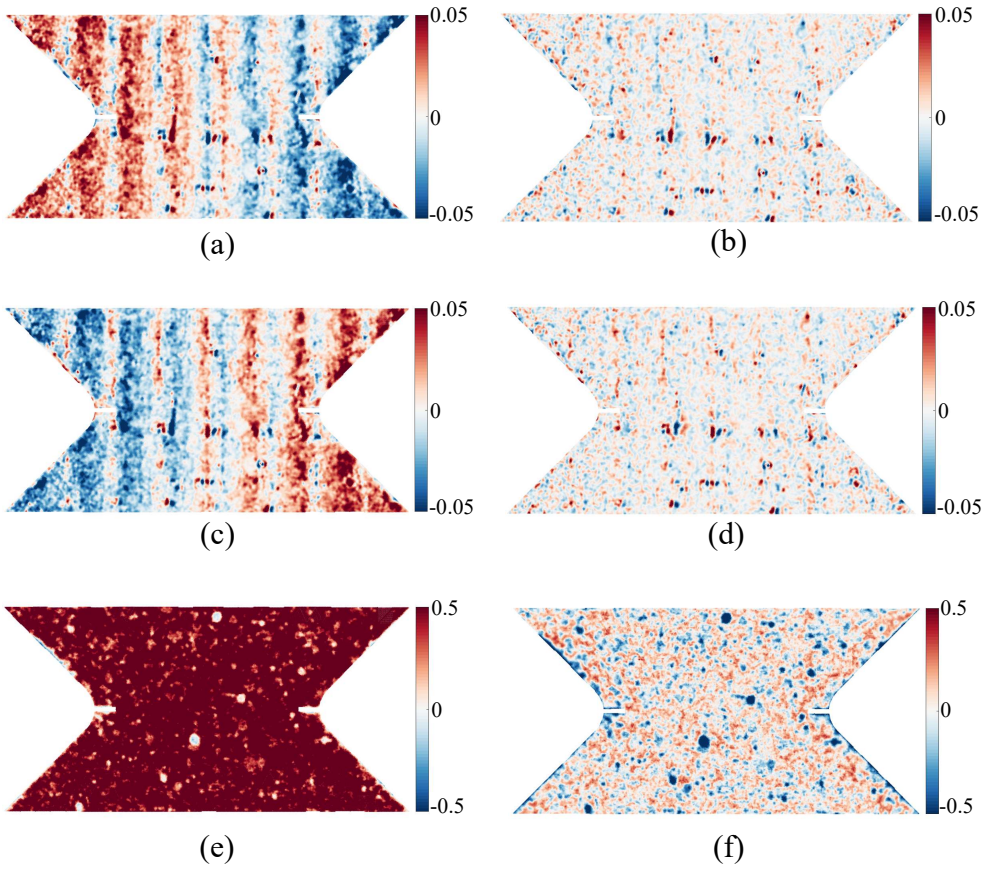

Fig. 4: Calibration residuals for cameras VL1, VL2, and IR (3) before (a,c,e) and after BCCs (b,d,f), respectively.

The calibration residual histograms are displayed in Figure 5(a-c) alongside the global residuals (Figure 5(d)). After BCCs, the residuals were more centered about zero than before, thus indicating a decrease in the residuals. This change is especially apparent for the IR camera, even though it is not Gaussian due to the invisible speckles in the IR spectrum. The global residuals were initially over 30% of the dynamic range, mainly due to the IR image. After BCCs, the residuals dropped to 6% and remained at this level. Given the fact that multimodal registrations were performed, the calibration was deemed successful.

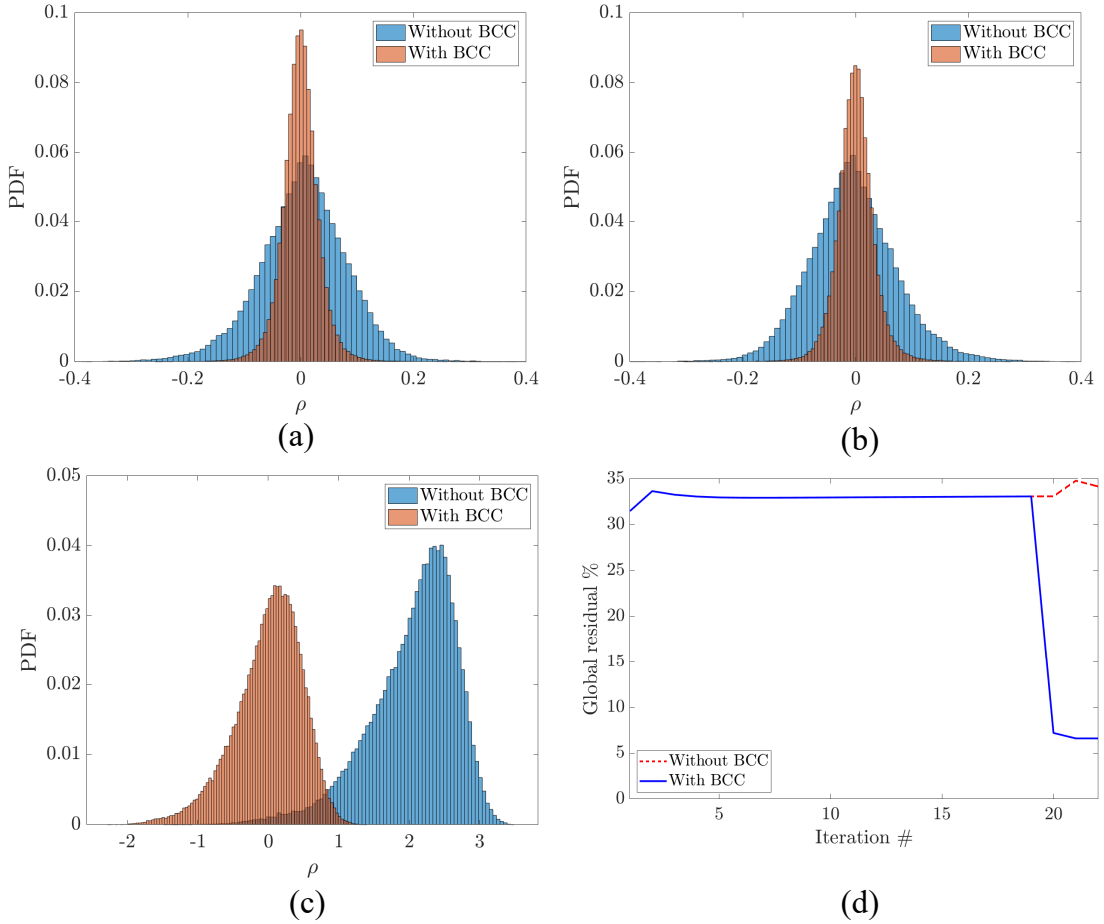

Fig. 5: Probability density functions of calibration residuals at convergence before and after BCCs for cameras VL1 (a), VL2 (b), and IR (3) (c). (d) Global calibration residuals expressed as a percentage of the dynamic range of the intrinsic texture.

4.2. *Thermomechanical fields*

The hybrid multiview correlation results are now presented. All three cameras were utilized for the displacement measurements. The results are displayed for the critical instants depicted in Figure 3. For each of them, the maximum principal strain ϵ_1 and shear strain γ_{xy} fields are shown alongside the displacement field in the loading direction and the temperature field (Equation (16)) of the IR camera expressed in digital levels (DL). The calibration of the emissivity of the speckle pattern was not performed since two types of speckles were present, one of which had identical emissivity as the sample surface, thus rendering it indistinguishable. With no calibration, the digital levels could not be converted to Celsius degrees. The BC-corrected residuals are also displayed for

each camera.

The results displayed in Figures 6 and 7 correspond to the third loading peak (Figure 3). By comparing Figure 6(a) and (b), it is concluded that two shear bands emanating from the notch roots were the dominant features. These shear bands are attributed to the shape of the modified Arcan sample and the underlying woven architecture (Figure 2) [52]. The presence of shear is also observed in the displacement field along the loading direction (Figure 6(c)) since a gradient is distinguished between the central and the peripheral regions. From the temperature fields (Figure 6(d)) the difference in emissivity of the speckle pattern and the sample surface is clearly distinguished. However, no notable changes in the temperature are detected.

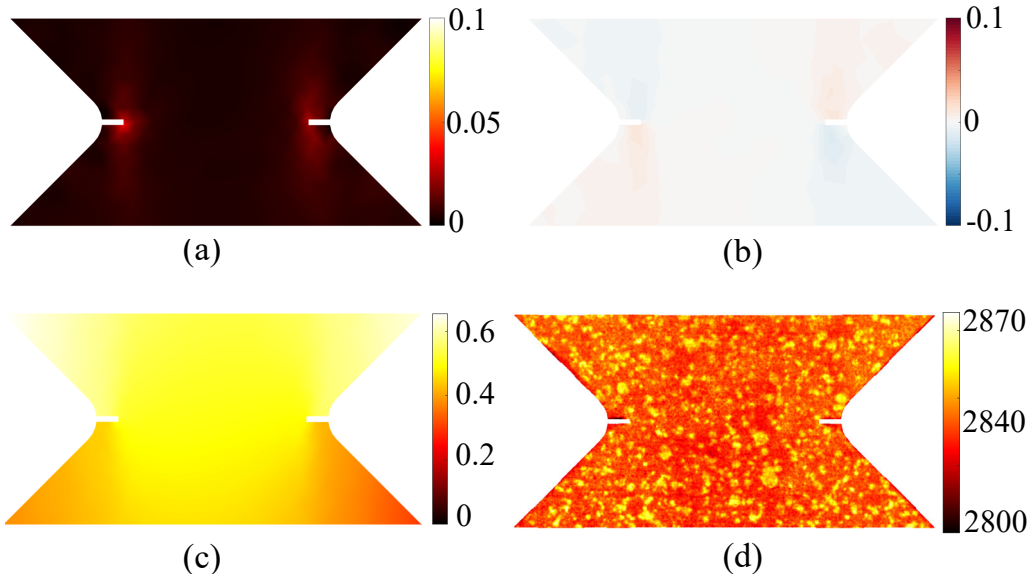

Fig. 6: Hybrid multiview correlation results for point 1a (Figure 3). (a) ϵ_1 field, (b) γ_{xy} field, (c) displacement field in the y-direction expressed in mm, and (d) IR temperature field expressed in digital levels (Equation (16)).

The correlation residuals are very effective in detecting surface cracks [3] since the conservation of gray/digital levels (Equation (13)) is no longer satisfied. In Figure 7(a,b), a small crack is detected around the left notch. Since the notches were cut with a scroll saw, damage was induced in the sample. The same crack is not observed on the IR residuals. This difference may be explained by the fact that the IR camera spatial resolution was insufficient to capture such tiny events. The effect of BCCs is shown in the histogram

of IR residuals (Figure 7(d)). After correcting BC, the residuals are centered about zero and have a smaller scatter.

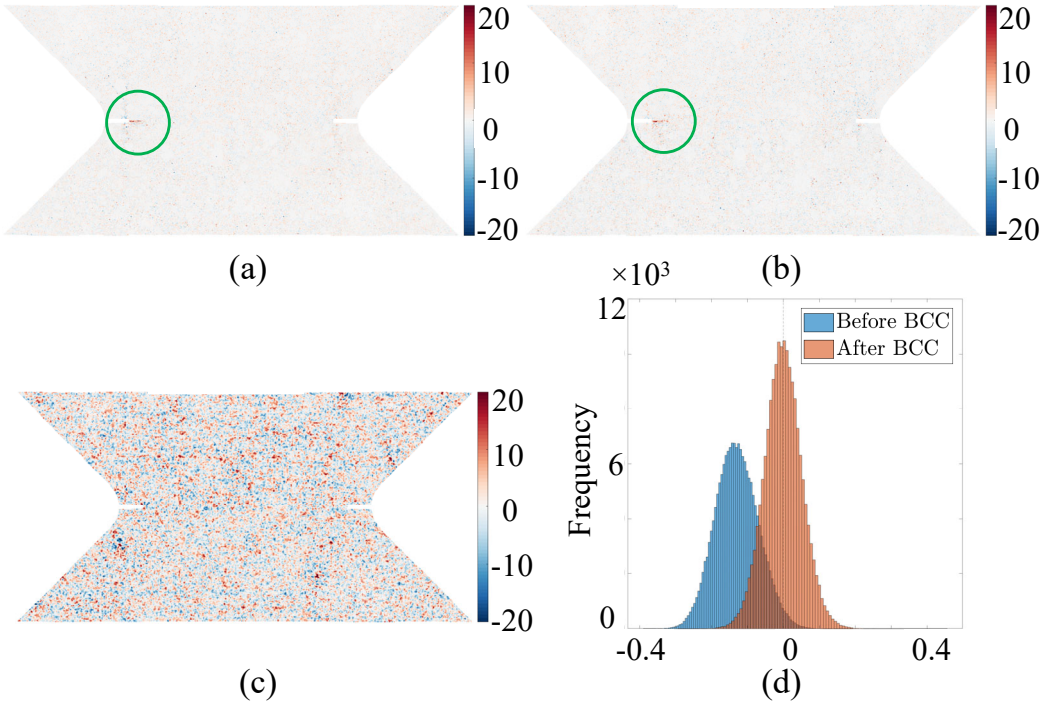

Fig. 7: Correlation residuals for point 1a (Figure 3) expressed as a percentage of the dynamic range of individual reference images for cameras VL1 (a), VL2 (b), IR (3) (c). (d) Histogram of IR residuals. The green circle denotes damage developed in the gauge region.

Next, the results for the fifth loading peak (Figure 3) are reported. The dominant shear bands are slightly more pronounced than previously (Figure 8(a,b)). There are no high gradients observed in the displacement field along the loading direction (Figure 8(c)), except between the central and peripheral areas. These gradients are attributed to stiffness differences of various parts (the sample was manufactured by water jet cutting, where the woven yarns were cut, whereas the central yarns were not). The rigidity of the peripheral regions was lower due to the sample geometry, resulting in higher strain/stress concentrations and lower plasticity threshold than that of the central region (Figure 8(c)). In the temperature field (Figure 8(d)) a gradient is also observed from top to bottom from lower to higher temperatures.

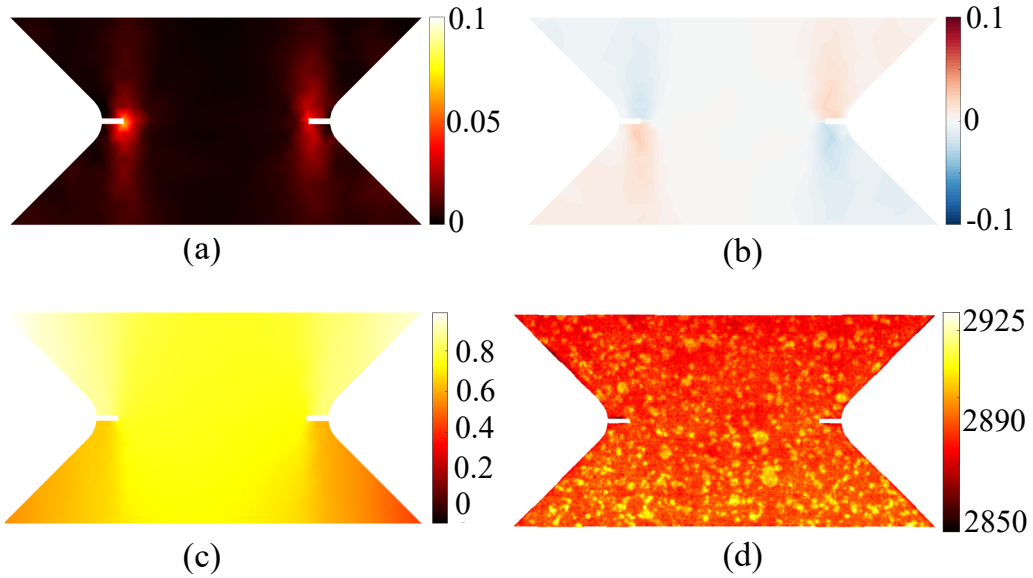

Fig. 8: Hybrid multiview correlation results for point 2a (Figure 3). (a) ϵ_1 field, (b) γ_{xy} field, (c) displacement field in the y-direction expressed in mm, and (d) IR temperature field expressed in digital levels (Equation (16)).

In Figure 9, the correlation residuals are displayed. From the visible light camera residuals (Figure 9(a,b)), another crack below the root of the left notch is observed. Above and below the right notch, vertically oriented increased residuals are observed. At this stage, permanent damage developed on the sample surface due to shear. The same tendency is not observed in the IR residuals (Figure 9(c,d)). Using BCCs, the residuals were lowered and centered about zero. By comparing Figures 9(d) and 7(d), it is concluded that before BCCs, the histograms were inverted. In Figure 7(d), the histogram peak was positive, whereas in Figure 9(d), it is negative. This difference is a drawback of the present *ex-situ* experiment since it was intermittently interrupted, and the temperature conditions changed between these cycles. With the inclusion of BCCs, this effect was mitigated.

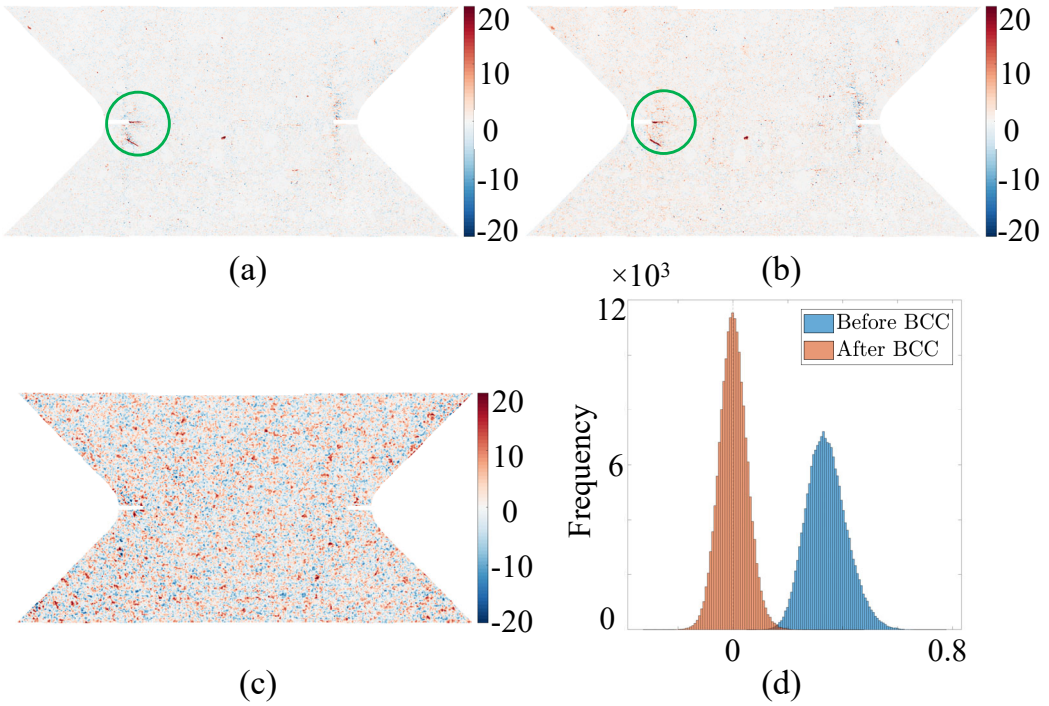

Fig. 9: Correlation residuals for point 2a (Figure 3) expressed in percentage of the dynamic range of individual reference images for cameras VL1 (a), VL2 (b), and IR (3) (c). (d) Histogram of IR residuals. The green circle denotes damage developed in the gauge region.

The results for the later stages of loading are shown in Figures 10 and 11. Compared to the previous stage, the strain levels of the shear bands increased (Figure 10(a,b)). Shear is also observed in the longitudinal displacement field (Figure 10(c)). Lower temperatures are observed in the middle of the ROI (Figure 10(d)) and the top part, which could further indicate thermoelastic effects.

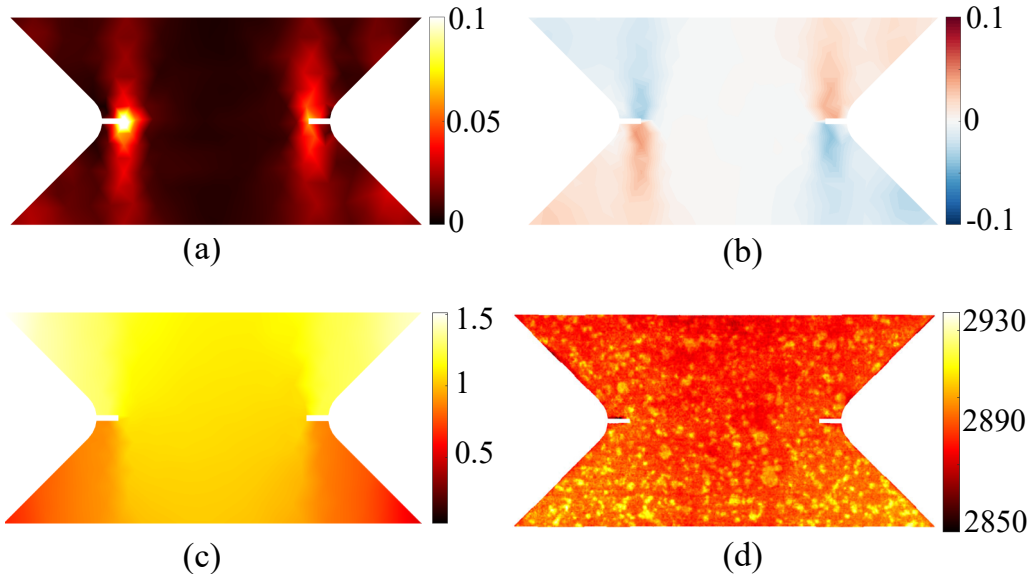

Fig. 10: Hybrid multiview correlation results for point 3a (Figure 3). (a) ϵ_1 field, (b) γ_{xy} field, (c) displacement field in the y-direction expressed in mm, and (d) IR temperature field expressed in digital levels (Equation (16)).

In the correlation residuals (Figure 11(a,b)), another crack is detected in the upper left area of the ROI perpendicular to the sample edge. Several horizontal cracks initiated around the central region of the sample, which correspond to surface matrix cracking [52]. The shearing effects did not degrade the speckle pattern. However, the same residuals observed in the visible light spectrum cannot be distinguished in the IR residuals due to the lower image resolution (Figure 11(c)). Severe changes are observed in the IR residual histogram (Figure 11(d)) before BCCs as a result of the *ex-situ* experimental protocol where temperature conditions changed while the sample was scanned. However, after BCCs, the residuals are centered at zero, indicating successful corrections.

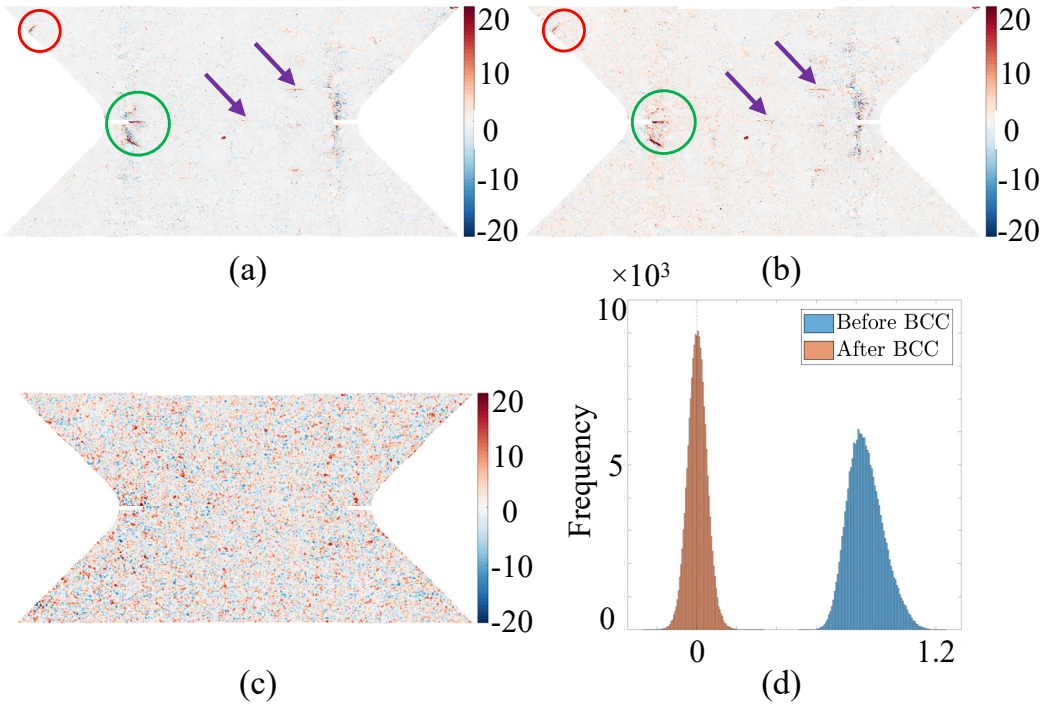

Fig. 11: Correlation residuals for point 3a (Figure 3) expressed in percentage of the dynamic range of individual reference images for cameras VL1 (a), VL2 (b), IR (3) (c). (d) Histogram of IR residuals. The green circle denotes damage developed in the gauge region, whereas the red circles highlights damage on the peripheral area.

For the peak of the fourth cycle, where the highest force level was reached, Figure 12 shows several noteworthy events. From the major principal strain and shear strain fields (Figure 12(a,b)), several strained bands are observed, namely, the two dominant shear bands and four additional ones on the peripheral areas of the ROI. The displacement in the longitudinal direction (Figure 12(c)) exhibits severe gradients as a result of shear. Using the IR modality, energy dissipation due to damage is observed mainly in the vicinity of the left notch (Figure 12(d)). From the change in the temperature field of the IR camera, the highest changes coincide with the highest strain levels. Furthermore, a slight increase in the temperature around the right notch where strains were also localized indicates that damage has started to develop, thus releasing energy.

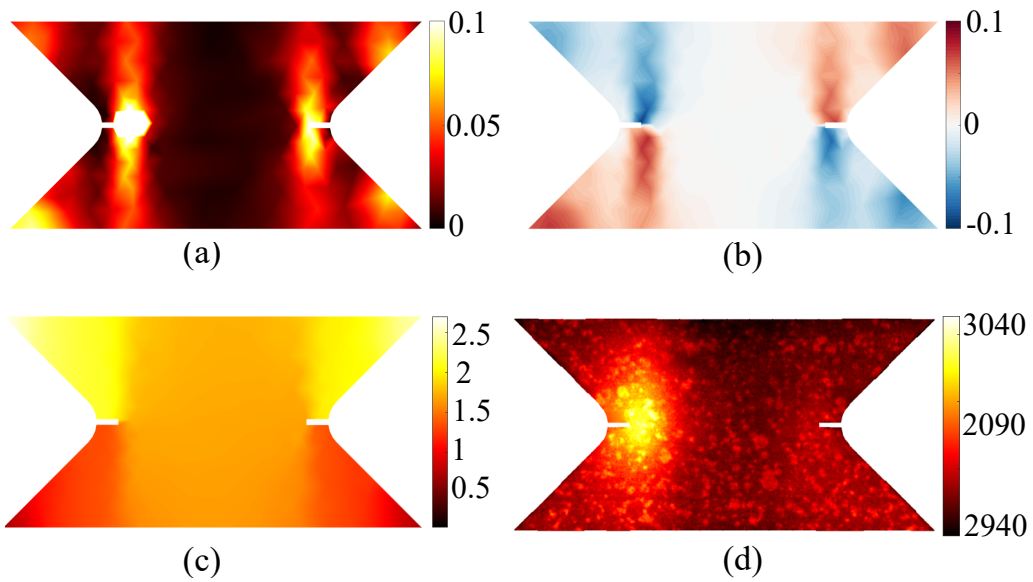

Fig. 12: Hybrid multiview correlation results for point 4a (Fig. 3). (a) ϵ_1 field, (b) γ_{xy} field, (c) displacement field in the y-direction expressed in mm and (d) IR temperature field expressed in digital levels (Equation (16)).

Similarly to the strain fields, several newly developed cracks are detected in the correlation residuals of the visible light cameras (Figure 13(a,b)). Along with the major damage at the root of the left notch, cracks on the peripheral edges of the ROI have also developed. Although the same small crack was not observed in the IR residuals (Figure 13(c)), the major damage event at the left notch is visible. Even with BCCs, the algorithm could not fully converge at this spot. The reason is twofold. First, the definition of the IR camera was much lower than that of the visible light cameras. Hence, it could not fully capture the developed crack. Second, at this position, the speckle pattern deteriorated; ergo, the conservation of gray levels was no longer satisfied even with BCCs. Yet, using BCCs, the histogram of digital level residuals (for the IR camera) was centered about zero and lowered (Figure 13(d)), which further confirmed the robustness of the algorithm even in events with significant dissipation due to damage. Furthermore, horizontal cracks are visible on the visible light camera residuals.

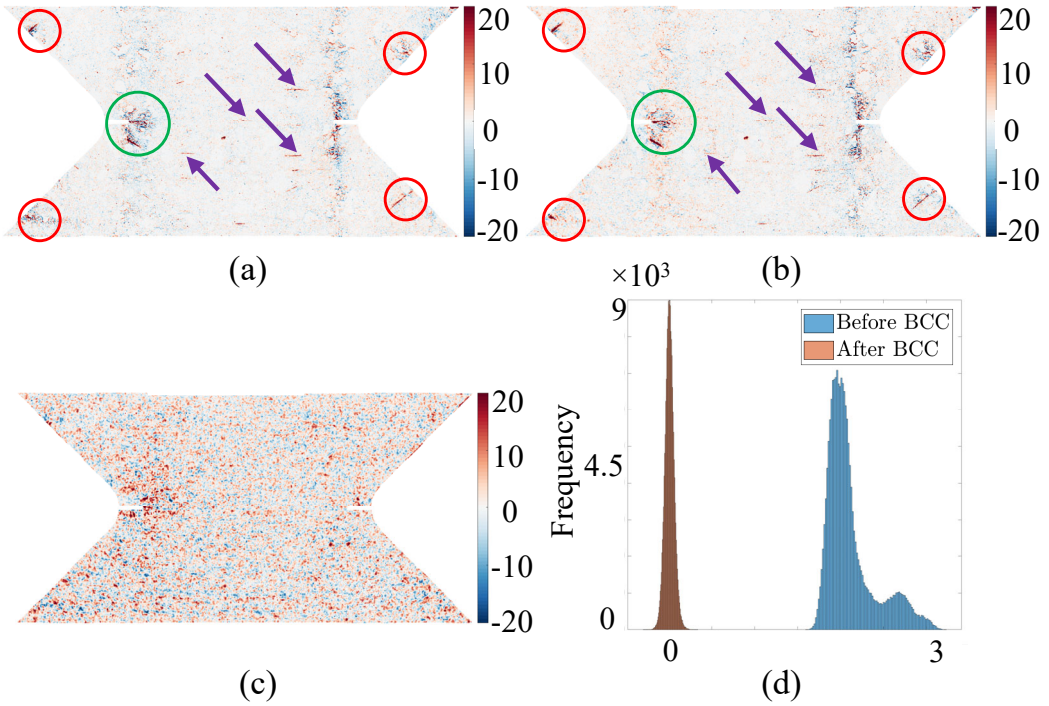

Fig. 13: Correlation residuals for point 4a (Figure 3) expressed as percentage of the dynamic range of individual reference images for camera VL1 (a), VL2 (b), and IR (3) (c). (d) Histogram of IR residuals. The green circle denotes damage developed in the gauge region, whereas the red circles highlight damage on the peripheral areas. Purple arrows highlight the horizontal cracks

Convergence was more challenging for the final loading cycle due to significant surface damage. This issue was primarily caused by the speckle pattern, which was crucial for accurate measurements but severely deteriorated around the notches. Brightness and contrast corrections could not (and should not) correct for damaged speckle pattern. To achieve convergence with the IR images included, the IR BCCs had to be initialized.

Using only the images acquired by the visible light cameras, the HMC algorithm converged, and the displacement fields were measured. Then, by resorting to a semi-hybrid method [52], pixel-wise changes in digital levels could be extracted from the IR images in a Lagrangian setting. Using the measured displacement fields, the FE mesh could be projected and deformed over the IR images using the nodal displacements projected onto the IR camera plane $\{\mathbf{u}^{IR}(t)\}$. The next step was determining the projector matrix $[\boldsymbol{\pi}]$, enabling for the interpolation of nodal values to any pixel position. Using the nodal

displacements, the displacement $\mathbf{u}^{IR}$ for any pixel position $\mathbf{x}$ then read

$$\mathbf{u}^{IR}(\mathbf{x},t) = [\boldsymbol{\pi}] \left\{ \mathbf{u}^{IR}(t) \right\} \tag{19}$$

The pixel-wise digital levels were extracted from the IR images in the Lagrangian frame

$$T\left(\mathbf{x},t\right) = g^{IR}(\mathbf{x} + \mathbf{u}^{IR}(\mathrm{x},t),t) \tag{20}$$

where g^{IRT} is the deformed IR image at time *t*. To use these data in the HMC procedure, the (Lagrangian) IR images had to be normalized (Equation (6)). For each time t, individual pixel brightness changes from the initial one, at time t_0, were estimated by calculating the difference of digital levels. These changes were then used as initialization for the BCCs of the IR camera images, which led to successful convergence.

The analysis of the major principal strain and longitudinal displacement fields (Figure 14(a,b)) revealed numerous strained bands near both notches. The strain levels were greater in both fields compared to the previous cycle. Very high gradients are thus observed in the longitudinal displacement field next to the left notch (Figure 14(c)) as well as for the lower peripheral areas. The change in the temperature field (Figure 14(d)) was located next to the left notch, with heat propagating outward. The digital level changes were slightly greater than for the previous cycle, and a slightly increased thermal signal was detected around the left notch.

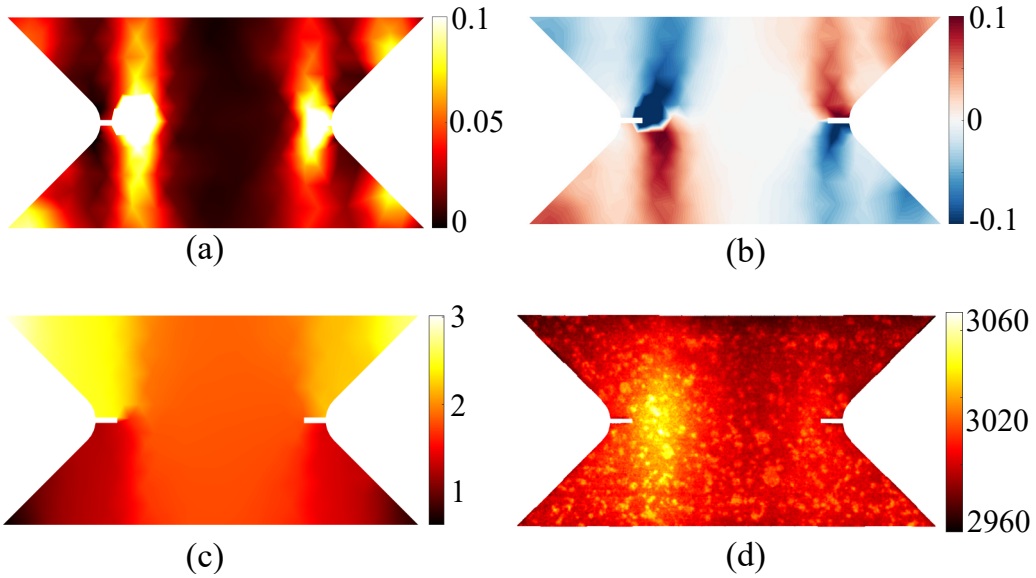

Fig. 14: Hybrid multiview correlation results for point 5a (Fig. 3). (a) ϵ_1 field, (b) γ_{xy} field, (c) displacement field in the y-direction expressed in mm and (d) IR temperature field expressed in digital levels (Equation (16)).

The examination of the correlation residuals (Figure 15(a,b)) confirms the development of surface damage. Notably, vertical residual stripes, indicative of shear bands, were more pronounced when emanating from the notches. Additionally, four new cracks developed around the V notches peripheral areas due to the sample geometry since these areas were less rigid than the middle one. In the correlation residuals for the IR images, the cracks are not visible due to the camera resolution. However, slightly increased residuals were detected around the left notch. Moreover, the histogram of digital level residuals for the IR camera was once again centered after BCCs, and the aforementioned brightness initialization provided a good initial guess for the registration algorithm, thus ensuring full convergence of the HM correlation scheme.

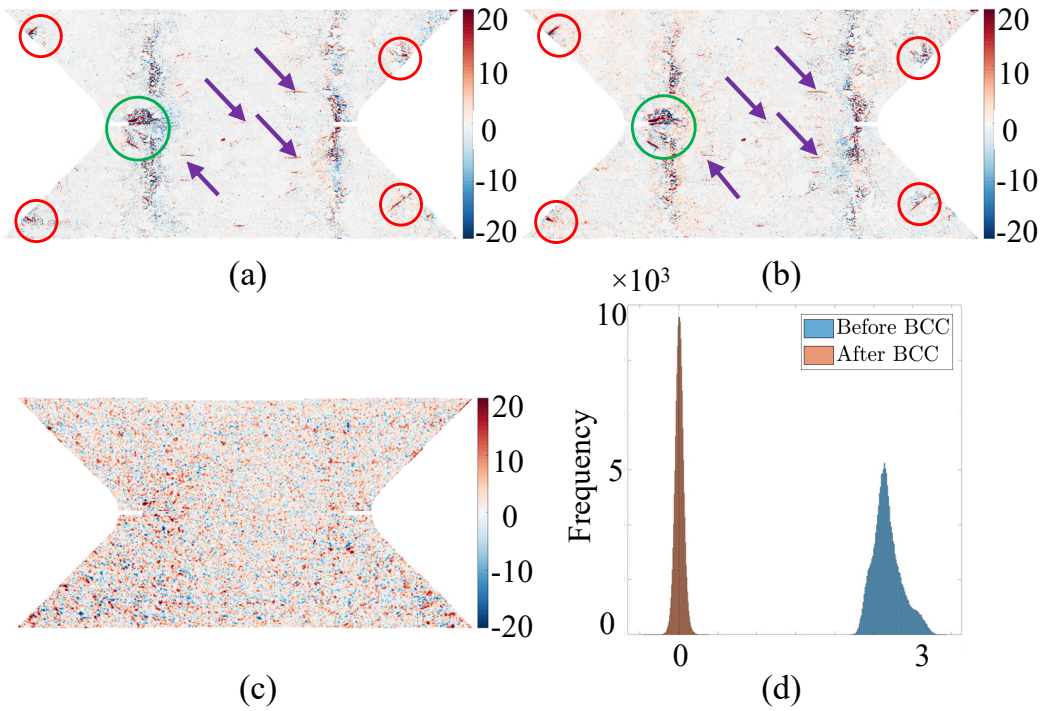

Fig. 15: Correlation residuals for point 5a (Figure 3) expressed as percentage of the dynamic range of individual reference images for camera VL1 (a), VL2 (b) and (IR) 3 (c). (d) Histogram of IR residuals. The green circle denotes damage developed in the gauge region, whereas the red circles highlight damage on the peripheral areas. Purple arrows highlight the horizontal cracks

4.3. DVC results

The DVC analyses were carried out using the same FE mesh discretization used for HMC analyses. The 2D mesh was repositioned over the CT slice of the external surface via mesh backtracking [53] to accurately describe the sample geometry in CT slices. The 3D DVC mesh was then extruded from the 2D mesh through the thickness and converted into 4-noded tetrahedra.

Due to the different nature of the three modalities, the noise levels were very different. To evaluate the noise levels for HMC, 20 images with the hybrid optical setup were captured in the unloaded state. After the calibration step, HMC was performed on these images, and the standard deviation was evaluated over the measured displacement fields. For DVC, the uncertainty quantification was similar. DVC was independently performed with the first HQ scan and the subsequent bis and rbm scans. The comparison between HMC and DVC uncertainties is shown in Figure 16 for different DVC regular-

ization lengths (see Appendix B). It is observed that with low mechanical regularization lengths, the DVC displacement and major principal strain uncertainties were higher than for HMC. Therefore, a higher regularization length (256 voxels) was used so that the DVC and HMC uncertainty levels were of the same order of magnitude.

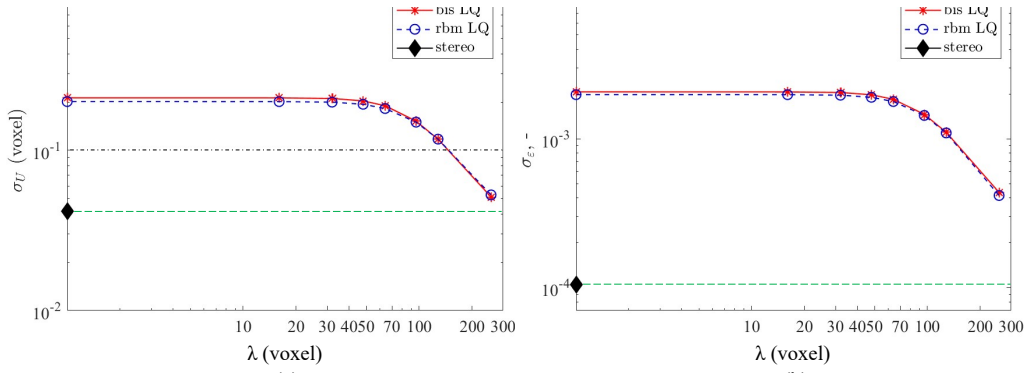

Fig. 16: Standard DVC uncertainties for different regularization lengths compared to hybrid multiview correlation levels (green dashed lines) for the displacements (a) and major principal strains (b).

The DVC results are presented for each scan acquired in the unloaded state (Figure 3). In Figure 17, the shear stain fields are displayed for each scan, and in Figure 19 the corresponding DVC residuals were thresholded (*i.e.*, the gray levels within [-110,110] were omitted). Conversely, the shear strains measured via HMC are displayed in Figure 18 for the corresponding DVC stages. It is worth noting that the dynamic range of the strain fields was changed between the scans to highlight the localized phenomena.

For the first two scans (Figure 17(a,b)), strained zones (*i.e.* shear bands) are observed around both notches, which correspond to permanent strains, whereas in the middle of the sample, the strain levels were the lowest. The geometry of the sample itself caused this effect since it was weakened around the V notches. The same two stages calculated with HMC (Figure 18(a,b)) exhibit similar strain levels. Two opposite and asymmetric strained zones developed around the notches, corresponding to tensile and compressive stress zones [5]. After the second loading cycle (Figures 17(b) and 18(b)), the strain distribution remained similar where slightly higher strain levels around the notches were achieved with HM correlation. In the residual fields of the same scans (Figure 19(a,b)), no distinguishable events are visible within the ROI.

In the third scan (Figure 17(c)), the permanent shear strain bands were even more pronounced, with slightly increased levels around both notches. The lowest strain levels remained in the middle region of the sample. The geometry of the sample and its architecture explain this trend. The yarns were not cut in the middle region, thus contributing to increased rigidity and negligible permanent strains. Although similar shear strain distributions were achieved with HM correlation (Figure 18(c)), the strain levels were again slightly higher around the notches, and the shear bands were more pronounced, especially on the peripheral areas of the ROI.

In the shear strain field of the fourth scan (Figure 17(d)), the strain levels around the notches and in the strained bands were higher as expected since, at this stage, damage developed on the surface and the root of the notch in the bulk (Figure 19(d)). The distribution of shear strains was similar to that for HMC (Figure 18(d)). However, the strain levels calculated via HMC were higher, mainly since the damaged zone developed on the surface, as is visible in the DVC residual field (Figure 19(d)). Similar residual bands emanating from the left notch were reported previously (Figure 13).

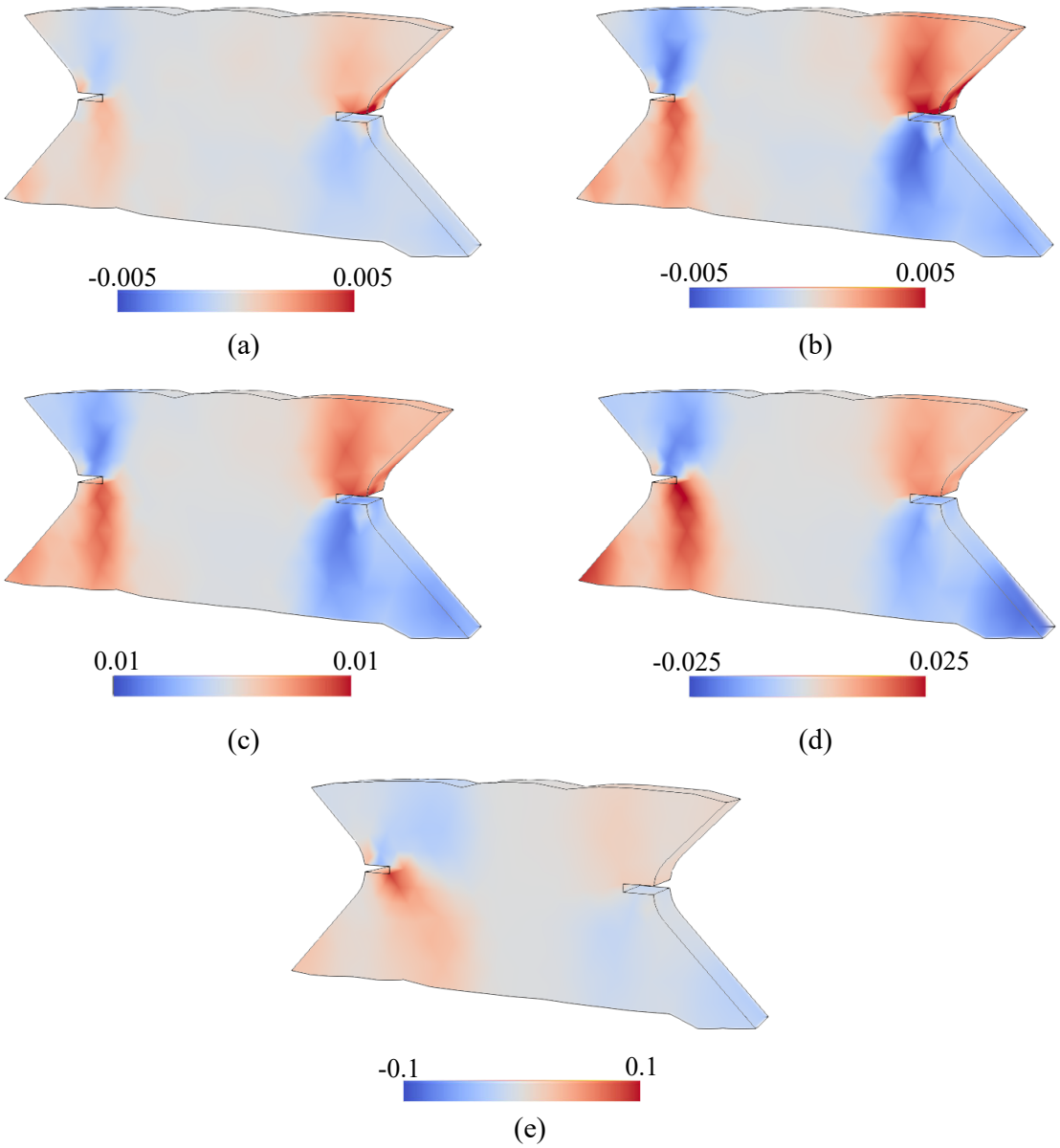

Fig. 17: DVC shear strain γ_{xy} fields for scans 1 (a), 2 (b), 3 (c), 4 (d), and 5 (e).

In the shear strain field of the last scan (Figure 17(e)), the distribution around the left notch changed compared to previous scans, which is also visible for HMC (Figure 18(e)). This phenomenon was due to the increased damage zone, mainly on the sample surface. The middle region still exhibited lower strain levels due to the increased rigidity compared to the weakened notched areas. Furthermore, higher strain levels were obtained via HMC in the peripheral regions. The reason is twofold. First, a larger ROI could be used,

and second, no regularization was used in HMC analyses. An area of increased residuals around the right notch is visible in DVC residuals (Figure 19(e)), which was not observed in HMC (Figure 15). This result indicates that, around the right notch, damage developed within the composite sample. A low heat signature is also visible on the IR image (Figure 14 (d)), indicating growing damage within the bulk.

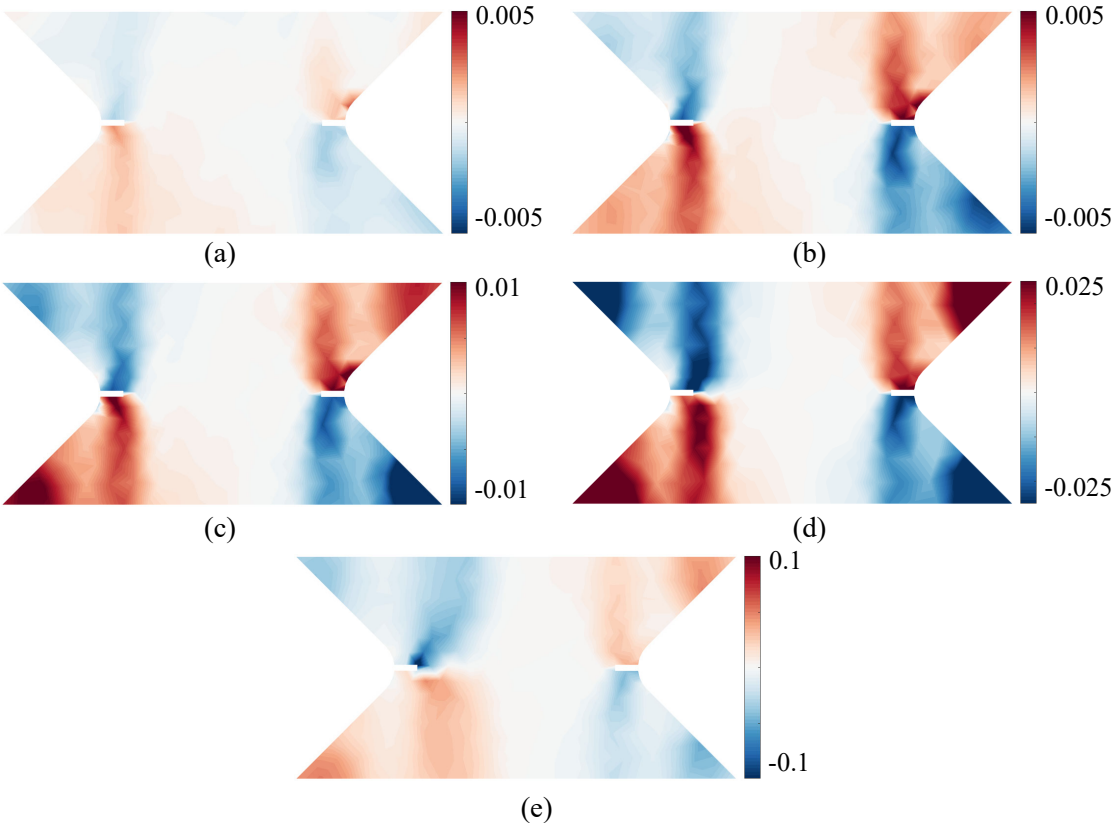

Fig. 18: HMC shear strain γ_{xy} fields corresponding to scans 1 (a), 2 (b), 3 (c), 4 (d), and 5 (e).

The area of increased residuals also widened, which corresponds to damage-affected regions. When comparing the DVC residual field to its HMC counterpart, the vertical residual bands corresponding to the shear strain bands were not seen in the DVC analyses until the last scan (Figure 19(e)). The sample architecture explains this finding and the higher shear strain levels. During loading, the yarns located at the positions of the notches were stretched. Alongside the yarns, the surface was also stretched. However, the yarns experienced higher elastic spring-back after unloading than the surface. This effect caused the breakage and discoloration of the speckle pattern, which is visible as

strain and residual bands using HMC. This observation does not disqualify the achieved strains, yet it explains why higher shear strains were obtained via HMC. In the CT scans, the speckle pattern was slightly visible, and for the most part, it was unbroken except for the damaged zones around the left notch. This result further shows that damage around the right notch developed within the material.

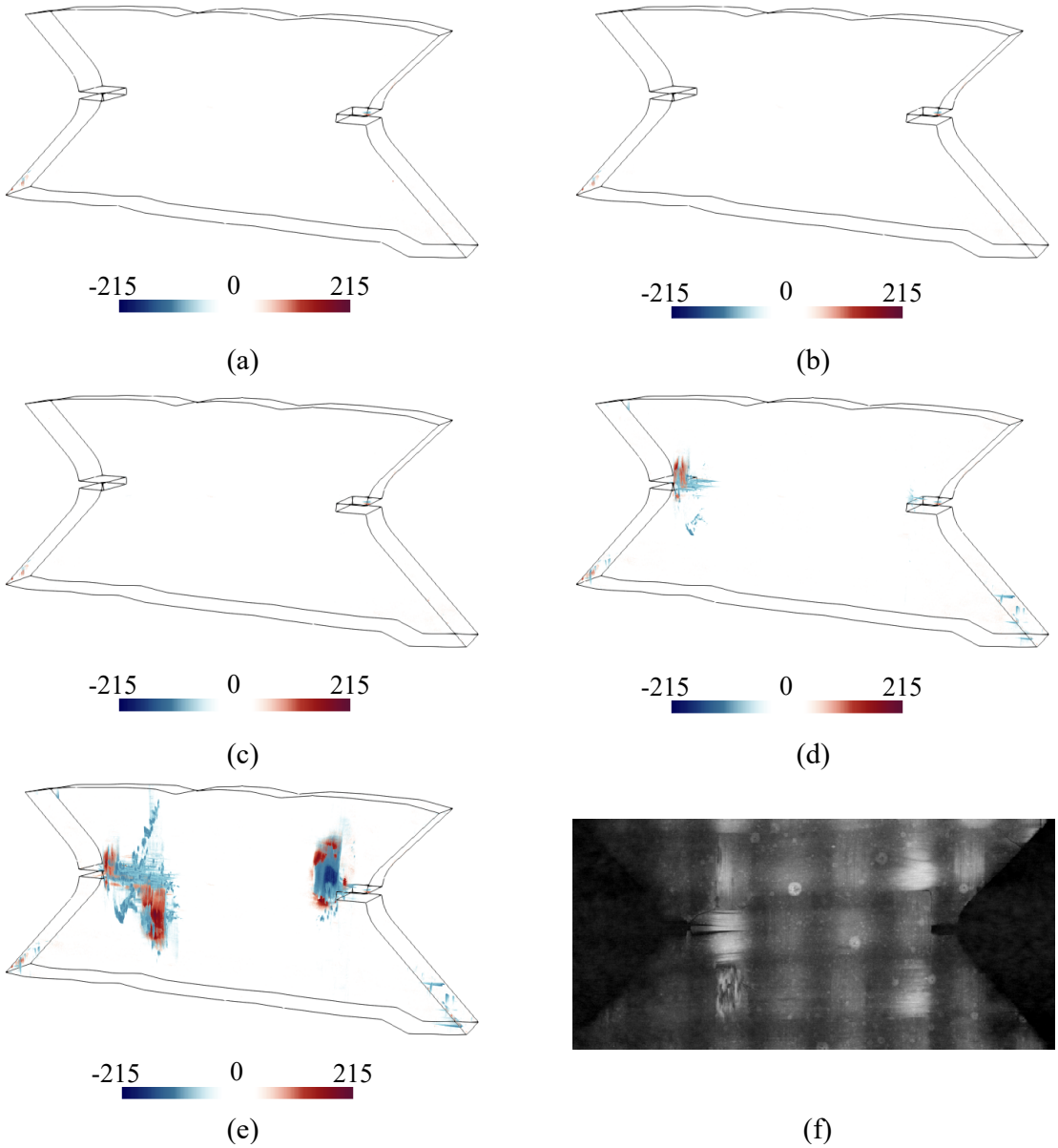

Fig. 19: DVC correlation residuals for scans 1 (a), 2 (b), 3 (c), 4 (d), 5 (e). (f) surface slice of CT scan 5 with the damaged speckle pattern.

5. Discussion

This section aims to interpret and compare HMC and DVC results:
- first, the major principal strain levels obtained with a virtual strain gauge are compared for both measurement methods;
- second, the correlation residuals are compared to assess the effectiveness of damage characterization. One key benefit of employing the multimodal framework lies in its use of a *unique* FE mesh. Consequently, identical nodes were selected within the virtual gauge to ensure full consistency.

Figure 20 compares HMC and DVC strains. The reported strain levels were determined by averaging the strains at the chosen nodes. Three different cases were considered:

- In Case #1, the virtual gauge included 3D FE nodes both on the surfaces and within the bulk. This configuration was chosen to assess the impact of bulk strains on those measured at the surface.

- Conversely, Case #2 exclusively focused on surface strains, which were extracted from the 3D strain field and averaged.

- Case #3 involved utilizing DVC surface displacements to calculate the strain fields, effectively omitting any direct or indirect influence from bulk activities. This scenario mirrors the HMC conditions, enabling a direct comparison between surface strain measurements.

The analysis of Figure 20(a) reveals that, in scans acquired before the experiment started, the average strain levels detected by DVC were consistently three times higher than those measured by HMC. This discrepancy is attributed to the elevated uncertainties inherent to *ex-situ* CT scans for which setting the system to strictly equivalent parameters was difficult (Figure 16). Notably, the results from HMC align most closely with those of Case #3. This result further validates the consistency of the proposed methodology.

A distinct variation between Cases #1 and #2 throughout the experiment is observed. Such differences underline the significance of bulk strains, which were, on average, lower than surface strains, thus reducing the overall strain levels. Furthermore, by calculating average nodal strains through the thickness, it was possible to observe the differences between the surface and bulk strains (Figure 20 (b)). Only scans 3,4 and 5 were considered, since the results from the previous scans did not display any significant damage (Figure 19). The surface observed by HMC was located at 0 thickness. It is concluded that damage was predominantly accumulating on the observed sample surface due to the highest mean strain fluctuations and observed 3D correlation residuals (Figure 19 (e)). Additionally, it is also noted that the standard deviation within the bulk was lower than on the surfaces since for the latter the differences between the highest and lowest strain levels are much more pronounced. It also emphasizes the importance of considering bulk strains and illustrates the subtle interplay of strain and damage distributions throughout the experiment.

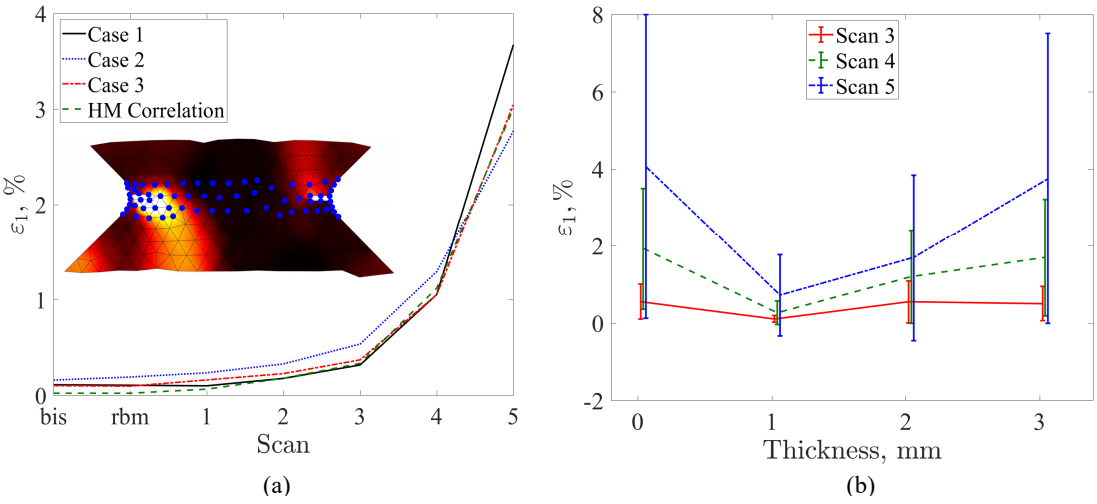

Fig. 20: (a) Comparison of mean nodal major principal strain levels using DVC and HMC extracted from a virtual gauge including the blue nodes illustrated in the FE mesh (inset). See text for explanations of cases #1, #2, and #3. (b) Average strain values through the sample thickness for DVC measurement with the corresponding standard deviation (error bars) for scans 3-5. The error bars are slightly shifted for the sake of legibility.

Figure 21 displays the corrected CT volume for the final scan, where most damage has developed. This volume was corrected with the measured DVC displacement field

(Equation (22)) to show it in the reference (Lagrangian) configuration. The gray level difference between the reference and the corrected deformed volumes results in the correlation residuals, highlighting areas where brightness conservation was not satisfied due to accumulated damage.

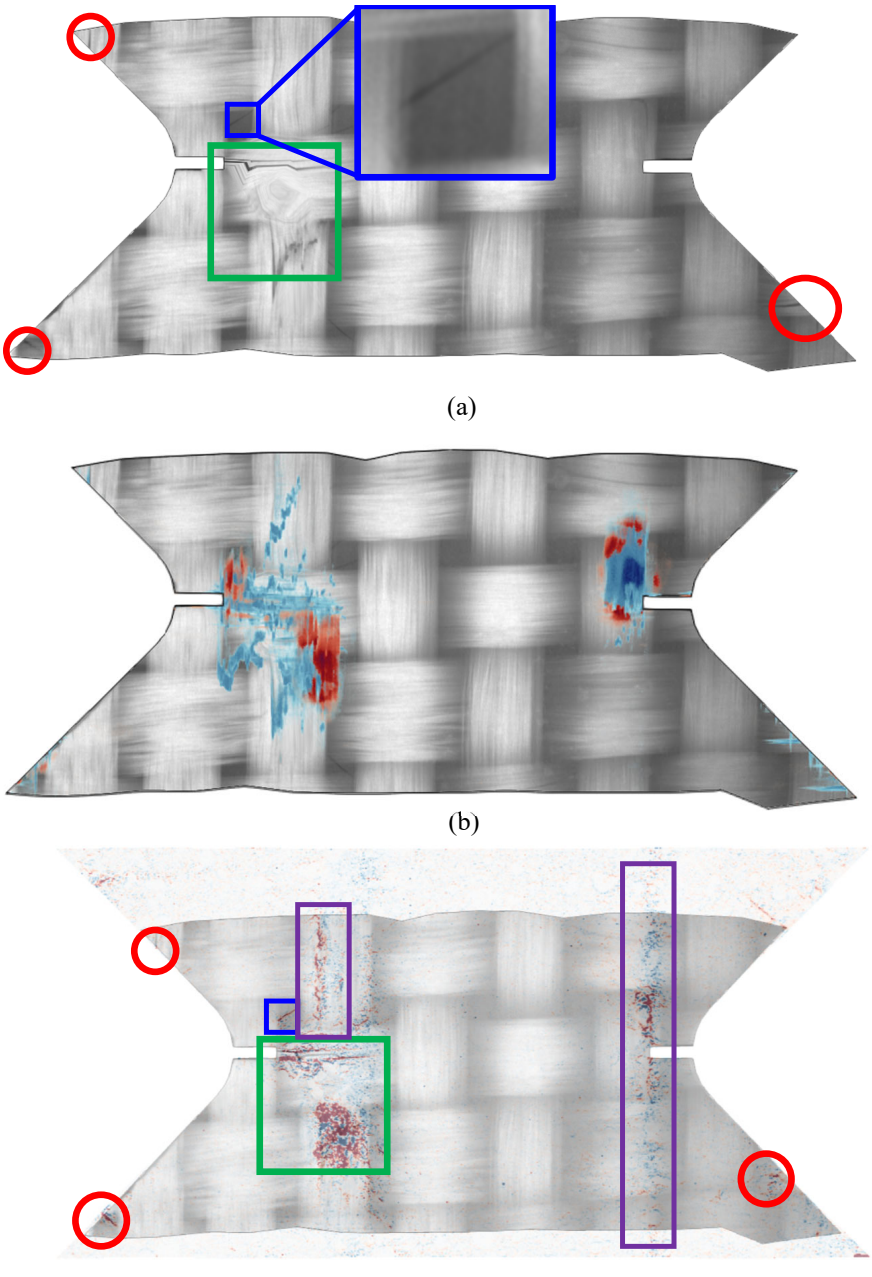

(a)

(b)

(c)

Fig. 21: Corrected deformed scan 5 (surface view) (a) with depicted damage zones, (b) laid over the corresponding DVC residual map, and (c) laid over HMC residuals of camera 1 at the same loading stage. The green and blue squares denote the major damage developed in the gauge region, whereas the red circles highlight damage on the peripheral areas. The purple rectangles denote the vertical residual HM correlation bands.

Figure 21(a) highlights damage on the corrected volume. The red circles depict cracks developing on the peripheral areas of the sample, which was also observed in HMC residuals laid over the corrected volume (Figure 21(c)). The main crack that developed in the matrix (blue square) is visible in the DVC and HMC results. A significant difference is observed in the DVC and HMC residuals (Figure 21(b,c)). The vertical bands observable in the HMC results are not visible in the DVC residuals. Additionally, the residual bands laid over the corrected volume correspond to yarn edges. It is concluded that shear did occur. However, there was no significant damage within the bulk of the sample, mainly on the speckle pattern. The cracking of the speckle pattern thus explained the absence of vertical residual bands in DVC analyses.

Several damage mechanisms were determined from the present results. The green regions depict the major damage observed with all three modalities, which corresponds to yarn breakage. The red circles denote intra-yarn debonding, which was only revealed by having access to the bulk architecture of the material. The blue square highlights matrix cracking. Using the latter, horizontal surface matrix cracks across the ROI (Figure 14) were detected but not distinguished using DVC. This finding highlights the drawback of the *ex-situ* CT protocol since the surface cracks closed while unloaded.

6. Conclusion and outlook

In this research, a tensile test was conducted on a woven glass fiber sample with two notches using the Modified Arcan Fixture (MAF). The used hybrid optical setup consisted of two visible light cameras and one infrared camera. To enrich the analysis, X-ray tomography was introduced as a third modality, thus creating a multimodal framework in which all imaging devices complemented each other. The HM correlation approach was not employed previously for the characterization of composite, only metals [36, 34]. Furthermore, by adding a third modality further enriches the experimental protocol and the composite characterization.

The key findings are as follows:

- Brightness and contrast corrections (BCCs) proved helpful in detecting damage using the infrared images. For the visible light images, BCCs did not significantly reduce the residuals. This observation demonstrates that the gray levels were essentially conserved (except in the damaged zones at the end of the test).

- Combining X-ray tomography with the hybrid multiview framework with a *unique* FE discretization revealed multiple damage mechanisms, namely, surface and bulk matrix cracking, yarn breakage, and intra-yarn debonding.

- Damage underwent an asymmetric development around both notches, thereby indicating a significant influence of the underlying architecture of the woven fabric.

The multimodal framework presented in this study is not limited to a specific type of material or loading history. The procedure was designed to be robust and versatile. Given the capabilities of the MAF to apply different loading regimes to planar samples, the next step is to explore how woven FRPs respond under more complex loading scenarios. Such analyses will provide deeper insight into damage development, thus enhancing the potential applications of the studied material in various industries.

Acknowledgements

This work was performed within the FULLINSPECT project supported by the Croatian Science Foundation (UIP-2019-04-5460 Grant). AZ was also supported through the Incoming International Scholarship Program of ENS Paris-Saclay. This work was also partially supported by the NPOO.C3.2.R3-I1.04.0121.

CRediT author statement

Zaplatić, A. - Conceptualization, Methodology, Software, Formal analysis, Investigation, Data Curation, Writing - Original Draft

Tomičević, Z. - Conceptualization, Methodology, Formal analysis, Investigation, Data Curation, Project administration, Funding acquisition, Supervision, Writing - Review &

Editing

Chang, X. - Software, Writing - Review & Editing

Kosec, P. - Resources, Writing - Review & Editing

Roux, S. - Conceptualization, Writing - Review & Editing

Hild, F. - Conceptualization, Methodology, Investigation, Data Curation, Supervision, Writing - Review & Editing

Declaration of competing interest

The authors have no conflict of interest to declare.

Declaration of generative AI in scientific writing

The authors declare that no generative AI was employed.

Appendix A

This appendix gathers the theoretical parts for DVC and the XCT scanning parameters.

FE-based Digital Volume Correlation

FE-based Digital Volume Correlation is the 3D extension of 2D (surface) digital image correlation (DIC). Instead of 2D images, DVC deals with reconstructed volumes where each voxel contains gray levels determined by the absorption coefficients to X-rays. The methodology is identical to 2D FE-based DIC where the gray level conservation is assumed between the reference volume f^{3D} and the deformed volume g^{3D}

$$f^{3D}\left(\mathbf{x}\right) = g^{3D}\left(\mathbf{x} + \mathbf{u}\left(\mathbf{x}\right)\right) \tag{21}$$

where $\mathbf{x}$ is the voxel position, and $\mathbf{u}\left(\mathbf{x}\right)$ the displacement field. The unknown displacement field is obtained by minimizing the sum of squared differences

$$\Omega^2_{DVC} = \sum_{ROI} \left(f^{3D}\left(\mathbf{x}\right) - g^{3D}\left(\mathbf{x} + \mathbf{u}\left(\mathbf{x}\right)\right)\right)^2 \tag{22}$$

in which the gray level residuals are minimized over the ROI. The displacement field is parameterized as

$$\mathbf{u}(\mathbf{x}) = \sum_{i=1}^{N_{DOF}} u_i \mathbf{\Psi}_i(\mathbf{x}) \tag{23}$$

where $\mathbf{\Psi}_i$ are the shape functions of the FE mesh, and u_i the nodal displacements. The summand of the cost function is linearized, and Ω^2_{DVC} is iteratively minimized with a Gauss-Newton scheme [54]. The ill-posedness of this framework is further reduced by adding mechanical regularization [46, 47], which is based on the equilibrium gap in linear elasticity. Within this framework, the L2-norm of the unbalanced bulk nodal forces and traction-free surfaces is considered. The equilibrium gap cost function is defined as

$$\Omega^2_b(\{\mathbf{u}\}) = \{\mathbf{u}\}^\top [\mathbf{K}_b]^\top [\mathbf{K}_b] \{\mathbf{u}\} \tag{24}$$

where $[\mathbf{K}_b]$ is the partial stiffness matrix for the bulk and traction-free nodes. The nodal DOFs on the loaded boundaries are not included, and additional penalization is required since the external forces are unknown [47]. Another cost function is introduced

$$\Omega_s^2(\{\mathbf{u}\}) = \{\mathbf{u}\}^\top [\mathbf{K}_s]^\top [\mathbf{L}][\mathbf{K}_s]\{\mathbf{u}\} \tag{25}$$

where $[\mathbf{L}]$ is the Laplace-Beltrami operator, and $[\mathbf{K}_s]$ the partial stiffness matrix for the boundary nodes. All three cost functions are combined in a single global cost function Ω_t with proper weighting

$$\Omega_t^2(\{\mathbf{u}\}) = \widetilde{\Omega}_{DVC}^2(\{\mathbf{u}\}) + \omega_b \widetilde{\Omega}_b^2(\{\mathbf{u}\}) + \omega_s \widetilde{\Omega}_s^2(\{\mathbf{u}\}) \tag{26}$$

with

$$\widetilde{\Omega}_{DVC}^2(\{\mathbf{u}\}) = \frac{\Omega_{DVC}^2(\{\mathbf{u}\})}{\{\mathbf{v}\}^\top [\mathbf{M}]\{\mathbf{v}\}} \quad , \quad \widetilde{\Omega}_b^2(\{\mathbf{u}\}) = \frac{\Omega_b^2(\{\mathbf{u}\})}{\Omega_b(\{\mathbf{v}\})} \quad , \quad \widetilde{\Omega}_s^2(\{\mathbf{u}\}) = \frac{\Omega_s(\{\mathbf{u}\})}{\Omega_s(\{\mathbf{v}\})} \tag{27}$$

where $\{\mathbf{v}\}$ gathers the nodal displacements associated with a trial displacement field defined for a shear wave of wavevector $\mathbf{k}$, and the weighted penalties are defined for the chosen regularization lengths λ

$$\omega_b = (\lambda_b \, |\mathbf{k}|)^4 \quad , \quad \omega_s = (\lambda_s \, |\mathbf{k}|)^4 \tag{28}$$

Mechanical regularization can be considered a low-pass filter, which imposes smoothness of measured displacement fields through the regularization lengths λ. It should be noted that mechanical regularization is active only for lengths larger than the element size.

CT scanning parameters

Table 3 details the hardware specifications of the employed CT scanner. Due to the scanner design, a filter for polymers was mandatory to avoid damaging the detector.

Table 3: Hardware parameters of the CT scans

CT scanner	WENZEL® exaCT® S130
X-Ray source	Hamamatsu L9181-02
Filter	built-in for polymers
Voltage	80 kV
Current	190 µA
Focal point size	5 µm
Detector - X-ray source distance	205 mm
Object - X-ray source distance	54 mm
Detector	Flat detector (3Mpx)
Detector definition	2304×1300 px

Two types of scans were acquired, designated as HQ and LQ. The corresponding parameters are listed in Table 4; the first scan with HQ conditions, whereas all the others were acquired with the LQ parameters. The scanning parameters for both scan qualities were identical, except for the number of projections, which was almost three times higher for the HQ setting.

Table 4: CT scans acquisition parameters

Scan quality	HQ	LQ
Number of projections	2100	720
Angular amplitude	$0.17°$	$0.5°$
Projection acquisition speed	0.05 pr./s	0.22 pr./s
Scanning duration	3h 40 min	55 min
Gray scale amplitude	16 bit (converted to 8 bit)	
Volume size	$2234 \times 2234 \times 979$ vx	
Field of view	$35.7 \times 35.7 \times 15.67$ mm	
Volume scale	1 vx = 16 µm	
Texture	Natural	

References

[1] M. E. Torbali, A. Zolotas, N. P. Avdelidis, A state-of-the-art review of non-destructive testing image fusion and critical insights on the inspection of aerospace composites towards sustainable maintenance repair operations, Applied Sciences 13 (2023) 2732. doi:10.3390/app13042732.

[2] R. Hsissou, R. Seghiri, Z. Benzekri, M. Hilali, M. Rafik, A. Elharfi, Polymer composite materials: A comprehensive review, Composite Structures 262 (2021) 113640. doi:10.1016/j.compstruct.2021.113640.

[3] A. Vrgoč, Z. Tomičević, B. Smaniotto, F. Hild, Application of different imaging techniques for the characterization of damage in fiber reinforced polymer, Composites Part A: Applied Science and Manufacturing 150 (11 2021). doi:10.1016/j.compositesa.2021.106576.

[4] Q. Guo, Y. Zhang, D. Li, X. Sun, M. Li, L. Chen, Experimental characterization of the compressive properties and failure mechanism of novel multiaxial 3d woven composites, Composites Communications 28 (2021) 100905. doi:10.1016/j.coco.2021.100905.

[5] A. Zaplatić, Z. Tomičević, D. Čakmak, F. Hild, Improvement of the arcan setup for the investigation of thin sheet behavior under shear loading, Experimental Mechanics 62 (2022) 313–332. doi:10.1007/s11340-021-00762-1.

[6] M. A. Sutton, Computer vision-based, noncontacting deformation measurements in mechanics: A generational transformation, Applied Mechanics Reviews 65 (2013). doi:10.1115/1.4024984.

[7] J. Holmes, S. Sommacal, R. Das, Z. Stachurski, P. Compston, Digital image and volume correlation for deformation and damage characterisation of fibre-reinforced composites: A review, Composite Structures 315 (2023) 116994. doi:10.1016/j.compstruct.2023.116994.

URL https://linkinghub.elsevier.com/retrieve/pii/S0263822323003380

[8] C. Ibarra-Castanedo, J. R. Tarpani, X. P. V. Maldague, Nondestructive testing with thermography, European Journal of Physics 34 (2013) S91. doi:10.1088/0143-0807/34/6/S91.

[9] J. Zalameda, W. Winfree, Detection and characterization of damage in quasi-static loaded composite structures using passive thermography, Sensors 18 (2018) 3562. doi:10.3390/s18103562.

[10] A. Buljac, C. Jailin, A. Mendoza, J. Neggers, T. Taillandier-Thomas, A. Bouterf, B. Smaniotto, F. Hild, S. Roux, Digital volume correlation: Review of progress and challenges, Experimental Mechanics 58 (2018). doi:10.1007/s11340-018-0390-7.

[11] A. Vrgoč, Z. Tomičević, B. Smaniotto, F. Hild, Damage characterization in fiber reinforced polymer via digital volume correlation. coupled systems mechanics, Coupled System Mechanics 10 (2021) 545–560. doi:10.12989/csm.2021.10.6.545.
URL https://hal.science/hal-03482350

[12] G. Broggiato, Adaptive image correlation technique for full-field strain measurement, in: C. Pappalettere (Ed.), 12th International Conference on Experimental Mechanics, McGraw Hill, Lilan (Italy), 2004, pp. 420–421.

[13] Y. Sun, J. Pang, C. Wong, F. Su, Finite-element formulation for a digital image correlation method, Applied Optics 44 (34) (2005) 7357–7363.

[14] G. Besnard, F. Hild, S. Roux, "finite-element" displacement fields analysis from digital images: Application to portevin-le châtelier bands, Experimental Mechanics 46 (2006) 789–803. doi:10.1007/s11340-006-9824-8.

[15] F. Hild, S. Roux, Comparison of local and global approaches to digital image correlation, Experimental Mechanics 52 (2012) 1503–1519. doi:10.1007/s11340-012-9603-7.

[16] M. Flores, D. Mollenhauer, V. Runatunga, T. Beberniss, D. Rapking, M. Pankow, High-speed 3d digital image correlation of low-velocity impacts on composite plates, Composites Part B: Engineering 131 (2017) 153–164. doi:https://doi.org/10.1016/j.compositesb.2017.07.078.

[17] R. Fouque, R. Bouclier, J.-C. passieux, J.-N. ël Périé, Stereo digital image correlation: formulations and perspectives, Comptes Rendus. Mécanique 349 (2021) 453–463. doi:https://doi.org/10.5802/crmeca.93.

[18] M. Sutton, J. Yan, V. Tiwari, H. Schreier, J. Orteu, The effect of out-of-plane motion on 2d and 3d digital image correlation measurements, Optics and Lasers in Engineering 46 (2008) 746–757. doi:10.1016/j.optlaseng.2008.05.005.

[19] X. Chang, C. L. Gourriéreca, L. Turpin, M. Berny, F. Hild, S. Roux, Proper generalized decomposition stereocorrelation to measure kinematic fields for high speed impact on laminated glass, Computer Methods in Applied Mechanics and Engineering 415 (2023) 116217. doi:10.1016/j.cma.2023.116217.

[20] B. Beaubier, J.-E. Dufour, F. Hild, S. Roux, S. Lavernhe, K. L. Taillard, Cad-based calibration and shape measurement with stereodic principle and application on test and industrial parts, Experimental Mechanics 54 (2014) 329–341. doi:ff10.1007/s11340-013-9794-6ff.ffhal-00974363.

[21] M. A. Sutton, J. J. Orteu, H. Schreier, Image correlation for shape, motion and deformation measurements: Basic concepts, theory and applications, Springer US, 2009. doi:10.1007/978-0-387-78747-3.

[22] J.-E. Dufour, B. Beaubier, F. Hild, S. Roux, Cad-based displacement measurements

with stereo-dic, Experimental Mechanics 55 (2015) 1657–1668. doi:https://doi.org/10.1007/s11340-015-0065-6.

[23] G. Besnard, J.-M. Lagrange, F. Hild, S. Roux, C. Voltz, Characterization of necking phenomena in high speed experiments by using a single camera, EURASIP Journal on Image and Video Processing 2010 (2010) 215956.
URL https://hal.science/hal-00497354

[24] L. Yu, B. Pan, Single-camera stereo-digital image correlation with a four-mirror adapter: optimized design and validation, Optics and Lasers in Engineering 87 (2016) 120–128. doi:10.1016/j.optlaseng.2016.03.014.

[25] M. Berny, T. Archer, P. Beauchêne, A. Mavel, F. Hild, Displacement uncertainty quantifications in t3-stereocorrelation, Experimental Mechanics 61 (2021) 771–790. doi:10.1007/s11340-021-00690-0.

[26] J.-E. Dufour, F. Hild, S. Roux, Shape, displacement and mechanical properties from isogeometric multiview stereocorrelation, The Journal of Strain Analysis for Engineering Design 50 (2015) 470–487. doi:10.1177/0309324715592530.
URL https://hal.archives-ouvertes.fr/hal-01198921

[27] L. Dubreuil, J.-E. Dufour, Y. Quinsat, F. Hild, Mesh-based shape measurements with stereocorrelation principle and first results, Experimental Mechanics 56 (2016) 1231–1242. doi:10.1007/s11340-016-0158-.

[28] J.-E. Pierré, J.-C. Passieux, J.-N. ël Périé, Finite element stereo digital image correlation: Framework and mechanical regularization, Experimental mechanics 57 (2017) pages443–456. doi:10.1007/s11340-016-0246-y.

[29] K. S.A., F. Brachelet, F. Breaban, D. Defer, Defect detection in cfrp by infrared thermography with co2 laser excitation compared to conventional lock-in infrared thermography, Composites Part B: Engineering 69 (2015) 1–5. doi:https://doi.org/10.1016/j.compositesb.2014.09.018.

[30] C. Maierhofer, M. Röllig, M. Gower, M. Lodeiro, G. Baker, C. Monte, A. Adibekyan, B. Gutschwager, L. Knazowicka, A. Blahut, Evaluation of different techniques of active thermography for quantification of artificial defects in fiber-reinforced composites using thermal and phase contrast data analysis, International Journal of Thermophysics 39 (2018). doi:10.1007/s10765-018-2378-z.

[31] V. Munoz, B. Valès, M. Perrin, M. L. Pastor, H. Welemane, A. Cantarel, M. Karama, Damage detection in cfrp by coupling acoustic emission and infrared thermography, Composites Part B: Engineering 85 (2016) 68–75. doi:10.1016/j.compositesb.2015.09.011.

[32] J. Zalameda, W. Winfree, Passive thermography measurement of damage depth during composites load testing, Frontiers in Mechanical Engineering 7 (2021) 651149. doi:10.3389/fmech.2021.651149.

[33] A. Charbal, J. E. Dufour, F. Hild, M. Poncelet, L. Vincent, S. Roux, Hybrid stereocorrelation using infrared and visible light cameras, Experimental Mechanics 56 (2016) 845–860. doi:10.1007/s11340-016-0127-4.

[34] Y. Wang, A. Charbal, F. Hild, S. Roux, L. Vincent, Crack initiation and propagation under thermal fatigue of austenitic stainless steel, International Journal of Fatigue 124 (2019) 149–166. doi:10.1016/j.ijfatigue.2019.02.036.

[35] Y. Wang, A. Charbal, J. E. Dufour, F. Hild, S. Roux, L. Vincent, Hybrid multiview correlation for measuring and monitoring thermomechanical fatigue test, Experimental Mechanics 60 (2020) 13–33. doi:10.1007/s11340-019-00500-8.

[36] A. Charbal, S. Roux, F. Hild, L. Vincent, Spatiotemporal regularization for digital image correlation: Application to infrared camera frames, International Journal for Numerical Methods in Engineering 114 (2018) 1331–1349. doi:10.1002/nme.5788.

[37] M. Gao, Z. Zhou, K. Ding, X. Wang, Detection of crack defects in carbon fiber composites using passive infrared thermography, Ferroelectrics 607 (2023) 154–172. doi:10.1080/00150193.2023.2198383.

[38] A. Charbal, S. Roux, F. Hild, L. Vincent, Regularised digital-level corrections for infrared image correlation, Quantitative InfraRed Thermography Journal 15 (2018) 172–193. doi:10.1080/17686733.2018.1425955.

[39] V. Sciuti, R. Canto, J. Neggers, F. Hild, On the benefits of correcting brightness and contrast in global digital image correlation: Monitoring cracks during curing and drying of a refractory castable, Optics and Lasers in Engineering 136 (2021) 106316,. doi:10.1016/j.optlaseng.2020.106316.

[40] M. Stamm, P. Krüger, H. Pfeiffer, B. Köhler, J. Reynaert, M. Wevers, In-plane heat-wave thermography as digital inspection technique for fasteners in aircraft fuselage panels, Applied Sciences 11 (2021) 132. doi:10.3390/app11010132.

[41] E. Maire, P. J. Withers, Quantitative x-ray tomography, International Materials Reviews 59 (2014) 1–43. doi:10.1179/1743280413Y.0000000023.

[42] A. Vrgoč, Z. Tomičević, B. Smaniotto, F. Hild, Characterization of glass fiber reinforced polymer via digital volume correlation: Quantification of strain activity and damage growth, Composites Science and Technology 234 (2023) 109932. doi:10.1016/j.compscitech.2023.109932.

[43] J. Holmes, S. Sommacal, R. Das, Z. Stachurski, P. Compston, Characterisation of off-axis tensile behaviour and mesoscale deformation of woven carbon-fibre/peek using digital image correlation and x-ray computed tomography, Composites Part B: Engineering 229 (2022) 109448. doi:https://doi.org/10.1016/j.compositesb.2021.109448.

[44] A. Vrgoč, Z. Tomičević, B. Smaniotto, F. Hild, Characterization of glass fiber reinforced polymer via digital volume correlation: Investigation of notch sensitiv-

ity, Mechanics of Materials 177 (2023) 104552. doi:10.1016/j.mechmat.2022.104552.

[45] Z. Tomičević, A. Bouterf, R. Surma, F. Hild, Damage observation in glass fiber reinforced composites via μ-tomography, Materials Today: Proceedings 12 (2019) 185–191. doi:10.1016/j.matpr.2019.03.093.

[46] Z. Tomičevć, F. Hild, S. Roux, Mechanics-aided digital image correlation, Journal of Strain Analysis for Engineering Design 48 (2013) 330–343. doi:10.1177/0309324713482457.

[47] A. Mendoza, J. Neggers, F. Hild, S. Roux, Complete mechanical regularization applied to digital image and volume correlation, Computer Methods in Applied Mechanics and Engineering 355 (2019) 27–43. doi:10.1016/j.cma.2019.06.005.

[48] T. Sathishkumar, S. Satheeshkumar, J. Naveen, Glass fiber-reinforced polymer composites - a review, Journal of Reinforced Plastics and Composites 33 (2014) 1258–1275. doi:10.1177/0731684414530790.

[49] V. Lepetit, F. Moreno-Noguer, P. Fua, Epnp: An accurate o(n) solution to the pnp problem, International Journal of Computer Vision 81 (2009) 155–166. doi:10.1007/s11263-008-0152-6.

[50] F. Barone, M. Marrazzo, C. J. Oton, Camera calibration with weighted direct linear transformation and anisotropic uncertainties of image control points, Sensors 20 (2020) 1175. doi:10.3390/s20041175.

[51] X. Chang, C. L. Gourriérec, F. Hild, S. Roux, Brightness and contrast corrections for stereocorrelationglobal and instantaneous formulation with spatial regularization, Mechanical Systems and Signal Processing 208 (2024) 111057. doi:doi.org/10.1016/j.ymssp.2023.111057.

[52] A. Zaplatić, Z. Tomičević, X. Chang, I. Skozrit, S. Roux, F. Hild, Hybrid infrared-visible multiview correlation to study damage in a woven composite complex-shaped specimen, Coupled Systems Mechanics 12 (5 2023). doi:doi.org/10.12989/csm.2023.12.5.000.

[53] F. dell'Isola, P. Seppecher, M. Spagnuolo, E. Barchiesi, F. Hild, T. Lekszycki, I. Giorgio, L. Placidi, U. Andreaus, M. Cuomo, S. Eugster, A. Pfaff, K. Hoschke, R. Langkemper, E. Turco, R. Sarikaya, A. Misra, M. De Angelo, F. D'Annibale, A. Bouterf, X. Pinelli, A. Misra, B. Desmorat, M. Pawlikowski, C. Dupuy, D. Scerrato, P. Peyre, M. Laudato, L. Manzari, P. Göransson, C. Hesch, S. Hesch, P. Franciosi, J. Dirrenberger, F. Maurin, Z. Vangelatos, C. Grigoropoulos, V. Melissinaki, M. Farsari, W. Muller, E. Abali, C. Liebold, G. Ganzosch, P. Harrison, R. Drobnicki, L. Igumnov, F. Alzahrani, T. Hayat, Advances in Pantographic Structures: Design, Manufacturing, Models, Experiments and Image Analyses, Continuum Mechanics and Thermodynamics 31 (4) (2019) 1231–1282.

[54] S. Roux, F. Hild, P. Viot, D. Bernard, Three-dimensional image correlation from x-ray computed tomography of solid foam, Composites Part A: Applied Science and Manufacturing 39 (2008) 1253–1265. doi:10.1016/j.compositesa.2007.11.011.

List of Figures

List of Tables